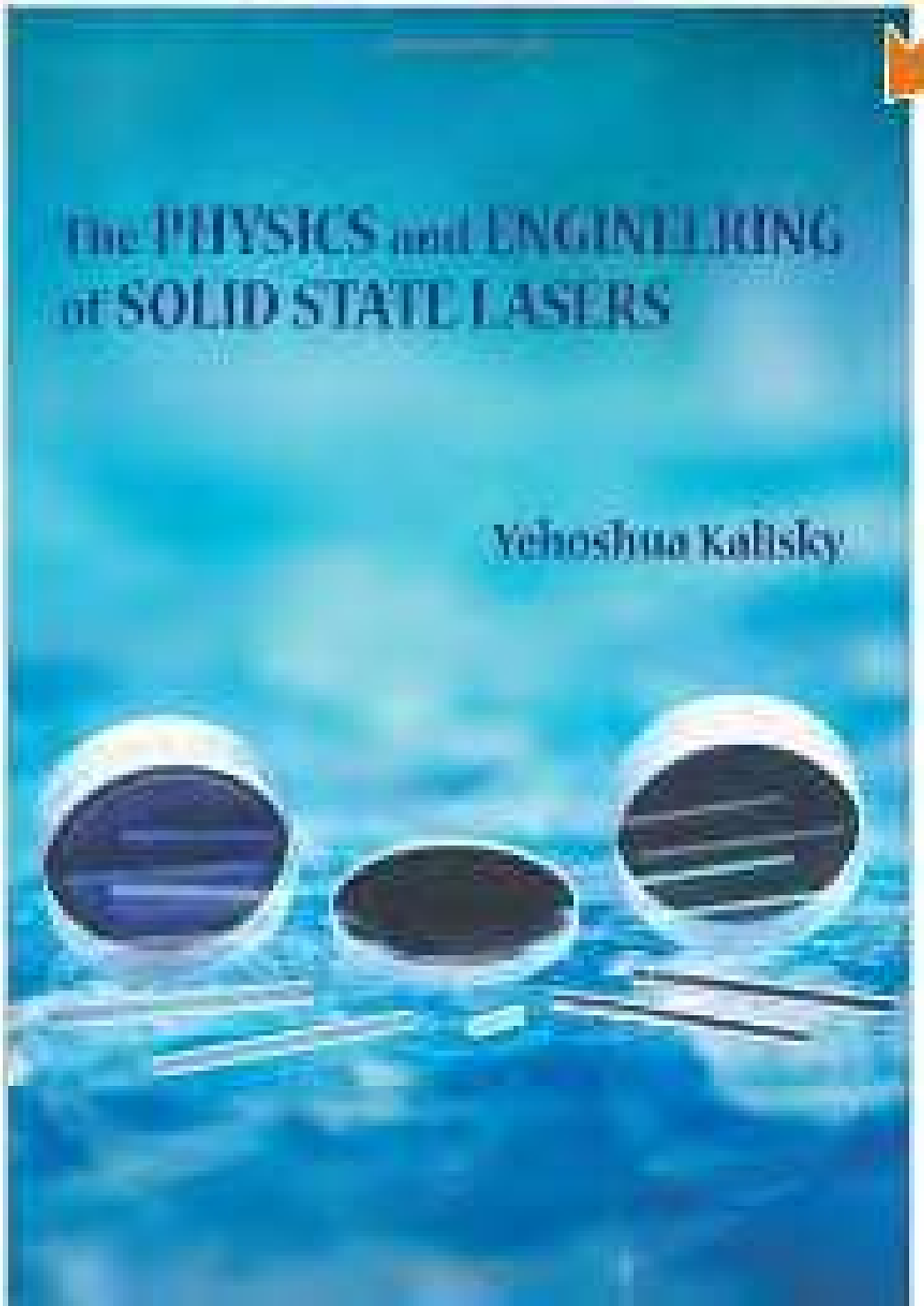

The PHYSICS and ENGINEERING of SOLID STATE LASERS

Tutorial Texts Series

- *The Physics and Engineering of Solid State Lasers*, Yehoshua Kalisky, Vol. TT71
- *Thermal Infrared Characterization of Ground Targets and Backgrounds, Second Edition*, Pieter A. Jacobs, Vol. TT70
- *Introduction to Confocal Fluorescence Microscopy*, Michiel Müller, Vol. TT69
- *Artificial Neural Networks: An Introduction*, Kevin L. Priddy and Paul E. Keller, Vol. TT68
- *Basics of Code Division Multiple Access (CDMA)*, Raghuveer Rao and Sohail Dianat, Vol. TT67
- *Optical Imaging in Projection Microlithography*, Alfred Kwok-Kit Wong, Vol. TT66
- *Metrics for High-Quality Specular Surfaces*, Lionel R. Baker, Vol. TT65
- *Field Mathematics for Electromagnetics, Photonics, and Materials Science*, Bernard Maxum, Vol. TT64
- *High-Fidelity Medical Imaging Displays*, Aldo Badano, Michael J. Flynn, and Jerzy Kanicki, Vol. TT63
- *Diffractive Optics–Design, Fabrication, and Test*, Donald C. O'Shea, Thomas J. Suleski, Alan D. Kathman, and Dennis W. Prather, Vol. TT62
- *Fourier-Transform Spectroscopy Instrumentation Engineering*, Vidi Saptari, Vol. TT61
- *The Power- and Energy-Handling Capability of Optical Materials, Components, and Systems*, Roger M. Wood, Vol. TT60
- *Hands-on Morphological Image Processing*, Edward R. Dougherty, Roberto A. Lotufo, Vol. TT59
- *Integrated Optomechanical Analysis*, Keith B. Doyle, Victor L. Genberg, Gregory J. Michels, Vol. TT58
- *Thin-Film Design: Modulated Thickness and Other Stopband Design Methods*, Bruce Perilloux, Vol. TT57
- *Optische Grundlagen für Infrarotsysteme*, Max J. Riedl, Vol. TT56
- *An Engineering Introduction to Biotechnology*, J. Patrick Fitch, Vol. TT55
- *Image Performance in CRT Displays*, Kenneth Compton, Vol. TT54
- *Introduction to Laser Diode-Pumped Solid State Lasers*, Richard Scheps, Vol. TT53
- *Modulation Transfer Function in Optical and Electro-Optical Systems*, Glenn D. Boreman, Vol. TT52
- *Uncooled Thermal Imaging Arrays, Systems, and Applications*, Paul W. Kruse, Vol. TT51
- *Fundamentals of Antennas*, Christos G. Christodoulou and Parveen Wahid, Vol. TT50
- *Basics of Spectroscopy*, David W. Ball, Vol. TT49
- *Optical Design Fundamentals for Infrared Systems, Second Edition*, Max J. Riedl, Vol. TT48
- *Resolution Enhancement Techniques in Optical Lithography*, Alfred Kwok-Kit Wong, Vol. TT47
- *Copper Interconnect Technology*, Christoph Steinbrüchel and Barry L. Chin, Vol. TT46
- *Optical Design for Visual Systems*, Bruce H. Walker, Vol. TT45
- *Fundamentals of Contamination Control*, Alan C. Tribble, Vol. TT44
- *Evolutionary Computation: Principles and Practice for Signal Processing*, David Fogel, Vol. TT43
- *Infrared Optics and Zoom Lenses*, Allen Mann, Vol. TT42
- *Introduction to Adaptive Optics*, Robert K. Tyson, Vol. TT41
- *Fractal and Wavelet Image Compression Techniques*, Stephen Welstead, Vol. TT40
- *Analysis of Sampled Imaging Systems*, R. H. Vollmerhausen and R. G. Driggers, Vol. TT39
- *Tissue Optics: Light Scattering Methods and Instruments for Medical Diagnosis*, Valery Tuchin, Vol. TT38
- *Fundamentos de Electro-Óptica para Ingenieros*, Glenn D. Boreman, translated by Javier Alda, Vol. TT37
- *Infrared Design Examples*, William L. Wolfe, Vol. TT36
- *Sensor and Data Fusion Concepts and Applications, Second Edition*, L. A. Klein, Vol. TT35
- *Practical Applications of Infrared Thermal Sensing and Imaging Equipment, Second Edition*, Herbert Kaplan, Vol. TT34
- *Fundamentals of Machine Vision*, Harley R. Myler, Vol. TT33
- *Design and Mounting of Prisms and Small Mirrors in Optical Instruments*, Paul R. Yoder, Jr., Vol. TT32
- *Basic Electro-Optics for Electrical Engineers*, Glenn D. Boreman, Vol. TT31
- *Optical Engineering Fundamentals*, Bruce H. Walker, Vol. TT30
- *Introduction to Radiometry*, William L. Wolfe, Vol. TT29
- *Lithography Process Control*, Harry J. Levinson, Vol. TT28

The PHYSICS and ENGINEERING of SOLID STATE LASERS

Yehoshua Kalisky

Tutorial Texts in Optical Engineering
Volume TT71

SPIE
PRESS

Bellingham, Washington USA

Library of Congress Cataloging-in-Publication Data

Kalisky, Yehoshua Y.
The physics and engineering of solid state lasers / Yehoshua Kalisky.
p. cm. — (Tutorial texts in optical engineering ; v. TT 71)
Includes bibliographical references and index.
ISBN 0-8194-6094-X (alk. paper)
1. Solid-state lasers. I. Title. II. Series.

TA1705.K34 2005
621.36'61—dc22 2005026104

Published by

SPIE—The International Society for Optical Engineering
P.O. Box 10
Bellingham, Washington 98227-0010 USA
Phone: +1 360 676 3290
Fax: +1 360 647 1445
Email: spie@spie.org
Web: http://spie.org

Printed in the United States of America.

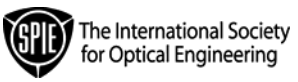

Introduction to the Series

Since its conception in 1989, the Tutorial Texts series has grown to more than 60 titles covering many diverse fields of science and engineering. When the series was started, the goal of the series was to provide a way to make the material presented in SPIE short courses available to those who could not attend, and to provide a reference text for those who could. Many of the texts in this series are generated from notes that were presented during these short courses. But as stand-alone documents, short course notes do not generally serve the student or reader well. Short course notes typically are developed on the assumption that supporting material will be presented verbally to complement the notes, which are generally written in summary form to highlight key technical topics and therefore are not intended as stand-alone documents. Additionally, the figures, tables, and other graphically formatted information accompanying the notes require the further explanation given during the instructor's lecture. Thus, by adding the appropriate detail presented during the lecture, the course material can be read and used independently in a tutorial fashion.

What separates the books in this series from other technical monographs and textbooks is the way in which the material is presented. To keep in line with the tutorial nature of the series, many of the topics presented in these texts are followed by detailed examples that further explain the concepts presented. Many pictures and illustrations are included with each text and, where appropriate, tabular reference data are also included.

The topics within the series have grown from the initial areas of geometrical optics, optical detectors, and image processing to include the emerging fields of nanotechnology, biomedical optics, and micromachining. When a proposal for a text is received, each proposal is evaluated to determine the relevance of the proposed topic. This initial reviewing process has been very helpful to authors in identifying, early in the writing process, the need for additional material or other changes in approach that would serve to strengthen the text. Once a manuscript is completed, it is peer reviewed to ensure that chapters communicate accurately the essential ingredients of the processes and technologies under discussion.

It is my goal to maintain the style and quality of books in the series, and to further expand the topic areas to include new emerging fields as they become of interest to our reading audience.

Arthur R. Weeks, Jr.
University of Central Florida

Dedicated to the memory of my parents

and my father-in-law

Contents

List of Abbreviations / xiii

Preface / xv

Chapter 1 Introduction / 1

1.1 Historical Background / 1
1.1.1 Early developments / 1
1.1.2 Technological developments / 2
1.2 Laser Materials / 3
1.2.1 Elements of a typical laser oscillator / 3
1.2.1.1 Gain medium / 4
1.2.1.2 The laser pumping unit and pumping methods / 4
1.2.2 Optics / 5
References / 6

Chapter 2 Solid State Laser Materials / 7

2.1 Properties / 7
2.1.1 Optics / 8
2.1.2 Material design / 8
2.1.3 Mechanical design / 9
2.2 Doping Ions / 11
2.2.1 Laser host materials / 13
2.3 General Properties of Hosts / 13
2.3.1 Optical properties / 13
2.3.2 Chemical properties / 14
2.3.3 Mechanical properties / 14
2.3.4 Thermal properties / 14
References / 15

Chapter 3 Structure and Bonding of Solids / 17

3.1 Crystal Structure / 17
3.1.1 Types of crystals / 18
3.2 Crystal Binding / 18

3.2.1 Van der Waals interaction / 19
3.2.2 Ionic bonding / 20
3.2.3 Covalent bonding / 22
References / 24

Chapter 4 Garnet Crystals as Laser Hosts / 25

4.1 Physical Characteristics of Garnets and Mixed Garnets / 27
4.2 Chromium- and Neodymium-Doped Garnets / 28
4.3 Disordered (Mixed) Garnets / 33
4.4 Glass and Crystalline Ceramics / 35
References / 40

Chapter 5 Fluoride Laser Crystals: $YLiF_4$ (YLF) / 43

5.1 Thermal and Mechanical Properties of YLF / 43
5.1.1 Estimate of thermal load at fracture / 44
5.2 Nonradiative Losses in YLF / 50
5.3 Neodymium-Doped YLF / 51
5.4 Holmium-Doped YLF / 53
5.5 Thulium-Doped YLF / 54
5.6 Other Fluoride Crystals / 55
5.7 Cascade Emission / 57
5.8 Upconversion / 58
5.8.1 Applications to upconversion / 60
References / 62

Chapter 6 Photophysics of Solid State Laser Materials / 67

6.1 Properties of the Lasing Ion / 67
6.1.1 Absorption / 67
6.1.1.1 Homogeneous and nonhomogeneous broadening / 73
6.1.2 Spontaneous emission / 73
6.1.3 Stimulated emission / 74
6.1.4 Oscillator strength / 75
6.2 Nonradiative Transition / 79
6.2.1 Energy gap and temperature dependence of multiphonon relaxation / 80
6.2.2 Temperature dependence of nonradiative relaxation / 88
References / 90

Chapter 7 Energy Transfer / 93

7.1 Introduction / 93
7.2 Radiative Energy Transfer / 93
7.3 Nonradiative Energy Transfer / 94

7.3.1 Basic mechanisms of energy transfer / 94
7.3.1.1 Resonant energy transfer / 94
7.3.1.2 Exchange interaction / 96
7.3.1.3 Phonon-assisted energy transfer / 97
7.3.1.4 Pathways of excited state relaxation / 98
7.3.1.5 Statistical model (Inokuti-Hirayama model) / 100
References / 103

Chapter 8 Lasing Efficiency and Sensitization / 105

8.1 Introduction / 105
8.2 Why Is Energy Transfer Needed? / 105
8.2.1 Examples of CTH-doped systems / 107
8.3 Temperature Effects / 108
8.4 The Effect of Tm^{3+} Concentration / 110
8.5 The Effect of Cr^{3+} Concentration / 113
8.6 Nature of Ionic Interaction / 113
8.6.1 Cr-Tm interaction / 113
8.6.2 Tm-Tm interaction / 114
8.6.3 Tm-Ho interaction / 116
8.6.4 Ho-Tm back interaction / 117
8.6.5 Selective energy transfer / 121
References / 122

Chapter 9 Two-Micron Lasers: Holmium- and Thulium-Doped Crystals / 125

9.1 Introduction / 125
9.2 Advantages of the Holmium Laser / 127
9.2.1 Utilizing energy transfer / 127
9.3 Conventional Pumping / 128
9.3.1 CW laser operation / 128
9.3.2 Pulsed operation of holmium lasers / 130
9.4 Diode Pumping / 130
9.4.1 End-pumped 2-μm lasers / 130
9.4.2 Side-pumped 2-μm lasers / 136
References / 137

Chapter 10 Yb:YAG Laser / 141

10.1 Introduction / 141
10.2 End-pumping / 145
10.3 Side-Pumping / 147
10.4 Face-Pumping or Thin Disk Configuration / 149
References / 154

Chapter 11 More on Other Crystals: Fluorides and Vanadates / 157

11.1 Introduction / 157
11.2 Laser Crystals: YLF ($YLiF_4$) and YVO_4 / 158
11.3 Pumping Schemes / 158
11.3.1 Diode end-pumping of Nd:YLF / 161
11.3.2 Side-pumping of Nd:YLF / 165
11.4 Diode End-Pumping of Nd:YVO_4 and Nd:$GdVO_4$ / 166
11.4.1 Advantages and disadvantages of vanadate crystals / 166
11.4.2 Q-switching and mode-locking operation / 176
References / 183

Appendix: Diode-Pumped Solid State Lasers / 189

A.1 Introduction / 189
A.2 Advantages of Diode-Pumping / 189
A.3 Pumping Schemes / 191
A.4 Longitudinal Pumping / 191
A.5 Transverse Pumping / 194
A.6 Types of Diodes / 196
A.7 Temperature Control / 198
References / 200

Index / 201

List of Abbreviations

AR	antireflecting
ASE	amplified spontaneous emission
at. %	atomic percent
BEL	lanthanum beryllate
CLBO	cesium-lithium triborate
CPA	chirped pulse amplification
CTH	chromium-thulium-holmium (Cr:Tm:Ho)
CW	continuous wave
DH	double heterostructure
EDD	electric dipole-dipole
EDQ	electric dipole-quadrupole
EM	electromagnetic
EQQ	electric quadrupole-quadrupole
ESA	excited state absorption
FWHM	full width at half maximum
gcd	greatest common divisor
$GDVO_4$	gadolinium vanadate
GGG	gadolinium-gallium garnet
GRIN lens	graded-index lens
GSAG	gallium-scandium-aluminum garnet
GSGG	gadolinium-scandium-gallium garnet
HR	high reflectivity
HRC	high reflectivity coating
HT	high transmission
KTP	potassium tytanyl phosphate, $KTiOPO_4$
LBO	lithium triborate
LDPSSL	laser diode-pumped solid state lasers
LED	light-emitting diode
LGVO	lanthanum-gadolinium vanadate
LIDAR	light detection and ranging
MOPA	multipass oscillator/amplifier
MPR	multiphonon relaxation
M-SLED	monolithic surface-emitting laser diodes
MTTF	mean time to failure
NA	numerical aperture

OPO	optical parametric oscillation
PPKTP	periodically poled KTP
PPLN	periodically poled lithium niobate
QCW	quasi-continuous wave
QW	quantum well
RESG	rare-earth-doped scandium garnet
RGB	red, green, and blue
ROC	radius of curvature
SESAM	semiconductor saturable absorber mirror
SHG	second harmonic generation
TE	thermoelectric
VCR	variable configuration resonator
VPS	virtual point source
YAG	yttrium-aluminum garnet
YAP	yttrium aluminum perovskite
YLF	yttrium-lithium-fluoride
YSAG	yttrium-scandium-aluminum garnet
YSGG	yttrium-scandium-gallium garnet
YVO_4	yttrium vanadate

Preface

The last decade has seen important technological developments in various aspects of solid state lasers and their applications. As a result, there has been a need in the scientific community to integrate several disciplines such as solid state physics, materials science, photophysics, and dynamic processes in solids to get a better insight into the physics and engineering of solid state lasers. This book is motivated by this need.

The main purpose of this text is to provide a detailed overview and understanding of the mutual influences between the physical and dynamic processes in solids and their lasing properties. This text provides detailed and comprehensive information about the physics of optical dynamics and energy transfer in solids and their effects on the properties of solid state lasers and laser materials. It analyzes the properties of rare-earth or transition-metal-ion-doped crystals, glasses, and ceramics, and the effect of crystal field perturbations on the spectral properties of rare earth and transition-metal ions. It describes the factors influencing the development of new laser materials and discusses the various approaches and considerations for developing new materials, including relevant data tables of basic parameters intended to help with laser design. The text discusses material issues in a manner a laser engineer can comprehend and apply easily to the design of flashlamp and diode-pumped solid state lasers. Finally, the text also provides information about recent developments and technological advances in solid state lasers and photonics that use novel materials and techniques.

The book is based on my short course, "Novel Materials for Coherent Radiation and Frequency Conversion," presented during several Photonics West meetings in San Jose, California (U.S.A.) and the course "The Physics and Engineering of Solid State Lasers," presented during Photonics Europe in Strasbourg, France.

I would like to extend my gratitude to Professor Renata Reisfeld of the Hebrew University in Jerusalem, Israel; Professor Georges Boulon of the University of Lyon in Villeurbanne, France; and Dr. Milan R. Kokta of Saint Gobain Crystals and Detectors in Washougal, Washington (U.S.A.), for their support and inspiration.

Last but not least, I would like to thank SPIE for promoting the idea of writing a book on this topic and Sharon Streams and Margaret Thayer for their valuable comments and patience.

Yehoshua Kalisky
Beer-Sheva, Israel
February 2006

Chapter 1

Introduction

1.1 Historical Background

1.1.1 Early developments

This section outlines the basic historical developments related to solid state laser materials and technology. It shows briefly how advances in basic science related to rare-earth-ion spectroscopy progressed, together with an understanding of physical processes in solids and solid state materials, which led to the first operation of the laser and subsequently to many technological advances.

In 1907, Becquerel made early observations of a rare earth's luminescence at low temperatures. During the years 1930–1940, an extensive theoretical analysis of the spectra of rare-earth ions was conducted, led by scientists such as Bethe, Kramers, Van Vleck, Racach, and others.

From 1961 through 1968, Dieke and others conducted research that led to the full assignment of the energy levels of trivalent rare-earth trichlorides. This whole assignment was accompanied by theoretical calculations of the transition strengths (mainly the electric dipole but also the magnetic dipole transitions) among various electronic levels in rare-earth ions.

Parallel to these developments, technology progressed toward the development of laser devices. Although in 1917 Einstein defined the concept of stimulated emission and formulated the relationship between induced and spontaneous transitions, Schawlow, Townes, Basov, and Prokhorov, who pioneered the theoretical predictions of laser action, made significant progress in the field in 1954. In 1960, Maiman operated the first ruby laser; this was soon followed by the operation of U^{3+}:CaF_2 by Sorokin and Stevenson. In 1961, Snitzer operated the first Nd:glass laser. In the same year, Johnson et al. built and operated the first CW laser based on a Nd:$CaWO_4$ laser. During the years 1964–1966, Johnson, Geusic, Van Uitert, and others conducted intensive research at Bell Telephone Laboratories toward the development of new inorganic hosts for laser materials based on various trivalent rare earths, mainly Nd^{3+} and Ho^{3+}. The main hosts investigated were various garnets, such as $Y_3Al_5O_{12}$ (YAG), $Gd_3Ga_5O_{12}$ (GGG), and $Y_3Ga_5O_{12}$ (YGG). This

work led to the first operation of a Nd:YAG laser at 300 K, as well as the first operation of a Ho:YAG laser at 77 K. This holmium laser used the concepts of cascade energy-transfer phenomena to enhance lasing efficiency, a process which will be described later in this book.

Further developments occurred in the field of the physics of solid state materials related to lasers from 1948 through 1954. Forster and Dexter developed macroscopic energy transfer and ion-ion interactions. Dexter used the physical assumptions and the mathematical formalism developed by Forster to explain the intermolecular interactions in liquids. Based on Forster's theory, Dexter was able to describe the mechanism of ion-ion interactions and energy-transfer processes. By 1965–1966, Dieke, Weber, and others developed an understanding of the lifetime dependence of excited electronic levels on the energy gap between the excited level and lower levels. Inokuti and Hirayama in 1965 extended the energy-transfer models into microscopic models, which included the statistical distribution of the interacting ions. The microscopic models were investigated in various glasses doped with rare-earth ions by using narrowband laser excitation, following the absorption by another light source (hole burning) or by following the time-resolved emission. Yen, Weber, and co-workers used the last method, also known as *site selection spectroscopy*, mainly from 1970 to 1980. Other methods, such as hole burning and optical dephasing, have been used extensively to evaluate the energy migration among similar sites.

1.1.2 Technological developments[1–3]

Parallel to developments in the solid state laser field have been numerous technological developments. Johnson, Dietz, and Guggenheim reported the first operation of tunable solid state lasers in 1963. They operated divalent 3d transition-metal ions in fluoride crystals, which were followed by other lasing ions and consequently operating wavelength was extended beyond 2 μm. In 1969, the laser operation of disordered materials such as Nd:YLF and Nd:$YAlO_3$ (YALO) was also demonstrated. Progress in the operation of holmium-, thulium-, and erbium-doped crystals (such as YLF, YAG, and $CaWO_4$, both CW and pumped) at 77 K and 300 K was achieved between 1970 and 1978. New schemes for holmium lasers that produced efficient systems capable of delivering high-output energy at room temperature were introduced from 1985 to 1987. A breakthrough in tunable laser technology was the invention (in 1979) of the alexandrite laser based on the Cr^{3+}:$BeAl_2O_4$ crystal. The Ti:Sapphire laser, invented by Moulton in 1982, became a commercial product in 1989. The 1961–1970 decade was characterized by inventions that shaped the technological world two decades later. The first frequency-doubling and Q-switching lasers were invented in 1961. In 1964, Johnson and Ballman applied these inventions to the frequency and self-frequency doubling of rare-earth-doped ions. These technological advances triggered the further development of applications. The first ruby laser rangefinder was introduced during the Vietnam War in 1969.

Starting in 1970, numerous laser applications have been developed in medicine, industry, basic research (mainly in ultrashort pulses), and optical parametric oscillator (OPO) systems. New nonlinear crystals, mainly for second harmonic generation (SHG), were synthesized and commercialized: the $KTiOPO_4$ (KTP) in 1978, the $LiNbO_3$ in 1985, and the β-BaB_2O_4 (BBO) in 1988. Major events in the 1980s and 1990s were the development and commercialization of diode-pumped systems and ultrafast laser sources based on tunable solid state lasers. Keyes et al. developed the first light-emitting diode (LED)-pumped laser in 1964. However, the development of the first GaAlAs diode laser in 1970 and its commercialization in 1975 led to the first 100-mW diode laser becoming available in 1981, followed by the rapid development of commercial diode-pumped Nd:YAG lasers (1985–1987). Similar progress was obtained with other diode-pumped systems based on other ion-doped (Tm^{3+}, Ho^{3+}, Er^{3+}) hosts, such as oxide, fluorides, vanadates, and garnets, to form laser crystals.

In the field of tunable solid state lasers, two major developments have occurred: first, the mode locking of the Ti:sapphire laser (1991) and the pushing of the temporal pulsewidth into the 11-fs and 5-fs range (1992, 1997, respectively); second, the development of other candidates for tunable laser sources, such as the colquiriite family of crystals (1993–1998, Cr:LiCAF, Cr:LiSAF, etc.), Cr^{4+}-doped garnets, and forsterite (Mg_2SiO_4) tunable sources for mid-IR lasers for the femtosecond temporal regime (1994–1998).

Presently, there are many types of lasers that cover a wide range of wavelength, from deep UV to the far IR, and over a wide variety of output power levels (up to 10 kW) and use novel diode-pumping configurations and geometries. A new generation of compact, robust, reliable microlasers, waveguide lasers, and thin disk lasers are well established and are being implemented in commercial systems covering a wide array of wavelengths.

1.2 Laser Materials

Lasers are defined as electro-optical devices that generate or amplify light. The amplification of the laser light is carried out via the physical processes of generating population inversion in an upper state and stimulated photon emission in the presence of an external radiation field that is applied to the atom. The main characteristic of the coherent radiation is that it is driven by an external radiation field with which it is coherent. The laser emission occurs at a large variety of wavelengths, ranging from the IR through the visible and into the UV spectral range.

1.2.1 Elements of a typical laser oscillator

Generally, the laser oscillator consists of the following main elements, essential for its operation as an amplifying medium:

- Laser medium
- Pumping unit
- Optical feedback elements
- Auxiliary units such as the cooling system and heat-removal, electrical, or other units essential for proper operation

A schematic layout of a laser system and its elements is presented in Fig. 1.1. The following section elaborates on laser components as depicted in the figure.

1.2.1.1 Gain medium

The *gain medium*, or active element, of a laser can be either in a solid state, liquid, or gas phase. Gain media are found in the following phases:

Solid state: composed of inorganic ions in various doping densities and a host.

Liquid: usually composed of organic dyes that are soluble in water or various organic solvents.

Gases/plasma: composed of various mixtures of gases that emit coherent radiation through electronic or vibrational transitions.

1.2.1.2 The laser pumping unit and pumping methods

Several pumping methods exist, based on two main technologies: electrical methods (electrical or RF discharge), used to pump gas lasers, and optical technologies, used for pumping solid state and dye lasers.

Since this book is devoted to solid state lasers, it concentrates on optical pumping. The various laser pumping units are characterized by their geometry, namely transverse or longitudinal pumping, as well as the spectral distribution of the pumping source. The optical pumping sources are typically lamps, lasers, and diode lasers. They can be either pulsed or continuous wave (CW). A pump lamp has a broad spectral distribution (i.e., emission over a wide spectral range), which can be further controlled by the current density of the source. Lasers and diode devices

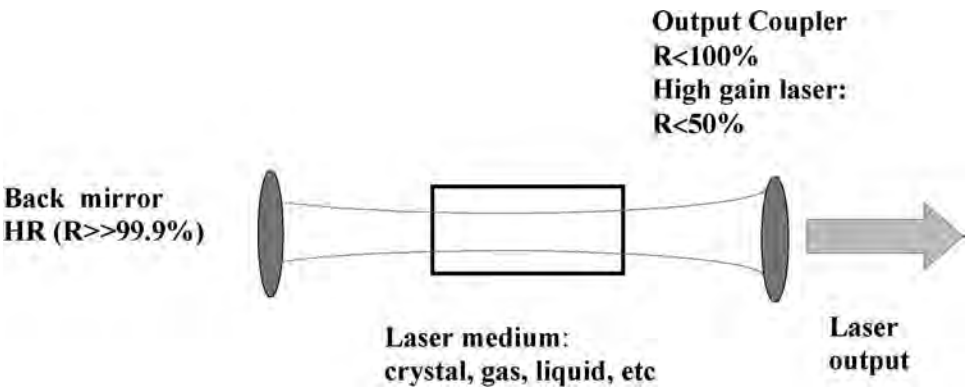

Figure 1.1 A schematic general layout of a laser system. R is the mirror reflectivity; HR stands for high reflectivity coating.

have a definite wavelength, which overlaps an intense absorption line of the gain medium.

The pumping methods are divided into two main categories: direct or indirect conversion of the pumping energy (*direct* or *indirect pumping*, respectively), the latter of which is achieved by using nonlinear optical devices. Direct pumping yields both broadband and narrowband emissions. The broadband emission, namely tunability, is based on transition-metal ions, while the narrowband emission is based on rare-earth ions, doped as a single or a combination of ions. The indirect pump energy conversion employs either energy-transfer processes (resonant or nonresonant), as well as nonlinear optical devices such as

- Frequency doubling (KTP-$KTiOPO_4$, BBO-βBaB_2O_4, LBO-LiB_3O_5, PPKTP-periodically poled KTP, PPLN-periodically poled lithium niobate)
- Frequency shifting (OPO, Raman shifting)
- Upconversion processes

1.2.2 Optics

The subject of laser-related optics can be divided into two main issues: optics and optical techniques related to the optical resonator (the optical feedback unit, including nonlinear optics), and the issues in optics and optical technology related to optical-element coatings.

Nonlinear optical elements comprise an important subject, as mentioned in Sec. 1.2.1.2. Useful information about this topic can be found in Refs. 2 and 4, and in Chapter 11. Nonlinear optical materials exhibit a unique property for which the refractive index, n, is a function of the electric field vector $\mathbf{E}$ of the light wave, according to the relation

$$n(\mathbf{E}) = n_0 + n_1\mathbf{E} + n_2\mathbf{E}^2 + \cdots, \tag{1.1}$$

where n_0 is the refractive index in the absence of an electric field (the "linear optics" regime), and n_1, n_2, are the coefficients of the series expansion of $n(\mathbf{E})$. This expansion includes nonlinear elements and therefore is termed nonlinear optics. The propagation of an electromagnetic (EM) wave through a material produces changes in the spatial and temporal distribution of electrical charges via displacement of the valence electrons from their normal orbits. The intense field (or perturbation) creates electric dipoles, e.g., polarization. Under a small EM field, the polarization depends linearly on $\mathbf{E}$. In a strong field, a nonlinear response is induced. Therefore, the electric polarization, P, of nonlinear optical materials is related to the applied electric field, $\mathbf{E}$, by the expression

$$P(\mathbf{E}) = \kappa_0\mathbf{E} + \chi^{(2)}\mathbf{E}^2 + \chi^{(3)}\mathbf{E}^3 + \cdots, \tag{1.2}$$

where κ_0 is the dielectric susceptibility in the absence of an applied electric field; $\chi^{(2)}$, $\chi^{(3)}$, and so on are the nonlinear susceptibility coefficients. One should mention here that in the general case of anisotropic crystals, quantities such as n, κ,

and χ are represented by tensors of the order $n + 1$, where n is the number of the applied fields.

Usually, when describing optical materials, the description assumes that the linear response between the electric field and the electric polarization is dominant, e.g., $\kappa_0 \gg \chi^{(2)}\mathbf{E}^2$, and therefore, the optical properties that result from such dependence are linear and produce relatively simple effects. Nonlinearity affects both the frequency and amplitude of the transmitted waves. As an example, if two monochromatic waves with frequencies ω_1 and ω_2 propagate through crystals having a square nonlinear response [$\chi^{(2)} \neq 0$], new light waves with combination frequencies will be created. In other words, the sum frequency ω_3 and the difference frequency ω_4 will be generated:

$$\omega_3 = \omega_1 + \omega_2, \tag{1.3a}$$

$$\omega_4 = \omega_2 - \omega_1. \tag{1.3b}$$

These equations represent the basic phenomena of how nonlinear optical materials are utilized for frequency conversion: in one case, sum frequency generation (ω_3), and in the other, difference frequency generation (ω_4) is obtained, respectively. A well-known situation is SHG, in which $\omega_2 = \omega_1$, and therefore $\omega_3 = 2\omega_1$. An example for such frequency conversion is the generation of green emission at 532 nm by SHG of the 1064-nm emission of Nd:YAG laser. Another important phenomenon is parametric oscillation, which involves the appearance of two light waves with frequencies ω_1 and ω_2 in the presence of a light field with a frequency of ω_3. This process, optical parametric oscillation (OPO), is the opposite of SHG or frequency doubling. If OPO elements are coupled in tandem, the tuning range of a 1.06-μm laser can be extended up to 8 μm.

Besides these elements, we should also bear in mind that auxiliary elements such as electronics (power supply), mechanics (thermal and mechanical properties), and detection and diagnostic systems, are an integral part of any laser system.

References

1. A. Yariv, "Optical Electronics," *The Holt, Rinehart and Winston Series in Electrical Engineering*, 4th Edition, Saunders College Publishing (1991).
2. O. Svelto, *Principles of Lasers*, 4th Edition, Plenum Press, New York and London (1998).
3. A. E. Siegman, *Lasers*, University Science Books, Mill Valley, California (1986).
4. A. C. Newell and J. M. Moloney, *Nonlinear Optics*, Addison-Wesley Publishing Company (1991).

Chapter 2

Solid State Laser Materials

2.1 Properties

Solid state lasers are widely used in medicine, industry, scientific research, spectroscopy, and remote sensing applications. They also comprise a dominant part of the overall laser market. Solid state lasers possess the following unique characteristics:

- Reliability and robustness
- High level of safety
- User-friendly
- Maintenance-free
- Low-cost performance, high-volume production
- Compact size
- Wide range of wavelength selection

A solid state laser is an active solid state material that under certain conditions can emit coherent radiation. It is composed of an ion—either rare earth or transition metal—and a solid host. The host can be crystals, disordered or amorphous materials (such as glass), glass ceramic (which is a combination of crystalline-ordered structure and glassy phases disordered structure), or mixed crystals. The combination of the dopant and the host will determine the properties of the laser material in terms of:

- Optical properties
- Lasing wavelength
- Spectral bandwidth
- Fluorescence lifetime
- Emission and absorption cross sections

The optical properties of an undoped solid state laser host can be summarized as follows:

- Transmission spectra
- Scattering of light through the crystal
- UV absorption and color-center formation upon UV radiation
- Refractive index: anisotropy as well as changes with the temperature
- Polarization, birefringence, or refraction
- Effect of the phonon energy of the lasing host on radiative and nonradiative processes within the electronic levels of the doped ion
- Symmetric properties of the host
- Crystal field within the ionic site

When the host is doped with ions, additional optical and physical parameters are dominant:

- Radiative and nonradiative rates within the electronic levels of the lasing ion
- Excited state absorption and multiphoton excitations
- Absorption coefficients (or cross sections) at the relevant pumping transitions
- Emission cross section of the lasing transition
- Absorption cross section of the lasing wavelength–ground state absorption

The multidisciplinary field of solid state lasers encompasses several subjects. In designing a solid state laser system, the disciplines that generally must be addressed and optimized are discussed below.

2.1.1 Optics

The general subject of optics includes the following issues:

- Specification of the optical elements to the desired system
- Laser cavity design
- Optimization of the system pumping conditions to ensure efficient performance; for example, mode-matching, e.g., matching the pump and cavity mode volumes in laser pumping
- Fiber optics design when optical fibers are used, such as fiber-coupled diode laser arrays or use of fiber optics to deliver the laser output

2.1.2 Material design

Material design is important because it defines the type of laser material, namely, the type of the active ion and the appropriate host. By defining the laser material, the assumption is made that the following parameters can be controlled and improved:

- The emission wavelength of the laser material
- Emission and absorption cross sections (absorption coefficient per atomic density), which are important to achieve highly efficient laser systems
- Enhancement of the laser quantum efficiency (the fraction of atoms in a metastable lasing level relative to the total excited atoms, or the ratio between the number of laser photons and the number of the pump photons)
- Enhancement of the pumping efficiency of the laser system, which contributes to the overall laser efficiency and includes other efficiencies owing to the pump source, such as:
  - Radiation transfer (the fraction of the radiation transferred to the laser gain relative to the total useful radiation emitted by the pumping source)
  - Absorption and quantum gap (the energy difference between the excited level and the emitting metastable lasing level)
  - Mode-matching (the ratio between the pump and the cavity mode volumes)
  - Extraction of the available laser energy

The proper choice of laser material is necessary in order to obtain good mechanical, thermal, and radiation-resistant properties.

2.1.3 Mechanical design

Effective mechanical design involves thermal management, thermal load, cooling the lasing element, its response to environmental changes, and finding the thermal parameters of the host.

Optimizing the above parameters is the main aim of a laser designer or engineer and will lead eventually to a lower pumping threshold and a more efficient system.

To summarize, a mechanical design includes several nonoptical aspects in a laser system, such as:

- Thermal and mechanical properties of the laser host
- Thermal management
- Thermal-load issues
- Cooling techniques

Those lasers are based mainly on rare-earth-doped crystals or transition-metal-doped crystals. The processes that involve pumping relaxation and lasing are complicated and need a careful analysis of both the physical phenomena and material properties. This chapter presents the assumptions leading to proper design of a laser-host material, which eventually leads to an efficient lasing system.

The primary applications of solid state lasers are presented in Table 2.1. As a result of their characteristics, solid state lasers are used for a large variety of applications. The main applications of those with narrowband and broadband emission are presented in Table 2.1.

Table 2.1 Main current applications for narrowband and broadband solid state lasers (excluding fiber lasers).

Laser type	Application
Nd:YAG (1.06 μm)	Medical, industrial, military, target illuminators, marking
Nd:YAG (532 nm, 1.32 μm)	Medical, printing, entertainment
Ho:YAG, YLF (2.1 μm)	Medical, remote sensing, contaminant analysis, military
Er:YAG (2.9 μm)	Medical (dentistry, dermatology), blood drawing and sampling
Ti:Sapphire (700–1000 nm)	Spectroscopy, ultrafast mid-IR lasers
Cr:LiCAF, LiSAF, LiSGaF (800–1100 nm)	Ultrafast spectroscopy, tunable sources
Ce:LiCAF, LiSAF (280–310 nm)	Tunable UV sources, chemical analysis
Cr^{4+}:crystals (1.3–1.6 mm)	Ultrafast sources, tunable lasers, chemical analysis

As can be observed from Table 2.1, solid state lasers are attractive candidates for industrial, medical, and basic research applications. The total market for all types of solid state lasers for 2003 was $914 million (U.S.); it is predicted to be $1,471 million by 2008, with a 10% annual average growth rate.[1] For special applications of solid state lasers, their unique design considerations must be taken into account.

Generally, solid state laser materials possess a relatively high absorption cross section for a certain wavelength (λ), high quantum efficiency for fluorescence at the lasing transition, and a sharp emission line between inner electronic energy levels. The absorption cross section of a system, $\sigma(\lambda)$, can be derived from the absorption coefficient of the system. Assume a light intensity I_λ at certain wavelength λ passing through an absorbing medium of a molar concentration C and thickness dl. The relative change in the light intensity resulting from absorption is

$$\frac{dI_\lambda}{I_\lambda} = -\alpha'(\lambda) \times C \times dl = \alpha(\lambda) \times dl, \tag{2.1}$$

where $\alpha'(\lambda) \times C = \alpha(\lambda)$ is the absorption coefficient of the system (in units of cm^{-1}), dI_λ is the change in light intensity, and I_λ is the intensity of the incident light. The absorption coefficient $\alpha(\lambda)$ is related to the absorption cross section $\sigma(\lambda)$ through $\alpha(\lambda) = \sigma(\lambda) \times N$, where N is the density of atoms per unit volume.

Active solid laser materials consist of an active ion such as transition metals or rare-earth ions (lanthanides or actinides series) embedded in an inorganic host such as crystals or glasses of different compositions. The combination of the host and dopant will determine the properties of the laser material in terms of spectroscopic properties, such as lasing wavelength, spectral bandwidth, and the fluorescence lifetime of the emitting level; and the physical properties, such as hardness, thermal conductivity, and damage threshold.

The most common dopants for mid-IR lasers are rare-earth ions. The optical transitions are within the partially filled f-levels. These levels are shielded from

the external crystal field; therefore, the spectra of rare-earth-doped materials are only slightly affected by that field. Since the optical transitions are between f-shell electronic levels, these are forbidden transitions, which become allowed only by breaking the symmetry of the crystal.

2.2 Doping Ions

The active lasing ion doped in a host has some definite spectroscopic characteristics of the laser emission. These characteristics are a result of the spectral properties (wavelength, bandwidth, lifetime of the emitting level) of the active ion. The spectroscopic nomenclature is defined below.

The atomic energy term, which designates an energy level having the same values of **L**, **J**, and **S** in a Russell-Saunders coupling, will be symbolized by $^{2\mathbf{S}+1}\mathbf{L}_{\mathrm{J}}$, where $\mathbf{L} = \Sigma l_i$ is the resultant angular momentum having values of $\mathbf{L} = 0, 1, 2, 3, 4, \ldots$. Each value of **L** is symbolized by S, P, D, F, G, H ..., respectively. The superscript $2\mathbf{S}+1$ is the multiplicity of the term resulting from electronic spin, where **S** is the resultant vector sum of the electronic spin defined by $\mathbf{S} = \Sigma s_i$, where s is the spin of individual electron i. The vector addition of the spin and the angular momentum is $\vec{\mathbf{J}} = \vec{\mathbf{L}} + \vec{\mathbf{S}}$, which is the subscript of **L**. The total angular momentum defined above has discrete values characterized by the quantum number J:

$$J = (L + S), (L + S - 1), (L + S - 2) \ldots |L - S|. \tag{2.2}$$

The electrons in a closed shell do not contribute to the electronic transitions; only the outer unpaired electrons contribute. In the case of rare-earth ions, the electrons in the f shell are shielded by lower-quantum-number energy levels owing to the contraction of the f shell towards the nucleus. The f shell is filled with electrons, up to a maximum of 14. The levels are filled in the order shown in Fig. 2.1.

The electronic structure of rare-earth elements can be described by the complete electronic structure of a noble gas (Xe) with $5s^2 5p^6$ outer electrons and additional 4f levels partially filled. The element neodymium (Nd), for example, has a complete xenon structure with an additional four electrons in the subshell 4f and two electrons in the 6s level. This structure is symbolized by the notation $[\mathrm{Xe}]4f^4 6s^2$. For Nd^{3+}, the ionic electronic structure will be $[\mathrm{Xe}]4f^3$. The f-electrons are therefore isolated and minimally influenced by the external crystal field. For rare-earth ions, this fact is reflected by their relatively narrow absorption and emission spectral lines and the longer lifetime of the excited electronic energy levels.

The electronic transition probability between two quantum states ψ_i and ψ_f is proportional to $|\vec{\boldsymbol{\mu}}|^2$, where $\vec{\boldsymbol{\mu}}$ is defined as the transition moment integral,

$$\vec{\boldsymbol{\mu}} = \langle \psi_\mathrm{i} | e \times \mathbf{r} | \psi_\mathrm{f} \rangle, \tag{2.3}$$

where ψ_i is the wavefunction in the initial quantum state, ψ_f is the wavefunction of the final state, $e \times \mathbf{r}$ is the dipole moment vector, e is the electronic charge,

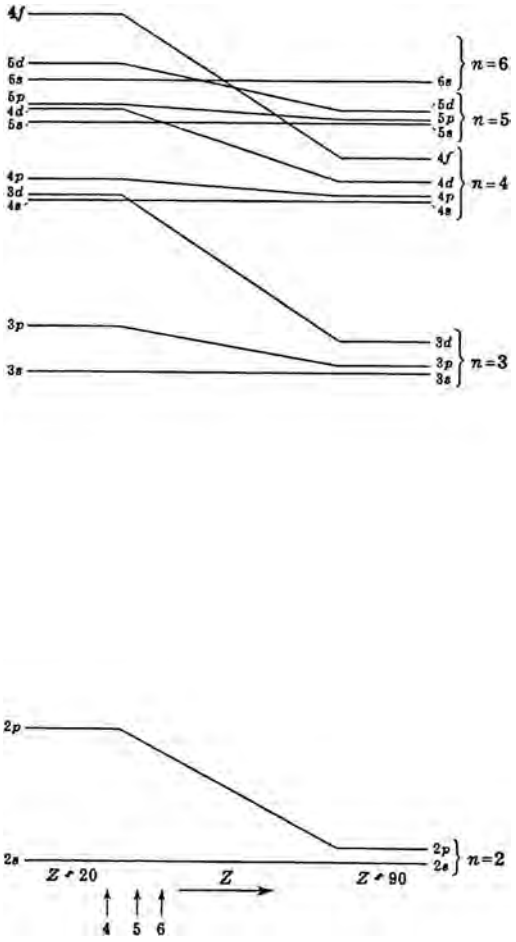

Figure 2.1 A schematic representation of energy levels and the sequence of filling the shells with electrons for low and high nuclear charge (Z). (Reprinted from Ref. 2 with permission from Dover Publications.)

and $\mathbf{r} = r(x, y, z)$ is the displacement operator. The displacement operator is an antisymmetric (odd parity) function of space; therefore, the electronic transition intensity or transition probabilities between states of the same symmetry (or the same parity) are parity forbidden because the transition moment integral of symmetric function multiplied by antisymmetric function will have a value of $\vec{\mu} = 0$ (Laporte-forbidden transitions). An electronic transition induced by the transition moment, $\vec{\mu}$, is partially allowed by admixing terms of opposite symmetry to the functions under integration. In this case, the active ion is subjected to an external electric field by the neighboring atoms or ions, and in the case where the rare-earth ion is located in a site of low symmetry, this admixture is possible. A transition that is induced by an external electric field is defined as *forced electric dipole transition*. The electronic levels involved in this transition now have small elements

of opposite parity, and since the vector product is an antisymmetric function of the space, the odd elements in the wavefunction will make the transition allowed (e.g., $\vec{\mu} \neq 0$). Practically, this is achieved by lowering the structural symmetry of the solid state host. As a result, the transition moment $\vec{\mu}$ becomes allowed in highly disordered hosts like glasses or partially disordered solid state materials such as glass ceramics or imperfect crystals. A summary of the spectroscopic properties of rare-earth-doped solids can be found in Refs. 3 and 4.

2.2.1 Laser host materials

Generally, there are three groups of laser hosts:

1. Ordered materials such as crystals;
2. Disordered media such as glasses or amorphous materials; and
3. Materials that incorporate the properties of both glasses and crystals (glass ceramics).

Generally, a candidate for a host laser material should exhibit good optical, mechanical, and thermal properties, as will be discussed in the following section.

2.3 General Properties of Hosts

2.3.1 Optical properties

Laser-host materials have optical properties that include transmission of light through the crystal, scattering, absorption in the UV (which is extremely important in the case of flashlamp-pumped lasers), and resistance to color-center formation under UV excitation. Changes of the refraction index with temperature, polarization properties of the host as a result of birefringence, and the effect of the host on radiative and nonradiative processes must also be considered. The nonradiative processes in a doped host occur via the phonon energies of the network-forming molecules of the crystal, and are also affected by the symmetric properties of the host and the crystal field within the ionic site. All these properties will be discussed separately.

Upon doping the crystal with the active ion, the optical and spectroscopic properties of the lasing ion must also be considered. As a general rule, it is essential to minimize the processes that increase optical losses in the crystal. Therefore, absorption of light through the crystal and scattering of the transmitted light in the crystal will be minimized, reducing the total optical loss. In a doped crystal, it is also desirable to minimize the nonradiative rates, excited state absorption, or multiphoton excitations to ensure the pumping light is used efficiently.

2.3.2 Chemical properties

Chemical properties important for a laser material include chemical inertness, crystallographic matching between the size of the host unit cell and the ionic radius of the dopant, and charge compensation to maintain the electrical neutrality of the host.

2.3.3 Mechanical properties

The mechanical properties of a laser host include hardness, strain, and elastic modulus. The mechanical properties are important for two reasons: (1) good mechanical properties will enable the crystal to sustain the extreme conditions of pumping and laser energy flux; and (2) good mechanical properties simplify the fabrication technique while drilling the crystal out of the boule and later in the steps of cutting and polishing. These advantages make the product more cost-effective.

2.3.4 Thermal properties

Thermal properties, which include thermal conductivity, the thermal shock parameter, and the thermal expansion coefficient of the crystal, are important parameters in the design of a laser crystal. Temperature gradients in the laser crystal will lead to gradients in the refraction index, and hence to poor beam quality. Assuming a rod under the thermal gradient of initial length l_0 and elongation of Δl, Fig. 2.2 shows the details.

The main mechanical/thermal parameters of any solid state laser material are crucial to the proper operation of any solid state lasers. They include:

- Hardness (h)
- Damage threshold
- Thermal conductivity, k (thermal gradients are the main source for poor laser beam quality)
- Thermal shock parameter, R
- Thermal expansion coefficient, α
- Thermal stress (σ), thermal strain (ε), and modulus of elasticity ($Y = \sigma/\varepsilon$); here, the thermal strain is defined as $\varepsilon = \Delta l / l_0$, where l_0 is the initial length of a rod and Δl is the elongation of the rod

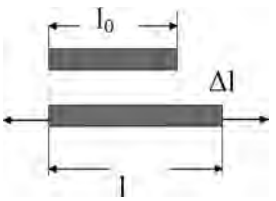

Figure 2.2 Parameters used for the definition of strain and stress in a solid. Here, l_0 is the initial length of a rod and Δl is the elongation of the rod.

The properties of most common laser hosts were discussed in detail by Kaminskii[3] and Koechner.[5] In the following chapters, the properties of most common hosts, mainly of those used for mid-IR lasers, will be discussed.

The most common hosts used for mid-IR lasers are oxides such as yttrium aluminum garnet (YAG) and other kinds of garnets, as well as oxide hosts based on aluminates and silicates. Another family of widely used crystals is based on fluorides such as yttrium lithium fluoride (YLF), barium yttrium, or ytterbium fluoride (BaY_2F_8 or $BaYb_2F_8$, respectively), or vanadates such as YVO_4 or $GdVO_4$. The family of disordered materials includes various types of glasses, especially oxides and fluorides. Glass ceramics, which combine properties of both glasses and crystals, will be discussed as well.

References

1. "Solid State, Gas and Dye Lasers: Outlook for the Future," BCC Report GB-292 (2003).
2. G. Herzberg, *Atomic Spectra and Atomic Structure*, Dover Publications, New York, 148 (1944).
3. A. Kaminskii, *Laser Crystals, Their Physics and Properties*, Springer-Verlag, Berlin, Heidelberg, and New York (1981).
4. R. Reisfeld and C. K. Jorgensen, "Lasers and excited states of rare earth," *Inorganic Chemistry Concepts* **1**, Springer-Verlag, Berlin, Heidelberg, and New York (1977).
5. W. Koechner, *Solid State Laser Engineering*, 5th Revised and Updated Edition, Springer-Verlag, Berlin, Heidelberg, and NewYork (1999).

Chapter 3

Structure and Bonding of Solids

3.1 Crystal Structure

A solid state material can be in an ordered or disordered state.[1] An ordered structure is the basis for an ideal crystal, while a disordered state can be either in a glassy or amorphous state. An ideal crystalline state consists of an infinite repetition of the same crystal lattice; this structure itself contains a single atom or group of atoms or molecules.

A lattice is a group of space points arranged periodically. These points are a mathematical representation of the crystal structure. When atoms or molecules, defined as the basis of atoms, are coupled to these periodic space points in a one-to-one correspondence, the crystal structure is defined. The lattice is defined by three translation vectors $\mathbf{a}_1$, $\mathbf{a}_2$, and $\mathbf{a}_3$, and three corresponding arbitrary integers u_1, u_2, and u_3, whereas the smallest unit that defines lattice structure is the lattice-unit cell.

A translation operation T on the lattice structure will yield the same lattice structure. This translation operation is defined by a crystal translation vector,

$$T = u_1\mathbf{a}_1 + u_2\mathbf{a}_2 + u_3\mathbf{a}_3. \tag{3.1}$$

This translation vector displaces the crystal from a point located at r to a point located at r',

$$r' = r + u_1\mathbf{a}_1 + u_2\mathbf{a}_2 + u_3\mathbf{a}_3, \tag{3.2}$$

where the set of points r' above defines a lattice.

The regular structure of a crystal allows symmetry operations, which results in an identical structure after the symmetry operation. These symmetry operations are called *point operations* and are performed around lattice (or other) points that define the repetitive unit-cell volume. The unit-cell volume that defines the repetitive crystal structure is called a *primitive cell*. The primitive cell corresponds to one lattice point and contains the minimum number of atoms or molecules that create

the basis for the crystal structure. The volume of a unit primitive cell with axes a_1, a_2, a_3 is given by

$$V_c = |a_1 \cdot a_2 \times a_3|. \tag{3.3}$$

3.1.1 Types of crystals

All three-dimensional lattices are grouped into seven types of cells: triclinic, monoclinic, orthorhombic, tetragonal, cubic, trigonal, and hexagonal. The cell axes of a cubic cell, for example, are $a_1 = a_2 = a_3$, and the angles between the axes are $\alpha = \beta = \gamma$.

The orientation of a crystal plane can be specified by indices (h k l) that are the indices of the plane. The plane indices for a cubic crystal are presented in Fig. 3.1. The index defined by a plane that cuts an axis on the negative side has a negative sign and will be symbolized by a minus sign above the index ($\bar{h}\,\bar{k}\,\bar{l}$).

3.2 Crystal Binding

The solid state phase is characterized by binding forces that are stronger than those in the liquid or gas phase. Several binding forces play a role in the solid state phase, as detailed below.

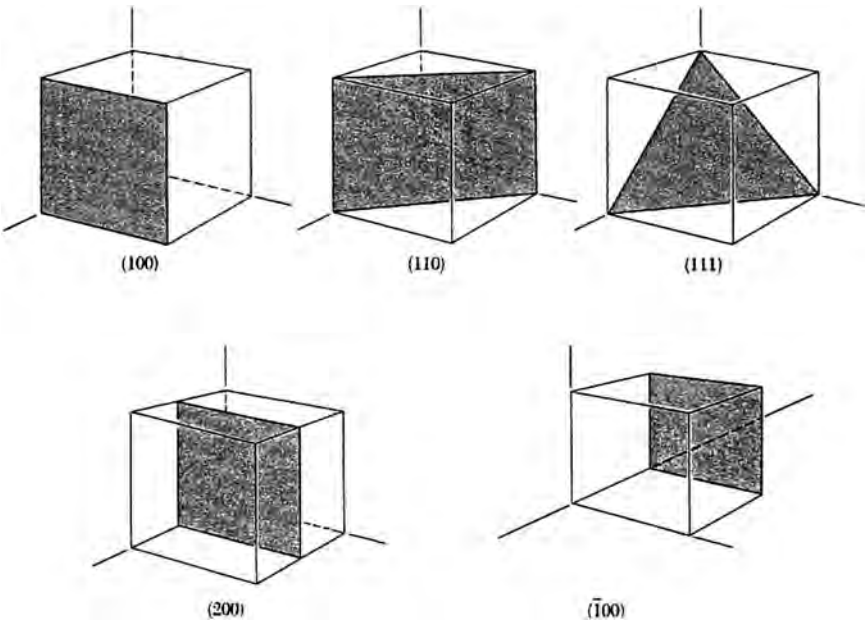

Figure 3.1 Indices of the main planes in a cubic crystal. (Reprinted from Ref. 1 with permission from John Wiley & Sons, Inc.)

3.2.1 Van der Waals interaction

A Van der Waals interaction results from local distortion of charge distribution around inert gas atoms at a distance R larger than their ionic radii. This distortion leads to local redistribution of the electrostatic charges around the atoms and to the formation of local induced dipole moments in the atoms of the crystal. A Van der Waals interaction is composed of two main forces: attractive and repulsive. The dipole moment interaction is a source for attractive forces between the crystal atoms at short distances. It varies as $-C/R^6$ where R is the separation between the two atoms and C is a constant proportional to the electronic polarizability, α, which is defined as $P = \alpha \cdot E_{\text{loc}}$, where P is the polarization defined as the dipole moment per unit volume and E_{loc} is the local electric field at the atom.

Repulsive forces have two main sources. First is the mutual overlap between the charge distribution wavefunctions around the atoms. When atoms are brought together, their charge distribution begins to overlap and the total energy of the atomic system is changed. At a close separation of the two atoms, the charge distribution overlap will increase until it reaches a point at which electrons from one atom will occupy states of the neighboring atom, thus violating the Pauli exclusion principle. To avoid this violation, electrons must occupy high energy states, thus increasing the total energy of the system.

The repulsive forces of the two nuclei comprise the second source for repulsive interaction. These forces also increase the total energy of the system. The repulsive potential behaves as B/R^{12}, where B is a positive constant and R is the interatomic distance. The exponent in the repulsive term indicates that the potential is strongly repulsive at very short interatomic distances. Therefore, the total potential of the two atoms at an interatomic distance R is given by the sum of the attractive and repulsive forces,

$$U(R) = \frac{B}{R^{12}} - \frac{C}{R^6}, \tag{3.4}$$

where B and C are empirical constants. Alternatively, Eq. (3.4) can be written as

$$U(R) = 4\varepsilon\left[\left(\frac{\sigma}{R}\right)^{12} - \left(\frac{\sigma}{R}\right)^{6}\right], \tag{3.5}$$

where ε and σ are parameters with the following constants:

$$4\varepsilon\sigma^6 = C, \tag{3.6}$$

$$4\varepsilon\sigma^{12} = B. \tag{3.7}$$

The potential presented in Eq. (3.5) is known as the Lennard-Jones potential and its dependence on the interatomic distance is presented in Fig. 3.2.

The Lennard-Jones expression is an approximation based on a two-parameter model that was developed to explain the interaction properties of the gaseous phase.

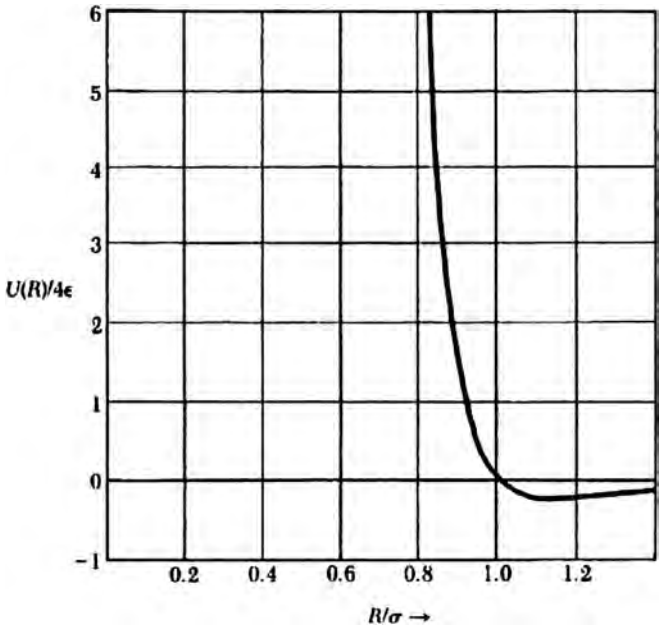

Figure 3.2 Interatomic interaction between two inert-gas atoms described by the Lennard-Jones potential. The force between the two atoms, given by $-\mathrm{d}U/\mathrm{d}R$, has a minimum value at $R/\sigma = 2^{1/6} \approx 1.12$, where the value of U at the minimum is $-\varepsilon$. (Reprinted from Ref. 1 with permission from John Wiley & Sons, Inc.)

The short-term repulsive term, which is proportional to R^{-12}, is not the exact description of that interaction. The repulsive forces can also be described by an exponential expression of the form $\lambda \exp(-r_{ij}/\rho)$ (Born-Mayer potential), as will be explained below, where r_{ij} represents a general definition of the interatomic distance between atom (or ion) i and j, and ρ is a measure of the repulsive interaction.

3.2.2 Ionic bonding

In the case of ionic crystals, bonding between the crystal ions is of a coulombic nature which results from electrostatic interaction between the charged ions. The electronic configurations of ionic crystals are closed electronic shells, like inert atoms. However, unlike inert gases, the formation of a closed-shell configuration leads to a charged atom. If we take sodium chloride as an example, the electronic configuration of neutral Na is $1S^2 2S^2 3S^1$ while that of the neutral Cl atom is $1S^2 2S^2 3S^2 3P^5$. The configuration of the ionic state with filled shells will be Na^+: $1S^2 2S^2 3S$, and for Cl^- it will be Cl^-: $1S^2 2S^2 3S^2 3P^6$.

The electrical charge distribution around the ions in the ionic crystal is approximately spherically symmetric, but is slightly distorted at short distances, close to the contact point. For ions with a charge $\pm q$, separated by an interionic distance r, the electrostatic field is given by $\pm q/r^2$, where the forces are attractive for charges of opposite signs and repulsive for charges of the same signs. Although there is

some charge polarization that may contribute to a Van der Waals interaction, even in ionic crystals, most of the interaction results from electrostatic interaction.

Assuming that U_{ij} is the electrostatic interaction between ions i and j, the sum of all the interactions regarding the ion i will be

$$U_i = \Sigma' U_{ij}. \tag{3.8}$$

The summation includes all ions except $i = j$. This interaction is the sum of repulsive forces previously defined (in the form of the Born-Mayer potential) and the coulombic potential,

$$U_{ij} = \lambda \exp\left(-\frac{r_{ij}}{\rho}\right) \pm \frac{q^2}{r_{ij}}, \tag{3.9}$$

where λ and ρ are empirical parameters (ρ is a measure of the range of repulsive interaction), $\pm q$ is the electrical charge on the ions, and $\pm q^2/r_{ij}$ indicates the interaction between charges of the same sign (repulsive) or opposite sign (attractive). The repulsive interaction can be represented alternatively by an expression that is proportional to R^{-12}, but the exponential representation in Eq. (3.9) describes the system more accurately.

The main contribution to the binding in ionic crystals is the electrostatic energy. The electrostatic energy per pair of any ions i, j is given by

$$E_{\text{elect}} = \frac{1}{N_p} \sum_j \frac{\pm e^2}{r_{ij}} = \frac{1}{N_p} \sum_j \frac{\pm e^2}{p_{ij} R}, \tag{3.10}$$

where r_{ij} is the interatomic distance between any reference atom i to another atom j; p_{ij} is the distance between atom i and any other atom j expressed in terms of R, the nearest-neighbor separation in the lattice; plus or minus signs depend on whether the ions are of the same or opposite charges; and N_p is the number of ion pairs. Generally, when having an equal number of ions with charges $+$Ze and $-$Ze (Z is the number of charges), the energy will be proportional to Z^2e^2, inversely proportional to the distance and therefore to the nearest-neighbor distance R, and will have total electrostatic energy similar to Eq. (3.17) per ion pair,

$$E_{\text{elect}} = -\frac{\alpha Z^2 e^2}{R}. \tag{3.11}$$

α is called the Madelung constant and is defined as

$$\alpha = \sum_j \frac{(\pm)}{p_{ij}}, \tag{3.12}$$

where the + sign applies to unlike charges and the − sign to similar charges. The Madelung constant, α, can be generalized to solid state structures as a general formula $A_{n1}B_{n2}$ ($n1$ and $n2$ are the number of atoms 1 and 2, respectively), assuming charge neutrality condition $n1Z_1 = n2Z_2$. It will be defined by

$$E_{\text{elect}} = -\frac{\alpha(n1 + n2)Z_1 Z_2 e^2}{2R}. \tag{3.13}$$

The total lattice energy with N pairs of ions is

$$E_{\text{Total}} = N \cdot U_i, \tag{3.14}$$

or, with the help of Eqs. (3.9) and (3.12),

$$E_{\text{Total}} = N\left(z'\lambda e^{-R/\rho} - \frac{\alpha q^2}{R}\right), \tag{3.15}$$

where z' is the number of nearest neighbors of any ion in the system. The repulsive energy can also be represented in the form of an inverse power law, and the total energy per ion pair is written as

$$E(r) = -\frac{\alpha e^2}{r} + \frac{C}{r^m}, \tag{3.16}$$

where r is the interionic distance, α is the Madelung constant, C is an empirical constant, and m ($6 \leq m \leq 10$) is the power of the short-range repulsive interaction.

3.2.3 Covalent bonding

A covalent or homopolar bond is a strong bonding formed by two electrons contributed by the two neutral atoms that form the molecular structure. Electrons that form the bond are partly localized in the contact region of the atoms; that is, they are shared electrons. The bonding energy depends on the spin orientation, so that the strongest bond corresponds to two antiparallel spins. This spin-dependent energy is called *exchange interaction*. If the electronic shells are not filled, the repulsive forces will weaken and the bond length will be shorter. Electrons can overlap efficiently to form a low- (bonding) or high-energy (antibonding) state. A more precise treatment of the covalent bonding in solids can be found in other sources.[2, 3]

In calculating the total energy of covalent solids, three main contributions to the total energy should be considered:

1. The promotion energy—the preparation of the isolated atoms,
2. The overlap interaction—energy between atoms brought together; and
3. The bond-formation energy.

An example for the promotion energy is the formation of sp^3 hybridization from two electrons in *s* and two electrons in *p* states in a CH_4 molecule: the ground state configuration of carbon is $2S^2\ 2P_x^1\ 2P_y^1$, which allows for the formation of two chemical bonds. By promoting a 2S electron to a 2p orbital, a new configuration is formed, namely $2S^1\ 2P_x^1\ 2P_y^1\ 2P_z^1$, with four unpaired electrons that may pair with four electrons provided by the other four atoms.

A change in the total energy of the system occurs during the overlap of the electron wavefunctions. As the overlap increases, changes occur in the kinetic energy of the electrons as well as in coulomb and exchange interactions. Overlap interaction results in some repulsive forces. The amount of energy gained by forming a bond is defined as *bond-formation energy*. The energy required to separate solids into the isolated atoms is called *cohesive energy* and is defined as

$$E_{\text{coh}} = -E_{\text{pro}} - V_0(d) + E_{\text{bond}}, \tag{3.17}$$

where E_{coh} is the cohesive energy, E_{pro} is the promotion energy, $V_0(d)$ is the overlap interaction, and E_{bond} is the bond-formation energy. The valence bond is a linear combination of atomic orbitals, leading to orbital overlap, which is responsible for the bonding state. These orbital combinations are termed *bonding orbitals* and the state a *bonding state*. In this state, the internuclear distance has an optimal value with minimum value of the total potential energy of the system. When the molecular orbital is the difference between the atomic orbitals, *antibonding orbitals* are

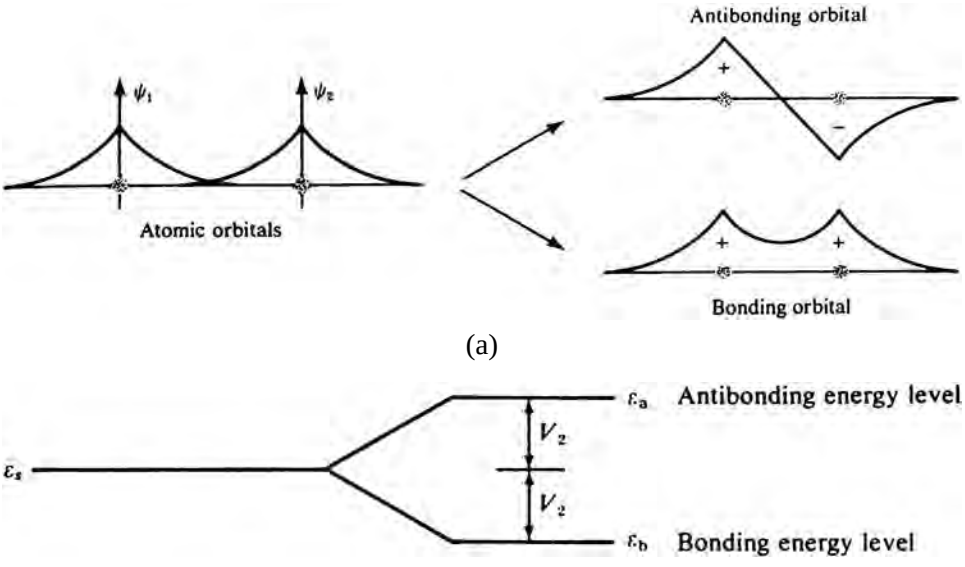

Figure 3.3 (a) The formation of bonding and antibonding combinations of atomic orbitals in a diatomic homopolar molecule. (b) The formation of the corresponding bonding and antibonding energy levels of atomic orbitals. (Reprinted from Ref. 3 with permission from Dover Publications.)

formed. This orbital, if occupied, contributes to the destabilization of a molecule and reduction in bond strength between the two atoms. The formation of bonding and antibonding combinations of atomic orbitals in a diatomic homopolar molecule and the corresponding bonding and antibonding energy levels are presented in Figs. 3.3(a) and (b), respectively.

References

1. C. Kittel, *Introduction to Solid State Physics*, 7th Edition, John Wiley & Sons, Inc. New York, Chichester, Brisbane, Toronto, and Singapore, 15 (1996).
2. N. W. Ashcroft and N. D. Mermin, *Solid State Physics*, Saunders College Publishing (1976).
3. W. A. Harrison, *Electronic Structure and the Properties of Solids*, Dover Publications, Inc., New York (1980).

Chapter 4

Garnet Crystals as Laser Hosts

This chapter reviews some of the latest results for solid state lasers based mainly on oxide and fluoride hosts. Many other types of hosts have been sought and used, but these materials demonstrate the most commonly used laser materials as well as much of the research that has been conducted in laser development and materials. The solid state laser, initially developed in the 1960s, has seen a tremendous burst of technological development in the last decade. Developments include various types of diode-pumped solid state lasers, tunable and ultrafast solid state lasers, codoped lasers in which separate ions absorb pump energy and emit laser radiation, and upconversion lasers in which the laser output wavelength is shorter than the pumping wavelength.

The family of garnet crystals is one of the most commonly used oxide crystal hosts for the lasing ion in solid lasers. The general composition of such a garnet is $A_3B_2C_3O_{12}$. The garnet structure is composed of a dodecahedral site (A) with a coordination number 8, an octahedral site (B) with a coordination number 6, and a tetrahedral site (C) of coordination number 4. Several examples of garnets used as laser materials can be found. The most commercially common material is the yttrium aluminum garnet (YAG), $Y_3Al_5O_{12}$.

Other examples of garnets are gadolinium-gallium garnet (GGG), $Gd_3Ga_5O_{12}$; gadolinium-scandium-gallium garnet (GSGG), $Gd_3Sc_2Ga_3O_{12}$; gadolinium-scandium-aluminum garnet (GSAG), $Gd_3Sc_2Al_3O_{12}$; and yttrium-scandium-aluminum garnet (YSAG), $Y_3Sc_5O_{12}$. Others include $Y_3Sc_2Ga_3O_{12}$ (YSGG) and $Gd_3Ga_5O_{12}$. These crystals have optical, thermal, and mechanical properties that make them suitable hosts for laser materials, as shown in Tables 4.1 and 4.2. The tables also contain for comparison the optical and mechanical properties of YLF. The properties of fluorides as a laser matrix will be discussed in more detail in Chapter 5. It is important to note that the YLF is a birefringent crystal, with an ordinary and an extraordinary index of refraction, denoted in Table 4.1 by n_o and n_e, respectively.

Crystal-growth technique and the fabrication of YAG are well-established procedures, and YAG is used by several companies as their main laser-host product. YAG and other garnets serve as a laser medium for Nd^{3+} as well as for mid-IR lasers such as Ho^{3+}, Tm^{3+}, and Er^{3+}. Substituting Y^{3+} and Al^{3+} with larger cations (Sc^{3+}, Gd^{3+}, or Ga^{3+}) yields a larger crystalline cell with a lower crystal

Table 4.1 A summary of the optical properties of YAG, GSGG, and YLF.*

Property	YLF ($YLiF_4$)	YAG ($Y_3Al_5O_{12}$)	GSGG ($Gd_3Sc_2Ga_3O_{12}$)
Index of refraction, n	$n_o = 1.443$ $n_e = 1.464$ at 628 nm $n_o = 1.448$ $n_e = 1.470$ at 1.06 μm	$n = 1.8347$ at 628 nm 1.82 at 1.06 μm	$n = 1.97$ at 628 nm $n = 1.925$ at 1.06 μm
dn/dT, $°C^{-1}$	-0.91×10^{-6} ordinary -2.86×10^{-6} extraordinary at 578 nm	8.9×10^{-6} at 1060 nm 7.3×10^{-6}	10.1×10^{-6} at 1060 nm
UV absorption	below 0.2 μm	≅380 nm	Color-center formation
Crystalline structure	Tetragonal	Cubic 12.01 Å lattice constant	Cubic 12.57 Å lattice constant
Nd^{3+} lifetime, μsec	480–520	240	—

*Most of the data for YLF and GSGG in Tables 4.1 and 4.2 were taken from product data sheets of Northrop Grumman Corporation Component Technologies, Poly-Scientific (formerly Litton Airtron). Most of the data for YAG were taken from the data sheet of Saint-Gobain Crystals and Detectors (formerly Union Carbide Crystal Products).

Table 4.2 A summary of the main thermal and mechanical properties of YLF, YAG, and GSGG at 300 K.

Property	YLF ($YLiF_4$)	YAG ($Y_3Al_5O_{12}$)	GSGG ($Gd_3Sc_2Ga_3O_{12}$)
Thermal conductivity, k (W/cm K)	0.06	0.13–0.12	0.058–0.07
Thermal expansion coeff., α ($°C^{-1}$)	a axis: 13×10^{-6} c axis: 8×10^{-6}	[100] 8.2×10^{-6} [110] 7.7×10^{-6} [111] 7.8×10^{-6}	7.8×10^{-6}
Thermal shock resistance (Watt/m)	140	800–1100	660
Growth temperature (°C)	820	1950–1970	1860
Density ($g\,cm^{-3}$)	3.99 undoped	4.46 ± 0.04	6.46 doped 6.439 undoped
Hardness (Moh)	4–5	8.5	7.5–8
Specific heat ($J\,g^{-1}\,K^{-1}$)	0.79	0.59	0.488

field. The Al^{3+} ion occupies two types of crystalline sites, e.g., the B and C sites mentioned above. The Sc^{3+} and Cr^{3+}(in cases that involve codoping the crystal with Cr^{3+}) replace the Al^{3+} in the octahedral site (B), while Ga^{3+} replaces the Al^{3+} in the tetrahedral site, and the Gd^{3+} replaces the Y^{3+} in the dodecahedral site.

4.1 Physical Characteristics of Garnets and Mixed Garnets[1]

Garnets based on scandium, gallium, or gadolinium such as GSAG, GSGG, and GGG exhibit a better distribution coefficient for Nd^{3+} since the main cation in YAG is replaced by Gd, Sc, or Ga, which have larger ionic radii like that of a Nd ion.[1] The distribution coefficient k of a crystal is another important parameter in crystal-growth technique. It is a measure of the segregation of the ion to be doped into the crystal and is defined as

$$C(s) = kC(m) * [1 - g(s)]^{k-1}, \tag{4.1}$$

where $C(m)$ is the concentration in the melt, $C(s)$ is the ion concentration in the solid sample at a certain distance along the crystal axis, $g(s)$ is the crystallized fraction of the melt, and k is the distribution coefficient.

The pulling technique, also known as the Czochralski method, is the crystal-growth method used for garnets. By using this method, relatively large crystals with high optical quality can be obtained. A detailed description of the method and definition of the parameters of Eq. (4.1) can be found in several reviews, for example by Kokta.[2]

The undoped YAG is easily grown by this method, at a rate of 1 cm/hour, from iridium crucibles under a nitrogen atmosphere containing 300–1000 ppm of oxygen. Doping YAG with Nd^{3+} creates difficulties as a result of its low distribution coefficient (0.16–0.18). The low distribution coefficient results in a very slow growth rate, on the order of 0.5 mm/hour.

As previously mentioned, ions such as Gd^{3+}, Sc^{3+}, or Ga^{3+} are larger than Y^{3+} or Al^{3+}. Therefore, their crystalline cell is larger and doping of rare-earth ions (like Nd^{3+}, Ho^{3+}, Er^{3+}, and other similar ions) is easier than with YAG. This clear advantage led to extensive scientific research in the 1980s and 1990s. Several attempts were made to synthesize Al-substituted scandium garnets[3] and scandium-substituted rare-earth aluminum garnets.[4] All the crystals were grown along <111> orientation with pull rates of about 0.015 in./hour or less and a 15-RPM rotation rate. As an example, the distribution coefficient of Nd is increased from 0.18 in YAG[5] to 0.6 in GSAG.[6] Denker et al.[1] also conducted a detailed spectroscopic study of Nd^{3+}-doped GSAG and GSGG, and concluded that the nature of energy migration among Nd^{3+} ions in these garnets is of a multipolar interaction with radiative lifetimes for Nd^{3+} of 310 ± 10 μs and 270 ± 10 μs, respectively.

Mixtures of transition-metal ions (Cr^{3+}) and rare-earth ions (such as Nd^{3+}) are used to improve the lasing properties of Nd-doped garnets. An efficient energy transfer Cr → Nd:YAG was studied years ago by Kiss et al.,[7] who gained a substantial improvement in laser efficiency (relative to Nd-only doped YAG). Efficient energy transfer in $Cr^{3+} \rightarrow Nd^{3+}$ systems is typical in other solid state hosts such as glasses. For example, there exists a strong dipole-dipole coupling between Cr^{3+} and Nd^{3+} in fluorophosphate glass,[8] with a linear dependence on Nd^{3+} concentration and a high transfer efficiency ($\approx 60\%$) for concentrations up

to 2.0 wt % of Nd^{3+}. The subject of Cr, Nd:YAG, and rare-earth-doped scandium garnets (RESG) such as GSGG, GSAG, YSAG, and YSGG was established in an excellent review by Smirnov and Shcherbakov in 1988.[9] The following discussion will serve as an introductory background to the broader subject of Cr^{3+} and other rare-earth-codoped hosts such as garnets, glasses, and other types of hosts.

4.2 Chromium- and Neodymium-Doped Garnets

Cr^{3+} occupies sites with octahedral symmetry and therefore the optical transitions within its 3d levels are Laporte forbidden. The configurational diagram of Cr^{3+} in an intermediate crystal field is shown schematically in Fig. 4.1; and the energy levels dependence on the ligand field strength in the d^3 system in an octahedral symmetry, based on the work of Tanabe-Sugano,[10, 11] are presented in Fig. 4.2. The $^2E \rightarrow {}^4A_2$ transition is a narrow, spin-forbidden transition, while the $^4T_2 \rightarrow {}^4A_2$ is a spin-allowed transition that is strongly coupled to the vibrational states. Therefore, this transition is broad enough to overlap with the useful absorption lines of rare-earth ions such as Nd^{3+}, Tm^{3+}, or Ho^{3+}.

This fact is important in improving the pumping efficiency of Nd^{3+} as well as other rare-earth lasers. In order to improve pumping efficiency, energy sensitizers that have broad, allowed transitions are being used. The sensitizer absorbs the useful energy and transfers it resonantly or nonresonantly to the higher levels of an

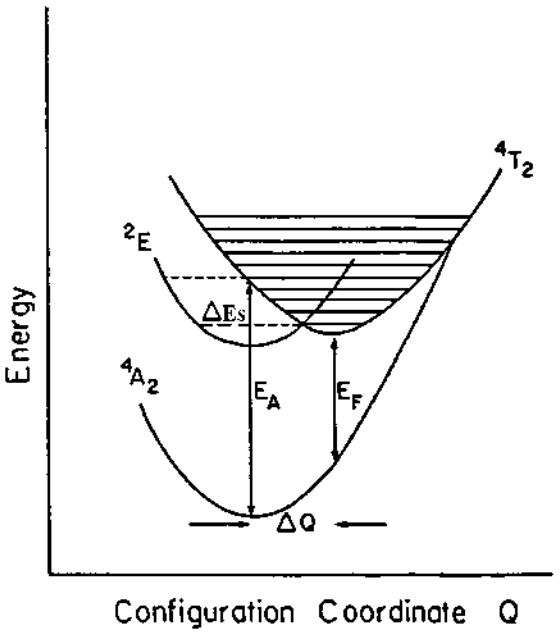

Figure 4.1 A schematic representation of the configuration coordinate diagram for Cr^{3+} in the octahedral site. E_A is the absorption energy, E_F is the fluorescence energy, ΔE_S is the Stokes shift.

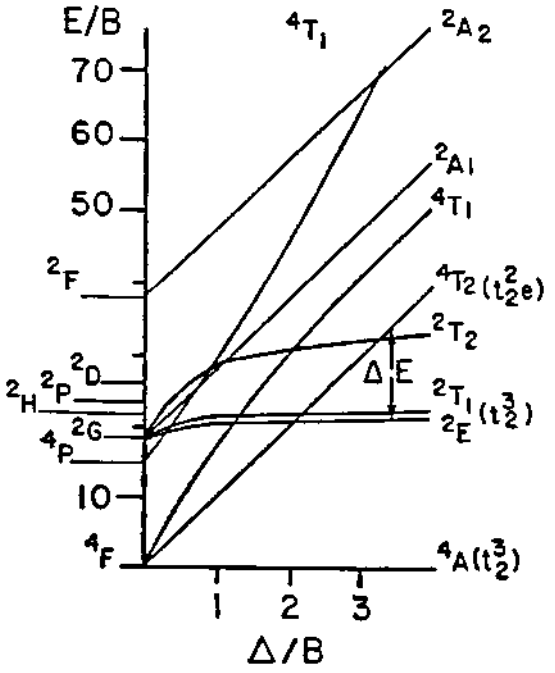

Figure 4.2 Energy-level dependence on the ligand field strength in a d^3 electronic configuration located in an octahedrally coordinated symmetry. (Reprinted from Ref. 11 with permission from The Physical Society of Japan.)

energy acceptor (activator) that emits it as fluorescence or laser radiation. This subject, which is of fundamental importance to an effective design of solid state laser materials, was reviewed in the past by several authors (see, for example, Refs. 12 and 13 and related references therein) and will be reviewed in Chapters 7 and 8.

From the Sugano-Tanabe diagram presented in Fig. 4.2, it is clear that the position of the $^4T_2$ level depends on the strength of the crystal field and hence on the crystal structure. Introducing Cr^{3+} into rare-earth scandium garnets such as GSGG, YSGG, GGG, GSAG, or LLGG $(La_3Lu_2)Ga_3O_{12}$ has two main advantages. First, the distribution coefficient of the doped Cr^{3+} ions is close to unity, and second, Cr^{3+} is subject to lower crystal fields in these garnets owing to their larger lattice constants relative to YAG. The lower crystal field leads to a decrease in the energy gap ΔE between $^4T_2$ and ^2E as depicted in Fig. 4.2. As a result of lowering $^4T_2$, Cr^{3+} becomes a better sensitizer since $^4T_2$ is closer in energy to the energy levels of the activator (energy-acceptor) ion. Table 4.3, based mainly on the data presented in the manuscript of Smirnov and Shcherbakov,[9] gives the values of some ΔE related to various hosts.

This section provides further analysis of the results of energy transfer Cr → Nd in some garnets. The analysis has important implications on other rare-earth-doped systems since the mechanism of an efficient energy transfer is similar to that in other rare-earth ions. Although the laser efficiency (defined in terms of slope efficiency) of Cr:Nd:GGG is higher than that of Nd:YAG, there were reports on ra-

diation defects at high chromium concentrations that mainly result from the high distribution coefficient of Cr^{3+} in GGG, which has a value of $\kappa_{Cr} \cong 3.3$.[15]

Doping of the Ga site (ionic radius of 0.62 Å) by Sc (ionic radius of 0.82 Å) yields lower crystal fields in the sites, therefore lowering the energy level $^4T_2$. This level has broad high-intensity absorption and emission in the visible. As was reported by several authors,[5, 16] the Cr^{3+} distribution coefficient in GSGG is close to unity with increasing radiation stability, even at high doping levels of chromium. Another advantage for the GSGG is the higher distribution coefficient for Nd^{3+} (0.75 for GSGG, 0.63 for GGG), which is a result of the higher lattice constant in GSGG relative to other garnets. Table 4.4 presents some values of distribution coefficients and crystal lattice constants for several garnets. From Table 4.4, the advantage of other garnets over YAG is clear.

As a result of these close-to-unity distribution coefficients, large, homogeneous GSGG crystals codoped with Cr^{3+} and Nd^{3+} can be fabricated.[15] Both Zharikov et al.[15, 16] and Pruss et al.[17] conducted spectroscopic and luminescence studies in GSGG codoped with Cr^{3+} and Nd^{3+} and demonstrated an efficient energy transfer $Cr^{3+} \rightarrow Nd^{3+}$. Pruss and Huber reported transfer efficiency of 86% within a 17-μs duration. A proof of efficient energy transfer Cr → Nd is given in Fig. 4.3, where the emission spectrum of Cr^{3+} and Nd^{3+} is observed by 647.1 nm excitation. In particular, Nd^{3+} emission of both $^4F_{3/2} \rightarrow {}^4I_{9/2}$ and $^4F_{3/2} \rightarrow {}^4I_{11/2}$ (peaking at

Table 4.3 Energy gap between $^4T_2$ and ^2E levels of Cr^{3+} in several garnets.

Energy gap ΔE (cm^{-1})	Laser host
350	YSGG
300–335	GGG
600	YGG
50	GSGG
1043	YAG
−1000	LLGG
10	(Ca,Zr)GGG*
481	YIGG**

*$(Gd,Ca)_3(Ga,Zr,Gd)_2Ga3O_{12}$ [Ref. 18].
**$Y_3(In,Ga)_2Ga_3O_{12}$ [Ref. 20].

Table 4.4 Distribution coefficient for Cr^{3+} and Nd^{3+} and lattice constant parameters for several garnets.

Host	Lattice constant (Å)	Distribution coefficient, Nd^{3+}	Distribution coefficient, Cr^{3+}
YAG	12.01	0.18[5]	
GGG	12.3844	0.63[6]	3.3[15]
Ca,Zr-sub GGG	12.4535*	N/A	2.8[18]
GSGG	12.561	0.75[15]	∼1[15]

*Average value as a result of a multisite structure in this host.

1.06 μm) was recorded by direct excitation into the Cr^{3+} ($^4A_2 \rightarrow {}^2E$) band, by using the 647.1-nm Kr-line laser.[17] The same authors also reported CW operation of Cr,Nd:GSGG with a slope efficiency of 41% while pumping into the Cr^{3+} absorption bands (647.1 nm). A lower slope efficiency, 36%, was obtained by pumping

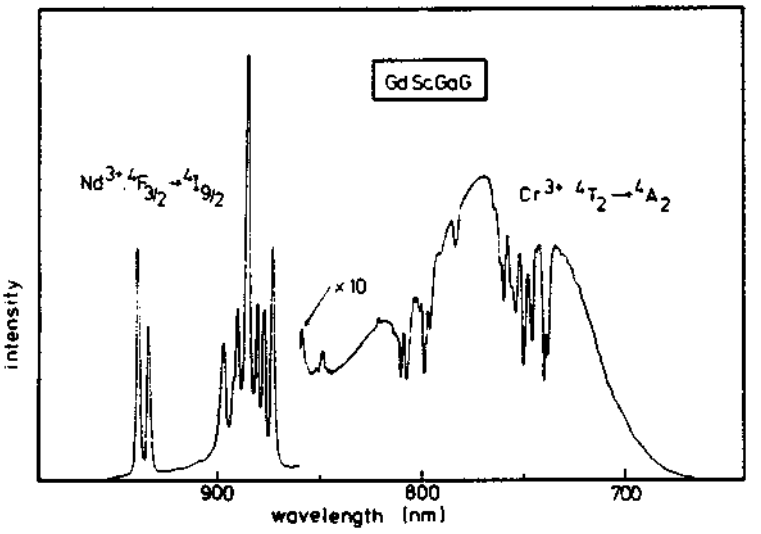

(a)

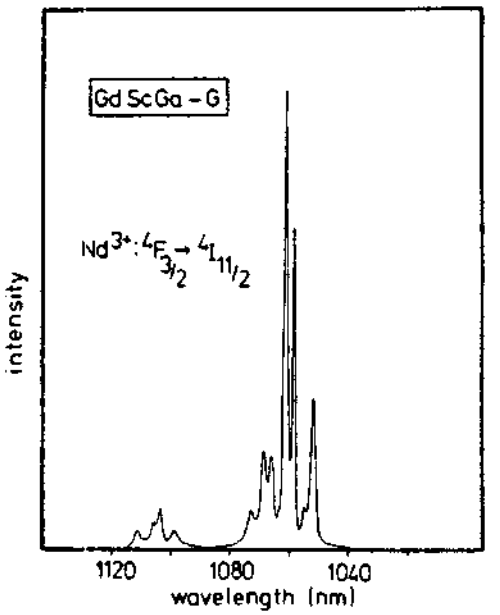

(b)

Figure 4.3 Emission spectrum of Cr,Nd:GSGG at ambient temperature excited into Cr^{3+} band at 647.1 nm: (a) 700–950 nm, and (b) 1040–1120 nm. (Reprinted from Ref. 17 with permission from Springer-Verlag.)

directly into the Nd^{3+} bands at 530.9 nm. The performance curve of this laser, pumped by Kr-line, is shown in Fig. 4.4.

At the same time, Zharikov et al.[15] compared the free-running laser performance of Cr:Nd:GSGG and Nd:GSGG. They found that the former was much more efficient than the latter. The improved performance of the codoped crystal can be seen in Fig. 4.5, which compares (under the same experimental conditions) the laser performance of the Nd:GSGG (curve 1) with the performance of the Cr:Nd:GSGG (curve 2), as well as that of Nd:YAG (curve 3).

They also characterized the energy transfer in the Cr → Nd system and found that the probability for energy-transfer experiments on Cr → Nd is higher in GSGG by a factor of ≅20 than in YAG.

For a Cr:Nd:YSGG, a free-running, pulsed operation with a slope efficiency of $\eta = 11.5\%$ was reported. Also, a maximum output energy with equal concentrations of 3×10^{20} cm^{-3} for both Cr^{3+} and Nd^{3+} yielded a total efficiency of 10.5% of 20 J. The Q-switched operation at a 50-Hz repetition rate yielded a slope efficiency of 5.4% with total efficiency of 3.6%. (Results for the lasing performance of Cr,Nd:RESG were summarized by Smirnov and Shcherbakov.[9])

Zharikov et al.[16] also compared the performance of a GSGG-codoped host with Nd:YAG. They found that Cr,Nd:GSGG performed better than Nd:YAG both in a free-running pulsed mode and a Q-switched mode. The slope efficiency for Cr,Nd:GSGG in a free-running mode was reported to be higher than in YAG by a factor of ≅3.5.

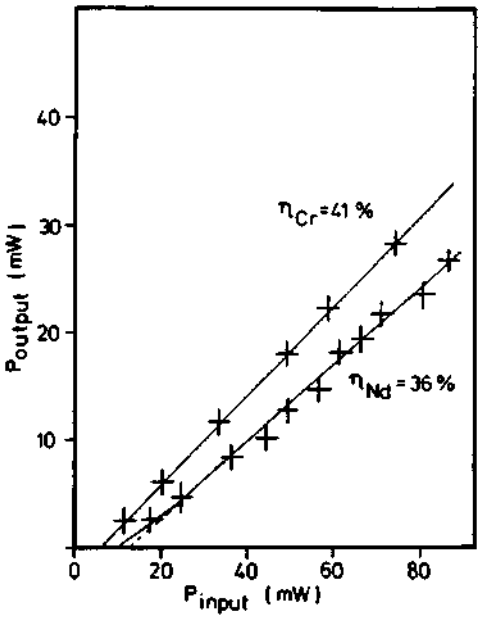

Figure 4.4 Performance of a Cr,Nd:GSGG laser pumped into Cr^{3+} absorption band $^4A_2 \rightarrow {}^4T_2$ and directly into Nd^{3+} levels. (Reprinted from Ref. 17 with permission from Springer-Verlag.)

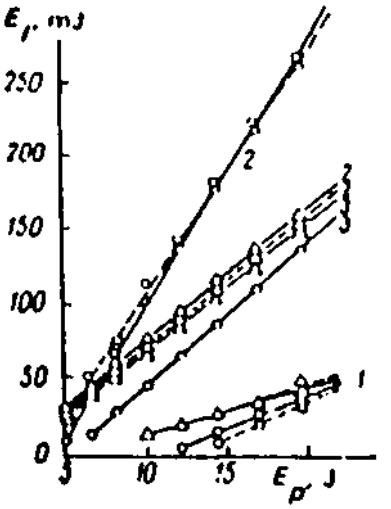

Figure 4.5 Dependence of the free-running output energy on the input energy of Nd:GSGG (curve 1), Cr:Nd:GSGG (curve 2), and Nd:YAG (curve 3) for two different output couplers: $R = 83\%$-Δ, and $R = 48\%$-O. (Reprinted from Ref. 15 with permission from the American Institute of Physics).

The results described in this section demonstrate that with a proper choice of host and sensitizer, the pumping efficiency of a laser system can be improved. However, there might be some financial limitations on the use of scandium-based garnets, which will be explored in the following section.

4.3 Disordered (Mixed) Garnets

As noted earlier, GSGG has a lower crystal field and therefore will lower the energy gap ΔE between $^4T_2$ and ^{2}E to a value of 50 cm^{-1} (see Table 4.3). The presence of expensive scandium is the biggest disadvantage of this material. In order to obtain a garnet with a lower crystal field, Brenier et al.[18] proposed the use of Ca,Zr-substituted GGG.

The three symmetry sites of garnet structure allow for multiple substitutions. For example, in the garnet GGG ($Gd_3Ga_5O_{12}$), which has symmetry—sites of Gd_3, dodecahedral, Ga_2, octahedral, and Ga_3, tetrahedral—the possibility exists that some Gd^{3+} will occupy the Ga octahedral sites. The garnet will have the chemical formula $[Gd_3]\{Ga_{2-x}Gd_x\}(Ga_3)O_{12}$. The difference in the ionic radii of Ga and Gd is a source for defect sites in the crystal. The disorder in the GGG crystal can be increased by multi-substitution of the garnet with Ca and Zr ions.

The Ca ions substitute for the Gd ions in the dodecahedral sites and the Zr ions substitute for the Ga ions in the octahedral sites. The increase in the disorder is accompanied by an increase in the average lattice constant, and thus a decrease in the crystal field as well as in the energy gap ($^4T_2$-^{2}E) to 10 cm^{-1}. The (Ca,Zr)-substituted GGG exhibits an intermediate disordered structure between pure crys-

talline and pure glassy structure. Table 4.3 presents comparative values of the energy gap for different garnets, including substituted garnets. The lowering in ΔE affects the performance of Cr^{3+} as a tunable laser and as an efficient sensitizer for rare-earth lasing ions. Cr^{3+}-doped GGG emission usually has an exponential profile at all temperatures. However, in (Ca,Zr)-GGG, the decay is nonexponential at low temperatures. The defects introduced into the crystal by Ca and Zr, which substitute for Gd and Ga, respectively, create a nonhomogeneous structure in the crystal. This will yield a wide distribution of the lattice constants as well as a distribution of the local crystal fields.

Grinberg et al. presented a theoretical treatment of the spectral and temporal characteristics of Cr^{3+} in Ca,Zr-substituted GGG.[19] In the case of intermediate crystal fields (as in the case of mixed garnets), the first electronic excited state in octahedrally coordinated Cr^{3+} is a mixture of the ^2E state and components of the Cr^{3+} $^4T_2$ state. The emission spectrum at low temperatures will have spectral characteristics of both electronic states.[19] The small energy gap between $^4T_2$ and ^2E (10 cm^{-1}) increases the tunability as well as the spectral overlap between Cr^{3+} emission and rare-earth ions' absorption, and consequently enhances the sensitization of a rare earth codoped with Cr^{3+}. By increasing the temperature, the population of the $^4T_2$ level will increase and the decay curve will have characteristics typical of this state. The $^4T_2$ will also decay faster as a result of the spin-allowed transitions from $^4T_2$ to the ground level, $^4A_2$. This is demonstrated in Fig. 4.6, where the decay curves of the mixed $^4T_2$ and ^2E are displayed at various temperatures.

Another variety of mixed garnets is based on chromium-doped $Y_3(In,Ga)Ga_3O_{12}$ (YIGG).[20] This material is close in its crystal-field strength to GSGG. The values of the energy gaps ΔE in Table 4.3 are proportional to the strength of the crystal field. As depicted in Table 4.3, the crystal field is lower in YIGG than in YAG and is comparable to garnets such as GSGG and GGG. The Cr^{3+} emission in this crystal exhibits a large Stokes shift, of 2490 cm^{-1} higher than

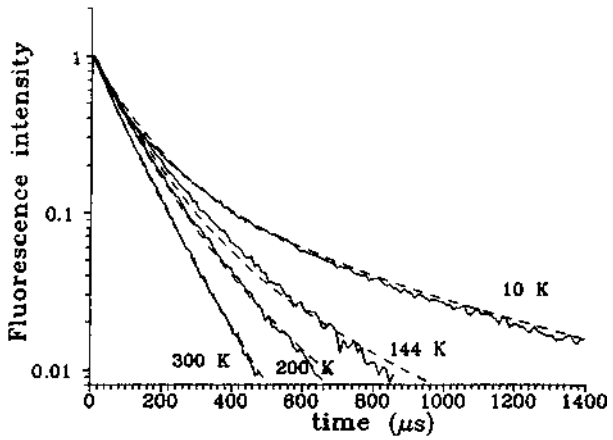

Figure 4.6 Fluorescence intensity decay curves of Cr^{3+} in (Ca, Zr)-GGG at various temperatures. (Reprinted from Ref. 19 with permission from Elsevier.)

other garnets such as YAG, GSGG, and GIGG. This fact has several advantages for YIGG:

- High luminescence efficiencies
- Small probability of self absorption of the emission from $^4T_2$ level, by a ground state reabsorption via the $^4A_2 \rightarrow {}^4T_2$ transition
- Broadband emission (a potential candidate for a tunable laser and a good sensitizer)
- Multisite structure reflected by its large inhomogeneous width as a result of replacement of In sites with the Ga octahedral sites and the difference in the ionic radii between In and Ga

4.4 Glass and Crystalline Ceramics

Glass ceramics comprise a class featuring a solid matrix with a heterogeneous structure of microcrystallites embedded into a mother glass matrix. Glass ceramics are obtained by first melting and then annealing the glass with some nucleating agents, such as TiO_2 or ZrO_2. During the thermal treatment, dispersed crystal nuclei are formed. Those materials incorporate the desired spectroscopic and thermomechanical properties of both mother glasses and crystals. They can therefore serve as potential efficient hosts for inorganic lasing ions when the unique properties of glassy hosts are required with improved thermal and mechanical properties. Improvement in the glass ceramics' transparency was obtained by replacing the TiO_2 with ZrO_2 and Ta_2O_5. In the case of Nd^{3+}-doped glass ceramics,[21] introducing La_2O_3 and $AlPO_4$ to replace some of the SiO_2 contents of the glass ceramics further improved the fluorescence intensity of Nd^{3+} by a factor of 3–4. The size of the crystallites obtained is between 0.5 and 0.1 μm, so the refractive indices of the glassy and crystalline phases are close enough to retain a high degree of transparency.

Cr^{3+}-doped glass ceramics can serve as a probe for studying the optical properties of glass ceramics and doped glass ceramics.[10, 22] Referring to the Sugano and Tanabe[10, 11] diagram for Cr^{3+} in octahedral symmetry, it can be observed that the spin-forbidden transition $^4A_2 \rightarrow {}^2E$ results from a transition among the lower set of the orbitals $(t_2)^3$. No change occurs in the symmetry of the electronic orbitals in the ground and excited states. Therefore, the equilibrium position of the ground and the excited configurations remains unchanged. This means a weak vibrational coupling and therefore a sharp emission line.

In the other case of the electronic transition, the spin-allowed transition $^4A_2 \rightarrow {}^4T_2$ arises from the t_2 set to the e-set. The e-orbitals are directed towards the ligands of the octahedron; that is, they contribute to the antibonding molecular orbitals. In the excited state, the one electron in the vicinity of the ligands causes a distortion that results from electrostatic repulsion. The distortion is accompanied by an increase in the equilibrium distance between Cr^{3+} and its ligands. The increase in

the equilibrium distance results in stronger interaction of the $^4T_2$ level with the vibrational modes, and therefore broadband transition.

From the Tanabe-Sugano diagram, we can observe that the energetic position of $^4T_2$ in octahedral symmetry is sensitive to the crystal field, which is related to the internuclear distance between Cr^{3+} and its ligands. Therefore, changing the structural properties of a particular host, namely an open or tightly closed structure, changes the crystal field to low, intermediate, and high, respectively. From Fig. 4.2, it is evident that for a high crystal-field strength, $^4T_2$ level is above ^2E; for low crystal-field strength, $^4T_2$ level is below ^2E; and in the intermediate case, the energies of $^4T_2$ and ^2E are equal. Therefore, doping Cr^{3+} in a medium that combines both glassy and crystalline structures (e.g., glass ceramics) will create combined spectroscopic properties in terms of emission spectra and lifetimes.[23] In this case, the emission is a combination of the $^2E \rightarrow {}^4A_2$ sharp-line emission and the $^4T_2 \rightarrow {}^4A_2$ vibrationally coupled broadband emission. By choosing a *low crystal-field host* (a host with an open structure), a broadband Cr^{3+} emission is obtained, as is clearly shown in Fig. 4.7. At room temperature, $^4T_2$ and ^2E levels are in thermal equilibrium. In a host with a low crystal-field strength, $^4T_2$ may be close or even below ^2E. In this case, the level $^4T_2$ is strongly coupled to the ground state $^4A_2$ via host phonons, as can also be seen in Fig. 4.7.

Glass ceramics exhibit multisite structure as a result of their glassy character. Since $^4T_2$ and ^2E are in thermal equilibrium, we expect to observe the same decay characteristics for the two levels. However, as a result of this multisite nature, Cr^{3+} will exhibit different and complex temporal characteristics for the two electronic levels. Time-resolved spectroscopy indicates that the $^2E \rightarrow {}^4A_2$ and $^4T_2 \rightarrow {}^4A_2$ transitions have different decay times and different time-dependent spectral characteristics. The decay curves measured separately are nonexponential even at 4.4 K. This is not a general rule; for example, in mullite with a stoichiometric formula $2Al_2O_3 \cdot SiO_2$, Kalisky et al.[24] used time-resolved spectroscopy and found that the parent glass has a multisite structure while no such evidence was found in the glass ceramic phase.

Polycrystalline ceramic lasers have been demonstrated recently as a source for a Nd laser. Polycrystalline ceramic laser material is an aggregate of crystalline grains (10-nm nanocrystals to 10-μm microcrystals in size and with a grain boundary of less than 1 nm), each randomly oriented with respect to the neighboring grains. The polycrystalline grains are sintered, that is, heated to temperatures slightly below their melting temperature (sintering). As a result of the sintering process, a bulk material with nanocrystallites is formed. YAG ceramics have little porosity, so there is very low scattering loss at the 1064-nm lasing wavelength. Optical properties such as absorption, emission, fluorescence lifetime, and damage threshold are identical to those observed in Nd:YAG. The Nd:YAG ceramic laser has several advantages over Nd:YAG single crystals. These include:

- Less expensive laser material and a fast preparation process.

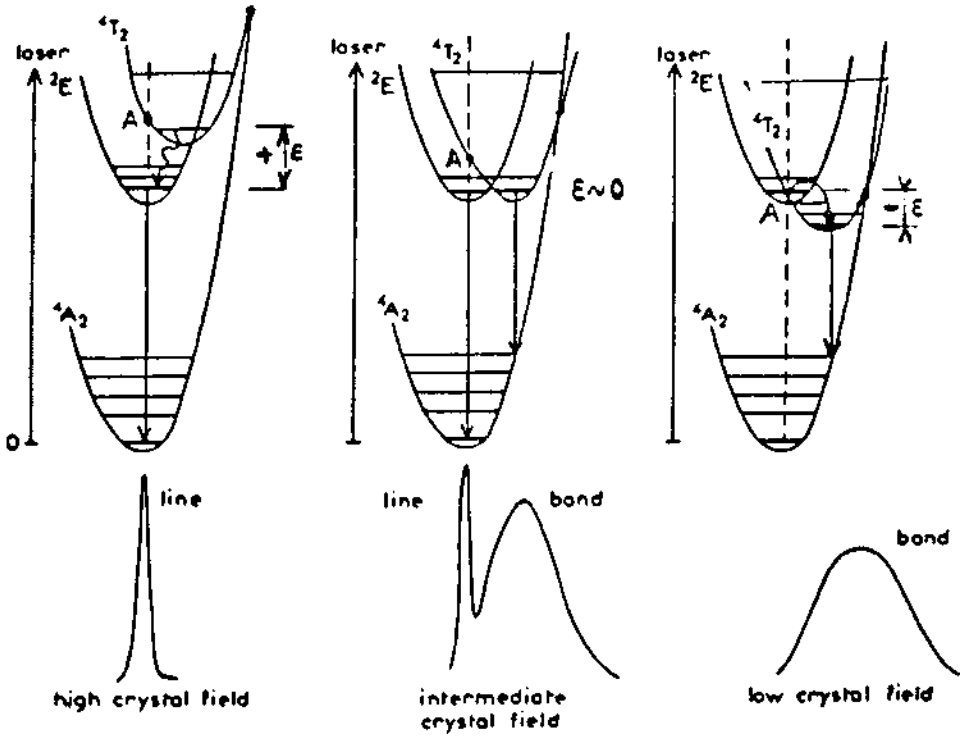

Figure 4.7 Configuration coordinate diagram for Cr^{3+} levels in octahedral symmetry, showing three cases of different crystal-field strengths. Excitation is into the vibronic levels of $^4T_2$. The $^2E \rightarrow {}^4A_2$ emission is a sharp line, while the vibrationally coupled $^4T_2 \rightarrow {}^4A_2$ transition is a broadband emission. (Reprinted from Ref. 23 with permission from Springer Science and Business Media.)

- Scaling—they are capable of large-size, easy, and less-expensive fabrication with the potential of scaling to samples of large size (presently, ceramics having ∅ 10 mm × 400 mm are being used).
- The possibility of mass-produced lasers with larger polycrystalline volumes than single crystals.
- A high neodymium doping level, up to 9 at. %.
- Multilayer and multicolor; e.g., different dopant elements and multifunctional ceramic structure.
- Superior mechanical properties and wavefront distortion compared to a YAG crystal (the thermal-shock parameter is $R \approx 1200$ W/m compared to $R \approx 790$ W/m in YAG and 118 W/m in SFAP $Sr_5(PO_4)_3F$).

These advantages present a promising potential pertaining to scaling the system, adding more flexibility in a diode-pumped configuration and in laser design.

The progress in diode-pumped Nd:YAG ceramic lasers has shown a remarkable development in recent years. The first operation of such a laser was reported in 1995 by Ikesue et al.[25] This laser yielded 70-mW output power at 1.06 μm,

with a slope efficiency of 28%. Later, Lu et al.[26, 27] reported end-pumping of 1 at. % and 2 at. % Nd ceramic, and 0.9 at. % Nd:YAG, with slope efficiencies of 58.5%, 55.4%, and 55.2%, respectively. The optical-to-optical conversion efficiencies were all above 50%. Side-pumping of $\varnothing = 3$ mm$\times$104 mm Nd:YAG ceramic, AR/AR coated on both sides, yielded 72 W at 290-W pumping power with 24.8% optical-optical efficiency.[26] The performances of the 1 at. % and 2 at. % Nd ceramics were almost identical to the Nd:YAG laser. A concentration quenching occurs at 4 at. % of Nd^{3+} relative to the 0.6 at. %, as is reflected in the different lifetimes: 96 μs for the high concentration as compared with 252 μs for the low doping level of 0.6 at. %.[28, 29] Efficient operation of a Nd:YAG ceramic laser, with maximum slope efficiency of 53%, was obtained at a doping range of 1.0–2.0 at. % of Nd^{3+}.[30] Presently, the 1% Nd:YAG ceramic laser ($\varnothing = 8$ mm $\times$203 mm) produces 1.46 kW, with optical-to-optical conversion efficiency of 42%, by employing diode side-pumping technology.[31] This result, although lower than the 1% Nd:YAG (1.72 kW, 49% optical-to-optical efficiency), indicates the potential of the Nd:YAG ceramic laser. At low pumping power levels, the Nd-ceramic YAG performed better than the single crystal Nd:YAG, with 110 W of output power under 300 W of pumping power, with slope efficiency of 41.2%.

Laser oscillation owing to the $^4F_{3/2} \rightarrow {}^4I_{13/2}$ ($\lambda \approx 1.32\,\mu$m) was first demonstrated with an unoptimized, end-pumped experimental setup. The maximum output power obtained was about 0.7 W.[31] Further improvements yielded 36-W output power under 290-W pumping power with 12.5% conversion efficiency.[32]

The possibility of obtaining reduced sample thickness as a result of high doping levels enhances the potential for producing Nd:YAG ceramics as compact and efficient microchip lasers. The losses in a 2.3 at. % Nd^{3+} ceramic YAG were found to be as low as that of a 0.9 at. % Nd:YAG single crystal; with 3.4 at. % doping level of Nd:YAG ceramic, the microchip output power obtained was 2.3 times higher than that obtained with a 0.9 at. % Nd:YAG single crystal,[33] or even better using a higher Nd^{3+} doping level. Although the increase of Nd^{3+} concentration reduces the effective emission lifetime, it is accompanied by inhomogeneous broadening that is favorable for diode pumping. It was found that 3.4 at. %-doped Nd^{3+} ceramic YAG has an absorption coefficient of $\cong$30 cm^{-1} at 808 nm, which allows the 847-μm thickness Nd-ceramics to operate efficiently and better than a single-crystal Nd:YAG laser.[28] The vacuum-sintering method used to fabricate ceramic laser materials is advantageous in producing crystals that are difficult to grow (with high optical quality and large size) by conventional crystal-growth methods. Such crystals include, for example, Nd:Y_2O_3 or Sc_2O_3, which have several favorable laser-material characteristics. The crystal is of excellent mechanical thermal and optical properties, with chemical stability and ruggedness, optical transmission over a broad spectral range, and broadband emission transition. The cubic optically isotropic crystal has a lattice constant of 10.6 Å and refraction index of 1.94. The thermal conductivity of pure Y_2O_3 is $k = 33$ W/m K, which is more than twice the corresponding value of Nd:YAG, and the thermal expansion coefficient is similar ($7 \times 10^{-6}\,K^{-1}$) to that of YAG. The Nd-doped Y_2O_3 ceramic has an

absorption band peaking at 806.6 nm, with an absorption coefficient of 12.8 cm^{-1} for a standard Nd^{3+} concentration. Therefore, it can be pumped by any commercial laser diode in this range. The lasing wavelengths of Nd:Y_2O_3 are $\lambda \approx 1074$ and $\lambda \approx 1078$ nm, with stimulated emission cross sections of 3.7×10^{-20} cm^2 and 4.2×10^{-20} cm^2, respectively. This Nd:Y_2O_3 ceramic laser produced 160 mW of output power with 32% slope efficiency without any AR coating, using a standard longitudinal pumping scheme.[34, 35] Recent high-resolution spectroscopic studies and laser experiments by Lupei et al.[36, 37] indicate that in concentrated Nd:YAG ceramics, the Nd^{3+} ions occupy the dodecahedral garnet site, but with minor site distribution and no aggregation. As occurs in the diluted single crystals, a statistical distribution occurs, which leads to random distribution of ions among the available sites with only minor pairing. Therefore, the state of Nd^{3+} in the Nd:YAG ceramics is similar to that of single crystals.[38] However, the YAG ceramics have the advantage of a more stoichiometric composition and uniform doping over the sample volume.

One of the main drawbacks of Nd:YAG laser crystals is the thermal-induced birefringence for laser crystals that are (111)-cut. Thermal-induced birefringence in Nd:YAG ceramics was observed to be similar to that in Nd:YAG single crystals. The amount of thermal-induced depolarization was found to be the same for both Nd:YAG ceramics and Nd:YAG single crystals with orientation (111), and at the same Nd^{3+} concentration.[39] The depolarization increased significantly for higher Nd^{3+} concentration (for the same absorption power), mainly as a result of the increase in the fractional thermal load at higher Nd^{3+} concentrations. As an example for such phenomena, for a Nd^{3+}concentration of 1.1–1.3 at. %, the thermal-induced depolarization for YAG single crystals and YAG ceramics were similar, while a sharp increase in depolarization was observed for Nd^{3+} concentrations of 2.0 at. % and 3.4 at. %. Therefore, although high doping levels of Nd^{3+} in YAG ceramics have some favorable characteristics, they may introduce disadvantages in terms of enhanced thermal-induced birefringence. Recently, Lu et al.[40] reported a 110-W CW output power from a ceramic Nd:YAG laser (41% slope efficiency) by using a homogeneous, symmetrical, ring-shaped pumping source. This is done through virtual point source (VPS) geometry using 32 sets of 10-W diode lasers with an 807-nm emission. The diodes are arranged in a ring-shaped geometry with high angular uniformity. The ring-shaped output beam was focused onto the crystal and the focused image was termed as the virtual point source.[41] Other crystals, such as Nd:YSAG (Nd:$Y_3Sc_xAl_{5-x}O_{12}$), which are useful for subpicosecond and mode-locking applications, are difficult to grow as single crystals. The Nd (1.0 at. %):YSAG can be manufactured as a high-quality ceramic laser medium with laser performance of 30% slope efficiency and larger bandwidth when compared to a single crystal, namely, 5.5 nm (FWHM) around 1.06 μm.[42]

References

1. B. I. Denker, V. V. Osiko, B. P. Starikov, et al., "Spectroscopic properties of neodymium-activated scandium garnets," *Sov. J. Quantun Electron.* **6**(3), 334–336 (1976).
2. M. R. Kokta, "Czochralski growth of oxide laser crystals," *Mat. Res. Soc. Symp.* **329**, 33–43 (1993).
3. M. R. Kokta, "Solubility enhancement of Nd^{3+} in scandium substituted rare-earth aluminum garnets," *J. Solid State Chem.* **8**, 39–42 (1973).
4. C. D. Brandle and J. C. Vanderleeden, "Growth, optical properties, and CW laser action of neodymium-doped gadolinium scandium aluminum garnet," *IEEE J. Quantum Electron.* **QE-10**(2), 67–71 (1974).
5. R. R. Monchamp, "The distribution coefficient of neodymium and lutetium in Czochralski grown $Y_3Al_5O_{12}$," *J. Cryst. Growth* **11**, 310–312 (1971).
6. C. D. Brandle and R. L. Barns, "Crystal stoichiometry and growth of rare earth garnets containing scandium," *J. Crys. Growth* **20**, 1–5 (1973).
7. Z. T. Kiss and R. C. Duncan, "Cross-pumped Cr^{3+}-Nd^{3+}:YAG laser system," *Appl. Phys. Lett.* **5**, 200–202 (1964).
8. R. Balda, J. Fernandez, A. de Pablos, and J. M. Fernandez-Navarro, "Cr^{3+}-Nd^{3+} energy transfer in fluorophosphate glass investigated by time-resolved laser spectroscopy," *Phys. Rev. B* (Condensed Matter) **48**(5), 2941–2948 (1993).
9. V. A. Smirnov and I. A. Shcherbakov, "Rare-earth scandium chromium garnets an active media for solid state lasers," *IEEE J. Quantum Electron.* **24**(6), 949–959 (1988).
10. S. Sugano, Y. Tanabe, and H. Kamimura, *Multiplets of Transition—Metal Ions in Crystals*, Academic Press, New York (1970).
11. Y. Tanabe and S. Sugano, "On the absorption spectra of complex ions," Part I, *J. Phys. Soc. Japan* **9**, 753–766 (1954); Part II, *J. Phys. Soc. Japan* **9**, 766–779 (1954).
12. R. Reisfeld and C. K. Jorgensen, "Lasers and excited states of rare earths," in *Inorganic Chemistry Concepts* **1**, Springer-Verlag, Berlin, Heidelberg, and New York (1977).
13. L. A. Riseberg and M. J. Weber, "Relaxation phenomena in rare-earth luminescence," in *Progress in Optics* **XIV**, 89–159, North-Holland (1976).
14. R. Reisfeld, "Potential uses of chromium (III) doped transparent glass ceramics in luminescent solar concentrators," *Electronic Structure of New Materials* Part I, Report No. 40, 7–34, The Swedish Academy of Engineering Sciences in Finland (1985).
15. E. V. Zharikov, N. N. Il'ichev, V. V. Laptev, et al., "Spectral luminescence and lasing properties of gadolinium scandium gallium garnet crystals activated with neodymium and chromium ions," *Sov. J. Quantum Electron.* **13**(1), 82–85 (1983), and references therein.

16. E. P. Zharikov, V. A. Zhitnyuk, G. M. Zverev, et al., "Active media for high-efficiency neodymium lasers with nonselective pumping," *Sov. J. Quantum Electron.* **12**(12), 1652–1653 (1982).
17. D. Pruss, G. Huber, and A. Beimowski, "Efficient Cr^{3+} sensitized Nd^{3+}:GdScGa-garnet laser at 1.06 μm," *Appl. Phys. B* **28**, 355–358 (1982).
18. A. Brenier, G. Boulon, C. Pedrini, and C. Madej, "Effects on Ca^{2+} Zr^{4+} ion pairs on spectroscopic properties of Cr^{3+} multisites in Cr^{3+}-doped $Gd_3Ga_5O_{12}$ garnets," *J. Appl. Phys.* **71**(12), 6062–6068 (1992).
19. M. Grinberg, A. Brenier, G. Boulon, C. Pedrini, and C. Madej, "Bandwidth and the time evolution of Cr^{3+} fluorescence in (Ca,Zr)-substituted $Gd_3Ga_5O_{12}$," *J. Lumin.* **55**, 303–314 (1993).
20. Y.-K. Li, B. Zhang, and Y.-x. Xia, "Spectral properties of a novel phonon terminated laser crystal YIGG:Cr^{3+}," in *Conference on Lasers and Electro-Optics* **11**, Paper CWJ37, 312, OSA Technical Digest Series (1993).
21. G. Muller and N. Neuroth, "Glass ceramic—a new laser host material," *J. Appl. Phys.* **44**(5), 2315–2318 (1973).
22. R. Reisfeld, M. Eyal, and G. Boulon, "Prospects of chromium(III) in transparent glass ceramics for tunable lasers," *Material Sciences* **15**(1), 5–44 (1989).
23. G. Boulon, "Effects of disorder on the spectral properties of Cr-doped glasses, glass ceramics and crystals," *Disordered Solids: Structures and Processes* **46**, 317–341, Plenum Press—Physical Sciences, New York, Kluwer Academic Publishers (1988).
24. Y. Kalisky, V. Poncon, G. Boulon, et al., "Time resolved spectroscopy of chromium (III) in mullite transparent glass-ceramics," *Chem. Phys. Letters* **136**(3,4), 368–370 (1987).
25. A. Ikesue, T. Kinoshita, K. Kamata, and K. Yoshida, "Fabrication and optical properties of high performance polycrystalline Nd:YAG ceramics for solid state lasers," *J. Am. Ceram. Soc.* **78**(9), 1033–1040 (1995).
26. J. Lu, T. Murai, K. Takaichi, et al., "Recent progress of Nd:YAG ceramic lasers," in *OSA Trends in Optics and Photonics (TOPS)* **50**, *Advanced Solid State Lasers*, 610–614 (2001).
27. J. Lu, M. Prabhu, J. Song, et al., "Highly efficient Nd:$Y_3Al_5O_{12}$ ceramic laser," *Jpn. J. of Appl. Phys.* **40**(6A), L552–554 (2001).
28. I. Shoji, S. Kurimura, Y. Sato, et al. "Optical properties and laser characteristics of highly Nd^{3+}-doped $Y_3Al_5O_{12}$ ceramics," *Appl. Phys. Lett.* **77**(7), 939–941 (2000).
29. J. Lu, T. Murai, K. Takaichi, et al., "72 W Nd:$Y_3Al_5O_{12}$ ceramic laser," *Appl. Phys. Lett.* **78**(23), 3586–3588 (2001).
30. J. Lu, M. Prabhu, J. Song, et al., "Optical properties and highly efficient laser oscillation of Nd:YAG ceramics," *Appl. Phys. B* **71**(4), 469–473 (2000).
31. J. Lu, T. Murai, K. Takaichi, et al., "1.46 kW CW Nd:YAG ceramic laser," in *OSA Trends in Optics and Photonics (TOPS)* **68**, *Advanced Solid State Lasers*, WE1-1-WE1-3, OSA Technical Digest, Postconference Edition (2002).

32. J. Lu, J. Lu, T. Murai, et al., "36-W diode-pumped continuous wave 1319 nm Nd:YAG ceramic laser," *Opt. Lett.* **27**(13), 1120–1122 (2002); also in J. Lu, T. Murai, K. Takaichi, et al., "New highly efficient 1.3 μm CW generation of $^4F_{3/2} \rightarrow {}^4I_{13/2}$ channel of nanocrystalline Nd^{3+}:$Y_3Al_5O_{12}$ ceramic laser under diode pumping," *Phys. Stat. Solidi A* **189**(2), R11–13 (2002).
33. I. Shoji, S. Kurimura, Y. Sato, et al., "Optical properties and laser oscillations of highly neodymium-doped YAG ceramics," *OSA Trends in Optics and Photonics* Vol. 34, *Advanced Solid State Lasers* 475–479 (2000); also in A. Ikesue, T. Taira, Y. Sato, and K. Yoshida, *J. Ceram. Soc. of Japan* **108**(4), 428–430 (2000).
34. J. Stone and C. A. Burrus, "Nd:Y_2O_3 single-crystal fiber laser: Room temperature cw operation at 1.07 and 1.35 μm wavelength," *J. Appl. Phys.* **49**(4), 2281–2287 (1978).
35. J. Lu, J. Lu, T. Murai, et al., "Highly efficient CW Nd:Y_2O_3 ceramic laser," in *OSA Trends in Optics and Photonics (TOPS)* **68**, *Advanced Solid State Lasers*, TuC2-1-TuC2-3, OSA Technical Digest, Postconference Edition (2002).
36. V. Lupei, A. Lupei, N. Pavel, T. Taira, and A. Ikesue, "Comparative investigation of spectroscopic and laser emission characteristics under direct 885 nm pump of concentrated Nd:YAG ceramics and crystals," *Appl. Phys. B* **73**(7), 757–762 (2001).
37. V. Lupei, T. Taira, A. Lupei, et al., "Spectroscopy and laser emission under hot band resonant pump in highly doped Nd:YAG ceramics," *Opt. Commun.* **195**(1–4), 225–232 (2001).
38. V. Lupei, A. Lupei, S. Georgescu, et al., "High resolution spectroscopy and emission decay in concentrated Nd:YAG ceramics," *J. Opt. Soc. Amer. B* **19**(3), 360–368 (2002).
39. I. Shoji, Y. Sato, S. Kimura, et al., "Thermal birefringence induced depolarization in Nd:YAG ceramics," *Opt. Lett.* **27**(4), 234–236 (2002).
40. J. Lu, H. Yagi, K. Takaichi, et al., "110 W ceramic Nd^{3+}:$Y_3Al_5O_{12}$ laser," *Appl. Phys. B* **79**, 25–28 (2004).
41. N. Uehara, K. Nakahara, and K. Ueda, "Continuous wave TEM_{00}-mode 26.5-W output virtual point source diode array pumped Nd:YAG laser," *Opt. Lett.* **20**, 1707–1709 (1995).
42. Y. Sato, I. Shoji, T. Taira, and A. Ikesue, "The spectroscopic properties and laser characteristics of polycrystalline Nd:$Y_3Sc_xAl_{5-x}O_{12}$ laser media," in *OSA Trends in Optics and Photonics* (TOPS) **83**, *Advanced Solid State Photonics* 444–450 (2003).

Chapter 5

Fluoride Laser Crystals: $YLiF_4$ (YLF)

Fluoride crystals are among the most important hosts for laser materials because of their special optical properties. Of these, $LiYF_4$ (YLF) is one of the most common rare-earth-doped laser materials, with a variety of efficient mid-IR laser lines from the UV (Ce^{3+}:YLF)[1] to mid–IR range. Generally, YLF has good optical properties with high transparency throughout the emission spectrum of the conventional sources used for pumping solid state lasers. YLF does not show UV damage, and it has lower nonradiative decay rates for processes occurring between electronic levels participating in the pumping and lasing process. YLF also has a low, two-photon absorption coefficient. Because of its low nonradiative rates, the material can be used for cascade emission[2] between intermediate levels as well as an up-converter, as will be discussed later.

YLF is also a good medium for mode locking at 1047 or 1053 nm and 1.313 μm as a result of its natural birefringence and low thermal lensing. Mode-locked pulses from YLF are shorter thanks to its broader linewidth, both for the 1047/1053-nm and 1.313-μm emission peaks. The crystallographic structure of $LiYF_4$ (or YLF) is the same as $CaWO_4$, which was developed years ago as a potential laser material.[3] However, when a trivalent rare-earth material substitutes for the Ca^{2+} ion, charge compensation is necessary. However, the process of charge compensation may result in inhomogeneities in the crystal and is a source of disordered crystal structure. No charge compensation is necessary with YLF throughout the doping process, since the trivalent rare-earth-ion substitutes for the Y^{3+} ion. As a result, a single undisturbed site exists. The crystal has tetragonal symmetry; the important optical and physical properties are shown in Tables 4.1 and 4.2. Figure 5.1 shows a schematic energy-level diagram of those levels participating in the lasing process in Nd:YLF.

5.1 Thermal and Mechanical Properties of YLF

Thermal and mechanical properties of αβHo:YLF were measured by Chicklis et al.[4] See also Tables 4.1 and 4.2. The authors described and analyzed the esti-

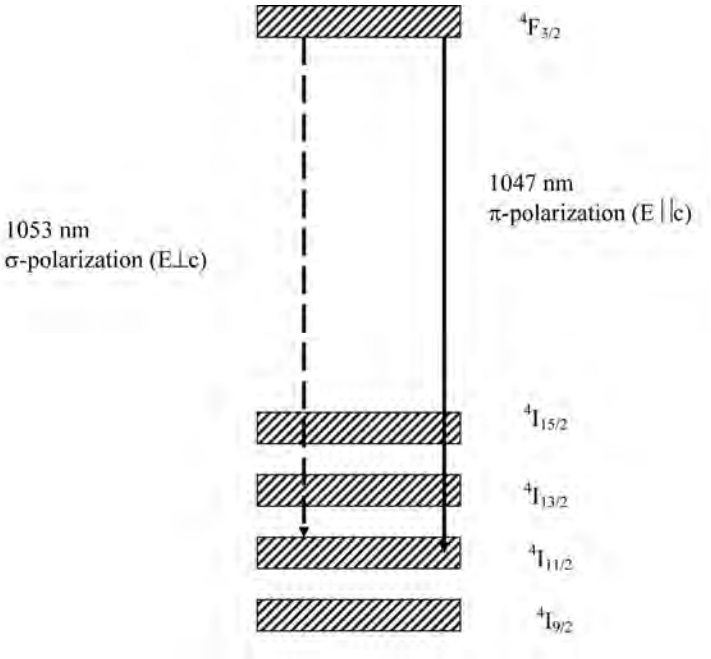

Figure 5.1 Schematic energy-level diagram of electronic levels participating in the lasing process in Nd:YLF. Broken line: 1053 nm (σ polarization, $E \perp c$); full line: 1047 nm (π polarization, $E||c$).

mated power loading at fracture. The following sections explain some of the concepts used in thermal-load analysis.

5.1.1 Estimate of thermal load at fracture

Unused energy deposited in a laser crystal is converted into heat. Two main reasons account for heat accumulation:

1. The quantum gap between the absorbed pump light and the lasing energies, e.g., the energy difference between absorbed pump light and fluorescence energies.
2. An inefficient pumping source. The spectral distribution of the pump light is broad relative to the narrow absorption lines of the lasing ion. The undesired pumping energy is absorbed by the host and is transformed into heat.

The heat generated owing to the above mechanisms and the radial heat flow resulting from the cooling process of the laser rod surface together cause the thermal effects in a laser rod.

In order to calculate the temperature distribution in a laser rod, these assumptions are made:

- The heat generates uniformly in the laser rod. The cooling process is uniform along the laser rod surface.
- The laser rod is an infinitely long cylindrical rod of radius r_0.
- The heat flow is radial.
- Small end effects occur.

The cross-sectional geometries generally used for lasers are cylindrical and heat removal is carried out through the circumferential surface of the cylinder. Therefore, radial temperature distribution has a parabolic profile, which is given by

$$T(r) = T(r_0) + \frac{1}{4K} Q\left(r_0^2 - r^2\right), \tag{5.1}$$

where $T(r)$ is the temperature at a distance r from the rod axis, $T(r_0)$ is the temperature at the rod surface, r_0 is the rod radius, K is the thermal conductivity, and Q is the heat per unit volume dissipated in the rod. As seen from Eq. (5.1), the radial temperature distribution inside a laser rod has a parabolic profile. Therefore, temperature gradients are formed inside the cylindrical laser rod, and these gradients lead to the following effects:

- Mechanical stresses inside the laser rod.
- Photoelastic effects and a change in the refraction index.
- Thermal lensing owing to changes in the refraction index.
- End-face curvature resulting from mechanical stresses relating to temperature gradients.
- Thermal-induced birefringence.
- Depolarization of polarized light.

The thermal load and the mechanical stresses formed inside the laser rod can lead to a rod fracture. The value of the thermal load at the fracture of a uniformly heated laser rod, cooled at the surface, is an important parameter in estimating the average output power available from a given host.

A stress distribution gradient is accompanied by a temperature gradient,[4]

$$\sigma_{\mathrm{r}}(r) = \frac{2\alpha \mathrm{E}}{(1-\mu)16k} Q\left(r^2 - r_0^2\right), \tag{5.2}$$

$$\sigma_{\theta}(r) = \frac{2\alpha \mathrm{E}}{(1-\mu)16k} Q\left(3r^2 - r_0^2\right), \tag{5.3}$$

$$\sigma_{z}(r) = \frac{2\alpha \mathrm{E}}{(1-\mu)16k} Q\left(4r^2 - 2r_0^2\right), \tag{5.4}$$

where the parameters appearing in Eqs. (5.2) to (5.4) are defined as $\sigma_{\mathrm{r}}(r)$, the radial stress at distance r; $\sigma_{\theta}(r)$, the tangential stress at distance r; $\sigma_{z}(r)$, the axial

stress at distance r; μ is Poisson's ratio; E is Young's modulus; and α is the thermal expansion coefficient. See Fig. 5.2 for a demonstration of these parameters. From these expressions, it is seen that the radial component of the stress disappears at the rod's surface while the tangential and axial components do not vanish. Therefore, the rod is under tension, which may cause it to crack. The value of the power loading per unit length for YLF is 11 W/cm, while for YAG it is 60 W/cm.

Perhaps one of the most important factors affecting the laser performance of YLF crystal is its refractive index. YLF has a negative change of refractive index with temperature: $\mathrm{d}n/\mathrm{d}T < 0$, where n is the refraction index and T is the crystal temperature. This minimizes the thermal lensing effects in the crystal and improves the fraction of the available power with the TEM_{00} mode, improving the beam quality. Assume an absorbing medium heated by radiation. If its temperature is increased by ΔT at a certain point owing to heat formation, the refractive index upon irradiation is given

$$n(\Delta T) = n(0) + \left(\frac{\mathrm{d}n}{\mathrm{d}T}\right) \cdot \Delta T, \tag{5.5}$$

where $n(0)$ is the refractive index at any point without pumping the absorbing medium and $\mathrm{d}n/\mathrm{d}T$ is the dependence of the refraction index on temperature.

Assuming also a cylindrical lasing medium cooled through its surface, the temperature will have maximum value along the axis and minimum value at the surface, and it will drop gradually from the center to the peripheral region. If the condition $\mathrm{d}n/\mathrm{d}T > 0$ is fulfilled, the axis region will be optically denser than the surface [according to Eq. (5.5)], and the radiation along the rod axis will be focused since rays will be deflected into the region containing a higher value of n. In the case of $\mathrm{d}n/\mathrm{d}T < 0$, the periphery will be denser than the axis, and rays propagating along the rod axis will be defocused. In the case of $\mathrm{d}n/\mathrm{d}T > 0$, the active element is identical to a convergent lens, and in the case of $\mathrm{d}n/\mathrm{d}T < 0$, it is identical to a divergent lens. The phenomenon in which the laser element acts as a lens is called *thermal lensing*. The radial temperature gradient causes a refractive index gradient along the radius of the crystal, giving the laser rod the characteristics of a graded index (GRIN) lens. Another contribution to thermal lensing is

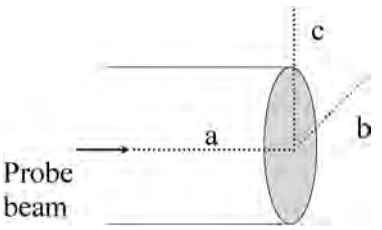

Figure 5.2 Crystallographic directions of the laser rod in the thermal lensing experiment performed by H. Vanherzeele. The σ polarization at 1053 nm is the ordinary polarization ($E \perp c$); π polarization at 1047 nm is the extraordinary polarization ($E || c$).

the effect of the crystal faces bending under strong thermomechanical stresses. Koechner[5] analyzed the thermal lensing effects in a Nd:YAG laser rod theoretically and experimentally under flashlamp pumping and external probe laser. The expression for the total focal length obtained by Koechner contains the GRIN lens contribution as well as elasto-optical terms, which contribute to the end-face curvature,

$$f = \frac{KA}{P_{\text{in}}\eta}\left[\frac{1}{2}\frac{\mathrm{d}n}{\mathrm{d}T} + \alpha C_{\text{r},\phi} n_0^3 + \frac{\alpha l_0 (n_0 - 1)}{L}\right], \tag{5.6}$$

where A is the rod cross section, K is the thermal conductivity of the laser rod, P_{in} is the input incident pump power, η is the heat dissipation factor ($Q = \eta \mathrm{P}_{\text{in}}$), n_0 is the refraction index at the center of the rod, α is the thermal expansion coefficient, l_0 is the depth of the end effect (the length up to the point where no significant contribution to surface bending occurs), L is the length of the laser rod, and $C_{\text{r},\phi}$ is a functional representation of electro-optical coefficients with the radial and tangential components of the orthogonal polarized light.

The combination of the two effects (radial temperature gradients and crystal-face bending) can be approximated by a thin lens located at the end of the laser rod, with dioptric power of[6]

$$D_{\text{R}} = D_{\text{E}} + D_T, \tag{5.7}$$

where D_{R} is the dioptric power of the overall thermal lensing, D_T is the GRIN lens effect, and D_{E} is the bending end effect of the laser rod. The depth of the end effect and the radius of the rod can be assumed to be roughly equal, e.g., $r_0 \approx l_0$. Therefore, the two contributions to thermal lensing, the GRIN lens, D_T, and the end effect D_{E}, are given respectively as

$$D_T = \frac{QL}{K}\left(\frac{1}{2}\frac{\mathrm{d}n}{\mathrm{d}T} + \alpha C_{r,\phi} n^3\right) \tag{5.8}$$

and

$$D_{\text{E}} = \frac{1}{K}[\alpha Q r_0 (n - 1)], \tag{5.9}$$

where Q is the heat generated in the laser rod per unit volume, K is the thermal conductivity, L is the length of the laser rod, T is the rod temperature, α is the thermal expansion coefficient, n is the refraction index, and r_0 is the radius of the rod. The end effect contribution to thermal lensing for homogeneous pumping was estimated to be about 20%; it is independent of the absorption coefficient. In the case of inhomogeneous pumping, such as longitudinal diode pumping, the actual magnitude of the absorption coefficient (or doping level), the pump spot

size, and the value of l_0 has to be considered in estimating the end effect lensing. For example, for a pump spot radius of 0.3 mm, rod diameter of $r_0 = 1.5$ mm, and absorption length of 2.5 mm, the fraction of the end effect lensing is 46% for a monolithic and 28% for an external resonator.

A comparative study and thermal lensing measurements in YLF and YAG[7] show that at 700-W average input power, the extraordinary polarization (π-polarized transition, $E||c$ of Nd:YLF with emission at $\lambda = 1047$ nm) has a focal length of the order of magnitude of meters, namely 60 ± 20 M, while the ordinary polarization (σ polarization, $E \perp c$ at $\lambda = 1053$ nm) had a weak thermal lensing effect, with a lower limit for the focal length of about ± 150 M. The measurements were taken using a probe beam at 633 nm and an intracavity polarizer for selecting the 1047-nm or 1053-nm transitions, then imaging the beam coming from the surface of the laser crystal by a focusing lens and an aperture. Changes in the transmission of the probe beam passing through the aperture during the laser operation were measured and the appropriate focal lengths were obtained. Thermal lensing for both types of polarizations is much weaker than that in Nd:YAG ($f_{\text{th}} = +8.3$ M).[7] The negative value of $\mathrm{d}n/\mathrm{d}T$ cancels most of the contribution from stress-optics effects to the total changes in the refraction index of the laser crystal. These changes are given by $n(r, \Delta T) = n_0 + \Delta n(r)_T + \Delta n(r)_\varepsilon{}^8 = n_0 + (\partial n/\partial T)_\varepsilon \Delta T + \Delta n(r)_\varepsilon$, where $n(r, \Delta T)$ is the radial variation of the refractive index with a temperature increase of ΔT, n_0 is the refractive index at the center of the rod, and $\Delta n(r)_{\text{T}}$ and $\Delta n(r)_\varepsilon$ are purely thermal- and stress-dependent changes of the refractive index, respectively. The stresses (or thermoelastic stresses) in the crystal create photoelastic effects in the crystal, which cause nonuniform variations in the refractive index of the heated medium. The variation $+\Delta n(r)_\varepsilon$ in the refractive index is caused by the photoelastic effect resulting from thermoelastic stresses in the heated medium. The coefficient $(\partial n/\partial T)_\varepsilon$ is the variation of the refractive index with temperature (under uniform heating) without any stresses. Since the thermally induced focal length of a solid state laser material depends on the relative contribution of the above refractive-index changes in YLF and they are of the same order of magnitude, we obtain $n(r) \cong n_0$, in the case of $\mathrm{d}n/\mathrm{d}T < 0$, which implies that YLF exhibits weak thermal effects. In longitudinally pumped solid state lasers, the inhomogeneous heat deposition is much more pronounced than that in transverse-pumped systems; therefore, it results in stress and strain and consequently laser rod fracture. A detailed investigation of the σ polarization with weak focusing effects was reported by Vanherzeele.[9] He measured thermal lensing in two directions, parallel and perpendicular to the c-axis (the laser rod axis was along the crystallographic a-axis); Fig. 5.2 illustrates the crystallographic directions of the laser rod in the experiment described in Ref. 9.

The method used in this experiment was similar to that reported in Ref. 7 except that the pinhole used was not circular, but a narrow slit positioned parallel or perpendicular to the c-axis in the (a, b) plane and (a, c) plane. It was found that

thermal lensing is different not only for the σ and π polarizations but also for (a, b) and (a, c) planes. For example, a σ polarization has a negative focal length, $f < 0$, for the (a, c) plane $(\sigma||c)$, and $f > 0$ for the (a, b) plane $(\sigma\perp c)$. This effect will lead to astigmatism and must be compensated for.[9]

When side diode pumping was used to pump Nd:YLF, it was found that thermal lensing was much stronger in a diode-pumped system as compared to a lamp-pumped Nd:YLF.[10] Specifically, at 30-W pumping power, the thermally induced focal length was about 70–80 cm, and it changed to 40–45 cm at the 60-W pumping level. The value of the thermal lensing coefficient (ξ) was extracted from

$$\frac{1}{f} = \xi\left(\frac{P}{A}\right), \tag{5.10}$$

where f is the focal length, P is the absorbed pumping power, and A is the laser rod cross-sectional area. It was found that ξ has the values of 2–3 $m^{-1}/kW/cm^2$.

The thermal lensing in the diode-pumping system is much higher than the flashlamp-pumped case, despite the fact that the total power deposited into a laser rod in a flashlamp-pumped system is much higher than in a diode-pumped system. Armstrong et al.[10] attributed this to the fact that the pumping density in the diode-pumping case is higher than in a lamp-pumped case. Thermal lensing in diode-pumped laser rods can be reduced significantly by using a variable configuration resonator (VCR) with compensatory optics or, alternatively, composite rods with a diffusion-bonded, undoped, end-cup[2, 11] sapphire plate, since the undoped section enhances the heat flow.[11] For a longitudinal diode-pumped Nd:YAG composite laser rod, a 47% reduction in thermal lensing and consequent increase of 89% in the maximum pump power was demonstrated.[6]

Temperature variations of the refractive index in YLF were investigated by Barnes and Gettemy.[12] The measurements were made in the visible spectral regime using an undoped YLF crystal prism. Results from the measured ordinary (n_o) and extraordinary (n_e) indices of refraction and their variation with temperature are presented in Table 5.1.

The temperature variation of the refractive indices of several oxide and fluoride crystals is presented in Table 5.2. It shows that fluorides generally have negative values of dn/dT, while oxides and other crystals, such as those listed in the table, have a positive change in refraction index with temperature and therefore will exhibit thermal lensing effects.

Table 5.1 Measured refraction indices and their variation with temperature for YLF. The values of dn_o/dT and dn_e/dT were measured several times and averaged. (Data taken from Ref. 12.)

λ (nm)	n_o	dn_o/dT ($°C^{-1}$)	n_e	dn_e/dT ($°C^{-1}$)
435.8	1.46136	-0.54×10^{-6}	1.48389	-2.44×10^{-6}
546.1	1.45599	-0.67×10^{-6}	1.47826	-2.30×10^{-6}
578.0	1.45499	-0.91×10^{-6}	1.47705	-2.86×10^{-6}

Table 5.2 Temperature variation of refractive indices of several crystals. (Data taken from Ref. 12.)

Crystal	$dn/dT \times 10^6$ ($^\circ C^{-1}$)	Crystal	$dn/dT \times 10^6$ ($^\circ C^{-1}$)
Al_2O_3	13.1	BaF_2	-18.6
SiO_2	10	CaF_2	-16.0
CdTe	93	LiF	-17 ± 0.2
Ge	396 ± 40	KCl	36.5 ± 0.2
Si	154 ± 15	NaCl	-31
ZnSe	10.7 ± 1		

5.2 Nonradiative Losses in YLF

Another important property of YLF is its low nonradiative decay rates. YLF has lower nonradiative losses than oxides since the phonon energy of fluorides is lower than that of oxides. This has several effects on the performance of rare-earth-doped fluorides:

- Rare-earth-doped fluorides are generally more efficient luminescent systems.
- Less heat is dissipated in the fluoride crystal as a result of lower nonradiative rates.
- As a result of the low nonradiative losses in fluorides, rare-earth-doped fluorides exhibit a longer fluorescence lifetime of the emitting level than the rare-earth-doped oxides.

As an example of the last statement, the $^4F_{3/2}$ lasing level of Nd^{3+} has a longer fluorescence lifetime in YLF than in the same concentration in YAG (see Table 5.3 for comparative data pertaining to the Nd:YLF and the Nd:YAG). This fact has an advantage in CW operation or for Q-switching applications, where Nd:YLF performs better than Nd:YAG. In this experiment, the laser rods of both Nd:YLF and Nd:YAG were 6.3 mm in diameter $\times$ 76 mm in length, doped with 1% Nd^{3+} (1.3×10^{20} cm^{-3} ion density), and AR coated on both sides at 1064 nm for YAG and 1050 nm for YLF.

The pump cavities used for the experiments were in a gold- or silver-plated single elliptical configuration. The optical resonator was a confocal resonator for both YLF and YAG, pumped by a tungsten-halogen lamp, with an output coupling

Table 5.3 Laser parameters for Nd:YLF and Nd:YAG.[13]

Parameter/host	YLF	YAG
Stimulated emission cross section, σ (cm^2)	1.2×10^{-19} (σ polarization) 1.8×10^{-19} (π polarization)	2.4×10^{-19}
Fluorescence lifetime of $^4F_{3/2}$, τ (μsec)	480–525	230–240
$P_{th}(YLF)/P_{th}$(YAG), P_{th} power at threshold	0.85	
η(YLF)/η(YAG), η slope efficiency	0.53	

reflectivity $R = 99\%$. When pumped by a krypton laser, the system consisted of a flat/flat resonator having an output coupling reflectivity of $R = 90\%$.

Since YLF has lower thermal lensing than YAG, it has a better beam quality even at high-average power operating conditions. Therefore, we expect a higher fraction of the available laser power in the TEM_{00} mode in YLF than will be seen in YAG. The TEM_{00} mode volume for Nd:YLF is larger by a factor of 4 than the mode volume observed in YAG, whereas the TEM_{00} mode average power for YLF is higher by a factor of two than in YAG.[13] YLF has lower nonradiative rates (within its electronic levels) than the oxides, and its emitting levels have a longer lifetime. In the case of Nd-doped fluorides like YLF or LaF_3, the longer lifetime of $^4F_{3/2}$ level of Nd:YLF is a source for excited state absorption (ESA). This phenomenon is another channel for the depletion of the lasing level $^4F_{3/2}$. As a result of this depletion, yellow emission and upconversion lasing in the Nd-doped LaF_3 has been observed. Seelert et al.[14] found that for pumping densities of 800 W/cm^2, the $^4F_{3/2}$ level is depopulated with a 30% reduction of the lifetime, which also reduces the storage potential of this level.

Numerous publications on the performance of rare-earth-doped YLF and other hosts can be found in professional publications and proceedings such as the Conference on Lasers and Electro-Optics (CLEO) or Advanced Solid State Lasers and Advanced Solid State Photonics. The specific cases of Nd, Tm, Ho, or Er as laser systems are of special importance and will be discussed below.

5.3 Neodymium-Doped YLF

One of the major applications of all the 1-μm pump lasers is to obtain wavelength diversity by using nonlinear crystals for frequency conversion to shorter wavelength (multiharmonic generation), or frequency shifting to longer wavelengths by optical parametric oscillators (OPO). For an efficient frequency conversion or shifting, it is necessary to have a 1-μm laser source with high peak power, high beam quality, narrowband emission, and relatively high average output power.

The special characteristics of Nd-doped YLF can be used to produce high peak power and a high-quality laser beam, mainly due to the longer fluorescence lifetime of the $^3F_{3/2}$ lasing level and the low thermal lensing. These lasers can be CW lamp pumped or diode pumped using two different geometries (side or longitudinal pumping).

One of the first picosecond (ps) terawatt (TW) oscillators at 1053 nm based on a Nd:YLF oscillator was developed by Mercer at al.[15] The birefringent nature of YLF was utilized to produce the ordinary ray (σ polarization, $E \perp c$) at 1053 nm. This diode-pumped, mode-locked Nd:YLF laser produced stable output—less than 3% in peak-to-peak energy variation in pulses of 1.6–2.5 ps duration. By using this system with chirped pulse amplification (CPA), a 5-TW output power was obtained. The typical mode-locked train was of about 2-ps pulsewidth duration with spectral bandwidth of 0.68 nm (184 GHz).

The long fluorescent lifetime of the $^4F_{3/2}$ emitting level of Nd:YLF (e.g., 480–525 μs compared with 240 μs in Nd:YAG) presents a significant advantage where there is a need to control the timing and magnitude of prelasing. By properly controlling the timing between the $LiNbO_3$ Pockels cell and the pumping diode, Turi et al.[16] reduced the buildup of the relaxation oscillations and minimized pre-lasing leakage.

Turi et al.[16] utilized the birefringent nature of YLF to extract the 1047-nm emission of Nd-doped YLF, the wide bandwidth of the Nd^{3+} emission, and the good beam quality even under thermal load to design a compact, ps, longitudinally diode-pumped Nd:YLF laser, with pulse energies ranging from 120 to 500 μJ at a 1-kHz repetition rate. Their experimental system, which is an astigmatically compensated folded cavity, ensured good overlap between the pump and laser fundamental transverse modes without the use of an external mode-limiting aperture. The experimental setup, which is commonly used in a longitudinally diode-pumped laser, is presented in Fig. 5.3.

A CW, near-diffraction-limited ($M^2 < 1.2$), multipass, side-diode-pumped Nd:YLF laser was operated by Harrison et al.[17] Output power scale-up could be obtained by using a side-pumping configuration, but the beam quality was much worse compared to that obtained using longitudinal pumping. The 20-W fiber-lensed bars were coupled to the YLF laser rod from both sides, but offset relative to each other's position to establish a planar gain region. Multiple passes through the gain medium were generated by coating the crystal end faces or by using external mirrors. Despite the clear limitations of the side-pumping configuration, this laser performed impressively in terms of beam quality and efficiency. This pumping configuration produced high optical efficiencies (>33%) both for the near-diffraction-limited and multimode laser beam. The good beam quality at TEM_{00} mode also resulted in efficient Q-switching and frequency doubling of the output. Further developments yielded efficient, multiharmonic generation.[18] The multipass Nd:YLF oscillator/amplifier (MOPA) system produced 37-W CW output power and 29-W Q-switched power (5-kHz repetition rate at 20-ns

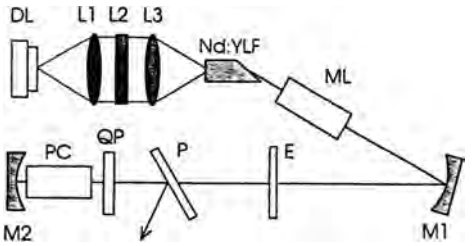

Figure 5.3 Schematic experimetal setup of a diode-pumped Nd:YLF laser, where DL is a 3-W diode laser; L1, L2, and L3 are spherical lenses; ML is the mode locker; M1 and M2 are high reflectors; E is the etalon; P is the thin film polarizer; QP is the quarter-wave plate; and PC is the Pockels cell. (Reprinted from Ref. 16 with permission from the Optical Society of America.)

pulsewidth, FWHM), with diffraction-limited beam quality. Using nonlinear crystals such as LBO and CLBO, the Q-switched system produced modulated laser light at frequencies up to 100 kHz, with output power of 14 W at 523.5 nm, 6.6 W at 262 nm, and 2 W at 209 nm. The 209-nm beam was generated by mixing the 262 nm with the 1047 nm in a CLBO Type I phase-matched crystal. The UV optics sustained UV irradiation. The damage threshold of the nonlinear UV crystals for the 262-nm laser occurred at a fluence of 3.4 J/cm^2, at a 5-kHz repetition rate. The conversion efficiency of the input fundamental beam (1047 nm) to the fourth harmonic output was ≈25%. The overall optical conversion efficiency was 7.6%.

Another approach, presented by Armstrong et al.,[10] utilized a symmetric, two-head diode side-pumping configuration with an efficient pump chamber to use the unabsorbed pumping power. They used two 20-W microlensed CW diode arrays, with emission centered at 797 nm. They used cylindrical lenses to compensate for anisotropic thermal lensing and obtained maximum output power using a two-head laser of 25 W with TEM_{00} beam quality at ≈120-W pumping power—an 18% optical-optical conversion efficiency.

The emission of Nd:YLF at 1047 nm can be used to amplify Yb:$Sr_5(PO_4)_3F$ Yb:SFAP diode-pumped emission. The advantage of the Nd:YLF laser stems from its emission wavelength of 1047 nm, which overlaps with the lasing emission of Yb:SFAP. These two lasers are good candidates for a diode-pumped oscillator/amplifier system. The hybrid Nd:YAG oscillator and Yb:SFAP amplifier generated ≈70 mJ of Q-switched (8-ns pulsewidth) output energy at 60 Hz and at ≈20 mJ of input oscillator energy on the amplifier.[19]

5.4 Holmium-Doped YLF

Crystals of αβHo:YLF with the stoichiometric composition $LiY_{1-x-y-z}Er_xTm_yHo_zF_4$, $x = 50\%$, $y = 5$–6.7%, $z = 0.25\%$–0.5% (atomic percent) are grown by a top-seeded solution technique in a high-purity inert atmosphere; argon (Ar) or helium (He) is used as the inert gas. Depending on the crystal-growth conditions, scattering inclusions appear in the YLF boules. When helium was used as the inert atmosphere, isolated bubbles parallel to the c-axis appeared. When Ar was used, YLF boules without bubbles and of uniform quality were obtained. These inclusions are formed as a result of chemical impurities such as Mg^{2+}, Ca^{2+} oxides and hydroxides, as well as thermal instabilities in the melt. They function as fine bubbles of microscopic size, which act as scattering centers. Chicklis et al.[4] noted that two types of precipitation phenomena should be distinguished: oxides that form rare-earth oxyfluorides and chemical complexes between impurities and oxygen. The rare-earth fluorides used for crystal growth should be of high purity without any metallic iron or carbon. The purity of the seeding and fluoride compounds is critical in eliminating grain boundaries in the boule. The impurity level affects the damage threshold of the laser crystal and the degradation of the optical properties of YLF rods upon UV radiation.

The crystal $YLiF_4$ is grown from the melt of LiF-YF_3, which melts incongruently at 819°C. Yttrium in the LiF-YF_3 system can be substituted up to 50% by other rare-earth ions heavier than Sm^{3+} without altering the physical properties of the crystal.

Devor et al.[20] describe in detail the preparation of YLF doped with Tm, Er, Ho in which the starting materials were R_2O_3 (R=Y, Er, Ho, Tm) of 99.999% purity. These were converted to RF_3 by reaction with aqueous HF at room temperature. To complete the conversion, the residue was dried and treated with HF at 700–800°C, where a conversion efficiency of 99.9% was achieved. The role of various oxides in the crystal growth and phase stability of fluorides was also investigated. It was found that levels as low as 10–15 ppm of oxygen would not alter the fluoride structures. At higher concentrations, up to 0.2% mole, oxyfluorides are formed and this phase co-crystallizes with the $LiYF_4$ phase at higher temperature. Upon cooling, a separate oxide phase could precipitate with the $LiYF_4$ crystal; this separate phase is incorporated into the YLF crystal.

Experiments conducted by Chicklis et al.[4] revealed that even in the presence of oxide compounds, a clear, scatter-free YLF can be obtained, since the oxide phase is rejected from the YLF phase and is precipitated separately. Also, it was found that the relation between the trace amounts of optical scattering centers and the oxide content in the melt is not simple, and that the formation of scattering centers depends also on the presence of other impurities such as OH^-, Mg^{2+}, and Ca^{2+}.

5.5 Thulium-Doped YLF

The optical characteristics of YLF indicate that this crystal is a suitable host for other rare-earth ions such as the Tm ion, which (similar to the Ho ion) is a source for laser emission ranging from 1.9 to 2 μm. Diode pumping of both Tm:YLF and Tm:YAG is an efficient process because of the *cross-relaxation processes* among the Tm^{3+} electronic levels, as will be shown in Chapter 9.

Tm:YLF, longitudinally pumped at $\lambda = 792$ nm, recently produced 36 W of a CW output power at 120 W of pumping power.[21]

A CW side-pumping of Tm:YLF using a multi-pass slab was operated in a scheme that is similar to the configuration used for multi-pass diode side-pumped Nd:YLF. For example, a three-pass laser resonator tuned to 1940 nm produced ≈28 W with 25% slope efficiency (see Fig. 9.10). The performance of the Tm:YLF diode side-pumped laser for three passes of the laser beam is presented in Fig. 5.4.[22]

This method of double, multipass side-pumping can be further improved to yield more efficient performance. As an example, for a five-pass laser resonator with an output coupler of $R = 87\%$, the laser operated in TEM_{00} mode with M^2 less than 1.3. The Tm:YLF laser produced 6.5 W of output power in the TEM_{00} mode, with 27% slope efficiency.[21] Using the same pumping setup but single-pass configuration yielded 11 W of multimode output power for a diode pump power of 60 W with 37% slope efficiency.

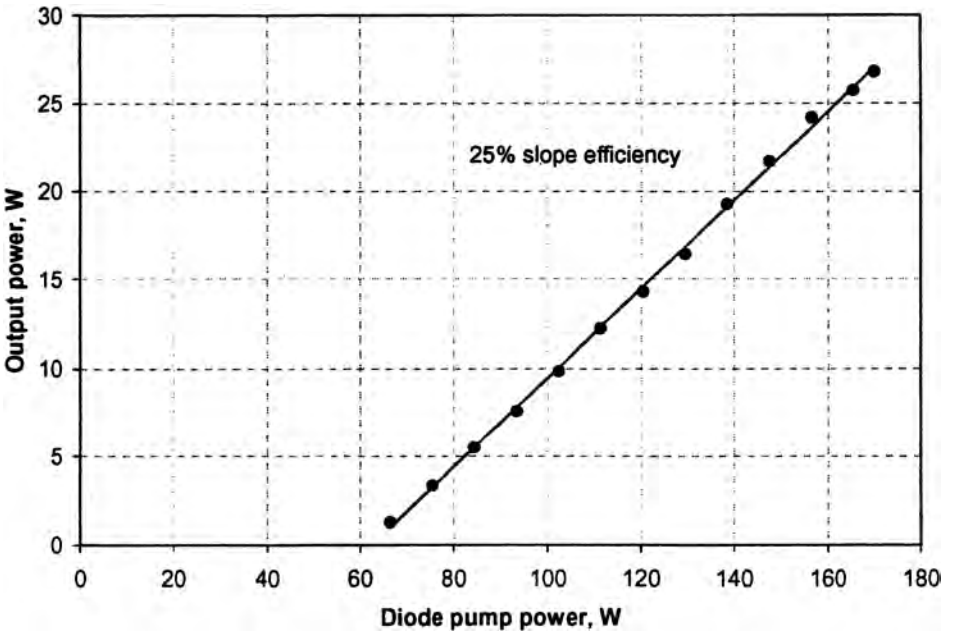

Figure 5.4 Output power of a CW side diode-pumped Tm:YLF laser in a multimode and TEM_{00} fundamental mode. (Reprinted from Ref. 22 with permission from the Optical Society of America.)

This laser was also tunable in the spectral range of 1905 nm to 2067 nm, centered at 1970 nm. It is important to note that the laser transition in the thulium ion, $^3F_4 \rightarrow {}^3H_6$, is of a quasi-three-level nature, since the laser terminates on the ground state manifold. Therefore, an increase in the pumping threshold is expected owing to ground state absorption when the laser mode passes through unpumped volume in the crystal. The multipass design minimizes the unpumped regions in the crystal and hence the thermal load, and therefore it increases the laser efficiency significantly.

Despite the limitations originating from the three-level nature of thulium and the ground state absorption, the thermal load in the Tm:YLF is lower than that of Nd:YLF, mainly because of the efficient pumping process in the thulium system resulting from the cross-relaxation process, as will be explained later. Therefore, with proper engineering, it is expected that Tm:YLF can perform as well as Nd:YLF.

5.6 Other Fluoride Crystals

BaY_2F_8 is another fluoride host for rare-earth-doped laser materials. The lasing and spectroscopic properties of Ho- or Er-doped BaY_2F_8 and $BaYb_2F_8$ will be discussed in more detail below.

BaY_2F_8 is a monoclinic crystal. One crystal axis is orthogonal to the plane containing the other two axes. Its lattice constants are $a = 6.97$, $b = 10.46$, and $c = 4.26$. The angle between the a and c axes is 99.7 deg. Axis b is normalized to the a, c plane. Figure 5.5 presents schematically the crystallographic and optical axes of BaY_2F_8.[23]

Since the main crystal axes are not orthogonal, the optical axes of the refractive index tensor do not coincide with them. As a result, the real and imaginary parts of the refraction index, which correspond to the refraction index of the material and to the absorption cross section, respectively, may have different orientations in the (a, c) plane. This phenomenon will lead to absorption and emission cross sections of different values, depending on the angle relative to the c axis. Dinndorf et al.[23] showed that for Nd:BaY_2F_8 the absorption cross section (σ_a) has a minimum value at 861 nm at an angle of $\theta_0 = 38$ deg $\pm$ 5 relative to the c axis and a maximum for 861 nm at 25° $\pm$ 4. A similar phenomenon was found for lanthanum beryllate, Nd:$La_2Be_2O_5$, denoted also as BEL. For BEL it was also found that an anisotropy of the absorption and emission cross sections occurs. This anisotropic behavior was found within the multiplets of the electronic transition $^4F_{3/2} \rightarrow {}^4I_{9/2}$. This doubly doped Tm:Ho:BaY_2F_8 crystal can be utilized to generate ultrafast pulses. It produced 20-mW average output power at a 100-MHz repetition rate, with sub-100-ps pulses at 2.06 μm ($^5I_7 \rightarrow {}^5I_8$ transition) at ambient temperature.[24]

The low-phonon fluoride hosts have significant advantages that stem from their low nonradiative losses. The principle of low-phonon hosts can be utilized in a glassy fiber-optic amplifier. For example, one of the optical transitions of the Pr^{3+} fiber amplifier that is relevant to optical communications is the transition $^1G_4 \rightarrow {}^3H_5$ ($\lambda_{me} \approx 1300$ nm).[25] This transition has a low emission quantum efficiency. The emission intensity can be increased by changing the host from fluorozirconate to one with lower phonon energies, such as mixed halide glasses. The nonradiative losses are also reflected in the measured lifetime of the $^1G_4$ level: While in fluorozirconate glass, the first e-folding time decay is $\cong$110 μs, and a value of 322 μs was measured for mixed halide glasses. The low nonradiative losses allow the generation of two types of lasers, as will be discussed later. In general, the fluoride hosts have lower nonradiative rates than do the oxide hosts. Be-

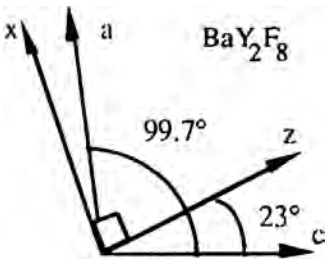

Figure 5.5 Crystallographic and optical axes in BaY_2F_8. (Reprinted from Ref. 23 with permission from the Optical Society of America.)

cause of the smaller nonradiative losses in fluorides, transitions between intermediate states become efficient. As in the case of $YLiF_4$, and other fluorides, BaY_2F_8 can be used for cascade emission to intermediate levels as well as for upconversion processes.[26, 27] Although this text will not analyze these processes, it outlines some typical observations made of fluorides hosts.

5.7 Cascade Emission

One example of cascade emission is the thulium YAG laser emission at 2.3 μm, which was obtained at room temperature by excitation at 781 nm (which is also the pump wavelength of the GaAlAs diode laser).[28]

This laser transition originates from the $^3H_4 \rightarrow {}^3H_5$ transition. The $^3H_4$ level of Tm^{3+} has a lifetime in the ms time regime. The lower lasing level $^3H_5$ has a lifetime of $\tau = 1.0$ ms and the lower Stark levels of this level are thermally unpopulated. The $^3H_4$ level can be sensitized by Cr^{3+} as well as via Yb^{3+} with anti-Stokes pumping of the $^3H_4$ level and lasing via the $^3H_4 \rightarrow {}^3H_5$ and $^3H_4 \rightarrow {}^3F_4$ transitions. These laser transitions are inefficient and possess high threshold energy. Direct excitation into $^3H_4$ level of Tm^{3+} (see Fig. 5.6) at 781 nm yielded 55 mJ output energy at 2.3 μm ($^3H_4 \rightarrow {}^3H_5$ transition) with 15% overall efficiency at room temperature. Also, cascade emission at 3.5 μm ($^3H_5 \rightarrow {}^3F_4$) or $^3F_4 \rightarrow {}^3H_6$ (1.83 μm) was observed because of the long lifetime of the metastable levels, which is a direct result of the low nonradiative processes in fluoride crystals.

Stimulated cascade emission lines in $Ho:BaY_2F_8$ were observed by Johnson and Guggenheim.[29] For $^5F_5 \rightarrow {}^5I_5$ (2.4 μm), $^5I_6 \rightarrow {}^5I_7$ (2.6 μm), and $^5I_7 \rightarrow {}^5I_8$ (2.1 μm) in the low temperature range, 22–77 K. The schematic energy-level diagram and the relevant laser transitions are presented in Fig. 5.7.

Another example of the clear advantage of fluoride over oxide hosts is the possibility of obtaining room-temperature operation of high-lying energy levels, such as the laser operation via the $^5I_5 \rightarrow {}^5I_6$ transition (at 3.9 μm) of $Ho:BaY_2F_8$ fluoride crystal, which yielded 30 mJ of output energy with a slope efficiency of 14.5% and ≈300 mJ of pumping power.

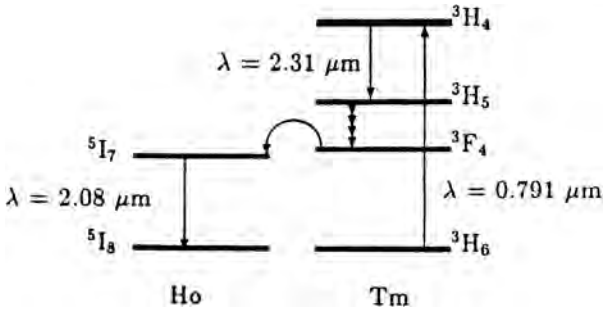

Figure 5.6 Pumping scheme and cascade laser emissions in Tm:Ho system. (Reprinted from Ref. 28.)

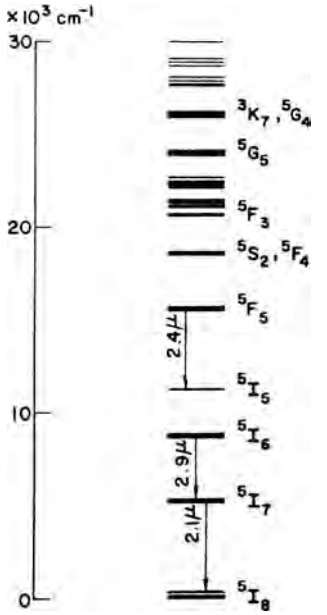

Figure 5.7 Energy-level diagram and cascade transitions in Ho^{3+}:BaY_2F_8. (Reprinted from Ref. 29 with permission from the IEEE and Lucent Technologies Inc./Bell Labs.)

5.8 Upconversion

Upconversion is a multistep process involving low frequency photons, which excite a metastable level that produces laser light with photons that are more energetic than the pump photons. The metastable intermediate energy levels act as a storage energy reservoir for the excitation pumping of photons to higher states, which occurs by energy transfer or excited state absorption of the pump photons. It can originate in a singly doped crystal or from cooperative energy transfer between two different rare-earth ions. Consider the Yb-Er and Yb-Ho systems, in which visible emission both in Ho^{3+} and Er^{3+}, via upconversion processes, was observed in a BaY_2F_8 crystal codoped with Yb^{3+} and Er^{3+} or Yb^{3+} and Ho^{3+}.[30] The pumping wavelength in these experiments was at 960 nm (via the $^2F_{7/2} \rightarrow {}^2F_{5/2}$ transition). A schematic representation of the infrared-pumped visible upconversion processes in Yb-Er and Yb-Ho in BaY_2F_8 are presented in Fig. 5.8.

The Yb-Er system shows two laser lines at $\lambda = 670.9$ nm ($^4F_{9/2} \rightarrow {}^4I_{15/2}$ transition) and at $\lambda = 550$ nm ($^4S_{3/2} \rightarrow {}^4I_{15/2}$). The red and the green emissions are three and two successive processes, respectively. An upconversion process via infrared pumping was found also in Ho:Yb:BaY_2F_8, while pumping was in the near IR. The 960-nm excitation ($^2F_{7/2} \rightarrow {}^2F_{5/2}$) yielded green emission of Ho^{3+} at 551.5 nm. In both cases, Yb-Er or Yb-Ho upconversion was observed at 77 K. The visible lasing in both Er and Ho was into the upper Stark components of the lowest electronic ground level of Er^{3+} ($^5I_{15/2}$) and Ho ($^5I_8$). The upper Stark level in Er^{3+} is 410 cm^{-1} above ground level, while in Ho^{3+}, the highest Stark level of

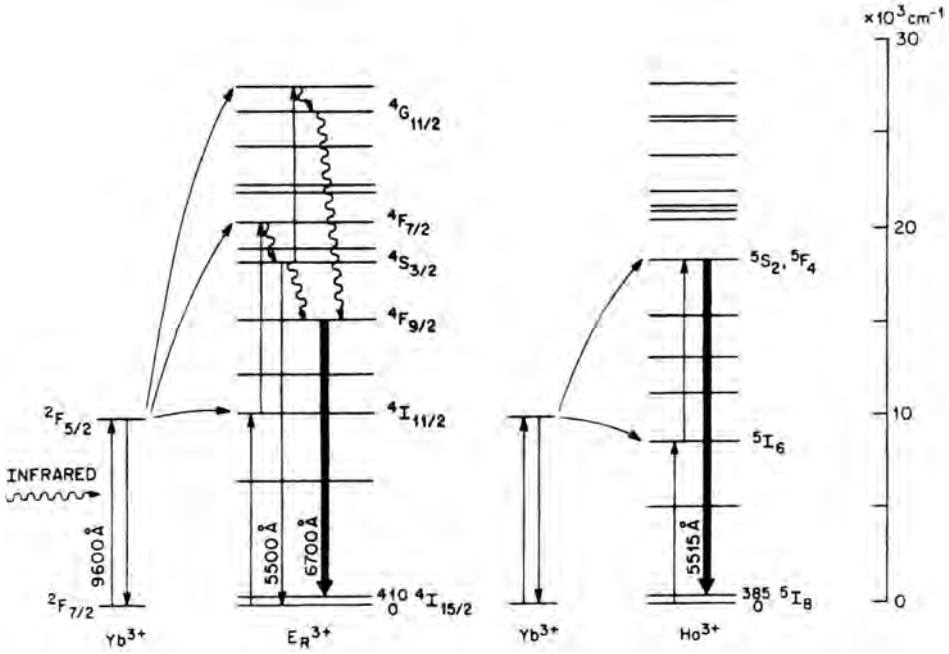

Figure 5.8 Infrared-to-visible upconversion in Yb^{3+}-Er^{3+} and Yb^{3+}-Ho^{3+}-doped BaY_2F_8. (Reprinted from Ref. 30 with permission from the American Institute of Physics and Lucent Technologies Inc./Bell Labs.)

the $^5I_8$ ground state manifold is 385 cm^{-1} above the ground level. By lowering the temperature to 77 K, the population of this level will decrease by a factor of ~300 and the system will become quasi-four-level.

An interesting phenomenon is a trio upconversion in the Er:YLF system,[27] where the excitation is carried out via the $^4I_{15/2} \rightarrow {}^4I_{13/2}$ transition (1.55 μm), with upconverted emission at a wavelength of 550 nm ($^4S_{3/2} \rightarrow {}^4I_{15/2}$). This process is a cooperative energy transfer involving three ions. The dependence of the upconverted 550-nm fluorescence on the incident intensity obeys a cubic power law. The risetime of the $^5S_{3/2}$ is long, approaching that of the $^5I_{13/2}$ level. The CW upconversion laser emission can be explained by the excitation of one Er^{3+} ion to the $^2H_{11/2}$ level, then de-excitation of two neighboring $^4I_{13/2}$ ions.

A green emission at wavelengths of $\lambda = 549.8$ nm ($^4S_{3/2} \rightarrow {}^4I_{15/2}$) at 77 K was also observed in Er:$YAlO_3$ by using either two-step infrared excitation or phonon-assisted cooperative energy transfer.[31] The authors used two dye lasers for the consecutive excitation: The first at 792.1 nm to excite the $^4I_{15/2} \rightarrow {}^4I_{9/2}$ was followed by nonradiative relaxations to populate $^4I_{11/2}$ and $^4I_{13/2}$, levels that have lifetimes in the ms range. A second dye laser at 839.8 nm excites the intermediate level $^4I_{11/2}$ into $^4F_{5/2}$, with subsequent nonradiative decay to $^4S_{3/2}$ and a green emission $^4S_{3/2} \rightarrow {}^4I_{15/2}$. The pumping and lasing pathways are displayed in Fig. 5.9. In addition to the two-step scheme, the $^4S_{3/2}$ level is populated by cooperative energy transfer that involves two Er^{3+} ions in the $^4I_{11/2}$ state. This can be demonstrated by block-

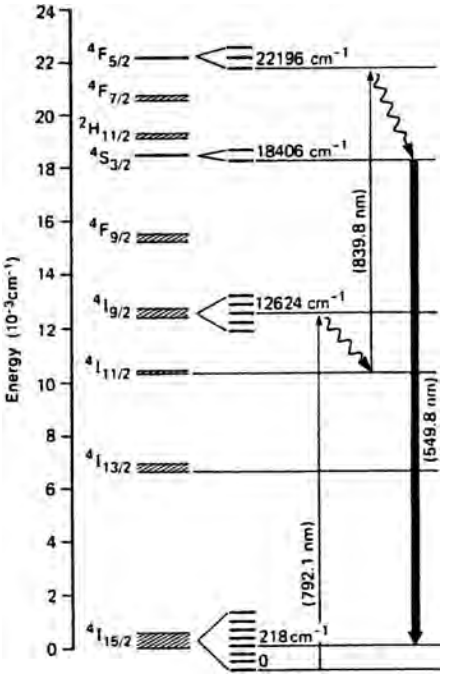

Figure 5.9 Energy-level diagram of Er^{3+} with pumping and lasing pathways. (Reprinted from Ref. 31 with permission from the American Institute of Physics.)

ing the second dye laser beam and observing the green fluorescence originating from the $^4S_{3/2}$ level.

Other green and blue transitions resulting from an upconversion process were reported by Hebert et al.[32] The laser crystal used for this upconversion experiment was 3 mm in length with a doping level of 1 at. % of Er^{3+} and output coupling transmission of T = 1%. They reported upconversion laser action at $\lambda = 469.7$ nm and $\lambda = 560.6$ nm in Er:YLF. The 560.6 nm ($^2H_{9/2} \rightarrow {}^4I_{13/2}$) laser emission was observed by excitation into $^4I_{9/2}$ (797 nm) or $^4I_{11/2}$ (968.9 nm). The transition was terminated on a Stark level, which is 162 cm^{-1} above the lowest component of $^4I_{13/2}$; this level has a 15-ms lifetime. Laser action in the blue, at $\lambda = 469.7$ nm, originating from the $^2P_{3/2} \rightarrow {}^4I_{11/2}$ transition, was observed as well. This multistep process involves multiexcitations and energy transfer.

5.8.1 Applications to upconversion

Upconversion is used in fiber laser technology to produce blue/green laser emission. The system is inexpensive, efficient, and a reliable source of light for a variety of applications in medicine, photography, and semiconductor wafer inspection.[21, 33] The phenomena can be utilized to fabricate a compact, low-cost, multicolor light source. For example, upconverted fluorescence in the red, green, blue, and UV spectra was obtained in a glassy thin film waveguide of

Tm:$BaYYbF_8$ when the pumping was into the Yb^{3+} absorption band at 960 nm ($^2F_{7/2} \rightarrow {}^2F_{5/2}$).[34]

Upconversion lasers are especially attractive when optical glass fibers are doped with rare-earth ions. Relatively high optical intensities and efficient photon conversions can be extracted as a result of the high energy density of the pumping source and the long length of the gain medium. Upconversion is a multistep process that requires a long-lived intermediate metastable level. This can be found in low-phonon hosts such as fluoride glasses. For example, the 455 nm ($^1D_2 \rightarrow {}^3H_4$) and 480 nm ($^1G_4 \rightarrow {}^3H_6$) upconversion laser emission of Tm^{3+} fluorozirconate fiber laser was obtained by IR pumping at 1120 nm or pumping at 645 nm and 1064 nm simultaneously. The role of the 1064-nm pumping is crucial to the process. The pumping and upconversion process is demonstrated in Fig. 5.10. The laser emission at 455 nm is obtained by filling the $^1D_2$ level and depleting the $^3H_4$ level. The two-step process starts with ground state absorption, $^3H_6 \rightarrow {}^3F_2, {}^3F_3$, followed by a fast multiphonon relaxation into a $^3F_4$ metastable state. The second step is excited state absorption $^3F_4 \rightarrow {}^1D_2$ followed by laser emission at 455 nm ($^1D_2 \rightarrow {}^3H_4$). Since the $^3F_4$ terminal level is long lived and creates a bottlenecking effect, it must be depopulated. The 1060-nm pumping radiation via the $^3H_4 \rightarrow {}^3F_2, {}^3F_3$ transition does this.

The 544-nm upconversion laser emission in Er^{3+} can be obtained in Er-doped fluoride glasses by pumping two 970-nm photos consecutively into the $^4I_{11/2}$ and $^4H_{11/2}$ levels, followed by 544-nm emission ($^4S_{3/2} \rightarrow {}^4I_{15/2}$ transition). The lifetimes of the $^4I_{11/2}$ and $^4S_{3/2}$ levels in fluoride glasses are 9 ms and 0.45 ms, respectively. The appropriate lifetimes of Er-doped silicate glass are 7 μs for $^4I_{11/2}$ and

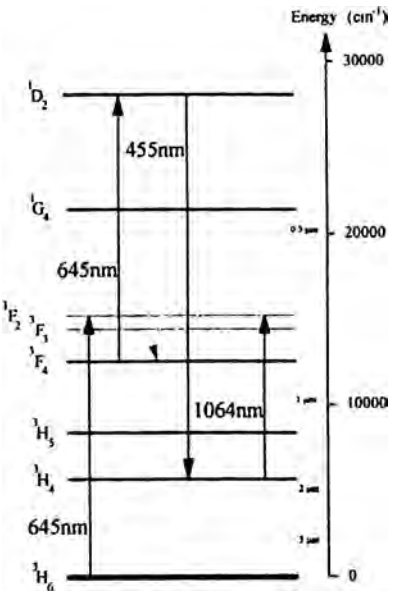

Figure 5.10 Energy-level diagram and pumping scheme of a Tm^{3+} upconversion laser. (Reprinted from Ref. 33 with permission from the Optical Society of America.)

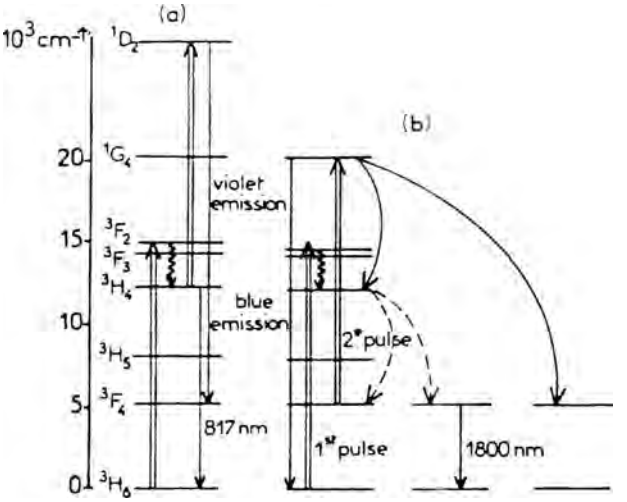

Figure 5.11 Upconversion by the looping mechanism in (a) Tm:$LiNbO_3$, and (b) Tm:GGG. The absorbed photons belong to two consecutive lasers (arrows). The curved arrows represent de-excitation processes. (Reprinted from Ref. 37 with permission from Elsevier.)

1 μs for $^4S_{3/2}$. Therefore, in Er-doped silicate glass, any $^4I_{11/2}$ excited state will decay nonradiatively to $^4I_{13/2}$ to produce the 1.55-μm laser emission, rather than the upconversion process. Blue/green lasers can be obtained with holmium-, erbium-, thulium-, and praseodymium-doped fluoride glasses or crystals.[26, 35, 36] Since the bandwidth of the absorption and the emission linewidth in glasses is broader than in crystals [for the laser transition $^4F_{3/2} \rightarrow {}^4I_{11/2}$, the transition linewidth (FWHM) is $\sim$300 cm^{-1} in Nd:phosphate glass compared to $\sim$4.4 cm^{-1} in Nd:YAG], the pump wavelength can vary by several nm over the absorption bandwidth without actually affecting the laser performance. (See the appendix for more details.) Also, the broad emission bandwidth allows tunability of the laser output. Sometimes, the upconverted population decays back to the first excited state through an efficient cross-relaxation process. This state can be used again for upconversion. This phenomenon, called a *loop mechanism*, was demonstrated in Tm^{3+}:$Gd_3Ga_5O_{12}$ (GGG).[37] In this example, Tm^{3+} was excited first by 660-nm photons into the $^3F_2$ state. The long-lived $^3F_4$ level (17.1 ms at 77 K) absorbed a second photon of 638 nm into the $^1G_4$ level. The above process leads to the blue emission $^1G_4 \rightarrow {}^3H_6$ ($\lambda = 484$ nm), as well as three ions in the $^3F_4$ level. The $^3F_4$ state was then ready to reabsorb photons and continue the process. The upconversion processes in Tm:$LiNbO_3$ and Tm:GGG are described schematically in Figs. 5.11(a) and (b).

References

1. F. Okada, S. Togawa, K. Ohta, and S. Koda, "Solid state ultraviolet tunable laser: A Ce^{3+} doped $LiYF_4$ crystal," *J. Appl. Phys.* **75**(1), 49–53 (1994).
2. L. Esterowitz, oral presentation (invited talk), "Longer Wavelength Lasers and Applications," *OE/LASE'94 Meeting*, Los Angeles, CA (1994).

3. K. Nassau and A. M. Broyer, "Calcium tungstate: Czochralski growth, perfection and substitution," *J. Appl. Phys*. **33**, 3064–3073 (1962).
4. E. P. Chicklis, R. C. Folweiler, C. S. Naiman, et al., "Development of Multiply Sensitized Ho:YLF as a Laser Material," Report no. ECOM-73-0066-F (1974).
5. W. Koechner, "Thermal lensing in a Nd:YAG laser rods," *Appl. Opt*. **9**(11), 2548–2553 (1970).
6. M. P. MacDonald, T. Graf, J. E. Balmer, and H. P. Weber, "Reducing thermal lensing in diode-pumped laser rods," *Opt. Commun.* **178**, 383–393 (2000).
7. J. E. Murray, "Pulsed gain and thermal lensing of Nd:$LiYF_4$," *IEEE J. Quantum Electron*. **QE-19**(4), 488–491 (1983).
8. W. Koechner, *Solid State Laser Engineering*, 4th Revised and Updated Edition, p. 400, Springer-Verlag, Berlin, Heidelberg, and New York (1996).
9. H. Vanherzeele, "Thermal lensing measurement and compensation in a continuous-wave mode-locked Nd:YLF laser," *Opt. Letters* **13**(5), 369–371 (1988).
10. M. Armstrong, X. Zhu, S. Gracewski, and R. J. D. Miller, "Development of a 25 W TEM_{00} diode-pumped Nd:YLF laser," *Opt. Commun.* **169**, 141–148 (1999).
11. R. Weber, B. Neuenschwander, M. MacDonald, M. B. Roos, and H. P. Weber, "Cooling schemes for longitudinally diode laser pumped Nd:YAG rods," *IEEE J. Quantum Electron.* **34**(6), 1046–1053 (1998).
12. N. P. Barnes and D. J. Gettemy, "Temperature variation of the refractive indices of yttrium lithium fluoride," *J. Opt. Soc. Amer.* **70**(10), 1244–1247 (1980).
13. T. M. Pollak, W. F. Wing, R. J. Grasso, E. P. Chicklis, and H. P. Jenssen, "CW laser operation of Nd:YLF," *IEEE J. Quantum Electron*. **QE-18**(2), 159–163 (1982).
14. W. Seelert, H. P. Kortz, and W. M. Yen, "Excited state absorption and $^4F_{3/2}$ lifetime shortening in diode pumped Nd:YLF Q-switched lasers," *OSA Proceedings on Advanced Solid State Lasers* **13**, 209–211 (1992).
15. I. P. Mercer, Z. Chang, C. N. Danson, et al., "Diode pumped picosecond Nd:YLF laser oscillator at 1053 nm," *Opt. Commun.* **107**, 77–82 (1994).
16. L. Turi and T. Juhasz, "Diode-pumped Nd:YLF all in one laser," *Opt. Letters* **20**(14), 1541–1543 (1995).
17. J. Harrison, P. F. Moulton, and G. A. Scott, "13-W, $M^2 < 1.2$ Nd:YLF laser pumped by a pair of 20-W diode laser bars," in *Conference on Lasers and Electro-Optics* **9**, post-deadline paper CPD 20-1, OSA Technical Digest Series (1995).
18. A. Finch, Y. Ohsako, J. Sakuma, et al., "Development of high-power, high repetition rate, diode-pumped, deep UV laser system," *OSA Trends in Optics and Photonics (TOPS)* **19**, *Advanced Solid State Lasers*, 16–18 (1998).
19. D. Jander and M. S. Bowers, "Diode-pumped Nd:YLF oscillator and Yb:S-FAP amplifier laser," in *OSA Trends in Optics and Photonics (TOPS)* **50**, *Advanced Solid State Lasers*, 182–185 (2001).

20. D. P. Devor, R. C. Pastor, M. Robinson, W. M. Akutagawa, and K. Arita, "Reactive Atmosphere Growth of 2.06 μm Laser Crystals," Report no. ECOM-74-0034-F (1974).
21. A. Dergachev, K. Wall, and P. F. Moulton, "A CW side pumped Tm:YLF laser," *OSA Trends in Optics and Photonics (TOPS)* **68**, *Advanced Solid State Lasers*, WA1, OSA Technical Digest Series, postconference edition (2002).
22. A. Dergachev and P. Moulton, "High-power, high energy diode-pumped Tm:YLF – Ho:YLF – ZGP laser system," *OSA Trends in Optics and Photonics (TOPS)* **68**, *Advanced Solid State Photonics*, 137–141 (2003).
23. K. M. Dinndorf, D. S. Knowles, M. Gojer, C. J. Taylor, and H. P. Jenssen, "Principal axes for transitions in monoclinic crystals," *OSA Proceedings on Advanced Solid State Lasers* **13**, 270–274 and references therein (1992).
24. G. Galzerano, M. Marano, S. Longhi, et al., "Sub-100-psecond Amplitude modulation mode-locked Tm-Ho-BaY_2F_8 laser at 2.06 μm," *Opt. Lett.* **28**(21), 2085–2087 (2003).
25. D. Fiehler, "Upconversion processes creates compact blue/green lasers," *Laser Focus World*, Nov. 1993, 95–102 (1993).
26. R. A. McFarlane, "Spectroscopic studies and upconversion laser operation of BaY_2F_8:Er 5%," *OSA Proceedings on Advanced Solid State Lasers* **13**, 275–279 (1992).
27. P. Xie and S. C. Rand, "Visible cooperative upconversion laser in Er:$LiYF_4$," *Opt. Letters* **17**(17), 1198–1200 (1992).
28. L. Esterowitz, "Diode pumped solid state lasers at 2 and 3 micron for biomedical field," *SPIE Proc.* **1182**, 49–58 (1989).
29. L. F. Johnson and H. J. Guggenheim, "Electronic-and phonon-terminated laser emission from Ho^{3+} in BaY_2F_8," *IEEE J. Quantum Electron*, **QE-10**(4), 442–449 (1974).
30. L. F. Johnson and H. J. Guggenheim, "Infrared pumped visible laser," *J. Appl. Phys.* **19**(2), 44–47 (1971).
31. A. J. Silversmith, W. Lenth, and R. Macfarlane, "Green infrared-pumped erbium upconversion laser," *Appl. Phys. Lett.* **51**(24), 1977–1979 (1987).
32. T. Hebert, R. Wannemacher, W. Lenth, and R. M. Macfarlane, "Blue and green CW upconversion lasing in Er:YLF4," *Appl. Phys. Lett.* **57**(17), 1729–1729 (1990); also see T. Hebert, R. M. Macfarlane, R. Wannemacher, and W. Lenth, *Conference on Lasers and Electro-Optics* **X**, 318, OSA Technical Digest Series (1990).
33. M. P. Le Flohic, J. Y. Allain, G. M. Stephan, and G. Maze, "Room-temperature continuous-wave upconversion laser at 455 nm in a Tm^{3+} fluorozirconate fiber," *Opt. Lett.* **19** (23), 1982–1984 (1994).
34. J. M. Chwalek and G. R. Paz-Pujalt, "Upconversion Tm^{3+} doped Ba-Y-Yb-F thin film waveguides for visible and ultraviolet light sources," *Appl. Phys. Lett.* **66**(4), 410–412 (1995).
35. R. A. McFarlane, "Dual wavelength visible upconversion laser," *Appl. Phys. Lett.* **54**(23), 2301–2302 (1989).

36. R. Brede, E. Heumann, J. Koetke, et al., "Green up-conversion laser emission in Er-doped crystals at room temperature," *Appl. Phys. Lett*. **63** (15), 2030–2031 (1993).
37. A. Brenier, C. Garapon, C. Madej, C. Pedrini, and G. Boulon, "Excited-state absorption in Tm^{3+} doped $LiNbO_3$:MgO and $Gd_3Ga_5O_{12}$ and looping mechanism," *J. of Luminescence* **62**, 147–156 (1994).

Chapter 6

Photophysics of Solid State Laser Materials

6.1 Properties of the Lasing Ion

Light emission occurs as a result of interaction between light and matter. Let us assume a two-level atom with levels 1 (ground state) and 2 (excited state). The energies of the ground and excited states are E_1 and E_2, respectively, and the energy difference is therefore given by the difference $\Delta E_{12} = E_2 - E_1$. When light with photons of energy equal to this difference is absorbed by the atomic or molecular system, an electron will be excited from level 1 to level 2. The energy of the photons is given by $\Delta E_{12} = E_{12} = h\nu_{12}$ (h is Planck's constant and ν_{12} is the frequency of light resulting from the level $1 \rightarrow 2$ transition). This energy is absorbed by an atom or a molecule that has energy levels, separated by ΔE, where these energy levels are the ground and the excited states. This kind of "quantum jump" of an electron between two states occurs in atomic systems between electronic levels; it can be extended to molecular systems, where vibrational and translational energy levels participate in the quantum jump. The interaction between light and matter involves the transition of electrons between different states. This interaction results in the absorption of photons (stimulated absorption) as well as spontaneous and stimulated emission. These processes can be described using Einstein's A and B coefficients, as will be described in the next paragraphs.

6.1.1 Absorption

The absorption of light by an object is a fundamental phenomenon in nature. Visible objects scatter the light that falls on them. However, colored objects absorb light at certain wavelengths (or frequencies), while scattering or transmitting other frequencies. For example, an object that will absorb all the frequencies in the visible range will appear black. A green object will absorb light throughout the visible spectral regime except that wavelength which defines the green color.

Let us assume that we have a nondegenerate two-level atomic system, with ground and excited states levels 1 and 2. Initially, the atom is in the ground state 1.

When an external electromagnetic field with a frequency of $h\nu_{12} = E_2 - E_1$ is applied to the atomic system, it is probable that the atom will undergo a transition from level 1 to level 2. This process is termed absorption. If N_1 is the volume density of the atoms in the ground state, the temporal rate of change of the density is given by the equation

$$\frac{dN_1}{dt} = W_{12}N_1, \tag{6.1}$$

where W_{12} is the absorption rate, which is related to the to the photon flux, I, by

$$W_{12} = \sigma_{12}I, \tag{6.2}$$

where σ_{12} is the absorption cross section. The intensity of a monochromatic light, I_λ, which propagates a distance Δz in an absorbing medium, is given by

$$I_\lambda(z) = I_\lambda(0)\exp[-\alpha(\lambda)\cdot\Delta z]. \tag{6.3}$$

$I_\lambda(0)$ is the initial light intensity at the entrance of the absorbing medium, $z = 0$, while $I_\lambda(z)$ is the final intensity after the light has propagated a distance Δz inside the absorbing material. The quantity α introduced in Eq. (6.3) is called the *absorption coefficient*. This equation is valid under thermal equilibrium conditions, $N_1 g_1 > N_2 g_2$, where g_1 and g_2 are the degeneracies of levels 1 and 2, respectively. The inverse magnitude, α^{-1}, measures the optical path for which the light intensity is decreased by a factor of e^{-1} as a result of absorption only by the medium. If it is assumed that the density of the absorbing medium is N atoms per unit volume, the absorption coefficient is related to the absorption cross section as

$$\alpha(\lambda) = N\sigma_{12}. \tag{6.4}$$

It should be noted that the absorption coefficient in this model can be obtained by two methods: The first is based on the imaginary part of the refraction index, the second on the rate at which an atom absorbs energy from an external field. In both cases, the energy absorption is described by a simple classical electron oscillator model, or Lorentz model, of the atom. The Lorentz model was developed before atomic structure was known. The model assumes that in the absence of external forces, the electron in the atom is in an equilibrium position. When an external electromagnetic field with a driving frequency ω is applied to the atomic system, the electron will be displaced from the equilibrium position and will oscillate back and forth, owing to elastic forces, at a natural frequency of ω_0.

The electron motion relative to the nucleus can be described by the rate equation

$$m\frac{d^2x}{dt^2} = e\cdot E(R,t) - C\cdot x, \tag{6.5}$$

where m is the reduced mass of the electron-nucleus system, R is the center-of-mass coordinate, E is the electromagnetic field, and $C \cdot x$ describes the oscillatory motion of the electron (C is the spring constant). This equation can also be written in terms of natural frequency, ω_0, as

$$\left(\frac{\mathrm{d}^2}{\mathrm{d}t^2} + \omega_0^2\right)x = \frac{e}{m}E(R,t), \tag{6.6}$$

where the electron natural frequency ω_0 is defined as $\omega_0 = \sqrt{C/m}$.

When a periodic external field is applied, the oscillatory motion of the bound electron is described in terms of a driven harmonic oscillator. If the electron is displaced by Δx from its equilibrium state, the dipole moment of the system is $P = e \cdot \Delta x$ (where e is the electron charge). The external field provides energy that maintains the oscillation at a frequency of the applied field, ω.

In the case of a damped oscillator, driven by external electric field, the equation of motion of the oscillating electron is

$$\frac{\mathrm{d}^2x}{\mathrm{d}t^2} + 2\gamma\frac{\mathrm{d}x}{\mathrm{d}t} + \omega_0^2 x = \vec{\varepsilon}\frac{e}{m}E_0\cos(\omega t - kz). \tag{6.7}$$

The term γ, introduced in Eq. (6.7) pertaining to the electron oscillator model, is the damping parameter of the average harmonic displacement of the electron, x is the average electron displacement, ω_0 is the natural oscillation frequency, e is the electron charge, m is the reduced mass of the electron-nucleus system, E_0 is the wave amplitude of the induced external field, and $\vec{\varepsilon}$ is a unit vector. It is assumed that the electric field in Eq. (6.7) is a plane wave that propagates along the z axis, with a wave vector k, which relates to the wavelength λ by $k = 2\pi/\lambda$. A damping parameter is also defined as $\Gamma = 2\gamma$.

The solution to Eq. (6.7) can be described by two components, one in phase and a second that is out of phase with the driving force,

$$x(t) = A\sin\omega t + B\cos\omega t, \tag{6.8}$$

where the coefficients A and B are given by

$$A = \frac{e \cdot E_0}{m}\frac{\Gamma\omega}{[(\omega_0^2 - \omega^2)^2 + (\Gamma\omega)^2]} = A_{\mathrm{ab}} \tag{6.9}$$

and

$$B = \frac{e \cdot E_0}{m}\frac{(\omega_0^2 - \omega^2)}{[(\omega_0^2 - \omega^2)^2 + (\Gamma\omega)^2]} = A_{\mathrm{disp}}. \tag{6.10}$$

The term A_{ab} is called the absorptive amplitude, while A_{disp} is called the dispersive amplitude. The averaged input absorption power is a consequence of the term

$A_{ab} \sin \omega t$. The term A_{disp} is averaged out to 0 over one oscillation cycle. It was found that the time-averaged, absorbed power over the oscillation period is given after some mathematical manipulation by

$$P_{av} = \frac{1}{2}(e \cdot E_0 \omega A_{ab}) = \frac{1}{2} m \alpha_0^2 \cdot \frac{\omega^2 \Gamma}{(\omega_0^2 - \omega^2)^2 + (\omega^2 \Gamma^2)} \tag{6.11}$$

and

$$\alpha_0 = e \cdot \frac{E_0}{m}. \tag{6.12}$$

The energy transfer from the driving field to the oscillatory system will be maximized at resonance, when $\omega = \omega_0$. The energy absorption by the system will be at maximum when the frequency of the driving force coincides with the natural frequency of the oscillating system. At resonance,

$$P_0 = \frac{1}{2} \frac{m \alpha_0^2}{\Gamma} \tag{6.13}$$

is obtained. Combining Eqs. (6.11) and (6.13) produces

$$P_{av} = P_0 \frac{\Gamma^2 \omega^2}{(\omega_0^2 - \omega^2) + \Gamma^2 \omega^2}. \tag{6.14}$$

The absorptive amplitude and power [Eqs. (6.9) and (6.14), respectively] depend on the quantity C that is defined as

$$C = (\omega_0^2 - \omega^2)^2 + \Gamma^2 \omega^2 = (\omega_0 - \omega)^2 (\omega_0 + \omega)^2 + \Gamma^2 \omega^2. \tag{6.15}$$

This quantity (C) is changed rapidly at resonance, when $\omega_0 = \omega$, or near resonance, where ω is within the range $\omega - 10\Gamma < \omega < \omega_0 + 10\Gamma$. On the other hand, the term with ω alone contributes a much slower variation in A. In near-resonance and weak damping conditions such as $\Gamma \ll \omega_0$, it is assumed that ω is equal to ω_0 in the expression C except in the factor $(\omega_0 - \omega)^2$ of the first term. Then C may be approximated as

$$C = (\omega_0 - \omega)^2 (\omega_0 + \omega_0)^2 + \Gamma^2 \omega_0^2 = 4\omega_0^2 \left[(\omega_0 - \omega)^2 + \left(\frac{1}{2} \Gamma \right)^2 \right]. \tag{6.16}$$

By inserting the last approximation for C into Eqs. (6.9) and (6.14), it can be observed that both the *absorptive amplitude* and the *averaged absorbed power* are proportional to the factor

$$\frac{[(1/2)\Gamma]^2}{(\omega_0 - \omega)^2 + [(1/2)\Gamma]^2}. \tag{6.17}$$

This frequency-dependent factor determines the lineshape of the absorption amplitude or the absorbed power. The origin of this lineshape, called a Lorentzian lineshape, can be understood if the statistical nature of the atomic system is considered. Therefore, the average time between collisions affects the temporal behavior of the driving EM field and should be included. These effects are included in the lineshape function g, which has the form

$$g(\omega - \omega_0) = \frac{T_2}{\pi} \frac{1}{[1 + (\omega_0 - \omega)^2 T_2^2]}, \tag{6.18}$$

where T_2 is the average time between two collisions. The lineshape $g(\omega - \omega_0)$ defines a Lorentzian lineshape. If one plots $g(\Delta\omega)$ vs. $\Delta\omega$, where $\Delta\omega = \omega - \omega_0$, one obtains a lineshape with a maximum at T_2/π and a FWHM intensity $(\Delta\omega_0)$ with a value of $2/T_2$. If the Lorentz statistical model for atomic collisions is introduced, the result is a relation of the average time between collisions (T_2) to the damping parameter γ by

$$T_2 = \frac{1}{\gamma}. \tag{6.19}$$

The Lorentzian lineshape is therefore a result of collision broadening between atoms. Collision effects are statistically averaged, so physical quantities associated with a Lorentzian lineshape are also averaged. The collision broadening dephases, i.e., the phase of the electron's oscillation before collision is uncorrelated to the phase after the collision. As a result of the collisions, the average displacement of the bound electron decays at a rate equal to the collision rate. The dephasing effect associated with atomic collisions appears as a damping parameter in Eqs. (6.7) and (6.20).

Equation (6.7) can be rewritten in terms of average electron displacement,

$$\frac{\mathrm{d}^2}{\mathrm{d}t^2}\langle x\rangle + 2\gamma \frac{\mathrm{d}}{\mathrm{d}t}\langle x\rangle + \omega_0^2\langle x\rangle = \vec{\mathbf{e}} \frac{e}{m} E_0 \cos(wt - kz), \tag{6.20}$$

where the parameters appearing in Eq. (6.20) have already been defined in Eq. (6.7).

The effect of the damping parameter γ, which includes the meaning of collision rate, should be emphasized here. The friction parameter or the collision rate dephases the electron oscillations so that the phase of the oscillatory motion of the electrons after the collision is completely uncorrelated to the precollision phase. This dephasing results from collisions between electrons, which leads to a decay of the average electron displacement. When no inelastic collisions occur, the oscillatory motion satisfies the Newton Equation [Eq. (6.6)],

$$\frac{\mathrm{d}^2 x}{\mathrm{d}t^2} + \omega_0^2 x = \varepsilon \cdot \frac{e}{m} E_0 \cos(\omega t - kz), \tag{6.21}$$

where the damping parameter was omitted. When elastic collisions are included, a change in the phase occurs and a damping parameter is introduced.

The damping parameter also produces broadening of the absorption line, yielding a broadened lineshape termed as Lorentzian. The broadening effect is equivalent to collision broadening and was described classically by Lorentz using Newton's classical equations of motion, assuming that the collision is fast compared to the time interval between two consecutive collisions, and that it is followed by the re-orientation of the direction of the electronic oscillations. On average, all of the orientations are of equal probability.

The absorption of external electromagnetic waves by an atomic system is significant near resonance. The broadening results from collisions and its classical description holds that when atomic collision occurs with a duration faster than the time interval between two consecutive collisions, enough time remains for the re-orientation displacement of the direction of electron oscillation, with an average electron displacement, which is frequency dependent. The energy absorbed by the electron-nucleus oscillating model (Lorentz model) follows a Lorenztian lineshape. The absorption cross section is given by

$$\sigma(\omega) = \frac{e^2}{2\varepsilon_0 mc} \frac{T_2}{[1 + (\omega_0 - \omega)^2 T_2^2]}, \tag{6.22}$$

where the absorption coefficient is obtained from Eq. (6.4),

$$\alpha(\omega) = N \cdot \sigma(\omega) = \frac{N \cdot e^2}{2\varepsilon_0 mc} \frac{T_2}{[1 + (\omega_0 - \omega)^2 T_2^2]}. \tag{6.23}$$

The absorption coefficient will have maximum value at resonance,

$$\alpha(\omega) = N \cdot \sigma(\omega) = \frac{N \cdot e^2 \cdot T_2}{2\varepsilon_0 mc} = \frac{N \cdot e^2 \cdot T_2}{\Delta\omega_0 \varepsilon_0 mc}, \tag{6.24}$$

where $\Delta\omega_0$ has been defined as the FWHM of a Lorentzian lineshape. The maximum absorption occurs when the driving frequency is equal to the natural frequency of the oscillating bound electrons. The intensity of the incident lightwave, which propagates a distance Δz inside an absorbing medium, obeys the exponential law given in Eq. (6.3).

Absorption is a stimulated process that requires electromagnetic radiation energy to excite the electron transition from the ground state to an excited level. The inverse process is the stimulated emission discussed below. In the case of stimulated absorption, the absorbed photon disappears into the absorbing medium. On the other hand, in the case of stimulated emission, the absorbing medium will emit an additional photon with the same energy, direction, and phase of the incident photon. This is the fundamental basis of laser action.

6.1.1.1 Homogeneous and nonhomogeneous broadening

Performing spectral analysis of an emission or absorption line will show that they are of a finite width. The function that describes the distribution of the intensity of a transition from state i to a certain state j versus the frequency ν is defined as the lineshape $g(\nu, \nu_0)$ of that transition. The central frequency of the lineshape function is defined by ν_0. The lineshape function is normalized according to

$$\int_{-\infty}^{+\infty} g(\nu)\,\mathrm{d}\nu = 1. \tag{6.25}$$

The lineshape function $g(\nu, \nu_0)$ is the probability of absorption or emission of photons per unit frequency, while $g(\nu, \nu_0)\,\mathrm{d}\nu$ is the probability of a transition in the energy range of $h\nu$ and $h(\nu + \mathrm{d}\nu)$. The linewidth function appears in the rate equations that describe spontaneous and stimulated emissions, and therefore the optical linewidth will have a definite bandwidth.

For solid state laser materials, the sources for the linewidth broadening are related either to inherent properties of the atomic system and affect individual atoms (homogeneous broadening) or to the collective properties of the system (inhomogeneous broadening). Homogeneous linewidth broadening results, for example, from the lifetime of the emitting level, thermal effects, and dipolar electric or magnetic interactions, while inhomogeneous broadening in solids results from site distribution, i.e., crystalline or glassy inhomogeneities. Homogeneous broadening is represented by Lorentzian lineshape, inhomogeneous by a Gaussian lineshape.

6.1.2 Spontaneous emission

The result of absorbing a photon by a nondegenerate atomic system with two energy levels 1 and 2 having population densities of N_1 and N_2, respectively, is that the atom is in the excited state, 2. This decays back to the ground state level 1 at a rate proportional to the upper level population,

$$\frac{\mathrm{d}N_2}{\mathrm{d}t} = -A_{21}N_2, \tag{6.26}$$

where A_{21} is the spontaneous transition rate or probability, e.g., the probability of the population decay from level 2 to level 1, per unit time. The spontaneous emission is an inherent property of all excited states and has an exponential decay with a lifetime equal to the reciprocal value of the spontaneous transition probability from the excited level 2,

$$N_2 = N_2(0)\exp\left(-\frac{t}{\tau_{21}}\right) = N_2(0)\exp(-t \cdot A_{21}), \tag{6.27}$$

where $N_2(0)$ is the population of the excited level N_2 at $t = 0$ and τ_{21} is the characteristic time constant of the excited state such that

$$\tau_{21} = A_{21}^{-1}. \tag{6.28}$$

In a case in which the excited state n has several radiative channels to other lower m states, the radiative rate is the sum over all the radiative processes from n to all lower states m,

$$A_n = \sum_m A_{nm}, \tag{6.29}$$

and the excited state lifetime is given by

$$\tau_n = \frac{1}{A_n} = \frac{1}{\sum_m A_{nm}}. \tag{6.30}$$

Classically, spontaneous radiation can be explained through the dependence of the excited state decay rate and power on the square of the dipole moment and the acceleration rate of this dipole, respectively.

6.1.3 Stimulated emission

Emission of EM radiation between two levels in an atomic or molecular system can be generated under the stimulation of an electromagnetic field with a frequency that is equal or near the transition frequency. In the presence of such a stimulating field, the atom will give up to the radiation field additional photons of exactly the same frequency, direction, and phase of the incident photon. In other words, it will fulfill the requirement for conservation of energy and momentum. In this case, the decay of the excited level is proportional to the population density, N_2, and also to the radiation density per unit frequency $\sigma_{21}(\nu_{21})$ of the induced electromagnetic radiation,

$$\frac{\mathrm{d}N_2}{\mathrm{d}t} = -B_{21}\rho_{21}(\nu_{21}) \cdot N_2. \tag{6.31}$$

The stimulated absorption rate is similarly

$$\frac{\mathrm{d}N_1}{\mathrm{d}t} = -B_{12}\rho_{12}(\nu_{12})N_1, \tag{6.32}$$

where B_{21} is the proportionality constant, also called the Einstein coefficient for stimulated emission, and B_{12} is the stimulated absorption coefficient. As can be seen, the emission of an atomic or molecular system in the presence of an external EM field consists of two contributions: photons that results from spontaneous emission, with a decay rate that is proportional to the spontaneous decay rate, A_{21},

and with phase independent of the external field; and stimulated emission or absorption, with a rate constant proportional to $\rho_{21}\nu_{(21)}B_{21}$ and to $\rho_{12}\nu_{(12)}B_{12}$, the stimulated emission intensity proportional to the energy density per unit frequency of the external field $\rho_{21}(\nu_{21})$ at frequency ν_{12} (here $\nu_{12} = \nu_{21}$, and $\rho_{12} = \rho_{21)}$.

The relation between the stimulated emission and absorption coefficients and the spontaneous emission coefficient is given by

$$B_{21} = \frac{c^3}{8\pi h\nu^3} A_{21} \tag{6.33}$$

and

$$\frac{g_1}{g_2}\frac{B_{12}}{B_{21}} = 1. \tag{6.34}$$

The stimulated absorption and emission coefficients describe the interaction of a photon with a two-level system, assuming that the radiation is in radiative thermal equilibrium, where the number of transitions per unit of time from $1 \rightarrow 2$ is equal to the number of transitions $2 \rightarrow 1$,

$$A_{21}N_2 + B_{21}\rho(\nu_{21})N_2 = B_{12}\rho(\nu_{12})N_1, \tag{6.35}$$

or more simply,

$$N_2[A_{21} + B_{21}\rho(\nu)] = B_{12}\rho(\nu)N_1. \tag{6.36}$$

These main photophysical processes based on Einstein probabilities are represented schematically in Fig. 6.1.

6.1.4 Oscillator strength

The concept of oscillator strength stems from the fact that the electron motion and its attraction to the nucleus can be described in terms of classical oscillator theory. Oscillator strength describes the relative strength of resonant oscillations of the bound electron/s in an atomic system. In other words, it measures the capability of an electron to have a relative oscillating mode or frequency. By knowing the oscillator strength value, it is possible to estimate the relative strength of several transitions that originate from that level. The relationship between the radiative rate and the absorption oscillator strength is

$$A_{21} = \frac{2\pi e^2}{\varepsilon_0 m_e c\lambda_{21}^2}\frac{g_1}{g_2} f_{12}, \tag{6.37}$$

where e is the electron charge, c is the speed of light, m_e is the electron mass, f_{12} is the oscillator strength of the $1 \rightarrow 2$ transition, λ_{12} is the transition wavelength, and ε_0 is the permittivity of a vacuum.

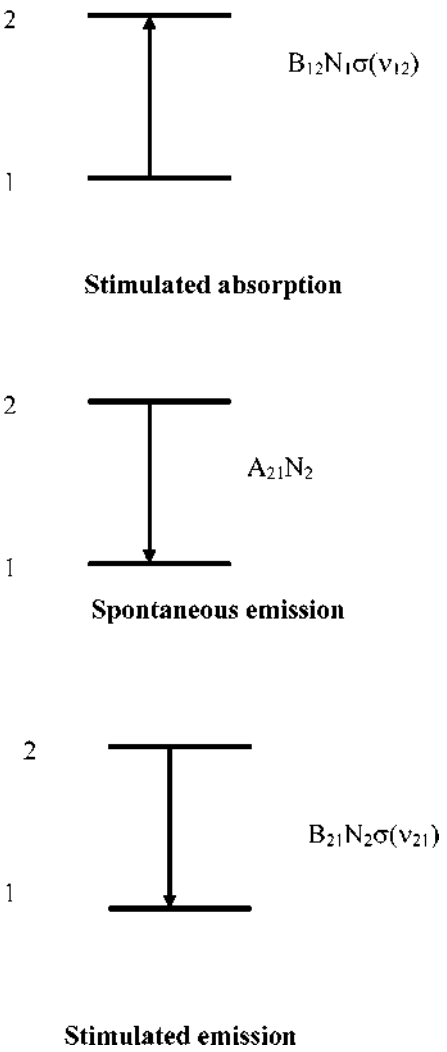

Figure 6.1 A schematic description of the main processes in an atomic system defined by Einstein coefficients.

Assume a multilevel atomic system that is excited from its ground state i to an excited state j by photons of energy equal to $E = h \cdot \nu$, where h is Planck's constant and $\nu = \nu_{exc}$ is the excitation frequency. Upon excitation, three pathways of the photophysical processes can be expected to occur:

- Radiative decay;
- Nonradiative decay, where part or all of the excitation energy is converted into vibrational quanta of the surrounding lattice; and
- Radiative and nonradiative energy transfer among the neighboring ions.

The rate of relaxation of any excited level depends on the relative contributions of the radiative $[W^{(\mathrm{rad})}]$ and nonradiative $[W^{(\mathrm{nr})}]$ rates. These contributions will dictate the overall lifetime and radiative quantum efficiency of the excited level.

The lifetime τ_j of the excited state j is given by

$$\frac{1}{\tau_j} = \sum_j W_{ji}^{(\mathrm{rad})} + \sum_i W_{ji}^{(\mathrm{nr})}, \tag{6.38}$$

where the summations are for transitions originating from quantum state j (the excited state) to all final unexcited states i, $W_{ji}^{(\mathrm{rad})}$ is the total probability of radiative transfer from level j to level i, and $W_{ji}^{(\mathrm{nr})}$ are the total probabilities for nonradiative decays from level j to all levels i. The quantum state i can be a final state either within the same atomic or molecular system, or in a neighboring atomic system, namely

$$\sum_{i,i'} W_{j,i\neq i'}^{(\mathrm{nr})} = \sum_i W_{ji}^{(\mathrm{nr})} + \sum_{i'} W_{ji'}^{(\mathrm{nr})}. \tag{6.39}$$

The first term in the right-hand side of the above equation represents the total nonradiative decay from level j to final states i within the same atomic or ionic system, while the second term in the right-hand side represents an energy-transfer process from an energy donor (D) to an energy acceptor, A, whose terminal quantum state is i'. The radiative and nonradiative probabilities include the participation of the host phonons in this dynamical process. This is called *phonon-assisted relaxation* or *phonon-assisted energy transfer*. The energy transfer is accompanied by an ion-ion multipolar interaction. The radiative quantum efficiency of the excited level j is equal to the ratio of photons emitted from level j to the number of photons excited into level j. The radiative quantum efficiency is defined by

$$\eta_j = \frac{\sum_i W_{ji}^{(\mathrm{rad})}}{\sum_i W_{ji}^{(\mathrm{rad})} + \sum_{i,i\copyright} W_{j,i\neq i'}^{(\mathrm{nr})}} = \tau_j \times \sum_i W_{ji}^{(\mathrm{rad})}, \tag{6.40}$$

with $\tau_j = \tau_{\mathrm{meas}}$, where τ_{meas} is the measured lifetime of the quantum state j. The relative probabilities for radiative and nonradiative decays between levels j and i may range from values of comparable magnitude to the values of two extreme cases: $W_{ji}^{(\mathrm{rad})} \ll W_{ji}^{(\mathrm{nr})}$ or $W_{ji}^{(\mathrm{rad})} \gg W_{ji}^{(\mathrm{nr})}$. The radiative quantum efficiency of a level j may therefore have limiting values ranging from zero to unity.

The branching ratio for a transition from level j to level i is defined as the ratio between $W_{ji}^{(\mathrm{rad})}$, the radiative transition probability from j to level i, and $\sum_i W_{ji}^{(\mathrm{rad})}$, the total transition probabilities from level j to all terminal levels i,

and is given by

$$\beta_{ji} = \frac{W_{ji}^{(\mathrm{rad})}}{\sum_i W_{ji}^{(\mathrm{rad})}}. \tag{6.41}$$

The radiative probability is an important parameter in laser analysis. It is related to the induced transition probabilities by the Einstein relation

$$(W_{21})_{\mathrm{ind}} = \frac{\lambda^2 \times I_\nu}{8\pi n^2 h\nu} \times W^{(\mathrm{rad})} g(\nu). \tag{6.42}$$

In this expression, n is the refractive index of the active medium, c is the speed of light in a vacuum, I_ν is the intensity of the inducing field, $g(\nu)$ is the normalized lineshape function for the transition from level j to level i, and ν is the frequency of the transition.

In order to calculate the values of $W^{(\mathrm{rad})}$, the positions of the relevant energy levels must be determined. In the case of rare-earth ions doped into a solid host, where the transitions are among f^N electronic levels, the energy-level positions depend on the coulombic interaction, spin-orbit interaction, and crystal-field effects, all shown in Fig. 6.2. In this figure, the magnitude of the energetic separation of the electronic states resulting from the various interactions is also presented. As can be seen, the coulombic interaction yields ^{2s+1}L terms separated by 10^4 cm^{-1}. The spin-orbit interaction results in a splitting of 10^3 cm^{-1}, while the crystal field of the solid host removes the $2J+1$ degeneracy and yields a manifold with spectral width of a few hundred cm^{-1}.

The radiative transitions between electronic levels of materials doped with rare-earth ions can be magnetic-dipole or electric-quadrupole transitions allowed by

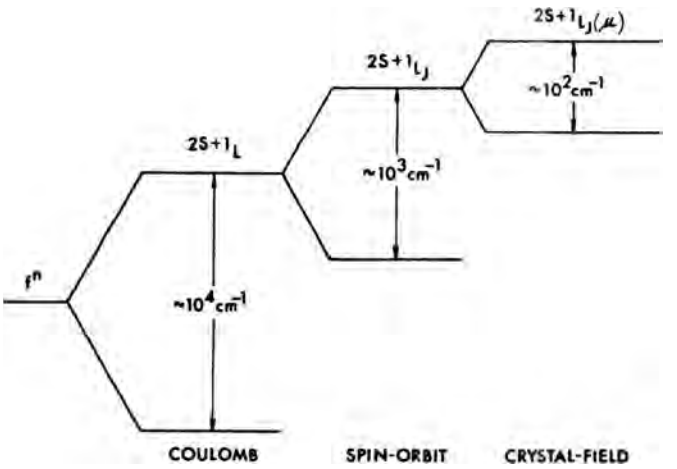

Figure 6.2 A schematic diagram of the splitting in f^N levels resulting from coulombic, spin-orbit, and crystal-field interactions. (Reprinted from Ref. 1 with permission from Marvin J. Weber.)

spectroscopic selection rules (parity-allowed transitions), or they can be electric-dipole transitions, which are parity forbidden. These transitions become partially allowed by the admixture of states with opposite parity into the f^N atomic level. The transitions between J states possess oscillator strength of the order of 10^{-6}. This admixture can occur, for example, when the rare-earth ion is situated in a site that does not have inversion symmetry. This type of transition is called a *forced electric dipole transition*. In a case in which the electric-dipole transitions become partially allowed, their contribution to the optical transitions predominates. The parity rules allowing magnetic-dipole and electric-quadrupole transitions contribute negligibly to the overall radiative decay rate. A theoretical treatment of radiative transition in such cases was introduced by Judd and Ofelt and was further applied to many cases by other authors.[1–4]

A practical case relevant to rare-earth ions is one in which the emitting level j is composed of two levels separated by an energy gap ΔE_j, which are in thermal equilibrium. In this case, the effective lifetime of level j is given by the formula

$$\frac{1}{\tau_{\text{eff}}} = \frac{\sum_j \left[\sum_i g_j \exp(-\Delta E_j/kT) \cdot W_{ji}^{(\text{rad})}\right]}{\sum_j g_j \cdot \exp(-\Delta E_j/kT)}, \tag{6.43}$$

where $W_{ji}^{(\text{rad})}$ is the radiative decay from levels j to all ground levels i, and g_j is the degeneracy of the jth level. In that case, the branching ratio defined by Eq. (6.41) takes the form of

$$\beta = \frac{\sum_j g_j(-\Delta E_j/kT)}{\sum_j \left[\sum_i g_j \exp(-\Delta E_j/kT) \cdot W_{ji}\right]}. \tag{6.44}$$

6.2 Nonradiative Transition

As explained earlier, three main processes dominate the decay of an excited state to the ground state: radiative decay, nonradiative decay, and energy transfer of the excitation into the neighboring ions.

Radiative decay occurs with a simultaneous emission of a photon having energy equal to the separation between the two levels in which the transition occurs. Nonradiative decay from excited state j' to the lower j state occurs via emission of one or more phonons. The total energy of the system is conserved, such that the total phonon energy emitted is equal to the energy gap ΔE_j between the adjacent levels participating in the nonradiative process,

$$p\hbar\omega = \Delta E_j, \tag{6.45}$$

where $\hbar\omega$ is the phonon energy and p is the number of phonons participating in the nonradiative process. These phonons are observed by the vibrational spectrum of the solid state host. If several phonons are emitted, the process is called *multi-phonon relaxation* (MPR). This MPR rate depends on two main parameters:

1. The energy gap ΔE between two neighboring relevant levels.
2. The temperature of the atomic or molecular system, via the phonon occupation probability.

The source of the multiphonon relaxation is the interaction of the electronic levels of the doped ion with the vibrations of the host.

Another pathway contributes to the relaxation of excited states—the energy transfer of excitation to neighboring ions. Energy transfer occurs via several mechanisms, such as a multipolar interaction, exchange mechanism, and energy migration or "diffusion." This process will be explained further in Chapter 7.

6.2.1 Energy gap and temperature dependence of multiphonon relaxation

Multiphonon relaxation occurs when the excited state decays nonradiatively with a simultaneous emission of several phonons. This process results from the interaction of the electronic levels of the emitting ion with the vibrations of the host crystal. These vibrations modulate and perturb the local field around the $4f^N$ electrons. Assuming a point-charge model, point ions are displaced around their equilibrium positions as a result of the orbit-lattice interaction,

$$V_{\text{ol}} = V_{\text{c}} + \sum V_i Q_i + \frac{1}{2} \sum_{i,j} V_{ij} Q_i Q_j + \cdots, \tag{6.46}$$

where V_{c} is the static crystal field, Q_i, Q_j are normal mode coordinates, and V_i, V_{ij} are the expansion coefficients defined as $V_i = \partial V_{\text{c}}/\partial Q_i$, $V_{ij} = \partial^2 V_{\text{c}}/\partial Q_i \partial Q_j$.

When the electronic transition in rare-earth ions is equal to the energy of one phonon mode, it is a *one-phonon process.* However, if the electronic transition is equal to several phonons, a higher-order process, a multiphonon relaxation (which is less probable than a one-phonon process) occurs. Single and multiphonon processes are presented in Fig. 6.3.

Dieke[6] noted years ago that if, in an atomic system, two spin-orbit levels were sufficiently close in their energetic position, the excited level would not emit photons. For LaF_3, for example, in order to observe fluorescence, the energy gap between the two spin-orbit levels should be $\Delta E \approx 1000\ \text{cm}^{-1}$. The qualitative reason was that for a gap of this magnitude and the cut-off in the phonon spectrum of $\approx 250\ \text{cm}^{-1}$, at least four phonons were needed for nonradiative decay, which makes the process less probable. The multiphonon decay rate of excited states can be analyzed in a more coherent way for two main cases:

1. The crystal parameters are constant and the energy gap is a variable.
2. The crystal/host parameters are variables, while the energy gap is constant.

The analysis of the MPR processes is based on several assumptions:

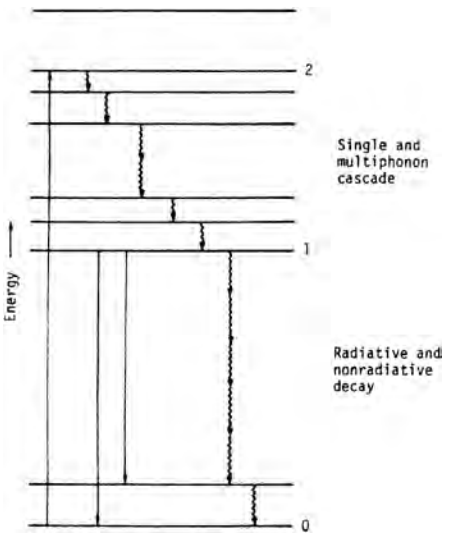

Figure 6.3 A schematic presentation of single and multiphonon decay processes. (Reprinted from Ref. 5 with permission from the American Physical Society.)

- Weak ion-lattice coupling.
- MPR is dominated by the number of phonons. In most cases, the lowest order MPR, with the most energetic phonons, dominates.
- Low-frequency, strongly coupled phonons are also possible.
- Conservation of energy is fulfilled.
- Single-frequency processes will dominate relative to multifrequency processes.
- The host vibrations are mostly dominant and mainly responsible for MPR.

The order of the MPR process of Er^{3+} ($^4S_{3/2} \rightarrow {}^4F_{9/2}$) ($\Delta E = 2930$ cm^{-1}) in germanate glass, having a phonon energy of $\hbar\omega = 890$ cm^{-1}, is $p \approx 3$, and for tellurite glass with $\hbar\omega = 675$ cm^{-1} is $p \approx 4$, implying that the MPR rate in tellurite glass will be higher than that in germanate glass. Table 6.1 presents the values of the main phonon energies in several commonly used laser hosts.

Consider now the situation of weak orbit-lattice coupling and a single-frequency model. The ratio of the pth order MPR to the $(p-1)$th order MPR rate is given by

$$\frac{W^{(p)}}{W^{(p-1)}} = \varepsilon \ll 1, \tag{6.47}$$

where ε is a coupling constant. The rate of the pth order MPR can be described approximately as

$$W^{(p)} \approx A\varepsilon^p. \tag{6.48}$$

Here, A is a constant and p is the order of the single-frequency MPR process.

Table 6.1 Phonon energies of several laser hosts.[2, 7]

Crystal	Type	Phonon energy (cm^{-1})
Tellurite	Glass-oxide	600–750
Germanate	Glass-oxide	800–975
Phosphate	Glass-oxide	1200–1350
Silicate	Glass-oxide	1000
Fluorophosphate	Glass-oxide	800–1050
YAG	Crystal-oxide	700
$YAlO_3$	Crystal-oxide	550–600
Y_2O_3	Crystal-oxide	430–550
$YLiF_4$	Crystal-oxide	400
LaF_3	Crystal fluoride	300–350
$LaCl_3$	Crystal chloride	260
$LiYF_4$	Crystal fluoride	400

Using Eq. (6.45) and assuming that the phonon with maximum energy is dominant in the MPR process (namely, the phonon with frequency $\omega = \omega_{\max}$), we obtain for Eq. (6.48) the energy-gap dependence,

$$W^{(p)} \approx A\varepsilon^p = A \times \exp(\ln \varepsilon \times p) = A \times \exp\left(\frac{\ln \varepsilon}{\hbar\omega} \times \Delta E\right). \tag{6.49}$$

Equation (6.49) can also be written as

$$W^{(\mathrm{P})} = W^{(\mathrm{NR})} = C \times \exp(-\alpha \Delta E), \tag{6.50}$$

where C and $\alpha = -\ln(\varepsilon)/\hbar\omega$ are host-dependent constants.

Equation (6.39) can be rewritten in a simpler way, where any excited level a is given by

$$\frac{1}{\tau_a} = \sum_b A_{ab} + \sum_b W_{ab}. \tag{6.51}$$

This equation has parameters similar to those in Eq. (6.38). A_{ab} and W_{ab} denote the radiative and nonradiative rates from excited level to a final level b, respectively, and τ_a is the lifetime of the excited state a.

Generally speaking, the multiphonon decay rate of an excited state is an exponential function of the energy gap ΔE between the excited level and the next lower level.[1] It takes a general form of

$$W^{(\mathrm{NR})} = W_0 \times \exp(-\alpha \Delta E), \tag{6.52}$$

where W_0 is the transition probability extrapolated to $\Delta E = 0$, and α that is defined in Eq. (6.50) provides the characteristics of the host phonon spectra and the electron-phonon coupling constant. Both constants are characteristic for a particular crystal. Where W_0 and α are not changed (e.g., for the same laser host), the

experimental result clearly indicates a logarithmic dependence of the multiphonon rate on the energy gap. The validity of the energy-gap law was demonstrated both in crystals and amorphous materials doped with a variety of rare-earth ions, and was summarized in numerous publications relevant to solid state laser materials.[2, 8, 9]

An example of the energy-gap law for rare-earth-ion-doped silicate glass is presented in Fig. 6.4.

For example, the multiphonon decay of $^4F_{3/2}$ level of Nd^{3+} ($\Delta E \approx 4800\ cm^{-1}$) was extracted from Fig. 6.4 and found to be $\approx 2 \times 10^2\ sec^{-1}$, in agreement with experimental results.

In a case in which the host parameters are variables for a given energy gap, it was found that the multiphonon rate is faster for hosts with higher phonon energies. For rare-earth ions doped in hosts with high phonon energies and multiphonon relaxation rates, the quantum efficiency of the fluorescence was found to be lower than for materials with low phonon energies. This is consistent with Eq. (6.40). The main reason for the host-dependent multiphonon rate is the cut-off frequency, ω_{max}, of the phonon spectrum for a particular solid state host. It was found in crystals and glasses that the phonons responsible for multiphonon relaxation are those associated with the vibrational modes of the crystal network, and for a second order—those associated with crystal modifiers. For an energy gap ΔE and a phonon energy ω_{max}, the number of phonons participating in the nonradiative

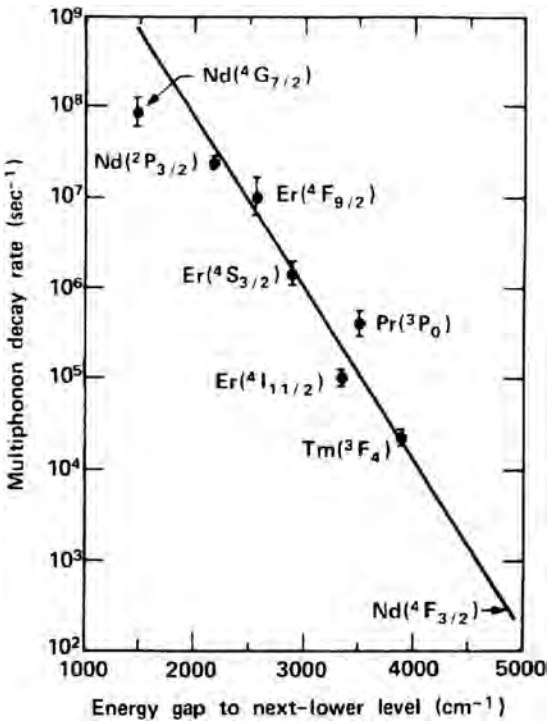

Figure 6.4 Energy-gap law for rare-earth-ion-doped silicate glass at 300 K. (Reprinted from Ref. 10 with permission from the IEEE.)

decay between two successive levels, with an energy gap ΔE, is given by

$$P \cong \frac{\Delta E}{\hbar \omega_{\max}}, \tag{6.53}$$

where p is the order of the nonradiative process. For two hosts, type 1 and type 2, with characteristic phonon frequencies $\omega_{\max}^{(1)}$ and $\omega_{\max}^{(2)}$, such that

$$\omega_{\max}^{(1)} > \omega_{\max}^{(2)}, \tag{6.54}$$

and for the same energy gap ΔE, the number of phonons participating in nonradiative decay will be

$$P^{(1)} \cong \frac{\Delta E}{\hbar \omega_{\max}^{(1)}} \quad \text{and} \quad P^{(2)} \cong \frac{\Delta E}{\hbar \omega_{\max}^{(2)}} \tag{6.55}$$

for host types 1 and 2, respectively. Since $P^{(1)} < P^{(2)}$, the process that requires fewer phonons will be more probable and one would expect to observe a faster multiphonon relaxation rate for the host with the higher phonon energy.

Quantitatively, this law shows an exponential behavior of the form

$$W^{(\mathrm{nr})}(\Delta E) = K \times \exp(-P), \tag{6.56}$$

where $W^{(\mathrm{nr})}(\Delta E)$ is the multiphonon decay rate for a certain energy gap, K is a proportional constant that depends on host parameters such as structure, lattice parameters, and crystal field, and P is the number of phonons needed to bridge the energy difference between two successive levels.

Example 1. Consider the multiphonon decay rate of $^4F_{9/2}$ level of Er^{3+} in oxide and fluoride crystalline hosts LaF_3 and Y_2O_3 (Ref. 9). For LaF_3, the relevant energy gap is $\Delta E = 2650\ \mathrm{cm}^{-1}$ and $h\omega_{\max} = 350\ \mathrm{cm}^{-1}$. The number of phonons needed to bridge the energy gap is represented by $p \cong 7$. For Y_2O_3, $\Delta E = 2516\ \mathrm{cm}^{-1}$ and $h\omega_{\max} = 550\ \mathrm{cm}^{-1}$; therefore, $p \cong 4$, and the multiphonon decay rate in the oxide will be faster than in fluorides. The rate for LaF_3 is $(4.4 \pm 1.5) \times 10^2\ \mathrm{s}^{-1}$, whereas for Y_2O_3 the multiphonon rate is $(1.7 \pm 0.6) \times 10^4\ \mathrm{s}^{-1}$, i.e., faster by a factor of $\approx$40, as expected. This fact is also reflected in the lifetime of the $^4F_{9/2}$ level of Er-doped crystals. In LaF_3, the lifetime is $(700 \pm 70)\ \mu\mathrm{s}$, while for Y_2O_3 it is $(50 \pm 15)\ \mu\mathrm{s}$. This rule is valid for any energy gap regardless of the type of the rare-earth ion. For a given crystal host, the critical parameter is the energy gap. The energy-gap dependence of the spontaneous multiphonon decay rates in LaF_3 and Y_2O_3 doped with various rare-earth ions clearly demonstrates the possibility of obtaining efficient emission from metastable levels with low energy gap in hosts with small phonon energies. This is also presented in Figs. 6.5(a) and (b).

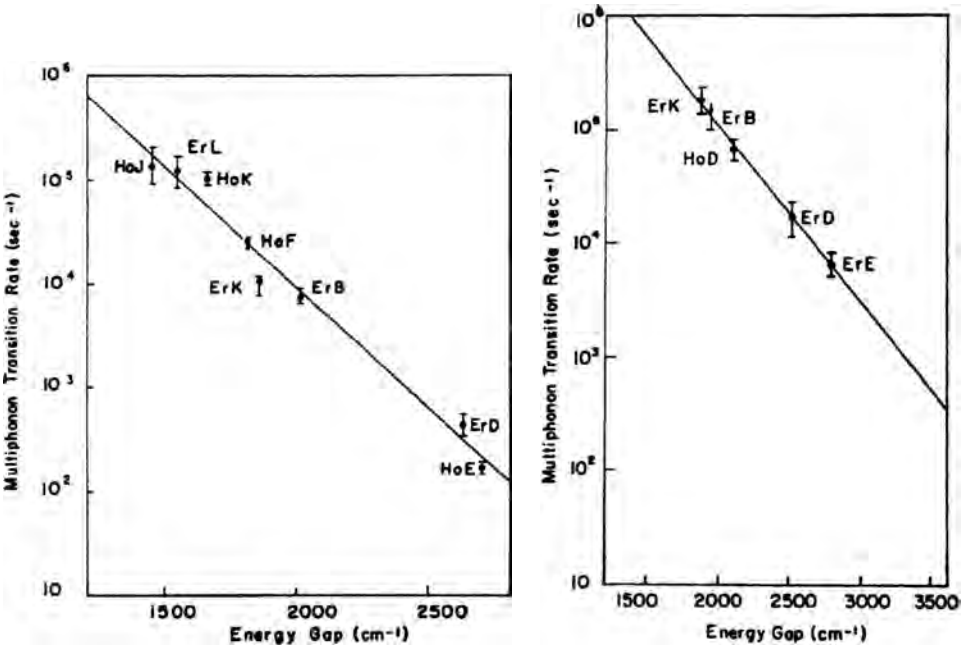

Figure 6.5 Energy-gap dependence of the spontaneous multiphonon decay rate for various rare-earth ions in (a) LaF_3, and (b) Y_2O_3 crystals. (Reprinted from Ref. 9 with permission from the American Physical Society.)

Example 2. For the $^5F_4, ^5S_2$ level of Ho^{3+}:LaF_3, with energy gap to the nearest level, $\Delta E = 2700$ cm^{-1}, and phonon energy of, $h\omega_{\max} = 350$ cm^{-1}, the multiphonon decay rate is $(1.9 \pm 0.2) \times 10^2$ s^{-1}, which is the same order of magnitude as in the Er($^2F_{9/2}$) level. The empirical energy-gap law fits well with the experimental results and makes it possible to predict multiphonon decay rates by extrapolating to a value of a known ΔE with 50% accuracy.[9] If changes occur within the orbit-lattice coupling or in static and dynamic crystal fields, a family of straight lines will be obtained. The dependence of MPR in a crystalline host (via the phonon energies) can be utilized to operate special laser systems at longer wavelengths. Figure 6.6 presents the nonradiative rate versus the energy gap between two neighboring levels in a fluoride crystal.[11] This type of behavior is similar in various oxide crystals as well. From Fig. 6.6, it can be seen that in most oxide and fluoride glasses, nonradiative processes dominate for energy gaps below $\approx$3700 cm^{-1} (2.6$-$2.8 μm). Below this, the MPR processes dominate and this affects the possibility of achieving an efficient laser operation. It is expected that low-phonon crystals will exhibit laser operation even at relatively small energy gaps because they require a large number of phonons in order to participate in the nonradiative process in accordance with Eq. (6.55).

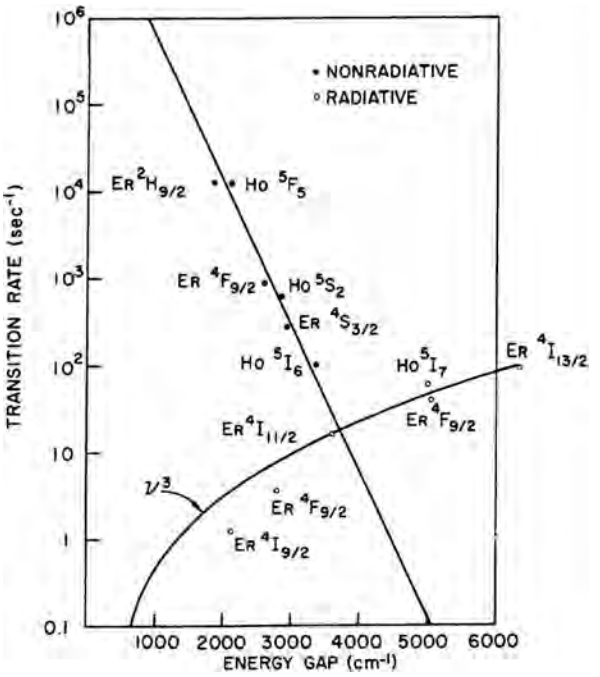

Figure 6.6 Radiative and nonradiative transition rates vs. energy gap for various rare-earth ions. (Reprinted from Ref. 11 with permission from the American Institute of Physics and Lucent Technologies Inc./Bell Labs.)

Low-phonon hosts can be used to fabricate efficient multi-wavelength channel waveguide laser sources emitting in the mid-IR. For example, Bhutta et al.[12] fabricated and operated a thin film, channel waveguide laser based on a low-phonon Nd:LaF_3 crystal. The waveguide was characterized both in terms of spectroscopic properties and laser operation. The structure (a 20-μm wide channel waveguide laser) offers a low threshold and relatively high efficiency (14% slope efficiency) CW waveguide laser emitting at various mid-IR wavelengths. Other materials with low phonon energies include $CaGaS_4$ ($\hbar\omega_{max} = 350$ cm^{-1}) and KPb_2Cl_5 ($\hbar\omega_{max} = 200$ cm^{-1}). These materials are denser than oxide or fluoride hosts and therefore have lower phonon energies. By doping these low-phonon crystals with Nd^{3+} or Dy^{3+}, it was possible to obtain laser emission among intermediate levels that in oxide hosts are usually quenched by nonradiative processes. Figure 6.7 presents energy-level structure and laser transitions in a Dy^{3+} ion. Both the 4.31 μm ($^6H_{11/2} \rightarrow {}^6H_{13/2}$) and 2.43 μm ($^6H_{9/2}$, $^6F_{11/2} \rightarrow {}^6H_{13/2}$) optical transitions could be obtained in these low-phonon materials.[13]

The MPR rates were relatively low in comparison with oxides or fluorides,[14] as can be observed from Figs. 6.8(a) and (b). These figures describe the nonradiative transition rates versus energy gap ΔE for several rare-earth ions in various oxide and fluoride crystals, Fig. 6.8(a), and for Nd^{3+}-doped KPb_2Cl_5, Fig. 6.8(b).

Another family of low-phonon energy materials is the heavy-metal oxide containing Pb^{2+}, Bi^{3+} and Ga^{3+}, and chalcogenide glasses that contain S, Se, and

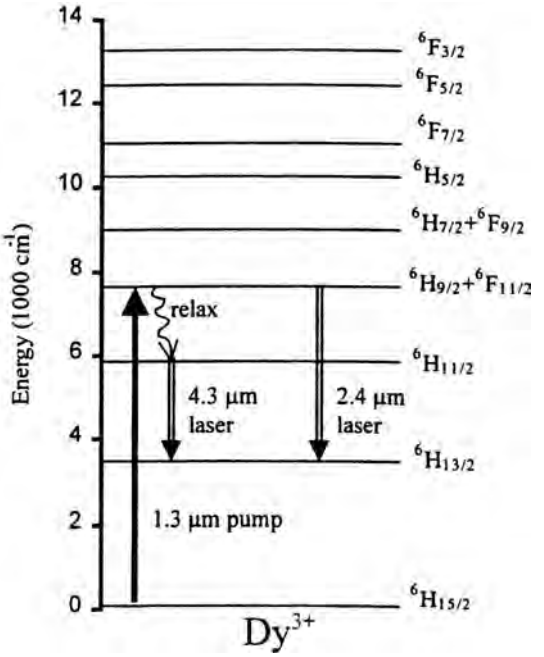

Figure 6.7 Energy-level structure and laser transitions in Dy^{3+}. (Reprinted from Ref. 13 with permission from the Optical Society of America. Credit must be given to the University of California, Lawrence Livermore National Laboratory, and the U.S. Department of Energy, under whose auspices the work was performed, when this information or a reproduction of it is used.)

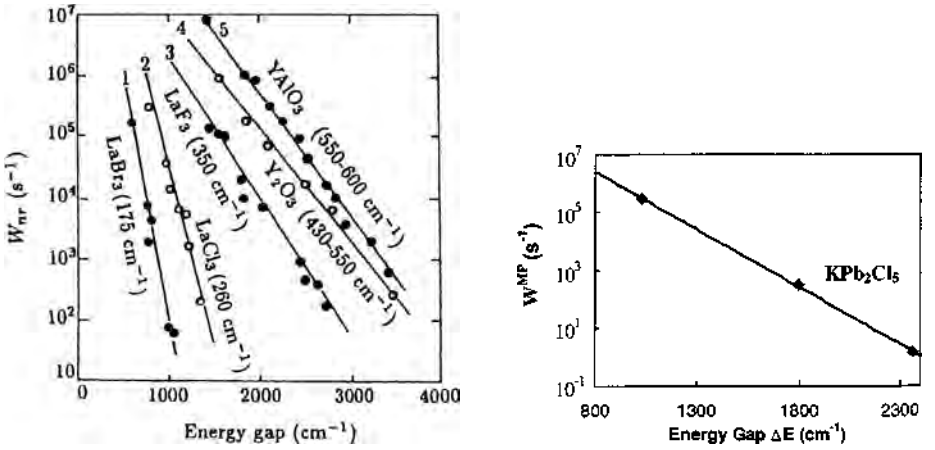

(a) (b)

Figure 6.8 (a) Multiphonon nonradiative transition probability vs. energy gap for several rare-earth ions in various oxide and fluoride crystals. (Reprinted from Ref. 14 with permission from World Scientific Publishing Co.) (b) Multiphonon transition probability vs. energy gap for Nd:KPb_2Cl_5. (Reprinted from Ref. 15 with permission from the Optical Society of America.)

Te. These IR-transparent glasses are useful hosts for rare-earth-doped IR fibers. Codoping these glasses with Er^{3+} and Pr^{3+} allows the Er^{3+} laser system of $^4I_{11/2} \rightarrow {}^4I_{13/2}$ at 2.9 μm transition to act as a four-level laser system, since the Pr^{3+} $^3F_4$, $^3F_3$ energy levels depopulate the terminal $^4I_{13/2}$ level of Er^{3+}, and this provides an effective way to achieve population inversion in the Er^{3+} laser system. Figure 6.9 presents the energy-level scheme of both Er^{3+} and Pr^{3+} and the relevant optical and nonradiative energy-transfer pathways.[16]

6.2.2 Temperature dependence of nonradiative relaxation

A multiphonon relaxation between two levels with an energy gap of ΔE is given by

$$W^{(\mathrm{nr})} = W_0 \prod (n_i + 1)^{P_i}. \tag{6.57}$$

Defining $W^{(\mathrm{nr})} = W(T)$, since temperature-dependent process are involved, gives P_i as the number of phonons emitted with energy $\hbar\omega_i$, such that $\sum_i P_i = P$, W_0 is the transition rate for spontaneous decay at $T = 0$ K, and n_i is the occupation number for the ith phonon mode. The value of n_i at a certain temperature T is given by Bose-Einstein statistics,

$$n_i = \left[\exp\left(\frac{\hbar\omega}{kT}\right) - 1 \right]^{-1}. \tag{6.58}$$

At a temperature of $T = 0$, $n_i = 0$, and the phonon modes are all in the ground state. The phonon modes will be thermally populated, with an increase in the multiphonon decay rates, as the temperature increases. If the energy gap between the excited state and the next lower level is ΔE, and P_i phonons having a frequency of

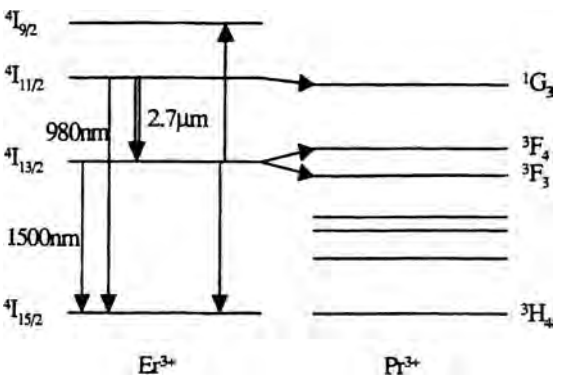

Figure 6.9 Energy-level scheme of Er^{3+} and Pr^{3+} system and the relevant optical and quenching pathways. (Reprinted from Ref. 16 with permission from the Optical Society of America.)

ω_i are emitted, the total energy of the phonons, which are necessary to conserve the energy, is given by

$$\sum_i P_i \hbar \omega_i = \Delta E, \tag{6.59}$$

where the summation i is over all the available phonon modes and energies.

The temperature dependence of the multiphonon process is given by inserting Eq. (6.58) into Eq. (6.57) for a single-frequency ω_i model,

$$W(T) = W(0) \prod_i \left[\frac{\exp(\hbar \omega_i / kT)}{\exp(\hbar \omega_i / kT - 1)} \right]^{-P_i}. \tag{6.60}$$

The above multiphonon decay model assumes multiphonon decay from a single level. In real cases, the upper and lower energy levels have Stark components with an energetic width of several hundred cm^{-1}. These components are in thermal equilibrium with each other within a very short time, compared with the multiphonon decay times from these levels. If one considers a decay from an upper multiplet j to a lower multiplet i separated by an energy gap ΔE_{ji}, the effective decay rate is the weighted average rates from each level, thus

$$W_{\text{eff}}(T) = \frac{\sum_j \sum_i W_{ji}(T) g_j \exp(-\Delta E_{ji}/kT)}{\sum_J g_j \exp(-\Delta E_{ji}/kT)}, \tag{6.61}$$

where W_{ji} is the individual decay rate from the jth multiplet to the ith multiplet and g_j is the degeneracy of the jth level.

It will be shown in several experimental examples that this simple phenomenological model gives a good fit to the temperature-dependent multiphonon decay rates. From this fit, one can obtain the number of phonons p emitted in the multiphonon relaxation. This should be consistent with the law of energy conservation relating the total energy and the maximum phonon energy, namely

$$P \times \hbar \omega_{\max} \cong \Delta E. \tag{6.62}$$

Example 3. This follows the analysis of Riseberg and Moos[9] for the decay of Er^{3+} ($^2H_{9/2} \rightarrow {}^2F_{3/2}$) in LaF_3. The energy gap ΔE is 1860 cm^{-1}, and the cut-off frequency of the phonon energy is $h\omega_{\max} \cong 350$ cm^{-1}. The theoretical fit to the experimental results assumes that 6 phonons (1860/310) are emitted. The results are presented in Fig. 6.10. By extrapolating the experimental results of the multiphonon relaxation rates vs. temperature to a zero absolute temperature, it is found that $W(0) = 1.1 \times 10^4$ s^{-1}. The $^2H_{9/2}$ level has a Stark splitting of $\cong$200 cm^{-1},

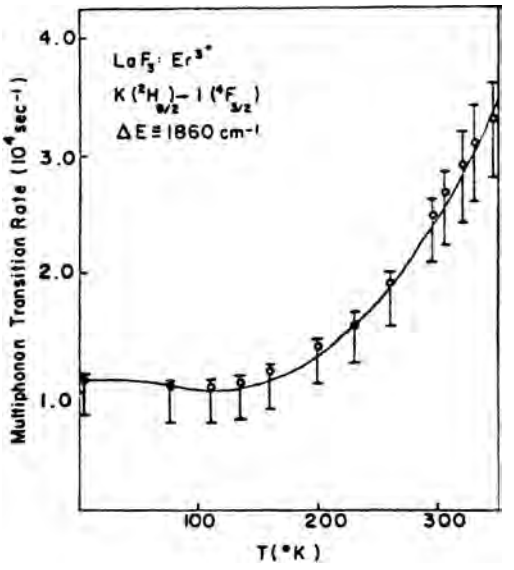

Figure 6.10 Temperature dependence of multipnonon relaxation transition rate in a $Er(^2H_{9/2} \rightarrow {}^4F_{3/2})$-doped LaF_3 crystal. The curve indicates the theoretical fit using Eq. (6.61). The error bars indicate absolute maximum error. (Reprinted from Ref. 9 with permission from the American Physical Society.)

with three nondecaying levels. Therefore, the theoretical fit will be of the form

$$W(T) = 1.1 \times 10^4 \left\{ \frac{\exp[(310)hc/kT]}{\exp[(310)hc/kT] - 1} \right\}^6 \left\{ 1 + 3\exp\left[(-200)\frac{hc}{kT} \right] \right\}^{-1}. \tag{6.63}$$

Finally, note that the possibility exists that several kinds of phonons participate in the multiphonon process. For the case of temperature-dependent, nonradiative decay from $^5F_4$, $^5S_2$ to $^5F_5$ with an energy gap of $\approx$2600 cm^{-1}, it was found that two kinds of phonon frequencies participate: three phonons of 650 cm^{-1} and two of 420 cm^{-1}.[17]

References

1. L. A. Riseberg and M. J. Weber, "Relaxation phenomena in rare-earth luminescence," *Progress in Optics* **XIV**, 89–159, North-Holland (1976).
2. R. Reisfeld, "Radiative and non-radiative transitions of rare-earth ions in glasses," in *Structure and Bonding* **22**, 123–175, Springer-Verlag, Berlin, Heidelberg, and New York (1975); see also Ref. 4, Chapter 2.
3. B. R. Judd, "Optical absorption intensities of rare earth ions," *Phys. Rev. B* **127**(3), 750–761 (1962).
4. G. S. Ofelt, "Intensities of crystal spectra of rare earth ions," *J. Chem. Phys*. **37**(3), 511–520 (1962).

5. C. B. Layne, W. H. Lowdermilk, and M. J. Weber, "Multiphonon relaxation of rare earth ions in oxide glasses," *Phys. Rev. B* **16**, 10–20 (1977).
6. G. H. Dieke, *Paramagnetic Resonance* **1**, 237, Academic Press, New York (1963).
7. A. Kaminskii, *Crystalline Lasers: Physical Processes and Operating Schemes*, CRC Press, Inc. (1996).
8. D. C. Brown, *High-Peak-Power Nd:Glass Laser Systems*, Springer-Verlag, Berlin, Heidelberg, and New York (1981).
9. L. A. Riseberg and H. W. Moos, "Multiphonon orbit-lattice relaxation of excited states of rare-earth ions in crystals," *Phys. Rev. B* **174**, 429–438 (1968).
10. C. B. Layne, W. H. Lowdermilk, and M. J. Weber, "Nonradiative relaxation of rare-earth ions in silicate laser glass," *IEEE J. Quantum Electron* **QE-11**, 798–799 (1975).
11. L. F. Johnson and H. J. Guggenheim, "Laser emission at 3 μm from Dy^{3+} in BaY_2F_8," *Appl. Phys. Lett.* **23**(2), 96–98 (1973).
12. T. Butta, A. M. Chardon, D. P. Shepherd, et al., "Low phonon energy, Nd:LaF_3 channel waveguide lasers fabricated by molecular beam epitaxy," *IEEE J. Quantum Electron* **37**(11), 1469–1477 (2001).
13. M. C. Nostrand, R. H. Page, S. A. Payne, et al., "Room temperature $CaGa_2S_4$:Dy^{3+} laser action at 2.43 μm and 4.31 μm and KPb_2Cl_5:Dy^{3+} laser action at 2.43 μm," *OSA Trends in Optics and Photonics (TOPS)* **26**, *Advanced Solid State Lasers*, 441–449 (1999).
14. F. Gan, *Laser Materials*, World Scientific, Singapore, New Jersey, London, and Hong Kong (1995).
15. M. C. Nostrand, R. H. Page, S. A. Payne, P. G. Schunemann, and L. I. Isaenko, "Laser demonstration of rare earth ions in low-phonon chloride and sulfide crystals," *OSA Trends in Optics and Photonics* **34**, *Advanced Solid State Lasers*, 459–463 (2000).
16. D. J. Coleman, S. D. Jackson, P. S. Golding, et al., "Heavy metal oxide and chalcogenide glasses as new hosts for Er^{3+} and Er^{3+}/Pr^{3+} mid-IR fiber lasers," *OSA Trends in Optics and Photonics (TOPS)* **34**, *Advanced Solid State Lasers*, 434–439 (2000).
17. R. Reisfeld and Y. Kalisky, "Analysis of 750 nm laser emission of Ho^{3+} in tellurite germanate and phosphate glasses," *Chem. Phys. Lett.* **75**, 443–447 (1980).

Chapter 6

Photophysics of Solid State Laser Materials

6.1 Properties of the Lasing Ion

Light emission occurs as a result of interaction between light and matter. Let us assume a two-level atom with levels 1 (ground state) and 2 (excited state). The energies of the ground and excited states are E_1 and E_2, respectively, and the energy difference is therefore given by the difference $\Delta E_{12} = E_2 - E_1$. When light with photons of energy equal to this difference is absorbed by the atomic or molecular system, an electron will be excited from level 1 to level 2. The energy of the photons is given by $\Delta E_{12} = E_{12} = h\nu_{12}$ (h is Planck's constant and ν_{12} is the frequency of light resulting from the level $1 \rightarrow 2$ transition). This energy is absorbed by an atom or a molecule that has energy levels, separated by ΔE, where these energy levels are the ground and the excited states. This kind of "quantum jump" of an electron between two states occurs in atomic systems between electronic levels; it can be extended to molecular systems, where vibrational and translational energy levels participate in the quantum jump. The interaction between light and matter involves the transition of electrons between different states. This interaction results in the absorption of photons (stimulated absorption) as well as spontaneous and stimulated emission. These processes can be described using Einstein's A and B coefficients, as will be described in the next paragraphs.

6.1.1 Absorption

The absorption of light by an object is a fundamental phenomenon in nature. Visible objects scatter the light that falls on them. However, colored objects absorb light at certain wavelengths (or frequencies), while scattering or transmitting other frequencies. For example, an object that will absorb all the frequencies in the visible range will appear black. A green object will absorb light throughout the visible spectral regime except that wavelength which defines the green color.

Let us assume that we have a nondegenerate two-level atomic system, with ground and excited states levels 1 and 2. Initially, the atom is in the ground state 1.

When an external electromagnetic field with a frequency of $h\nu_{12} = E_2 - E_1$ is applied to the atomic system, it is probable that the atom will undergo a transition from level 1 to level 2. This process is termed absorption. If N_1 is the volume density of the atoms in the ground state, the temporal rate of change of the density is given by the equation

$$\frac{dN_1}{dt} = W_{12}N_1, \tag{6.1}$$

where W_{12} is the absorption rate, which is related to the to the photon flux, I, by

$$W_{12} = \sigma_{12}I, \tag{6.2}$$

where σ_{12} is the absorption cross section. The intensity of a monochromatic light, I_λ, which propagates a distance Δz in an absorbing medium, is given by

$$I_\lambda(z) = I_\lambda(0)\exp[-\alpha(\lambda)\cdot\Delta z]. \tag{6.3}$$

$I_\lambda(0)$ is the initial light intensity at the entrance of the absorbing medium, $z = 0$, while $I_\lambda(z)$ is the final intensity after the light has propagated a distance Δz inside the absorbing material. The quantity α introduced in Eq. (6.3) is called the *absorption coefficient*. This equation is valid under thermal equilibrium conditions, $N_1 g_1 > N_2 g_2$, where g_1 and g_2 are the degeneracies of levels 1 and 2, respectively. The inverse magnitude, α^{-1}, measures the optical path for which the light intensity is decreased by a factor of e^{-1} as a result of absorption only by the medium. If it is assumed that the density of the absorbing medium is N atoms per unit volume, the absorption coefficient is related to the absorption cross section as

$$\alpha(\lambda) = N\sigma_{12}. \tag{6.4}$$

It should be noted that the absorption coefficient in this model can be obtained by two methods: The first is based on the imaginary part of the refraction index, the second on the rate at which an atom absorbs energy from an external field. In both cases, the energy absorption is described by a simple classical electron oscillator model, or Lorentz model, of the atom. The Lorentz model was developed before atomic structure was known. The model assumes that in the absence of external forces, the electron in the atom is in an equilibrium position. When an external electromagnetic field with a driving frequency ω is applied to the atomic system, the electron will be displaced from the equilibrium position and will oscillate back and forth, owing to elastic forces, at a natural frequency of ω_0.

The electron motion relative to the nucleus can be described by the rate equation

$$m\frac{d^2x}{dt^2} = e\cdot E(R,t) - C\cdot x, \tag{6.5}$$

where m is the reduced mass of the electron-nucleus system, R is the center-of-mass coordinate, E is the electromagnetic field, and $C \cdot x$ describes the oscillatory motion of the electron (C is the spring constant). This equation can also be written in terms of natural frequency, ω_0, as

$$\left(\frac{\mathrm{d}^2}{\mathrm{d}t^2} + \omega_0^2\right)x = \frac{e}{m}E(R,t), \tag{6.6}$$

where the electron natural frequency ω_0 is defined as $\omega_0 = \sqrt{C/m}$.

When a periodic external field is applied, the oscillatory motion of the bound electron is described in terms of a driven harmonic oscillator. If the electron is displaced by Δx from its equilibrium state, the dipole moment of the system is $P = e \cdot \Delta x$ (where e is the electron charge). The external field provides energy that maintains the oscillation at a frequency of the applied field, ω.

In the case of a damped oscillator, driven by external electric field, the equation of motion of the oscillating electron is

$$\frac{\mathrm{d}^2x}{\mathrm{d}t^2} + 2\gamma\frac{\mathrm{d}x}{\mathrm{d}t} + \omega_0^2 x = \vec{\varepsilon}\frac{e}{m}E_0\cos(\omega t - kz). \tag{6.7}$$

The term γ, introduced in Eq. (6.7) pertaining to the electron oscillator model, is the damping parameter of the average harmonic displacement of the electron, x is the average electron displacement, ω_0 is the natural oscillation frequency, e is the electron charge, m is the reduced mass of the electron-nucleus system, E_0 is the wave amplitude of the induced external field, and $\vec{\varepsilon}$ is a unit vector. It is assumed that the electric field in Eq. (6.7) is a plane wave that propagates along the z axis, with a wave vector k, which relates to the wavelength λ by $k = 2\pi/\lambda$. A damping parameter is also defined as $\Gamma = 2\gamma$.

The solution to Eq. (6.7) can be described by two components, one in phase and a second that is out of phase with the driving force,

$$x(t) = A\sin\omega t + B\cos\omega t, \tag{6.8}$$

where the coefficients A and B are given by

$$A = \frac{e \cdot E_0}{m}\frac{\Gamma\omega}{[(\omega_0^2 - \omega^2)^2 + (\Gamma\omega)^2]} = A_{\mathrm{ab}} \tag{6.9}$$

and

$$B = \frac{e \cdot E_0}{m}\frac{(\omega_0^2 - \omega^2)}{[(\omega_0^2 - \omega^2)^2 + (\Gamma\omega)^2]} = A_{\mathrm{disp}}. \tag{6.10}$$

The term A_{ab} is called the absorptive amplitude, while A_{disp} is called the dispersive amplitude. The averaged input absorption power is a consequence of the term

$A_{ab} \sin \omega t$. The term A_{disp} is averaged out to 0 over one oscillation cycle. It was found that the time-averaged, absorbed power over the oscillation period is given after some mathematical manipulation by

$$P_{av} = \frac{1}{2}(e \cdot E_0 \omega A_{ab}) = \frac{1}{2} m \alpha_0^2 \cdot \frac{\omega^2 \Gamma}{(\omega_0^2 - \omega^2)^2 + (\omega^2 \Gamma^2)} \tag{6.11}$$

and

$$\alpha_0 = e \cdot \frac{E_0}{m}. \tag{6.12}$$

The energy transfer from the driving field to the oscillatory system will be maximized at resonance, when $\omega = \omega_0$. The energy absorption by the system will be at maximum when the frequency of the driving force coincides with the natural frequency of the oscillating system. At resonance,

$$P_0 = \frac{1}{2} \frac{m \alpha_0^2}{\Gamma} \tag{6.13}$$

is obtained. Combining Eqs. (6.11) and (6.13) produces

$$P_{av} = P_0 \frac{\Gamma^2 \omega^2}{(\omega_0^2 - \omega^2) + \Gamma^2 \omega^2}. \tag{6.14}$$

The absorptive amplitude and power [Eqs. (6.9) and (6.14), respectively] depend on the quantity C that is defined as

$$C = (\omega_0^2 - \omega^2)^2 + \Gamma^2 \omega^2 = (\omega_0 - \omega)^2 (\omega_0 + \omega)^2 + \Gamma^2 \omega^2. \tag{6.15}$$

This quantity (C) is changed rapidly at resonance, when $\omega_0 = \omega$, or near resonance, where ω is within the range $\omega - 10\Gamma < \omega < \omega_0 + 10\Gamma$. On the other hand, the term with ω alone contributes a much slower variation in A. In near-resonance and weak damping conditions such as $\Gamma \ll \omega_0$, it is assumed that ω is equal to ω_0 in the expression C except in the factor $(\omega_0 - \omega)^2$ of the first term. Then C may be approximated as

$$C = (\omega_0 - \omega)^2 (\omega_0 + \omega_0)^2 + \Gamma^2 \omega_0^2 = 4\omega_0^2 \left[(\omega_0 - \omega)^2 + \left(\frac{1}{2} \Gamma \right)^2 \right]. \tag{6.16}$$

By inserting the last approximation for C into Eqs. (6.9) and (6.14), it can be observed that both the *absorptive amplitude* and the *averaged absorbed power* are proportional to the factor

$$\frac{[(1/2)\Gamma]^2}{(\omega_0 - \omega)^2 + [(1/2)\Gamma]^2}. \tag{6.17}$$

This frequency-dependent factor determines the lineshape of the absorption amplitude or the absorbed power. The origin of this lineshape, called a Lorentzian lineshape, can be understood if the statistical nature of the atomic system is considered. Therefore, the average time between collisions affects the temporal behavior of the driving EM field and should be included. These effects are included in the lineshape function g, which has the form

$$g(\omega - \omega_0) = \frac{T_2}{\pi} \frac{1}{[1 + (\omega_0 - \omega)^2 T_2^2]}, \tag{6.18}$$

where T_2 is the average time between two collisions. The lineshape $g(\omega - \omega_0)$ defines a Lorentzian lineshape. If one plots $g(\Delta\omega)$ vs. $\Delta\omega$, where $\Delta\omega = \omega - \omega_0$, one obtains a lineshape with a maximum at T_2/π and a FWHM intensity $(\Delta\omega_0)$ with a value of $2/T_2$. If the Lorentz statistical model for atomic collisions is introduced, the result is a relation of the average time between collisions (T_2) to the damping parameter γ by

$$T_2 = \frac{1}{\gamma}. \tag{6.19}$$

The Lorentzian lineshape is therefore a result of collision broadening between atoms. Collision effects are statistically averaged, so physical quantities associated with a Lorentzian lineshape are also averaged. The collision broadening dephases, i.e., the phase of the electron's oscillation before collision is uncorrelated to the phase after the collision. As a result of the collisions, the average displacement of the bound electron decays at a rate equal to the collision rate. The dephasing effect associated with atomic collisions appears as a damping parameter in Eqs. (6.7) and (6.20).

Equation (6.7) can be rewritten in terms of average electron displacement,

$$\frac{\mathrm{d}^2}{\mathrm{d}t^2}\langle x\rangle + 2\gamma \frac{\mathrm{d}}{\mathrm{d}t}\langle x\rangle + \omega_0^2\langle x\rangle = \vec{\mathbf{e}} \frac{e}{m} E_0 \cos(wt - kz), \tag{6.20}$$

where the parameters appearing in Eq. (6.20) have already been defined in Eq. (6.7).

The effect of the damping parameter γ, which includes the meaning of collision rate, should be emphasized here. The friction parameter or the collision rate dephases the electron oscillations so that the phase of the oscillatory motion of the electrons after the collision is completely uncorrelated to the precollision phase. This dephasing results from collisions between electrons, which leads to a decay of the average electron displacement. When no inelastic collisions occur, the oscillatory motion satisfies the Newton Equation [Eq. (6.6)],

$$\frac{\mathrm{d}^2 x}{\mathrm{d}t^2} + \omega_0^2 x = \varepsilon \cdot \frac{e}{m} E_0 \cos(\omega t - kz), \tag{6.21}$$

where the damping parameter was omitted. When elastic collisions are included, a change in the phase occurs and a damping parameter is introduced.

The damping parameter also produces broadening of the absorption line, yielding a broadened lineshape termed as Lorentzian. The broadening effect is equivalent to collision broadening and was described classically by Lorentz using Newton's classical equations of motion, assuming that the collision is fast compared to the time interval between two consecutive collisions, and that it is followed by the re-orientation of the direction of the electronic oscillations. On average, all of the orientations are of equal probability.

The absorption of external electromagnetic waves by an atomic system is significant near resonance. The broadening results from collisions and its classical description holds that when atomic collision occurs with a duration faster than the time interval between two consecutive collisions, enough time remains for the re-orientation displacement of the direction of electron oscillation, with an average electron displacement, which is frequency dependent. The energy absorbed by the electron-nucleus oscillating model (Lorentz model) follows a Lorenztian lineshape. The absorption cross section is given by

$$\sigma(\omega) = \frac{e^2}{2\varepsilon_0 mc} \frac{T_2}{[1 + (\omega_0 - \omega)^2 T_2^2]}, \tag{6.22}$$

where the absorption coefficient is obtained from Eq. (6.4),

$$\alpha(\omega) = N \cdot \sigma(\omega) = \frac{N \cdot e^2}{2\varepsilon_0 mc} \frac{T_2}{[1 + (\omega_0 - \omega)^2 T_2^2]}. \tag{6.23}$$

The absorption coefficient will have maximum value at resonance,

$$\alpha(\omega) = N \cdot \sigma(\omega) = \frac{N \cdot e^2 \cdot T_2}{2\varepsilon_0 mc} = \frac{N \cdot e^2 \cdot T_2}{\Delta\omega_0 \varepsilon_0 mc}, \tag{6.24}$$

where $\Delta\omega_0$ has been defined as the FWHM of a Lorentzian lineshape. The maximum absorption occurs when the driving frequency is equal to the natural frequency of the oscillating bound electrons. The intensity of the incident lightwave, which propagates a distance Δz inside an absorbing medium, obeys the exponential law given in Eq. (6.3).

Absorption is a stimulated process that requires electromagnetic radiation energy to excite the electron transition from the ground state to an excited level. The inverse process is the stimulated emission discussed below. In the case of stimulated absorption, the absorbed photon disappears into the absorbing medium. On the other hand, in the case of stimulated emission, the absorbing medium will emit an additional photon with the same energy, direction, and phase of the incident photon. This is the fundamental basis of laser action.

6.1.1.1 Homogeneous and nonhomogeneous broadening

Performing spectral analysis of an emission or absorption line will show that they are of a finite width. The function that describes the distribution of the intensity of a transition from state i to a certain state j versus the frequency ν is defined as the lineshape $g(\nu, \nu_0)$ of that transition. The central frequency of the lineshape function is defined by ν_0. The lineshape function is normalized according to

$$\int_{-\infty}^{+\infty} g(\nu)\,\mathrm{d}\nu = 1. \tag{6.25}$$

The lineshape function $g(\nu, \nu_0)$ is the probability of absorption or emission of photons per unit frequency, while $g(\nu, \nu_0)\,\mathrm{d}\nu$ is the probability of a transition in the energy range of $h\nu$ and $h(\nu + \mathrm{d}\nu)$. The linewidth function appears in the rate equations that describe spontaneous and stimulated emissions, and therefore the optical linewidth will have a definite bandwidth.

For solid state laser materials, the sources for the linewidth broadening are related either to inherent properties of the atomic system and affect individual atoms (homogeneous broadening) or to the collective properties of the system (inhomogeneous broadening). Homogeneous linewidth broadening results, for example, from the lifetime of the emitting level, thermal effects, and dipolar electric or magnetic interactions, while inhomogeneous broadening in solids results from site distribution, i.e., crystalline or glassy inhomogeneities. Homogeneous broadening is represented by Lorentzian lineshape, inhomogeneous by a Gaussian lineshape.

6.1.2 Spontaneous emission

The result of absorbing a photon by a nondegenerate atomic system with two energy levels 1 and 2 having population densities of N_1 and N_2, respectively, is that the atom is in the excited state, 2. This decays back to the ground state level 1 at a rate proportional to the upper level population,

$$\frac{\mathrm{d}N_2}{\mathrm{d}t} = -A_{21}N_2, \tag{6.26}$$

where A_{21} is the spontaneous transition rate or probability, e.g., the probability of the population decay from level 2 to level 1, per unit time. The spontaneous emission is an inherent property of all excited states and has an exponential decay with a lifetime equal to the reciprocal value of the spontaneous transition probability from the excited level 2,

$$N_2 = N_2(0)\exp\left(-\frac{t}{\tau_{21}}\right) = N_2(0)\exp(-t \cdot A_{21}), \tag{6.27}$$

where $N_2(0)$ is the population of the excited level N_2 at $t = 0$ and τ_{21} is the characteristic time constant of the excited state such that

$$\tau_{21} = A_{21}^{-1}. \tag{6.28}$$

In a case in which the excited state n has several radiative channels to other lower m states, the radiative rate is the sum over all the radiative processes from n to all lower states m,

$$A_n = \sum_m A_{nm}, \tag{6.29}$$

and the excited state lifetime is given by

$$\tau_n = \frac{1}{A_n} = \frac{1}{\sum_m A_{nm}}. \tag{6.30}$$

Classically, spontaneous radiation can be explained through the dependence of the excited state decay rate and power on the square of the dipole moment and the acceleration rate of this dipole, respectively.

6.1.3 Stimulated emission

Emission of EM radiation between two levels in an atomic or molecular system can be generated under the stimulation of an electromagnetic field with a frequency that is equal or near the transition frequency. In the presence of such a stimulating field, the atom will give up to the radiation field additional photons of exactly the same frequency, direction, and phase of the incident photon. In other words, it will fulfill the requirement for conservation of energy and momentum. In this case, the decay of the excited level is proportional to the population density, N_2, and also to the radiation density per unit frequency $\sigma_{21}(\nu_{21})$ of the induced electromagnetic radiation,

$$\frac{\mathrm{d}N_2}{\mathrm{d}t} = -B_{21}\rho_{21}(\nu_{21}) \cdot N_2. \tag{6.31}$$

The stimulated absorption rate is similarly

$$\frac{\mathrm{d}N_1}{\mathrm{d}t} = -B_{12}\rho_{12}(\nu_{12})N_1, \tag{6.32}$$

where B_{21} is the proportionality constant, also called the Einstein coefficient for stimulated emission, and B_{12} is the stimulated absorption coefficient. As can be seen, the emission of an atomic or molecular system in the presence of an external EM field consists of two contributions: photons that results from spontaneous emission, with a decay rate that is proportional to the spontaneous decay rate, A_{21},

and with phase independent of the external field; and stimulated emission or absorption, with a rate constant proportional to $\rho_{21}\nu_{(21)}B_{21}$ and to $\rho_{12}\nu_{(12)}B_{12}$, the stimulated emission intensity proportional to the energy density per unit frequency of the external field $\rho_{21}(\nu_{21})$ at frequency ν_{12} (here $\nu_{12} = \nu_{21}$, and $\rho_{12} = \rho_{21)}$.

The relation between the stimulated emission and absorption coefficients and the spontaneous emission coefficient is given by

$$B_{21} = \frac{c^3}{8\pi h\nu^3} A_{21} \tag{6.33}$$

and

$$\frac{g_1}{g_2}\frac{B_{12}}{B_{21}} = 1. \tag{6.34}$$

The stimulated absorption and emission coefficients describe the interaction of a photon with a two-level system, assuming that the radiation is in radiative thermal equilibrium, where the number of transitions per unit of time from $1 \rightarrow 2$ is equal to the number of transitions $2 \rightarrow 1$,

$$A_{21}N_2 + B_{21}\rho(\nu_{21})N_2 = B_{12}\rho(\nu_{12})N_1, \tag{6.35}$$

or more simply,

$$N_2[A_{21} + B_{21}\rho(\nu)] = B_{12}\rho(\nu)N_1. \tag{6.36}$$

These main photophysical processes based on Einstein probabilities are represented schematically in Fig. 6.1.

6.1.4 Oscillator strength

The concept of oscillator strength stems from the fact that the electron motion and its attraction to the nucleus can be described in terms of classical oscillator theory. Oscillator strength describes the relative strength of resonant oscillations of the bound electron/s in an atomic system. In other words, it measures the capability of an electron to have a relative oscillating mode or frequency. By knowing the oscillator strength value, it is possible to estimate the relative strength of several transitions that originate from that level. The relationship between the radiative rate and the absorption oscillator strength is

$$A_{21} = \frac{2\pi e^2}{\varepsilon_0 m_e c\lambda_{21}^2}\frac{g_1}{g_2} f_{12}, \tag{6.37}$$

where e is the electron charge, c is the speed of light, m_e is the electron mass, f_{12} is the oscillator strength of the $1 \rightarrow 2$ transition, λ_{12} is the transition wavelength, and ε_0 is the permittivity of a vacuum.

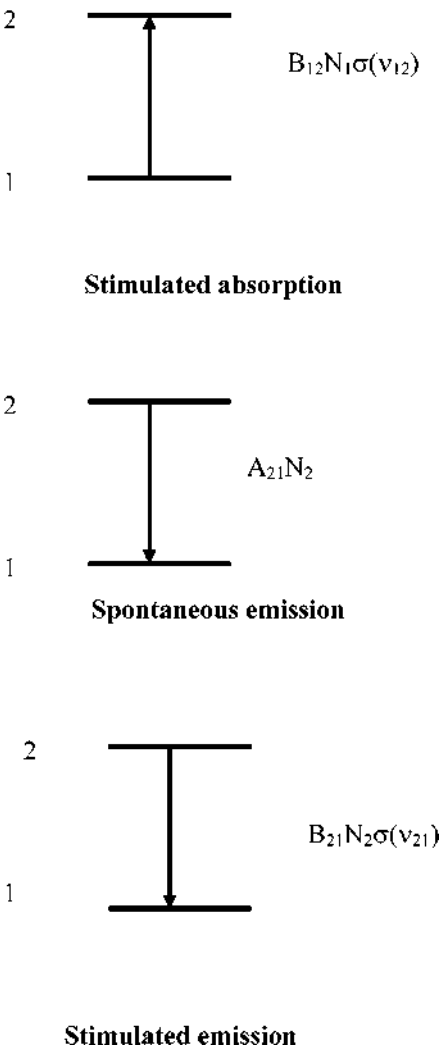

Figure 6.1 A schematic description of the main processes in an atomic system defined by Einstein coefficients.

Assume a multilevel atomic system that is excited from its ground state i to an excited state j by photons of energy equal to $E = h \cdot \nu$, where h is Planck's constant and $\nu = \nu_{exc}$ is the excitation frequency. Upon excitation, three pathways of the photophysical processes can be expected to occur:

- Radiative decay;
- Nonradiative decay, where part or all of the excitation energy is converted into vibrational quanta of the surrounding lattice; and
- Radiative and nonradiative energy transfer among the neighboring ions.

The rate of relaxation of any excited level depends on the relative contributions of the radiative $[W^{(\mathrm{rad})}]$ and nonradiative $[W^{(\mathrm{nr})}]$ rates. These contributions will dictate the overall lifetime and radiative quantum efficiency of the excited level.

The lifetime τ_j of the excited state j is given by

$$\frac{1}{\tau_j} = \sum_j W_{ji}^{(\mathrm{rad})} + \sum_i W_{ji}^{(\mathrm{nr})}, \tag{6.38}$$

where the summations are for transitions originating from quantum state j (the excited state) to all final unexcited states i, $W_{ji}^{(\mathrm{rad})}$ is the total probability of radiative transfer from level j to level i, and $W_{ji}^{(\mathrm{nr})}$ are the total probabilities for nonradiative decays from level j to all levels i. The quantum state i can be a final state either within the same atomic or molecular system, or in a neighboring atomic system, namely

$$\sum_{i,i'} W_{j,i\neq i'}^{(\mathrm{nr})} = \sum_i W_{ji}^{(\mathrm{nr})} + \sum_{i'} W_{ji'}^{(\mathrm{nr})}. \tag{6.39}$$

The first term in the right-hand side of the above equation represents the total nonradiative decay from level j to final states i within the same atomic or ionic system, while the second term in the right-hand side represents an energy-transfer process from an energy donor (D) to an energy acceptor, A, whose terminal quantum state is i'. The radiative and nonradiative probabilities include the participation of the host phonons in this dynamical process. This is called *phonon-assisted relaxation* or *phonon-assisted energy transfer*. The energy transfer is accompanied by an ion-ion multipolar interaction. The radiative quantum efficiency of the excited level j is equal to the ratio of photons emitted from level j to the number of photons excited into level j. The radiative quantum efficiency is defined by

$$\eta_j = \frac{\sum_i W_{ji}^{(\mathrm{rad})}}{\sum_i W_{ji}^{(\mathrm{rad})} + \sum_{i,i\copyright} W_{j,i\neq i'}^{(\mathrm{nr})}} = \tau_j \times \sum_i W_{ji}^{(\mathrm{rad})}, \tag{6.40}$$

with $\tau_j = \tau_{\mathrm{meas}}$, where τ_{meas} is the measured lifetime of the quantum state j. The relative probabilities for radiative and nonradiative decays between levels j and i may range from values of comparable magnitude to the values of two extreme cases: $W_{ji}^{(\mathrm{rad})} \ll W_{ji}^{(\mathrm{nr})}$ or $W_{ji}^{(\mathrm{rad})} \gg W_{ji}^{(\mathrm{nr})}$. The radiative quantum efficiency of a level j may therefore have limiting values ranging from zero to unity.

The branching ratio for a transition from level j to level i is defined as the ratio between $W_{ji}^{(\mathrm{rad})}$, the radiative transition probability from j to level i, and $\sum_i W_{ji}^{(\mathrm{rad})}$, the total transition probabilities from level j to all terminal levels i,

and is given by

$$\beta_{ji} = \frac{W_{ji}^{(\mathrm{rad})}}{\sum_i W_{ji}^{(\mathrm{rad})}}. \tag{6.41}$$

The radiative probability is an important parameter in laser analysis. It is related to the induced transition probabilities by the Einstein relation

$$(W_{21})_{\mathrm{ind}} = \frac{\lambda^2 \times I_\nu}{8\pi n^2 h\nu} \times W^{(\mathrm{rad})} g(\nu). \tag{6.42}$$

In this expression, n is the refractive index of the active medium, c is the speed of light in a vacuum, I_ν is the intensity of the inducing field, $g(\nu)$ is the normalized lineshape function for the transition from level j to level i, and ν is the frequency of the transition.

In order to calculate the values of $W^{(\mathrm{rad})}$, the positions of the relevant energy levels must be determined. In the case of rare-earth ions doped into a solid host, where the transitions are among f^N electronic levels, the energy-level positions depend on the coulombic interaction, spin-orbit interaction, and crystal-field effects, all shown in Fig. 6.2. In this figure, the magnitude of the energetic separation of the electronic states resulting from the various interactions is also presented. As can be seen, the coulombic interaction yields ^{2s+1}L terms separated by 10^4 cm^{-1}. The spin-orbit interaction results in a splitting of 10^3 cm^{-1}, while the crystal field of the solid host removes the $2J+1$ degeneracy and yields a manifold with spectral width of a few hundred cm^{-1}.

The radiative transitions between electronic levels of materials doped with rare-earth ions can be magnetic-dipole or electric-quadrupole transitions allowed by

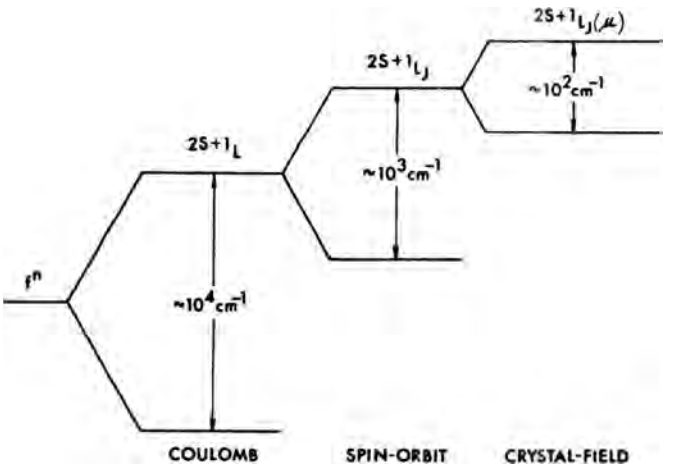

Figure 6.2 A schematic diagram of the splitting in f^N levels resulting from coulombic, spin-orbit, and crystal-field interactions. (Reprinted from Ref. 1 with permission from Marvin J. Weber.)

spectroscopic selection rules (parity-allowed transitions), or they can be electric-dipole transitions, which are parity forbidden. These transitions become partially allowed by the admixture of states with opposite parity into the f^N atomic level. The transitions between J states possess oscillator strength of the order of 10^{-6}. This admixture can occur, for example, when the rare-earth ion is situated in a site that does not have inversion symmetry. This type of transition is called a *forced electric dipole transition*. In a case in which the electric-dipole transitions become partially allowed, their contribution to the optical transitions predominates. The parity rules allowing magnetic-dipole and electric-quadrupole transitions contribute negligibly to the overall radiative decay rate. A theoretical treatment of radiative transition in such cases was introduced by Judd and Ofelt and was further applied to many cases by other authors.[1–4]

A practical case relevant to rare-earth ions is one in which the emitting level j is composed of two levels separated by an energy gap ΔE_j, which are in thermal equilibrium. In this case, the effective lifetime of level j is given by the formula

$$\frac{1}{\tau_{\text{eff}}} = \frac{\sum_j \left[\sum_i g_j \exp(-\Delta E_j/kT) \cdot W_{ji}^{(\text{rad})}\right]}{\sum_j g_j \cdot \exp(-\Delta E_j/kT)}, \tag{6.43}$$

where $W_{ji}^{(\text{rad})}$ is the radiative decay from levels j to all ground levels i, and g_j is the degeneracy of the jth level. In that case, the branching ratio defined by Eq. (6.41) takes the form of

$$\beta = \frac{\sum_j g_j(-\Delta E_j/kT)}{\sum_j \left[\sum_i g_j \exp(-\Delta E_j/kT) \cdot W_{ji}\right]}. \tag{6.44}$$

6.2 Nonradiative Transition

As explained earlier, three main processes dominate the decay of an excited state to the ground state: radiative decay, nonradiative decay, and energy transfer of the excitation into the neighboring ions.

Radiative decay occurs with a simultaneous emission of a photon having energy equal to the separation between the two levels in which the transition occurs. Nonradiative decay from excited state j' to the lower j state occurs via emission of one or more phonons. The total energy of the system is conserved, such that the total phonon energy emitted is equal to the energy gap ΔE_j between the adjacent levels participating in the nonradiative process,

$$p\hbar\omega = \Delta E_j, \tag{6.45}$$

where $\hbar\omega$ is the phonon energy and p is the number of phonons participating in the nonradiative process. These phonons are observed by the vibrational spectrum of the solid state host. If several phonons are emitted, the process is called *multi-phonon relaxation* (MPR). This MPR rate depends on two main parameters:

1. The energy gap ΔE between two neighboring relevant levels.
2. The temperature of the atomic or molecular system, via the phonon occupation probability.

The source of the multiphonon relaxation is the interaction of the electronic levels of the doped ion with the vibrations of the host.

Another pathway contributes to the relaxation of excited states—the energy transfer of excitation to neighboring ions. Energy transfer occurs via several mechanisms, such as a multipolar interaction, exchange mechanism, and energy migration or "diffusion." This process will be explained further in Chapter 7.

6.2.1 Energy gap and temperature dependence of multiphonon relaxation

Multiphonon relaxation occurs when the excited state decays nonradiatively with a simultaneous emission of several phonons. This process results from the interaction of the electronic levels of the emitting ion with the vibrations of the host crystal. These vibrations modulate and perturb the local field around the $4f^N$ electrons. Assuming a point-charge model, point ions are displaced around their equilibrium positions as a result of the orbit-lattice interaction,

$$V_{\text{ol}} = V_{\text{c}} + \sum V_i Q_i + \frac{1}{2} \sum_{i,j} V_{ij} Q_i Q_j + \cdots, \tag{6.46}$$

where V_{c} is the static crystal field, Q_i, Q_j are normal mode coordinates, and V_i, V_{ij} are the expansion coefficients defined as $V_i = \partial V_{\text{c}}/\partial Q_i$, $V_{ij} = \partial^2 V_{\text{c}}/\partial Q_i \partial Q_j$.

When the electronic transition in rare-earth ions is equal to the energy of one phonon mode, it is a *one-phonon process.* However, if the electronic transition is equal to several phonons, a higher-order process, a multiphonon relaxation (which is less probable than a one-phonon process) occurs. Single and multiphonon processes are presented in Fig. 6.3.

Dieke[6] noted years ago that if, in an atomic system, two spin-orbit levels were sufficiently close in their energetic position, the excited level would not emit photons. For LaF_3, for example, in order to observe fluorescence, the energy gap between the two spin-orbit levels should be $\Delta E \approx 1000\ \text{cm}^{-1}$. The qualitative reason was that for a gap of this magnitude and the cut-off in the phonon spectrum of $\approx 250\ \text{cm}^{-1}$, at least four phonons were needed for nonradiative decay, which makes the process less probable. The multiphonon decay rate of excited states can be analyzed in a more coherent way for two main cases:

1. The crystal parameters are constant and the energy gap is a variable.
2. The crystal/host parameters are variables, while the energy gap is constant.

The analysis of the MPR processes is based on several assumptions:

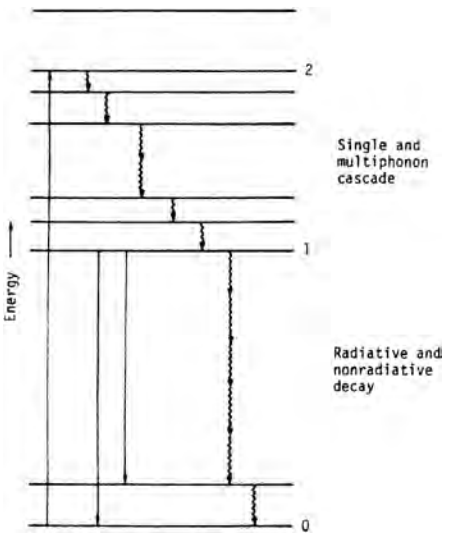

Figure 6.3 A schematic presentation of single and multiphonon decay processes. (Reprinted from Ref. 5 with permission from the American Physical Society.)

- Weak ion-lattice coupling.
- MPR is dominated by the number of phonons. In most cases, the lowest order MPR, with the most energetic phonons, dominates.
- Low-frequency, strongly coupled phonons are also possible.
- Conservation of energy is fulfilled.
- Single-frequency processes will dominate relative to multifrequency processes.
- The host vibrations are mostly dominant and mainly responsible for MPR.

The order of the MPR process of Er^{3+} ($^4S_{3/2} \rightarrow {}^4F_{9/2}$) ($\Delta E = 2930$ cm^{-1}) in germanate glass, having a phonon energy of $\hbar\omega = 890$ cm^{-1}, is $p \approx 3$, and for tellurite glass with $\hbar\omega = 675$ cm^{-1} is $p \approx 4$, implying that the MPR rate in tellurite glass will be higher than that in germanate glass. Table 6.1 presents the values of the main phonon energies in several commonly used laser hosts.

Consider now the situation of weak orbit-lattice coupling and a single-frequency model. The ratio of the pth order MPR to the $(p-1)$th order MPR rate is given by

$$\frac{W^{(p)}}{W^{(p-1)}} = \varepsilon \ll 1, \tag{6.47}$$

where ε is a coupling constant. The rate of the pth order MPR can be described approximately as

$$W^{(p)} \approx A\varepsilon^p. \tag{6.48}$$

Here, A is a constant and p is the order of the single-frequency MPR process.

Table 6.1 Phonon energies of several laser hosts.[2, 7]

Crystal	Type	Phonon energy (cm^{-1})
Tellurite	Glass-oxide	600–750
Germanate	Glass-oxide	800–975
Phosphate	Glass-oxide	1200–1350
Silicate	Glass-oxide	1000
Fluorophosphate	Glass-oxide	800–1050
YAG	Crystal-oxide	700
$YAlO_3$	Crystal-oxide	550–600
Y_2O_3	Crystal-oxide	430–550
$YLiF_4$	Crystal-oxide	400
LaF_3	Crystal fluoride	300–350
$LaCl_3$	Crystal chloride	260
$LiYF_4$	Crystal fluoride	400

Using Eq. (6.45) and assuming that the phonon with maximum energy is dominant in the MPR process (namely, the phonon with frequency $\omega = \omega_{\max}$), we obtain for Eq. (6.48) the energy-gap dependence,

$$W^{(p)} \approx A\varepsilon^p = A \times \exp(\ln \varepsilon \times p) = A \times \exp\left(\frac{\ln \varepsilon}{\hbar\omega} \times \Delta E\right). \tag{6.49}$$

Equation (6.49) can also be written as

$$W^{(\mathrm{P})} = W^{(\mathrm{NR})} = C \times \exp(-\alpha \Delta E), \tag{6.50}$$

where C and $\alpha = -\ln(\varepsilon)/\hbar\omega$ are host-dependent constants.

Equation (6.39) can be rewritten in a simpler way, where any excited level a is given by

$$\frac{1}{\tau_a} = \sum_b A_{ab} + \sum_b W_{ab}. \tag{6.51}$$

This equation has parameters similar to those in Eq. (6.38). A_{ab} and W_{ab} denote the radiative and nonradiative rates from excited level to a final level b, respectively, and τ_a is the lifetime of the excited state a.

Generally speaking, the multiphonon decay rate of an excited state is an exponential function of the energy gap ΔE between the excited level and the next lower level.[1] It takes a general form of

$$W^{(\mathrm{NR})} = W_0 \times \exp(-\alpha \Delta E), \tag{6.52}$$

where W_0 is the transition probability extrapolated to $\Delta E = 0$, and α that is defined in Eq. (6.50) provides the characteristics of the host phonon spectra and the electron-phonon coupling constant. Both constants are characteristic for a particular crystal. Where W_0 and α are not changed (e.g., for the same laser host), the

experimental result clearly indicates a logarithmic dependence of the multiphonon rate on the energy gap. The validity of the energy-gap law was demonstrated both in crystals and amorphous materials doped with a variety of rare-earth ions, and was summarized in numerous publications relevant to solid state laser materials.[2, 8, 9]

An example of the energy-gap law for rare-earth-ion-doped silicate glass is presented in Fig. 6.4.

For example, the multiphonon decay of $^4F_{3/2}$ level of Nd^{3+} ($\Delta E \approx 4800\ cm^{-1}$) was extracted from Fig. 6.4 and found to be $\approx 2 \times 10^2\ sec^{-1}$, in agreement with experimental results.

In a case in which the host parameters are variables for a given energy gap, it was found that the multiphonon rate is faster for hosts with higher phonon energies. For rare-earth ions doped in hosts with high phonon energies and multiphonon relaxation rates, the quantum efficiency of the fluorescence was found to be lower than for materials with low phonon energies. This is consistent with Eq. (6.40). The main reason for the host-dependent multiphonon rate is the cut-off frequency, ω_{max}, of the phonon spectrum for a particular solid state host. It was found in crystals and glasses that the phonons responsible for multiphonon relaxation are those associated with the vibrational modes of the crystal network, and for a second order—those associated with crystal modifiers. For an energy gap ΔE and a phonon energy ω_{max}, the number of phonons participating in the nonradiative

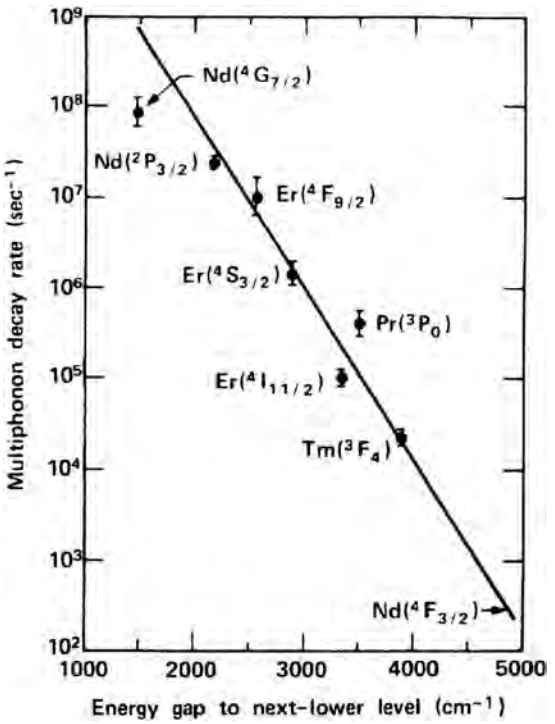

Figure 6.4 Energy-gap law for rare-earth-ion-doped silicate glass at 300 K. (Reprinted from Ref. 10 with permission from the IEEE.)

decay between two successive levels, with an energy gap ΔE, is given by

$$P \cong \frac{\Delta E}{\hbar \omega_{\max}}, \tag{6.53}$$

where p is the order of the nonradiative process. For two hosts, type 1 and type 2, with characteristic phonon frequencies $\omega_{\max}^{(1)}$ and $\omega_{\max}^{(2)}$, such that

$$\omega_{\max}^{(1)} > \omega_{\max}^{(2)}, \tag{6.54}$$

and for the same energy gap ΔE, the number of phonons participating in nonradiative decay will be

$$P^{(1)} \cong \frac{\Delta E}{\hbar \omega_{\max}^{(1)}} \quad \text{and} \quad P^{(2)} \cong \frac{\Delta E}{\hbar \omega_{\max}^{(2)}} \tag{6.55}$$

for host types 1 and 2, respectively. Since $P^{(1)} < P^{(2)}$, the process that requires fewer phonons will be more probable and one would expect to observe a faster multiphonon relaxation rate for the host with the higher phonon energy.

Quantitatively, this law shows an exponential behavior of the form

$$W^{(\mathrm{nr})}(\Delta E) = K \times \exp(-P), \tag{6.56}$$

where $W^{(\mathrm{nr})}(\Delta E)$ is the multiphonon decay rate for a certain energy gap, K is a proportional constant that depends on host parameters such as structure, lattice parameters, and crystal field, and P is the number of phonons needed to bridge the energy difference between two successive levels.

Example 1. Consider the multiphonon decay rate of $^4F_{9/2}$ level of Er^{3+} in oxide and fluoride crystalline hosts LaF_3 and Y_2O_3 (Ref. 9). For LaF_3, the relevant energy gap is $\Delta E = 2650\ \mathrm{cm}^{-1}$ and $h\omega_{\max} = 350\ \mathrm{cm}^{-1}$. The number of phonons needed to bridge the energy gap is represented by $p \cong 7$. For Y_2O_3, $\Delta E = 2516\ \mathrm{cm}^{-1}$ and $h\omega_{\max} = 550\ \mathrm{cm}^{-1}$; therefore, $p \cong 4$, and the multiphonon decay rate in the oxide will be faster than in fluorides. The rate for LaF_3 is $(4.4 \pm 1.5) \times 10^2\ \mathrm{s}^{-1}$, whereas for Y_2O_3 the multiphonon rate is $(1.7 \pm 0.6) \times 10^4\ \mathrm{s}^{-1}$, i.e., faster by a factor of $\approx$40, as expected. This fact is also reflected in the lifetime of the $^4F_{9/2}$ level of Er-doped crystals. In LaF_3, the lifetime is $(700 \pm 70)\ \mu\mathrm{s}$, while for Y_2O_3 it is $(50 \pm 15)\ \mu\mathrm{s}$. This rule is valid for any energy gap regardless of the type of the rare-earth ion. For a given crystal host, the critical parameter is the energy gap. The energy-gap dependence of the spontaneous multiphonon decay rates in LaF_3 and Y_2O_3 doped with various rare-earth ions clearly demonstrates the possibility of obtaining efficient emission from metastable levels with low energy gap in hosts with small phonon energies. This is also presented in Figs. 6.5(a) and (b).

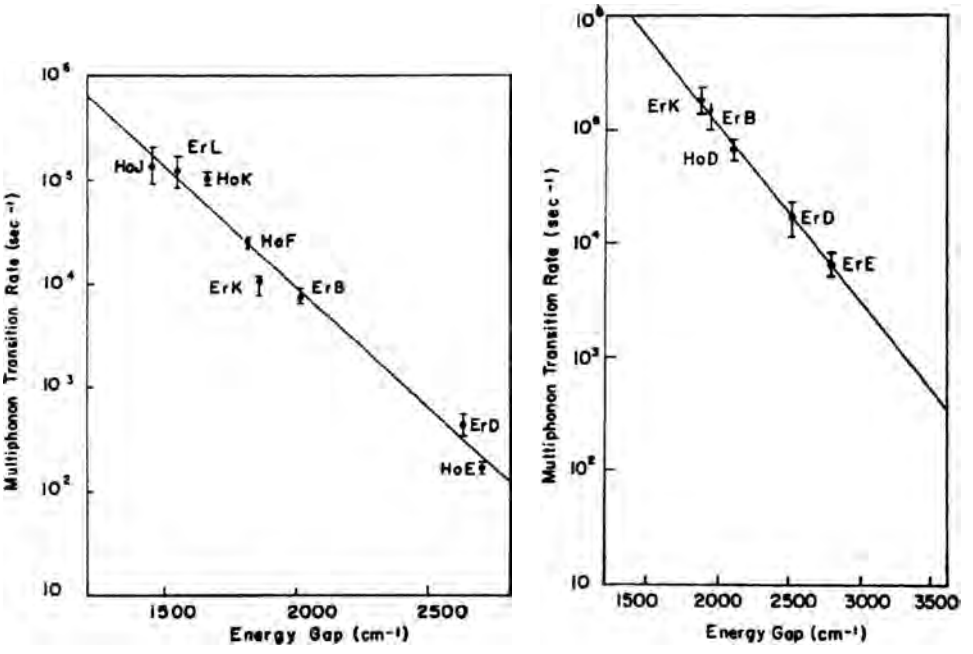

Figure 6.5 Energy-gap dependence of the spontaneous multiphonon decay rate for various rare-earth ions in (a) LaF_3, and (b) Y_2O_3 crystals. (Reprinted from Ref. 9 with permission from the American Physical Society.)

Example 2. For the $^5F_4, ^5S_2$ level of Ho^{3+}:LaF_3, with energy gap to the nearest level, $\Delta E = 2700$ cm^{-1}, and phonon energy of, $h\omega_{\max} = 350$ cm^{-1}, the multiphonon decay rate is $(1.9 \pm 0.2) \times 10^2$ s^{-1}, which is the same order of magnitude as in the Er($^2F_{9/2}$) level. The empirical energy-gap law fits well with the experimental results and makes it possible to predict multiphonon decay rates by extrapolating to a value of a known ΔE with 50% accuracy.[9] If changes occur within the orbit-lattice coupling or in static and dynamic crystal fields, a family of straight lines will be obtained. The dependence of MPR in a crystalline host (via the phonon energies) can be utilized to operate special laser systems at longer wavelengths. Figure 6.6 presents the nonradiative rate versus the energy gap between two neighboring levels in a fluoride crystal.[11] This type of behavior is similar in various oxide crystals as well. From Fig. 6.6, it can be seen that in most oxide and fluoride glasses, nonradiative processes dominate for energy gaps below $\approx$3700 cm^{-1} (2.6$-$2.8 μm). Below this, the MPR processes dominate and this affects the possibility of achieving an efficient laser operation. It is expected that low-phonon crystals will exhibit laser operation even at relatively small energy gaps because they require a large number of phonons in order to participate in the nonradiative process in accordance with Eq. (6.55).

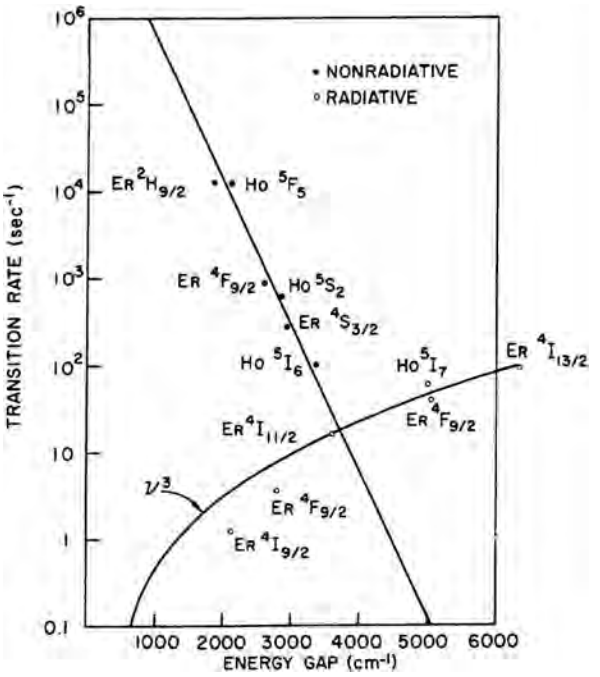

Figure 6.6 Radiative and nonradiative transition rates vs. energy gap for various rare-earth ions. (Reprinted from Ref. 11 with permission from the American Institute of Physics and Lucent Technologies Inc./Bell Labs.)

Low-phonon hosts can be used to fabricate efficient multi-wavelength channel waveguide laser sources emitting in the mid-IR. For example, Bhutta et al.[12] fabricated and operated a thin film, channel waveguide laser based on a low-phonon Nd:LaF_3 crystal. The waveguide was characterized both in terms of spectroscopic properties and laser operation. The structure (a 20-μm wide channel waveguide laser) offers a low threshold and relatively high efficiency (14% slope efficiency) CW waveguide laser emitting at various mid-IR wavelengths. Other materials with low phonon energies include $CaGaS_4$ ($\hbar\omega_{max} = 350$ cm^{-1}) and KPb_2Cl_5 ($\hbar\omega_{max} = 200$ cm^{-1}). These materials are denser than oxide or fluoride hosts and therefore have lower phonon energies. By doping these low-phonon crystals with Nd^{3+} or Dy^{3+}, it was possible to obtain laser emission among intermediate levels that in oxide hosts are usually quenched by nonradiative processes. Figure 6.7 presents energy-level structure and laser transitions in a Dy^{3+} ion. Both the 4.31 μm ($^6H_{11/2} \rightarrow {}^6H_{13/2}$) and 2.43 μm ($^6H_{9/2}$, $^6F_{11/2} \rightarrow {}^6H_{13/2}$) optical transitions could be obtained in these low-phonon materials.[13]

The MPR rates were relatively low in comparison with oxides or fluorides,[14] as can be observed from Figs. 6.8(a) and (b). These figures describe the nonradiative transition rates versus energy gap ΔE for several rare-earth ions in various oxide and fluoride crystals, Fig. 6.8(a), and for Nd^{3+}-doped KPb_2Cl_5, Fig. 6.8(b).

Another family of low-phonon energy materials is the heavy-metal oxide containing Pb^{2+}, Bi^{3+} and Ga^{3+}, and chalcogenide glasses that contain S, Se, and

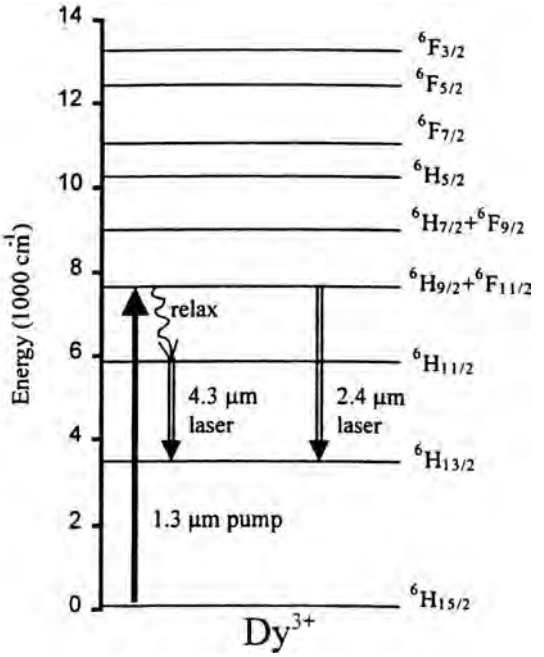

Figure 6.7 Energy-level structure and laser transitions in Dy^{3+}. (Reprinted from Ref. 13 with permission from the Optical Society of America. Credit must be given to the University of California, Lawrence Livermore National Laboratory, and the U.S. Department of Energy, under whose auspices the work was performed, when this information or a reproduction of it is used.)

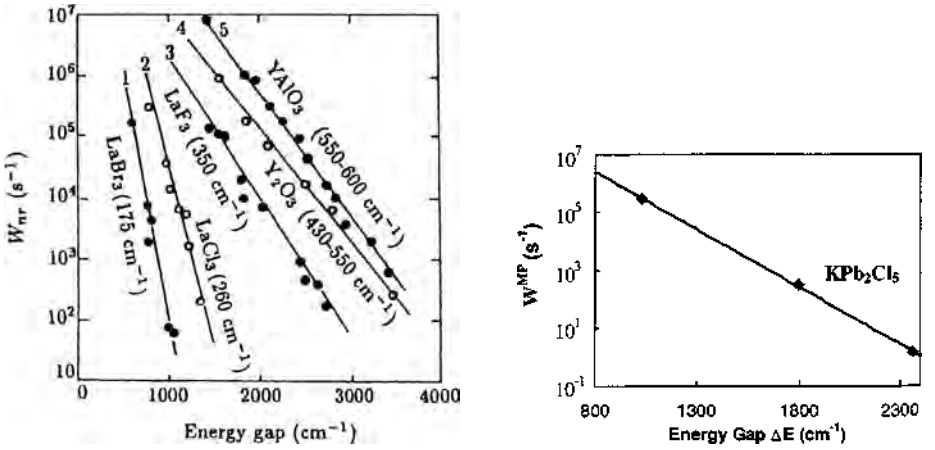

(a) (b)

Figure 6.8 (a) Multiphonon nonradiative transition probability vs. energy gap for several rare-earth ions in various oxide and fluoride crystals. (Reprinted from Ref. 14 with permission from World Scientific Publishing Co.) (b) Multiphonon transition probability vs. energy gap for Nd:KPb_2Cl_5. (Reprinted from Ref. 15 with permission from the Optical Society of America.)

Te. These IR-transparent glasses are useful hosts for rare-earth-doped IR fibers. Codoping these glasses with Er^{3+} and Pr^{3+} allows the Er^{3+} laser system of $^4I_{11/2} \rightarrow {}^4I_{13/2}$ at 2.9 μm transition to act as a four-level laser system, since the Pr^{3+} $^3F_4$, $^3F_3$ energy levels depopulate the terminal $^4I_{13/2}$ level of Er^{3+}, and this provides an effective way to achieve population inversion in the Er^{3+} laser system. Figure 6.9 presents the energy-level scheme of both Er^{3+} and Pr^{3+} and the relevant optical and nonradiative energy-transfer pathways.[16]

6.2.2 Temperature dependence of nonradiative relaxation

A multiphonon relaxation between two levels with an energy gap of ΔE is given by

$$W^{(\mathrm{nr})} = W_0 \prod (n_i + 1)^{P_i}. \tag{6.57}$$

Defining $W^{(\mathrm{nr})} = W(T)$, since temperature-dependent process are involved, gives P_i as the number of phonons emitted with energy $\hbar\omega_i$, such that $\sum_i P_i = P$, W_0 is the transition rate for spontaneous decay at $T = 0$ K, and n_i is the occupation number for the ith phonon mode. The value of n_i at a certain temperature T is given by Bose-Einstein statistics,

$$n_i = \left[\exp\left(\frac{\hbar\omega}{kT}\right) - 1 \right]^{-1}. \tag{6.58}$$

At a temperature of $T = 0$, $n_i = 0$, and the phonon modes are all in the ground state. The phonon modes will be thermally populated, with an increase in the multiphonon decay rates, as the temperature increases. If the energy gap between the excited state and the next lower level is ΔE, and P_i phonons having a frequency of

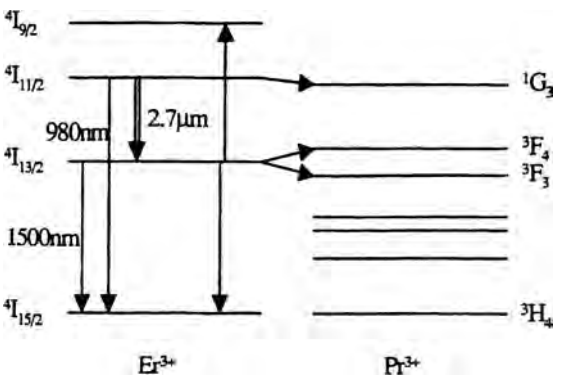

Figure 6.9 Energy-level scheme of Er^{3+} and Pr^{3+} system and the relevant optical and quenching pathways. (Reprinted from Ref. 16 with permission from the Optical Society of America.)

ω_i are emitted, the total energy of the phonons, which are necessary to conserve the energy, is given by

$$\sum_i P_i \hbar \omega_i = \Delta E, \tag{6.59}$$

where the summation i is over all the available phonon modes and energies.

The temperature dependence of the multiphonon process is given by inserting Eq. (6.58) into Eq. (6.57) for a single-frequency ω_i model,

$$W(T) = W(0) \prod_i \left[\frac{\exp(\hbar \omega_i / kT)}{\exp(\hbar \omega_i / kT - 1)} \right]^{-P_i}. \tag{6.60}$$

The above multiphonon decay model assumes multiphonon decay from a single level. In real cases, the upper and lower energy levels have Stark components with an energetic width of several hundred cm^{-1}. These components are in thermal equilibrium with each other within a very short time, compared with the multiphonon decay times from these levels. If one considers a decay from an upper multiplet j to a lower multiplet i separated by an energy gap ΔE_{ji}, the effective decay rate is the weighted average rates from each level, thus

$$W_{\text{eff}}(T) = \frac{\sum_j \sum_i W_{ji}(T) g_j \exp(-\Delta E_{ji}/kT)}{\sum_J g_j \exp(-\Delta E_{ji}/kT)}, \tag{6.61}$$

where W_{ji} is the individual decay rate from the jth multiplet to the ith multiplet and g_j is the degeneracy of the jth level.

It will be shown in several experimental examples that this simple phenomenological model gives a good fit to the temperature-dependent multiphonon decay rates. From this fit, one can obtain the number of phonons p emitted in the multiphonon relaxation. This should be consistent with the law of energy conservation relating the total energy and the maximum phonon energy, namely

$$P \times \hbar \omega_{\max} \cong \Delta E. \tag{6.62}$$

Example 3. This follows the analysis of Riseberg and Moos[9] for the decay of Er^{3+} ($^2H_{9/2} \rightarrow {}^2F_{3/2}$) in LaF_3. The energy gap ΔE is 1860 cm^{-1}, and the cut-off frequency of the phonon energy is $h\omega_{\max} \cong 350$ cm^{-1}. The theoretical fit to the experimental results assumes that 6 phonons (1860/310) are emitted. The results are presented in Fig. 6.10. By extrapolating the experimental results of the multiphonon relaxation rates vs. temperature to a zero absolute temperature, it is found that $W(0) = 1.1 \times 10^4$ s^{-1}. The $^2H_{9/2}$ level has a Stark splitting of $\cong$200 cm^{-1},

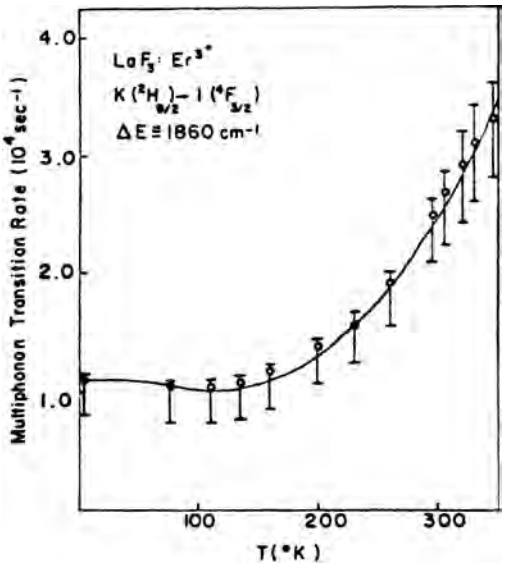

Figure 6.10 Temperature dependence of multipnonon relaxation transition rate in a $Er(^2H_{9/2} \rightarrow {}^4F_{3/2})$-doped LaF_3 crystal. The curve indicates the theoretical fit using Eq. (6.61). The error bars indicate absolute maximum error. (Reprinted from Ref. 9 with permission from the American Physical Society.)

with three nondecaying levels. Therefore, the theoretical fit will be of the form

$$W(T) = 1.1 \times 10^4 \left\{ \frac{\exp[(310)hc/kT]}{\exp[(310)hc/kT] - 1} \right\}^6 \left\{ 1 + 3\exp\left[(-200)\frac{hc}{kT} \right] \right\}^{-1}. \tag{6.63}$$

Finally, note that the possibility exists that several kinds of phonons participate in the multiphonon process. For the case of temperature-dependent, nonradiative decay from $^5F_4$, $^5S_2$ to $^5F_5$ with an energy gap of $\approx$2600 cm^{-1}, it was found that two kinds of phonon frequencies participate: three phonons of 650 cm^{-1} and two of 420 cm^{-1}.[17]

References

1. L. A. Riseberg and M. J. Weber, "Relaxation phenomena in rare-earth luminescence," *Progress in Optics* **XIV**, 89–159, North-Holland (1976).
2. R. Reisfeld, "Radiative and non-radiative transitions of rare-earth ions in glasses," in *Structure and Bonding* **22**, 123–175, Springer-Verlag, Berlin, Heidelberg, and New York (1975); see also Ref. 4, Chapter 2.
3. B. R. Judd, "Optical absorption intensities of rare earth ions," *Phys. Rev. B* **127**(3), 750–761 (1962).
4. G. S. Ofelt, "Intensities of crystal spectra of rare earth ions," *J. Chem. Phys*. **37**(3), 511–520 (1962).

5. C. B. Layne, W. H. Lowdermilk, and M. J. Weber, "Multiphonon relaxation of rare earth ions in oxide glasses," *Phys. Rev. B* **16**, 10–20 (1977).
6. G. H. Dieke, *Paramagnetic Resonance* **1**, 237, Academic Press, New York (1963).
7. A. Kaminskii, *Crystalline Lasers: Physical Processes and Operating Schemes*, CRC Press, Inc. (1996).
8. D. C. Brown, *High-Peak-Power Nd:Glass Laser Systems*, Springer-Verlag, Berlin, Heidelberg, and New York (1981).
9. L. A. Riseberg and H. W. Moos, "Multiphonon orbit-lattice relaxation of excited states of rare-earth ions in crystals," *Phys. Rev. B* **174**, 429–438 (1968).
10. C. B. Layne, W. H. Lowdermilk, and M. J. Weber, "Nonradiative relaxation of rare-earth ions in silicate laser glass," *IEEE J. Quantum Electron* **QE-11**, 798–799 (1975).
11. L. F. Johnson and H. J. Guggenheim, "Laser emission at 3 μm from Dy^{3+} in BaY_2F_8," *Appl. Phys. Lett.* **23**(2), 96–98 (1973).
12. T. Butta, A. M. Chardon, D. P. Shepherd, et al., "Low phonon energy, Nd:LaF_3 channel waveguide lasers fabricated by molecular beam epitaxy," *IEEE J. Quantum Electron* **37**(11), 1469–1477 (2001).
13. M. C. Nostrand, R. H. Page, S. A. Payne, et al., "Room temperature $CaGa_2S_4$:Dy^{3+} laser action at 2.43 μm and 4.31 μm and KPb_2Cl_5:Dy^{3+} laser action at 2.43 μm," *OSA Trends in Optics and Photonics (TOPS)* **26**, *Advanced Solid State Lasers*, 441–449 (1999).
14. F. Gan, *Laser Materials*, World Scientific, Singapore, New Jersey, London, and Hong Kong (1995).
15. M. C. Nostrand, R. H. Page, S. A. Payne, P. G. Schunemann, and L. I. Isaenko, "Laser demonstration of rare earth ions in low-phonon chloride and sulfide crystals," *OSA Trends in Optics and Photonics* **34**, *Advanced Solid State Lasers*, 459–463 (2000).
16. D. J. Coleman, S. D. Jackson, P. S. Golding, et al., "Heavy metal oxide and chalcogenide glasses as new hosts for Er^{3+} and Er^{3+}/Pr^{3+} mid-IR fiber lasers," *OSA Trends in Optics and Photonics (TOPS)* **34**, *Advanced Solid State Lasers*, 434–439 (2000).
17. R. Reisfeld and Y. Kalisky, "Analysis of 750 nm laser emission of Ho^{3+} in tellurite germanate and phosphate glasses," *Chem. Phys. Lett.* **75**, 443–447 (1980).

Chapter 8

Lasing Efficiency and Sensitization

8.1 Introduction

The following section will demonstrate the usefulness of sensitization in real systems, assuming dipole-dipole interaction. In particular, it will show how this phenomenon is utilized to both increase the lasing efficiency and decrease the threshold for laser action. It begins with an example of a laser system that is based on a combination of rare-earth and transition-metal ions, namely, a system codoped with Cr^{3+} and Tm^{3+} as sensitizers or energy donors and Ho^{3+} as an activator or energy acceptor. This subject was introduced in Chapter 5. A more detailed description that includes laser performance and pumping methods will be given in Chapter 9, which covers the 2-μm laser.

8.2 Why Is Energy Transfer Needed?

Holmium and thulium ions radiate over a wide spectral range from the visible to the mid-IR. The emission in the mid-IR, either coherent or incoherent, is a narrowband emission, and is centered around 2 μm. The exact emission peak depends slightly on the crystalline host. Since the electronic transitions in rare-earth ions, responsible for lasing, are partially allowed f-f transitions, one would expect smaller values for the oscillator strengths for the absorption lines of holmium (as well as other rare-earth ions). Also, the absorption lines of rare-earth ions, including the holmium ion, are narrow, which results in inefficient coupling between the absorption bands of a lasing medium and the emission lines of a pumping source such as a flashlamp or diode laser. This case is a classical example of the efficient utilization of energy sensitization. Hence, energy transfer is used to enhance the lasing efficiency of holmium- or thulium-based lasers emitting radiation in the spectral range of 1.8 to 2.1 μm. Mid-IR lasers, in the spectral range of 1.7 to 3 μm, based on rare-earth-doped ions, are useful light sources of both CW and pulsed free-running operation modes, as well as Q-switched or mode-locked configurations. Such systems can be singly-doped or codoped with other rare-earth ions (Tm^{3+}, Er^{3+}), or

with transition-metal ions such as Cr^{3+}. Sensitization of mid-IR emission is more efficient than in the visible, since the main channel for excitation depletion, e.g., the spontaneous emission rate of the sensitizer, is decreased with $1/\lambda^3$, which allows for energy accumulation in the upper states.

As stated above, the molecular system in which efficient energy transfer occurs involves crystals codoped with Cr:Tm:Ho (CTH), Er:Tm:Ho:YAG, or YLF (also known as $\alpha\beta Ho$:YAG or $\alpha\beta$Ho:YLF). The energy-level scheme of the CTH system is presented in Fig. 8.1.

The following properties of Cr^{3+} and Tm^{3+} are presently utilized as effective sensitizers:

1. Broadband absorption, owing to the fact that Cr^{3+} efficiently absorbs the emission of a conventional flashlamp.
2. Broadband and partially allowed emission of the Cr^{3+} ions, which overlaps well with the absorption bands of rare-earth ions such as Ho^{3+} and Tm^{3+}.
3. Cross-relaxation between two neighboring Tm^{3+} ions. This process leads to the creation of two excited Tm^{3+} ions with energy levels in resonance with the lasing level of Ho^{3+}.

It was reported a few years ago that a holmium laser in a CTH system is more efficient than the $\alpha\beta$Ho:YAG or $\alpha\beta$Ho:YLF system.[1] While the latter operated efficiently, both CW or pulsed, only at low or even cryogenic temperatures, the

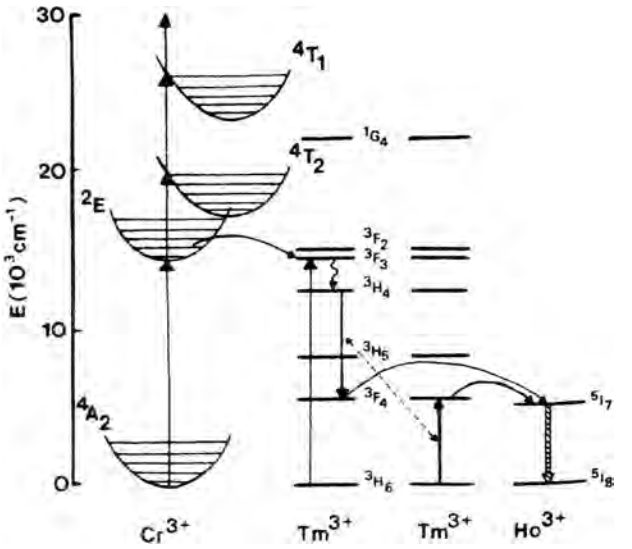

Figure 8.1 The energy-level and spectroscopic scheme of a crystalline system codoped with Cr^{3+}, Tm^{3+} and Ho^{3+} ions. The Cr^{3+} and Tm^{3+} are energy donors, while Ho^{3+} is the energy acceptor. The straight arrows indicate optical pumping, wavy arrows show nonradiative processes, dashed lines indicate cross-relaxation processes, and curved arrows show excitation transfer. (Reprinted from Ref. 22 with permission from the American Institute of Physics.)

CTH system operates efficiently even at ambient temperatures. Cryogenic conditions require special equipment and a constant supply of liquid nitrogen. These are obvious limitations in terms of flexibility, ease of use, size, and maintenance. However, these limitations do not apply in a CTH system, where a room-temperature operation is obtained easily. As indicated by Antipenko et al.,[1] the thermal load on the crystal is lowered due to an increase in pumping efficiency of the crystal. The quantum efficiency of the pumping band has values ranging from ≈0.7–1.1, depending on the measurement technique. This fact simplifies the operation of a holmium laser and makes it more appropriate for practical uses, which require a compact, efficient, easy-to-use and maintenance-free system.

8.2.1 Examples of CTH-doped systems

First, this text will examine several CTH systems as described in some publications. Kim et al.[2] analyzed the temperature dependence of 2.1 μm Ho^{3+} lasing in a Cr:Tm:Ho:YAG laser rod, in both free-running and Q-switched modes. Since their system was inefficient and unoptimized, lasing operation could be obtained only below 260 K. The normal mode operation of Ho (0.45 at. %):Tm (3.5 at. %):Cr (1.5 at. %):YAG as a function of the electrical input energy was carried out at various output couplers and at a temperature of 140 K. As expected, the slope efficiency and threshold energy increase, while the mirror reflectivity decreases (except for a mirror reflectivity of $R = 98\%$). It is also widely accepted that lowering the Tm^{3+} concentration will reduce the laser output energy so that any concentration in the range of 4.5 at. % to 6 at. % is a good choice. As an example, Kim et al.[2] showed that for 60-J electrical input energy, at 140 K, and with an output coupler of $R = 60\%$, there is a marked difference in 2.1-μm emission of holmium codoped with Tm^{3+} ions: for Tm (3.5 at. %), the output energy is ∼140-mJ/pulse, while for Tm^{3+} (2.5 at. %) it is only ∼100-mJ/pulse. Their observation of laser performance, namely, output energies and slope efficiencies, as a function of the operating temperature for various input energies shows a sharp decrease in laser performance with a temperature increase, similar to the results reported by Lotem et al. for Er:Tm:Ho:YAG and Er:Tm:Ho:YLF.[3] The dopant ion densities used for αβHo:YLF and αβHo:YAG are presented in Tables 8.1 and 8.2, respectively. The decrease of the laser output energy with the increase in temperature results directly from the thermal population of the upper Stark levels of the lasing ground level, as well as an increase of the upconversion processes that occur with the temperature increase. Upconversion causes lowering of the laser output energy, because

Table 8.1 Concentration of Cr^{3+} and rare-earth ions in YLF crystals.[3]

Concentration	Cr^{3+}	Er^{3+}	Tm^{3+}	Ho^{3+}	Host
at. %	–	30	10	0.3	YLF
ions/cm^3	–	4.2×10^{21}	1.4×10^{21}	4.2×10^{19}	YLF

Table 8.2 Concentration of Cr^{3+} and rare-earth ions in YAG crystals.[3, 6]

Concentration	Cr^{3+}	Er^{3+}	Tm^{3+}	Ho^{3+}	Host
at. %	1	–	5.76	0.36	YAG
ions/cm^3	2.3×10^{20}	–	8×10^{20}	5×10^{19}	YAG
ions/cm^3 (*)	7.7×10^{19}(**)	–	8×10^{20}	5×10^{19}	YAG

* Silver elliptical cavity yielded 5.1% slope efficiency at 300 K and 4.7% slope efficiency with a diffuse-reflecting cavity.
** Cr^{3+} concentration in at. %: 0.8 at. %.

it increases the upper-state losses. A possible upconversion mechanism in a Tm-Ho system is the depletion of $^5I_7$ level of Ho^{3+} to higher levels (such as $^5I_5$ or $^5F_2$, $^5S_2$) and subsequent transfer of the excitation into Tm^{3+} excited states. It is also possible to have upconversion in the CTH system, where high-lying levels of Tm^{3+} such as $^3H_5$, $^3F_3$, and $^3F_2$ are being excited.

8.3 Temperature Effects

The effect of temperature on laser efficiency and threshold is quite obvious. Since Ho^{3+} is a quasi-three-level system, it is necessary to cool the system to lower the lasing threshold. By cooling, one obtains a population of the lower Stark components of the $^5I_8$ level, and the system becomes quasi-4-level. However, one must consider the fact noted by Armagan et al.[4] pertaining to the temperature dependence of energy-transfer processes. According to Armagan et al., for a relatively high Tm^{3+} concentration, above 3.5% in CTH crystal, the Tm-Tm cross-relaxation rate between Tm^{3+} ground state ($^3H_4$) and Tm^{3+} excited state ($^3H_6$) manifolds dominates. Its rate decreases as the temperature increases, up to 200 K. Above 200 K, the cross-relaxation rates become approximately stable.

The concentration and temperature dependence of Tm-Tm cross-relaxation was further investigated by Armagan et al.[5] in Tm:YAG. Their results indicated that at 300 K the cross-relaxation rate of 6 at. % Tm was 1×10^{-6} s^{-1}, while for 0.75 at. % Tm^{3+} the rate was 100 times slower. Slight changes were observed at lower temperatures, even at 20 K. This phenomenon can be seen clearly in Fig. 8.2. There is an optimum value for the $^3H_4$ cross-relaxation rates for both Tm:YAG and Tm:YLF, and the rate in Tm:YLF is faster than in Tm:YAG. For example, at 300 K, the measured lifetime of $^3H_4$ level of Tm:YLF is $\approx$4.5 μs and that of Tm:YAG $\approx$11 μs. In the presence of Ho^{3+} (0.5 at. %), an energy transfer occurs from the $^3H_4$ level of Tm^{3+} to the $^5I_7$ level of Ho^{3+}. The efficiency of this transfer can be monitored by following the $^3H_4$ emission at 1.9 μm. The temporal response of the $^3H_4$ thulium level is much faster in YLF than in YAG because of the faster cross-relaxation in the Tm-Tm system and faster $Tm^{3+} \rightarrow Ho^{3+}$ energy transfer.

What happens to other processes in CTH crystal? The same authors found that the transfer rates of the $Cr^{3+} \rightarrow Tm^{3+}$ and $Tm^{3+} \rightarrow Ho^{3+}$ pairs have different temperature dependencies over a temperature range of 77–300 K. While the rate

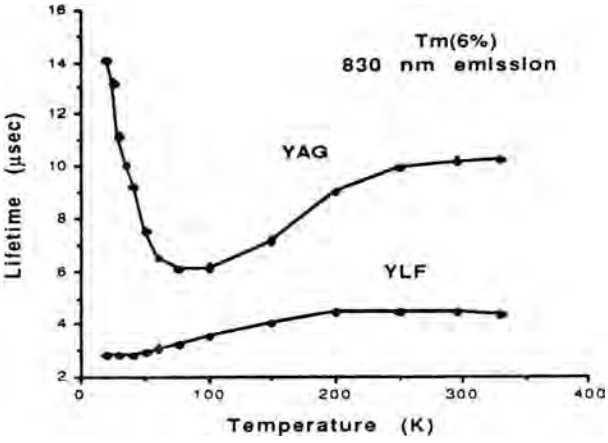

Figure 8.2 Temperature dependence of cross-relaxation rates among Tm (6 at. %) ions doped YAG and YLF. (Reprinted from Ref. 4 with permission from the Optical Society of America.)

of $Cr^{3+} \rightarrow Tm^{3+}$ energy transfer increases with temperature, the energy-transfer efficiency of $Tm^{3+}(^3F_4)$ manifold to $Ho^{3+}(^5I_7)$ manifold decreases. (The spectral overlap between Tm^{3+} emission and Ho^{3+} absorption decreases with the increase of the temperature.) The increase in the population density of Tm^{3+} ($^3F_4$) increases the probability of upconversion, which is concentration dependent. This implies that the slope efficiency and the output energy will follow the same temperature dependence pattern. The observation of a continuous decrease in laser performance with the increase in temperature above 200 K indicates that another loss mechanism is involved; namely, the upconversion process between Tm^{3+} ($^3F_4$ to $^3H_6$) and Ho^{3+} ($^5I_7$ to $^5I_5$). This is responsible for the constant decrease in laser performance. The continuous decrease in the slope efficiency and the increase in threshold energy as a function of temperature are not consistent with the behavior observed in $\alpha\beta$Ho:YLF and $\alpha\beta$Ho:YAG.[3]

Another interesting characteristic in the CTH crystal is the increase in threshold input energy as a function of the crystal temperature for various output coupling mirrors. Kim et al. explained the increase in threshold with the temperature as a combined effect of the ground state thermal population and the enhancement of the upper-level population loss, caused again by upconversion. Laser performance depends not only on the operating temperature but also on Tm^{3+} concentration, where the best results were obtained for a Tm^{3+} concentration of 4.5 at. %. However, one should analyze the results of Kim et al. with some caution since his laser system was not optimized. An attempt to optimize the dopant concentrations was carried out successfully by Quarles et al.,[6] who used a combination of dopants that are presented in Table 8.2.

The results of Quarles et al.[6] are quite impressive. In this work, they reported room-temperature operation of a pulsed holmium laser in YAG with slope efficiency of 5.1%. Others, such as Teichmann et al.,[7] reported slope efficiency of

3.3% and 17-J output energy. Excellent results were reported in other garnets: Alpat'ev et al. operated the Cr:Tm:Ho:YSGG (yttrium-scandium-gallium garnet) and obtained a slope efficiency of 3.1%.

Another interesting measurement made by Kim et al.[2] involved measuring the fluorescence of both 2.1 μm of Ho and 1.7 μm of Tm in a Ho:Tm (2.5 at. %):Cr:YAG as a function of temperature. Their results are presented in Fig. 8.3, which clearly shows that while the 2.1-μm fluorescence intensity decreases with temperature, the 1.7-μm emission intensity increases. This phenomenon indicates that the $^5I_7$ level is transferring its energy back to Tm^{3+} $^3F_4$ manifold. This will be discussed in the following sections.

8.4 The Effect of Tm^{3+} Concentration

Laser operation based on a CTH-doped YAG crystal depends partly on Tm^{3+} concentration because the thulium concentration controls both $Cr^{3+} \rightarrow Tm^{3+}$ energy transfer and $Tm^{3+} \rightarrow Tm^{3+}$ cross-relaxation between $^3H_4$ and $^3F_4$ manifolds. This is another example of practical use of the energy transfer phenomenon. The Cr → Tm energy-transfer rate increases with the increase of Tm^{3+} concentration at a constant temperature. As an example, the transfer rate for Cr^{3+} (1 at. %) and Tm^{3+} (2 at. %) at 300 K is 2.0×10^3 s^{-1}, while for Cr^{3+} (1 at. %), Tm^{3+} (5 at. %) the rate increases to 2.5×10^4 s^{-1}. Quarles et al.[6] estimated that the optimum Tm^{3+} concentration in a Tm:Ho:YAG for optimum room-temperature operation should be around 6 at. % or 8.3×10^{20} cm^{-3}. Bowman et al.[8, 9] reported the relatively efficient 2.1-μm, near-room-temperature operation of free-running and Q-switched CTH lasers using Cr^{3+} (0.8 at. %)-, Tm^{3+} (6 at. %)-, and Ho^{3+} (0.4 at. %)-doped YAG.

An optimized laser performance (free-running at normal modes) was obtained for a resonator of 29 cm long, with 80% reflective flat/flat output coupler and an ROC (radius of curvature) of 0.5 M concave back (high-reflectivity) mirror. The

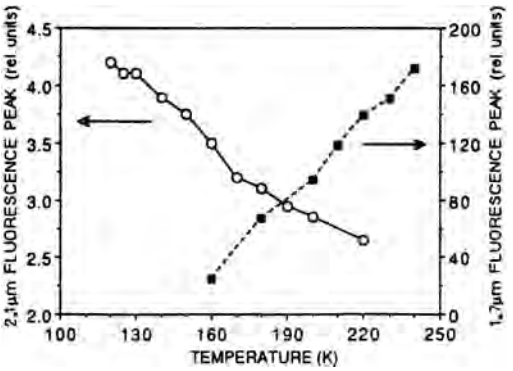

Figure 8.3 Temperature-dependent fluorescence emission at 2.1 μm (Ho^{3+}) and at 1.7 μm (Tm^{3+}) as a function of the crystal temperature at constant input energy. (Reprinted from Ref. 2 with permission from the Optical Society of America.)

laser emission was at 2.12 μm without any tuning elements, and the rods were all 5×67 mm, with flat AR coated faces. The maximum slope efficiencies of 3.7% and 3.6% were obtained for polished barrel laser rods, while lower efficiencies were obtained for ground finished barrels. This laser was also tuned continuously in the range 2.087 to 2.105 μm. In this system, Bowman et al.[8] observed a weak dependence of the slope efficiency on the output mirror reflectivities and the lasing wavelengths. On the other hand, the lasing threshold varied with the tuned emission wavelength. The blue-shifted emission required a higher threshold energy, while red-shifted emission was accompanied by relatively low threshold energy. The physical meaning of the blue-shifted and red-shifted emissions in Ho^{3+} are described schematically in Fig. 8.4.

This is explained by the fact that blue-shifted laser emission includes lasing to the ground thermally unpopulated levels; this requires higher pump energies. Another important issue is the effect of temperature on laser threshold energy and slope efficiency. The measurements were taken over a temperature range of $\pm 15°C$ around room temperature. As can be seen from Fig. 8.5, the laser threshold showed a roughly linear dependence on temperature, while slope efficiencies were found to be insensitive to temperature variations. Since the temperature range is small, these results do not represent a significant trend in holmium laser performance. However, in analyzing any temperature-dependent results in a CTH crystal, one must consider the fact that the thermal load in the CTH system is different from that of a YAG crystal since the thermal conductivities are different, and are 0.066 W/cm K and 0.13 W/cm K for CTH and YAG, respectively. In the Q-switched operating mode, short pulses with values in the range of 44–300 ns (FWHM) were obtained depending on the pumping power, which for a single short pulse contained only 30% of the energy available in the free-running mode.

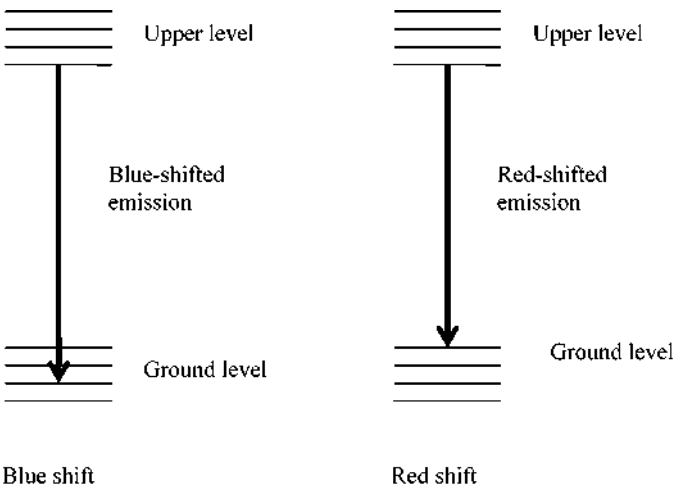

Figure 8.4 A simplified schematic description of blue- and red-shifted transitions in an atomic system.

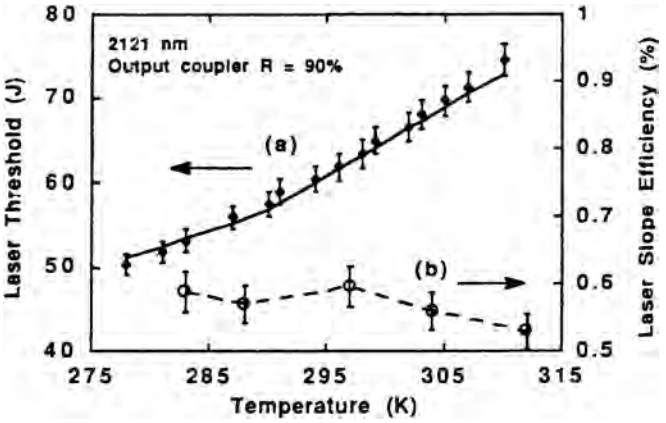

Figure 8.5 Temperature dependence of (a) laser threshold, and (b) slope efficiency, for the $^5I_7 \rightarrow {}^5I_8$ Ho^{3+} laser transition at 2.121 μm. (Reprinted from Ref. 8 with permission from the IEEE.)

The following processes, Cr → Tm, Tm → Tm → Tm, Tm → Ho energy transfer and the back transfer Ho → Tm, were investigated extensively in various garnets such as YSGG, GSAG, YAG, and others. The processes are important to the overall quantum efficiency in a CTH system, which is a product of six efficiencies:

1. Efficiency of ^2E because of the $^4A_2 \rightarrow {}^4T_2$, ^2E pumping process.
2. Energy-transfer efficiency $Cr^{3+}(^2E \rightarrow {}^4A_2) \rightarrow Tm^{3+}(^3H_6 \rightarrow {}^3H_4, {}^3F_3)$.
3. Fast energy migration among Tm^{3+} ions.
4. Cross-relaxation efficiency between adjacent ions: $Tm^{3+}(^3H_4) + Tm^{3+}(^3H_6) \rightarrow Tm^{3+}(^3F_4) + Tm^{3+}(^3F_4)$.
5. Energy transfer and thermalization between Tm and Ho levels: $Tm^{3+}(^3F_4 \rightarrow {}^3H_6) \rightarrow Ho^{3+}(^5I_8 \rightarrow {}^5I_7)$.
6. Laser emission: $^5I_7 \rightarrow {}^5I_8$ (≈2–2.1 μm) and thermalization between $^3F_4$ of Tm and $^5I_7$ of Ho levels.

The lossy processes that contribute to the heat load of the system are processes 1–3, while process 4 is very efficient. Process 5 is a near-resonant energy transfer, which is also efficient. However, it will be shown that energy transfer occurs efficiently only at an early time frame. It is followed by a relatively slow process of reversing the excitation energy from the energy acceptor back to the energy donor. In this text this process is called *back transfer*. Tm^{3+} ions interact efficiently as their ion density increases. This interaction is reflected by shortening the lifetime of the excited states. Armagan et al.[10] demonstrated the dependence of the decay rates of $^3H_4$ and $^3F_4$ levels of Tm^{3+} on the thulium ionic density. The sharp lifetime dependence on the concentration indicates very efficient cross-relaxation rates. Since all the decay curves were nonexponential, the lifetime was defined by the present authors as a normalized, integrated area under the decay curve. The measured lifetime of the $^3H_4$ level of Tm^{3+}, excited resonantly at 785.5 nm, is

shorter in YLF than in YAG. For example, using a doping level of 6 at. % Tm^{3+}, the $^3H_4$ lifetime was measured to be 10 μs and 5 μs for Tm:YAG and Tm:YLF, respectively. Both Cr → Tm and Tm → Tm interactions were found to be very efficient for Tm^{3+} densities (η_{Tm}) above 4×10^{20} cm^{-3} and for a fixed Cr^{3+} density of $\eta_{Cr} = 2 \times 10^{20}$ cm^{-3}. Generally, the Cr → Tm and Tm → Tm efficiencies at $\eta_{Tm} > 4 \times 10^{20}$ cm^{-3} were close to 90% and 100%, respectively. Assuming dipole-dipole interaction, the microparameter defined by Eq. (7.5) for the case of Tm-Tm cross-relaxation was found to be $C = 1.8 \times 10^{-39}$ cm^6/s.

8.5 The Effect of Cr^{3+} Concentration

Cr^{3+} density must be optimized for proper operation of a holmium laser based on the CTH crystal. Optimization is a compromise between two conflicting requirements: an increase in Cr^{3+} concentration provides an efficient absorption of the pumping light on the one hand, but on the other, lowering the Cr^{3+} concentration provides a uniform pump profile at the center of the laser rod, and therefore will produce reduced thermal-induced effects. Chromium-to-thulium energy-transfer efficiencies in a YAG crystal are very high over wide Cr^{3+} ion densities. Energy-transfer efficiencies vary from 98% to 95% for Cr^{3+} densities of 2.5×10^{20} cm^{-3} (2.7 at. %) and 0.46×10^{20} cm^{-3} (0.5 at. %), respectively. The Cr → Tm energy-transfer efficiencies, η, in YSGG are concentration dependent, with a value ranging from $\eta = 58\%$ for $n_{Cr} = 1$ at. % to $\eta = 93\%$ for $n_{Cr} = 2.9$ at. %. The optimum Cr^{3+} ion density was found to be 1 at. % or less. Experimentally, the laser operated efficiently with $n_{Cr} = 0.8$ at. % (7.7×10^{-19} cm^{-3}), similar to the experimental conditions of Bowman et al.[8]

8.6 Nature of Ionic Interaction

8.6.1 Cr-Tm interaction

This section will briefly analyze the spectroscopic data of the CTH system to understand the mechanism of energy transfer among the various ions participating in the excitation transfer. To help the reader follow the arguments, Fig. 8.6 shows the energy-level scheme and the pumping routes for the CTH system.

The process of the first step is a Cr → Tm energy transfer that was studied from the decay curve of Cr(^{2}E) by following the $^2E \rightarrow {}^4A_2$ transition. This decay is followed by Tm → Tm cross-relaxation and finally by Tm → Ho excitation transfer. All the relevant interactions are dipole-dipole. The Cr → Tm energy-transfer dependence on temperature variation has been found to result mainly from changes in the radiative transition probability of the chromium ion.[10] The excitation energy spreads over the Cr^{3+} system with a diffusion rate of 0.3×10^3 s^{-1} for Cr (2.0 at. %), Tm (1.5 at. %) at 270 K. The probability of the dipole-dipole Cr → Tm interaction, W_{SA}, is enhanced by the strong resonance between the Cr^{3+}

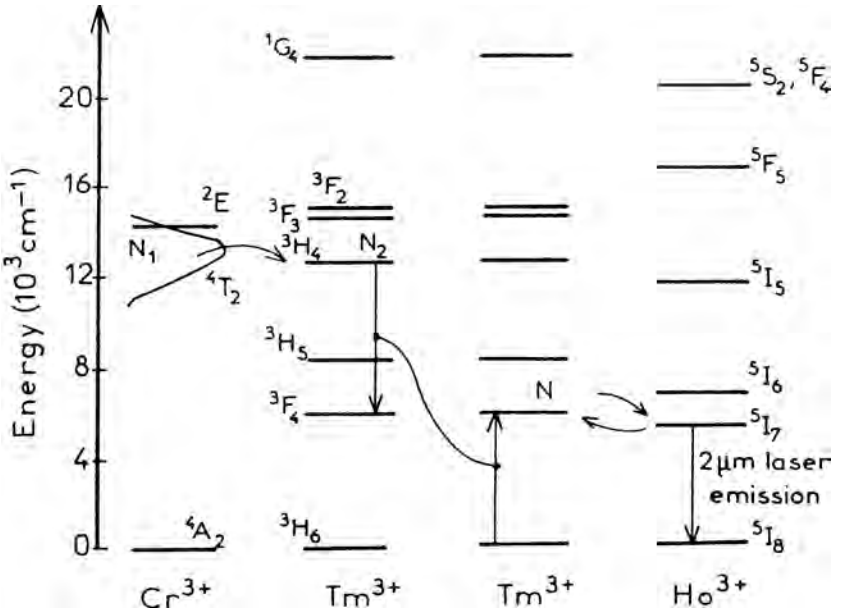

Figure 8.6 Energy levels and pumping routes for Cr^{3+}, Tm^{3+}, and Ho^{3+} in a CTH system. (Reprinted from Ref. 21 with permission from EDP Sciences).

($^2E \rightarrow {}^4A_2$) emission and the Tm^{3+} ($^3H_6 \rightarrow {}^3F_3$) absorption is given by Eq. (7.5) and is rewritten here for convenience:

$$W_{DA} = \frac{C_{DA}}{R^6}, \tag{8.1}$$

where C_{DA} is a microscopic dipole-dipole microparameter, which is proportional to the physical parameters typical of the ions participating in the interaction such as the overlap integral, and the natural lifetime of the energy donor. The $Cr(^2E) \rightarrow Tm(^3F_3)$ interaction was studied by following the kinetics of ^2E-level decay. This is a nonexponential decay, which reflects the statistical nature of the system, e.g., the fact that the energy acceptors are distributed randomly around energy donors. Assuming a dipole-dipole interaction, the microscopic interaction probability C_{DA} is calculated and found to be $C_{DA} = 1.2 \times 10^{-40}$ cm^6/s and 2×10^{-39} cm^6/s for YAG and YSAG, respectively. Others[11] provide the value for the microscopic interaction as $C_{DA} = 4.2 \times 10^{-39}$ cm^6/s^{-1} for $Cr \rightarrow Tm$ energy transfer in YAG. The values of C_{DA} for YSGG and GSAG are similar to that of YSAG reported above.

8.6.2 Tm-Tm interaction

Tm-Tm interaction is a cross-relaxation process in which one excited state of Tm^{3+} is converted into ions possessing two excited states of lower energies. More specifically, as shown in Fig. 8.7, the manifold $^3F_4$ excited state can decay to lower states

either radiatively or nonradiatively. Another pathway of energy migration occurs between adjacent ions—a cross-relaxation process that leads to two $^3H_4$ excited states. This process is equivalent to a spatial distribution among Tm^{3+} ions. The population of $^3H_4$ can be observed by following the fluorescence build-up of this level as a result of excitation to higher electronic levels in the Tm^{3+} manifold, or into the Cr^{3+} higher states. The population of the $^3H_4$ level in various garnets occurs on a time scale less than 100 μsec. The cross-relaxation efficiency (η) depends on Tm^{3+} concentration; for high enough Tm^{3+} doping densities, this cross-relaxation process is efficient and leads to a pump quantum efficiency of nearly 2. Table 8.3 provides the experimental and physical parameters of the cross-relaxation process: ion densities, microscopic dipole-dipole constants, and cross-relaxation rate constants for GSAG, YSGG, and YAG crystals.

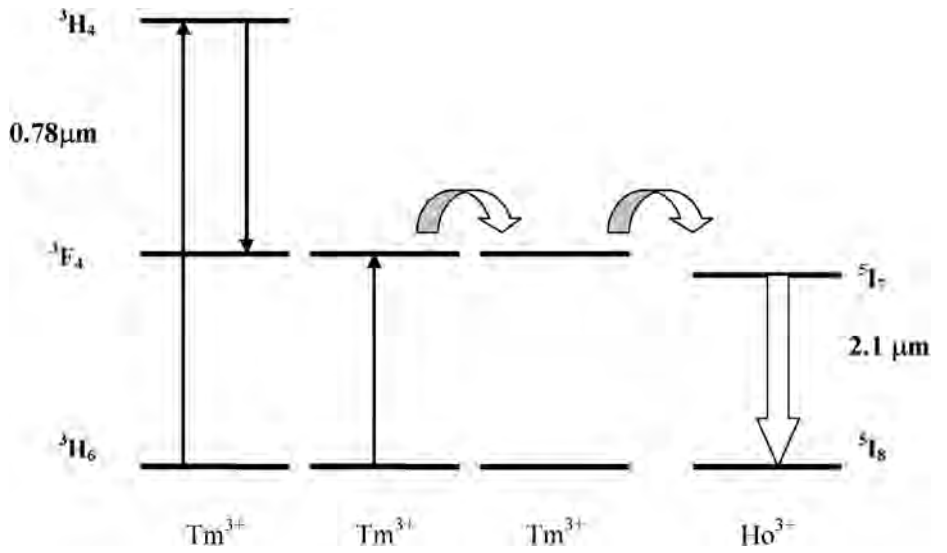

Figure 8.7 Energy-level diagram in a Tm:Ho:YAG system, illustrating the population of $^5I_7$ level of Ho^{3+} level via Tm-Tm cross-relaxation and energy migration, and Tm-Ho energy transfer. See text for more details on the cross-relaxation energy-transfer process.

Table 8.3 Experimental and physical parameters of Tm-Tm cross-relaxation. $K_{C.R.}$ is the cross-relaxation rate, C_{DA} is the microscopic interaction parameter, and η is the quantum efficiency of this process.

Host	Tm^{3+} density (cm^{-3})	Ho^{3+} density (cm^{-3})	C_{DA} (cm^6/s)	$K_{C.R.}$ (cm^3/s)	η
GSAG	1×10^{20} 20×10^{20}	0.1×10^{20}–0.5×10^{20}	1.1×10^{-39}	1.5×10^{-16}	1.68
YSGG	Same as GSAG	Same as GSAG	1.8×10^{-39}	2.5×10^{-16}	1.72
YAG	8.3×10^{20} 2.8×10^{20}	0.5×10^{20}		1×10^{-16}	≈2 1.6–1.77

The cross-relaxation between the Tm^{3+} ions is an efficient process that yields two excited Tm^{3+} ions according to the scheme $Tm^{3+}(^3H_6 \rightarrow {}^3H_4) \rightarrow Tm^{3+}(^3H_4 \rightarrow {}^3F_4)$, $Tm^{3+}(^3H_6 \rightarrow {}^3F_4)$ at rates that are indicated in Table 8.3 for various hosts. The fast cross-relaxation yields two Tm^{3+} ions in the $^3F_4$ metastable state for every ion that was initially excited into the $^3H_4$ Tm^{3+} electronic state. It is also worthwhile to note that as the Tm^{3+} concentration increases, the Tm-Tm cross-relaxation rate increases as well. Therefore, at higher Tm^{3+} concentrations, in the range of 8×10^{20} cm^{-3}, the cross-relaxation efficiency reaches a value of ≈2.

8.6.3 Tm-Ho interaction[12]

Ho^{3+} laser emission peaks at a wavelength of about 2.1 μm. This laser emission is obtained by excitation into Tm^{3+} manifold and subsequent Tm-Ho multipolar interaction and excitation transfer from $Tm(^3F_4)$ to $Ho(^5I_7)$. The rates of energy transfer from Tm to Ho and the back transfer from Ho to Tm are fast enough that these levels reach thermal equilibrium before the excitation has been used up. Figures 8.6 and 8.7 illustrate the dynamic processes in the CTH system and in the Tm:Ho:crystals.

The Tm-Ho energy transfer is a two-step process[13]: First, a fast spatial energy migration that occurs among the Tm^{3+} metastable level with a diffusion coefficient of $D = 4 \times 10^{-7}$ $cm^2\,s^{-1}$, or 43.5 ns average hopping time from ion to ion. A second process that follows the fast diffusion is a direct multipolar energy transfer and population of the $^5I_7$ level at a rate in the range of 2×10^{-16} cm^3/s to 5×10^{-16} cm^3/s (Refs. 12 and 14) for the same Tm^{3+} and Ho^{3+} densities presented in Table 8.3. This energy transfer is actually equivalent to the pumping process and consequently to the laser emission at 2.09 μm (for YAG) via $^5I_8 \rightarrow {}^5I_7$ transition. The Tm-Ho energy-transfer rate in YAG is smaller than the Tm-Tm cross-relaxation, which was measured by several authors as having a lowest value of 2.8×10^{-14} cm^2/s (Ref. 11). In fact, the Ho^{3+} emission can also be obtained by excitation to higher levels of Tm^{3+} ($^3H_4 \rightarrow {}^3H_6$, $^3H_4 \rightarrow {}^3H_5$) or by excitation into Cr^{3+} ($^4T_2$ level). The build-up of energy in $^5I_7$ level of Ho^{3+} is accomplished within an average time of 60–72 μs and is followed by an exponential decay of $\tau = 7.8$ ms.

The population of the thulium $^3F_4$ level in CTH:YAG is built up relatively quickly, in the μs time regime, and reaches its maximum after 1.8 μs. This build-up is followed by an exponential decay on a ms time scale, with a lifetime of $\tau = 7.2$ ms. The energy transfer from Tm^{3+} to Ho^{3+} $^5I_7$ level can be detected experimentally. For example, following the excitation of the $^3H_6 \rightarrow {}^3F_4$ transition (1.674 μm), a build-up of $^5I_7$ level of Ho^{3+} is observed on a time scale of ≈50 μs (measured at a time interval between 10% and 90% of the maximum amplitude). This build-up is followed by an exponential decay at 2.09 μm with a lifetime of $\tau = 7.8$ ms. It is interesting to note that the time evolution of Tm^{3+} ($^3F_4$) at 1.77 μm is faster than the build-up of Ho^{3+} ($^5I_7$) level at 2.09 μm. This is consistent with the high rates of the Tm-Tm cross-relaxation process relative to Tm-Ho

energy transfer. The fast build-up of $^3F_4$ level is followed by a long exponential decay (≈11.5 ms). This decay is on the same time scale as the $^5I_7$ build-up. This observation was further confirmed by following the time resolved spectra of both Tm($^3F_4$) and Ho($^5I_7$) after 300-μs time delay after the pumping pulse, where the Tm^{3+} spectrum almost disappeared and the Ho^{3+} spectrum peaked.[14] A similar phenomenon was observed in Tm-Ho pairs doped with other garnets (YSGG and GSAG) or other crystals. The Ho^{3+} build-up in YSGG crystal was accomplished within 80 μs and was followed by an exponential decay with a lifetime of ≈10–11 ms. Analysis of the interaction dynamics yielded the microscopic interaction microparameter C_{DA} for Tm → Ho energy transfer and Ho → Tm back transfer in YSGG,

$$C_{DA}(\text{Tm} \rightarrow \text{Ho}):\ 4.2 \times 10^{-40}\ \text{cm}^6\,\text{s}^{-1},$$
$$C_{DA}(\text{Ho} \rightarrow \text{Tm}):\ 3.5 \times 10^{-41}\ \text{cm}^6\,\text{s}^{-1}.$$

The mechanism of Tm → Ho interaction can be further elucidated by studying the well-known Er:Tm:Ho:YLF (αβHo:YLF) or Er:Tm:Ho:YAG (αβHo:YAG). This multistep sensitization has high quantum efficiency because of complex cross-relaxation processes among Er and Tm ions, which leads eventually to direct population of the $^5I_7$ manifold. Relevant information and references on this subject can be found in Ref. 15.

For Er:Tm:Ho:YLF (αβHo:YLF), it was found that excitation of the $^5I_7$ level of Ho^{3+}, excited via energy transfer from the $^3F_4$ level of Tm^{3+}, had a build-up duration (measured by the time interval from 10 to 90% of the maximum amplitude) of 44 μs. This build-up was again found to have an exponential waveform decay with a lifetime of $\tau = 6.8$–7.3 ms. The Tm^{3+} ($^3F_4$) showed a relatively fast build-up, with a value of 1.6 μs between 10 and 90% of the maximum amplitude. This build-up of Tm^{3+} ($^3F_4$) excitation was followed by an exponential decay of the $^3F_4$ level of Tm^{3+}, with $\tau = 6.4$ ms. The Tm^{3+} excitation in fluorides was also followed by energy transfer, which occurred rapidly.

8.6.4 Ho-Tm back interaction

The effective energy gap between Tm($^3F_4$) and Ho($^5I_7$) levels is ≈560 cm^{-1}. Therefore, the Tm → Ho transfer rate ($k_t = 2.0 \times 10^{-16}\ \text{cm}^3\,\text{s}^{-1}$) and the Ho → Tm back transfer ($k_{bt} = 2.6 \times 10^{-17}\ \text{cm}^3\,\text{s}^{-1}$) are fast enough, and thermal equilibrium is achieved easily after a certain time interval. The Tm → Ho transfer and back transfer are as efficient as the Tm-Tm cross-relaxation process. This can be seen from the transfer rates of the energy-transfer and cross-relaxation phenomena that are of the same order of magnitude, as shown in Table 8.3.

A close inspection at higher temporal resolution[12] and ambient temperature of Tm^{3+} ($^3F_4 \rightarrow {}^3H_6$) and Ho^{3+}($^5I_7 \rightarrow {}^5I_8$) decay curves in a Cr:Tm:Ho:YAG system reveals that Tm^{3+} decay is a combination of a relatively fast (≈100 μs) and

a slow (7–8 ms) component. The Ho^{3+} decay, on the other hand, is a single exponential decay (≈8 ms) with a build-up duration of the same order of magnitude as the Tm^{3+} "fast" component. Figures 8.8(a) and (b) show the faster component of Tm^{3+} decay and the build-up of holmium emission, respectively. The holmium emission was obtained by thulium ion excitation into a near resonant level via $^3H_6 \rightarrow {}^3H_5$ transition. Both results are displayed on a 20 μs/div time scale. The

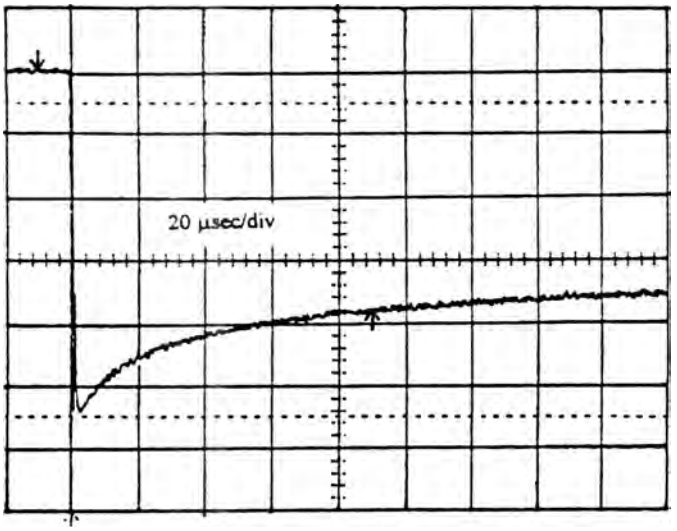

(a)

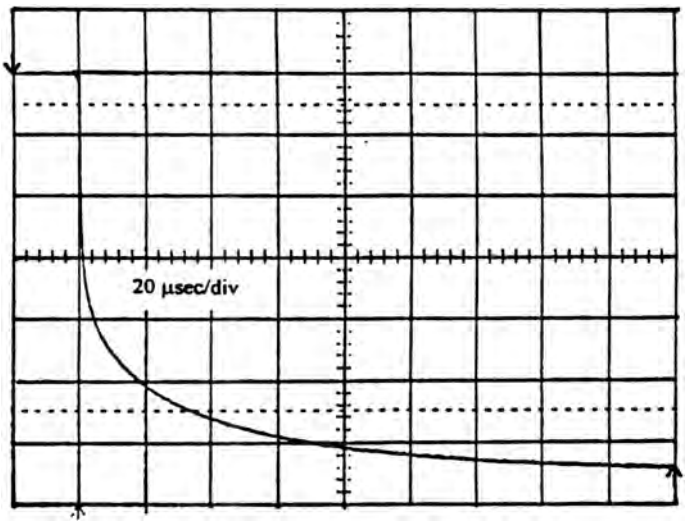

(b)

Figure 8.8 (a) A room temperature decay of Tm^{3+} ($^3F_4 \rightarrow {}^3H_6$) excited at 1.171 μm ($^3H_6 \rightarrow {}^3H_5$) transition; (b) a build-up of Ho^{3+} ($^5I_7 \rightarrow {}^5I_8$) emission at ambient temperature followed by Tm^{3+} excitation ($^3H_6 \rightarrow {}^3H_5$ transition). (Reprinted from Ref. 12.)

faster component of thulium decay is responsible for the energy transfer to the $^5I_7$ level of holmium, and this is reflected by the duration of the build-up, which is shown in Fig. 8.8(b). However, the longer component of thulium decay, with a lifetime comparable to that of holmium decay, results from the back transfer process. The same picture is observed in αβHo:YLF. Figure 8.9(a) displays the decay of

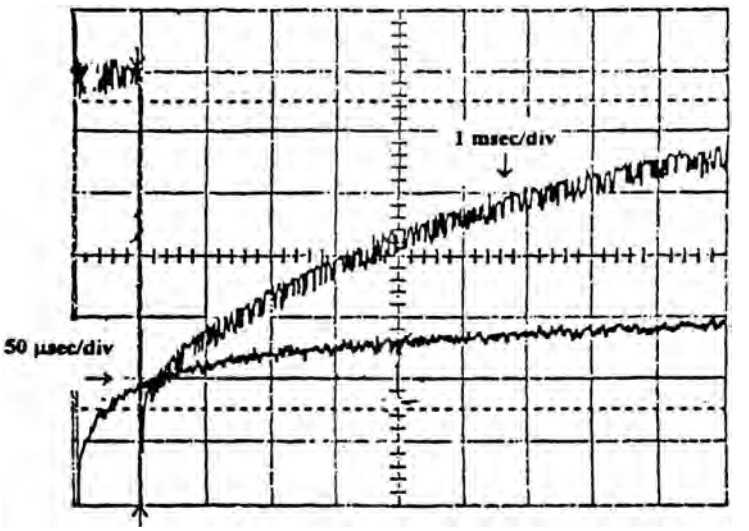

(a)

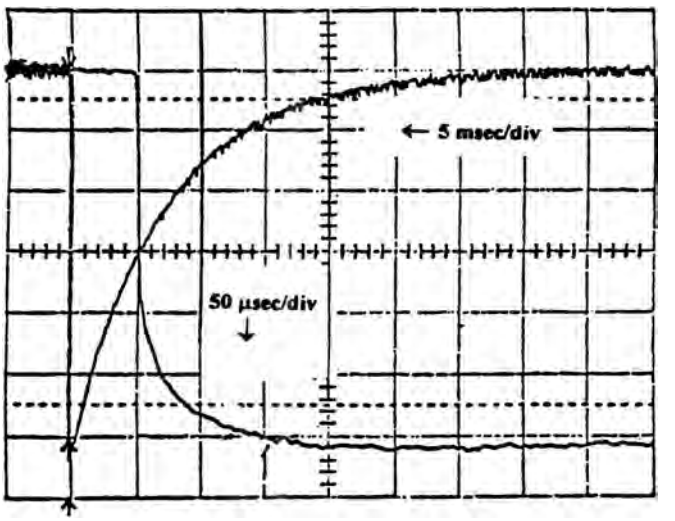

(b)

Figure 8.9 (a) A room-temperature decay of Tm^{3+} ($^3F_4 \rightarrow {}^3H_6$) excited at 1.171 μm ($^3H_6 \rightarrow {}^3H_5$) transition. Also displayed on the 1 ms/div time scale is the long-time component of the Tm^{3+} decay. (b) A build-up of Ho^{3+} ($^5I_7 \rightarrow {}^5I_8$) emission at ambient temperature followed by Tm^{3+} excitation ($^3H_6 \rightarrow {}^3H_5$ transition). Also displayed on the 5 ms/div time scale is the long-time component of Ho^{3+} ($^5I_7 \rightarrow {}^5I_8$) decay. (Reprinted from Ref. 12.)

Tm^{3+} ($^3F_4 \rightarrow {}^3H_6$) on a time scale showing both the fast and slow components of Tm^{3+} decay curves. The "fast" component is displayed in the same figure but on a 50 μs/div for clarity. This decay correlates well with the build-up of holmium emission $^5I_7 \rightarrow {}^5I_8$ transition, which is shown in Fig. 8.9(b), on the same temporal resolution, again at ambient temperature. The "long" component of the Tm^{3+} decay results from feedback—back transfer from Ho($^5I_8$) to Tm ($^3F_4$) levels.

To conclude the considerations of dynamical processes in a multiply-doped crystal, the thulium decay curve is nonexponential with fast and slow parts. The early time of the Tm^{3+} decay (at 1.77 μm) results from fast filling of the $^3F_4$ level, resulting from the Tm-Tm cross-relaxation process. This is followed by energy transfer to the Ho^{3+} $^5I_7$ level, which decays exponentially. The build-up of the $^5I_7$ level of Ho^{3+} is identical to the Tm^{3+} fast decay, while the rest of the waveform of the $^5I_7$ level is exponential with a lifetime of ≈8 ms. The long-duration part of the Tm^{3+} $^3F_4$ decay on a time scale of $t > 200$ μs is a result of thermalization and back transfer.[8, 16]

The multiply doped Cr:Er:Tm:Ho:YAG[17] crystal can be utilized to obtain a laser system that can be switched among several operating laser wavelengths. In particular, by changing the pumping pulse length it was possible to obtain laser emission of Er^{3+} at 2.9 μm (short pulse length, <200 μs), Ho^{3+} emission at 2.1 μm (long pulse length, >500 μs), or both wavelengths at an intermediate pulse length of the order of 350–500 μs. The laser produced ≈1.0 J of 2.1 μm and ≈0.5 J at ≈2.9 μm. The laser output energy of Ho^{3+} and Er^{3+} as a function of the electrical pumping energy is shown in Fig. 8.10.

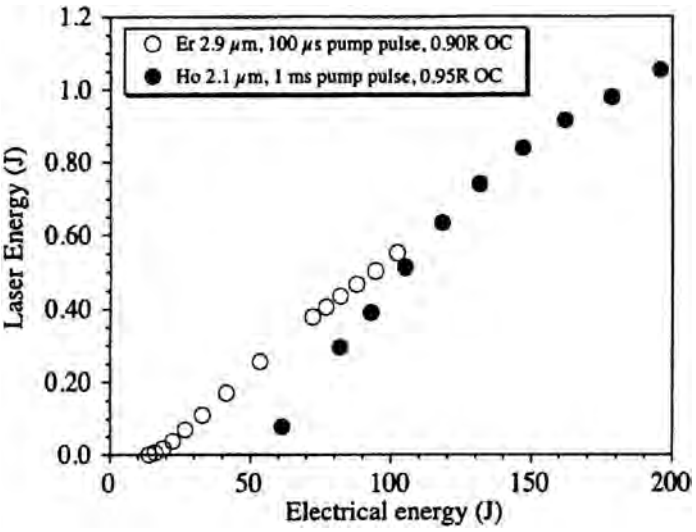

Figure 8.10 Laser energy as a function of electrical pumping energy for Ho^{3+} (2.1 μm) and Er^{3+} (2.9 μm) in Cr:Er:Tm:Ho:YAG laser crystal. (Reprinted from Ref. 17 with permission from the American Institute of Physics.)

8.6.5 Selective energy transfer

Cr^{3+} doped garnets such as GSGG ($Gd_3Sc_2Ga_3O_{12}$)[18] or YAG[19] exhibit multisite structure of Cr^{3+}, which leads to new absorption peaks in different garnets. For YAG, the new Cr^{3+} sites appear both in the absorption and excitation spectra, in the spectral range 685–690 nm, at low temperature.[19] The energy transfer is not an average interaction over the entire volume, but rather a physical process between subsites. This is clearly presented in Fig. 8.11 for a sample of Cr:Tm:Ho:YAG excited at 532 nm at 4.4 K.

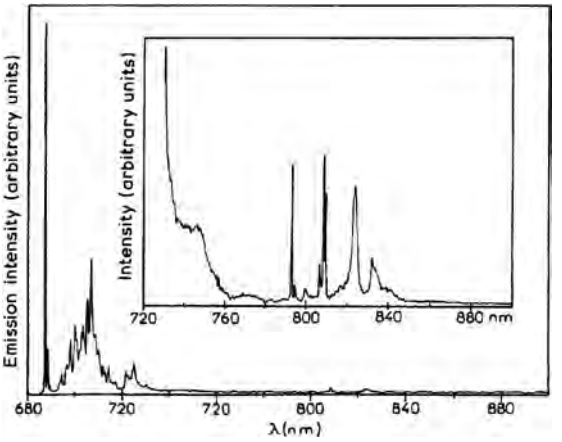

(a)

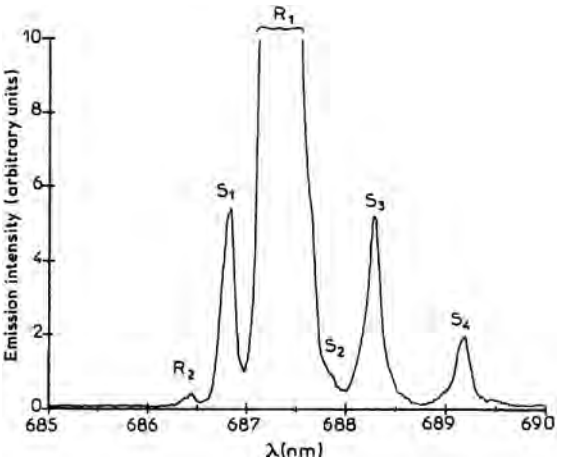

(b)

Figure 8.11 (a) Emission spectra of Cr:Tm:Ho:YAG at 4.4 K under 532-nm laser excitation. Inset: Tm^{3+} emission lines ($^3H_4 \rightarrow {}^3H_6$ transition) taken at 4.4 K under 532-nm excitation. (b) Emission spectra of Cr^{3+} in CTH:YAG at 4.4 K under 532-nm excitation, with five peaks resulting from nonequivalent sites. (Reprinted from Ref. 19 with permission from Springer Science and Business Media.)

The sites that appear in the Cr^{3+} emission lines are denoted by R and S as follows: S_1 (686.8 nm), S_2 (687.55 nm), S_3 (688.2 nm), S_4 (689.1 nm), R_1 (687.3 nm), and R_2 (686.4 nm). Also, unidentified sites are denoted by X_1 (687.0 nm) and X_2 (687.45 nm), and the Y site is attributed to a perturbed Cr^{3+} site owing to the presence of Tm^{3+} in its proximity. Y sites, located at 687.2 nm, will be assigned as paired (with a thulium ion) and R sites are assigned as the unpaired Cr^{3+}, with a thulium ion. Selective excitation into various S and R lines yields selective emission of Cr^{3+} sites, which sensitize Tm^{3+} selectively as well. Energy transfer occurs mainly from Y_1 and R sites to two Tm^{3+} sites, which can be detected by monitoring the Tm^{3+} emission at 806.6 nm and 809.8 nm.

The microscopic site structure and interionic interaction in a CTH crystal indicate that there are nonequivalent Cr^{3+} and Tm^{3+} sites in YAG. As discussed in Chapter 7, the theoretical model developed by Rotman et al.[20] assumes a correlation between the presence of energy donors and the spatial distribution of energy acceptors. The model presented in Ref. 20 is therefore an expansion of the Forster-Dexter and Inokuti-Hirayama standard assumption (denoted here as the "standard model" with a random distribution of acceptor ions around energy donors). In the modified model, multisite structure exists, and the acceptor distribution densities are affected by the donor ions. We can define regions of enhanced placement of acceptors. As observed in the case of Cr:Tm:Ho:YAG, there is a multisite structure with a correlation between Cr^{3+} and Tm^{3+} sites, which is reflected by their different spectral characteristics. The monitored Tm^{3+} emission peaks at 806.6 nm and 809.8 nm were attributed to Tm^{3+} being paired and unpaired, respectively, with Cr^{3+}. In other cases—namely, Tm^{3+} paired emissions via paired or unpaired Cr^{3+} pumping, or when Tm^{3+} emissions paired with Cr^{3+} ions are pumped—a strong correlation effect is observed.

References

1. B. M. Antipenko, A. S. Glebov, T. I. Kiseleva, and V. A. Pis'mennyi, "2.12 μm Ho:YAG laser," *Sov. Tech. Phys*. **11**(6), 284–285 (1985).
2. K. H. Kim, Y. S. Choi, N. P. Barnes, et al., "Investigation of 2.1-μm lasing properties of Ho:Tm:Cr:YAG crystals under flash-lamp pumping at various operating conditions," *Appl. Optics* **32**(12), 2066–2074 (1993).
3. H. Lotem, Y. Kalisky, J. Kagan, and D. Sagie, "A 2 μm holmium laser," *IEEE J. Quantun Electron* **24**, 1193–1200 (1988).
4. G. Armagan, A. M. Buoncristiani, A. T. Inge, and B. Di Bartolo, "Comparison of spectroscopic properties of Tm and Ho in YAG and YLF crystals," *Advanced Solid State Lasers* **10**, 166–168, OSA Proceedings Series (1991).
5. G. Armagan, A. M. Buoncristiani, and B. Di Bartolo, "Energy transfer and thermalization in YAG:Tm,Ho," *J. Luminescence* **48** & **49**, 171–174 (1991).
6. G. J. Quarles, A. Rosenbaum, I. D. Abella, C. L. Marquardt, and L. Esterowitz, "Efficient room temperature operation of Cr^{3+} sensitized, flashlamp-pumped, 2 μm lasers," *Opt. Quantum Electron* **22**, S 141–S 152 (1990); see also Ref. 1.

7. H. O. Teichmann, E. Duczynski, and G. Huber, "17 J Ho-laser at 2 microns," *SPIE Proc.* **1021**, 74–81 (1988).
8. S. R. Bowman, M. J. Winings, R. C. Y. Auyeung, et al., "Laser and spectral properties of Cr,Tm,Ho:YAG at 2.1 μm," *IEEE J. Quantum Electron.* **27**(9), 2142–2149 (1991).
9. S. R. Bowman, M. J. Winings, S. Searles, and B. J. Feldman, "Short pulsed 2.1 μm laser performance of Cr,Tm,Ho:YAG," *IEEE J. Quantum Electron.* **27**(5), 1129–1131 (1991).
10. G. Armagan, A. M. Buoncristiani, B. DiBartolo, et al., "Energy transfer processes among Cr, Tm, and Ho ions in yttrium aluminum garnet crystals," *Tunable Solid State Lasers* **5**, 222–226 (1989).
11. E. W. Duczynski, G. Huber, V. G. Ostroumov, and I. A. Shcherbakov, "CW double cross-pumping of the $^5I_7 \rightarrow {}^5I_8$ laser transition in Ho^{3+}-doped garnets," *Appl. Phys. Lett.* **48**(23), 1562–1563 (1986).
12. Y. Kalisky, S. R. Rotman, G. Boulon, C. Pedrini, and A. Brenier, "Spectroscopy properties, energy transfer dynamics, and laser performance of thulium holmium doped laser systems," *SPIE Proc.* **2138**, 5–16 (1994).
13. V. A. French and R. C. Powell, "Laser-induced grating measurements of energy migration in Tm:Ho:YAG," *Opt. Lett.* **16**(9), 666–668 (1991).
14. R. R. Petrin, M. G. Jani, R. C. Powell, and M. R. Kokta, "Spectral dynamics of laser pumped $Y_3Al_5O_{12}$:Tm,Ho lasers," *Opt. Mater.* **1**, 111–124 (1992).
15. I. T. Sorokina, "Crystalline mid-IR lasers," in *Solid State Mid-Infrared Laser Sources*, *Topics in Applied Physics*, 255–349, Springer-Verlag, Berlin and Heidelberg (2003).
16. G. Ozen and B. DiBartolo, "Energy transfer and thermalization in $LiYF_4$:Tm,Ho," *Appl. Phys. B* **70**, 189–193 (2000).
17. B. W. Walsh, K. E. Murray, and N. P. Barnes, "Cr:Er:Tm:Ho:yttrium aluminum garnet laser exhibiting dual wavelength lasing at 2.1 and 2.9 μm: Spectroscopy and laser performance," *J. Appl. Phys.* **91**(1), 11–17 (2003).
18. T. P. J. Han, M. A. Scott, F. Jacque, H. G. Gallagher, and B. Henderson, "Nd^{3+}-Cr^{3+} pairs in $Gd_3Sc_2Ga_3O_{12}$ garnet crystals," *Chem. Phys. Lett.* **208** (1,2), 63–67 (1993).
19. W. Nie, Y. Kalisky, C. Pedrini, A. Monteil, and G. Boulon, "Energy transfer from Cr^{3+} multisites to Tm^{3+} multisites in yttrium aluminum garnet," *Optical and Quantum Electronics* **22**, S123–S131 (1990).
20. See Chapter 7, especially Sec. 7.3.1.5, and Refs. 10 and 11 therein.
21. Y. Kalisky, J. Kagan, A. Brenier, C. Pedrini, and G. Boulon, "Spectroscopic properties and operation of pulsed holmium laser," *J. de Physique IV, Colloque C7*, supplement au *Journal de Physique III* **1**, 319–322 (1991).
22. G. Quarles, A. Rosenbaum, C. L. Marquardt, and L. Esterowitz, "High efficiency 2.09 μm flashlamp-pumped laser," *Appl. Phys. Lett.* **55**(11), 1062–1064 (1989).

Chapter 9

Two-Micron Lasers: Holmium- and Thulium-Doped Crystals

9.1 Introduction

Solid state lasers doped with Ho^{3+}, Tm^{3+}, or Er^{3+} have several important potential uses: medical applications,[1] eye-safe rangefinders, pump sources for OPO, light detection and ranging (LIDAR) applications,[2] wind velocity measurements,[3] and atmospheric measurements to monitor the health of our planet.[4]

Holmium lasers emit radiation around the 2-μm wavelength range, peaking at ~2.1 μm, resulting from the $^5I_7 \rightarrow {}^5I_8$ electronic transition. Stimulated emission in Ho^{3+}-doped $CaWO_4$ was first reported by Johnson et al.[5] Later, stimulated emission was obtained in singly doped Ho^{3+}glasses[6] (lithium-magnesium-aluminum silicate), with emission peaking at 2.08 um and operating at 77 K. In the latter case, the output pulses were associated with internal Q-switching, which depends on small amounts of added iron (Fe^{2+}). Also, laser emission at ~2.1 μm in a $Ho^{3+}-$doped single crystal of HoF_3 at 77 K was obtained.[7] The cavity in this case was an elliptical cylinder and the threshold energy of ~1-J/pulse. The laser transition terminal level was assigned to the highest Stark energy levels of the $^5I_8$ ground state. This J level is located at 532 cm^{-1}, relative to the lowest-energy J-Stark component. It is worthwhile to note that this system is relatively efficient despite the three-level nature of the holmium laser because of the efficient cooling of the crystal. By cooling, the high-energy-lying Stark components are depopulated and population inversion can be easily achieved.

Another way to increase the population inversion and hence lasing efficiency in the holmium lasing system is to use energy transfer from efficient absorbers to the $^5I_7$ lasing level of Ho^{3+}. This will be discussed further in this chapter. The first experiments that utilized energy transfer were conducted by Johnson et al.[8] by codoping Ho^{3+} with Yb^{3+}, Tm^{3+}, and Er^{3+} ions in YAG. The laser operated at 77 K to enhance its efficiency. Output power obtained was 7.6 W at a wavelength of 2.12 μm, while the input power was 550 W. The optical transitions of Ho^{3+}cover only 11% of the spectral region of 0.6 to 2 μm. Codoping with Er, Yb,

and Tm provides an extension of up to 89% of this spectral range. A blackbody, tungsten-halogen source served as the CW pumping source. At the temperature of 3000 K, its spectral distribution lies in the 0.6–2 μm region and results in a pumping efficiency of 62%. If one assumes nonradiative losses, the maximum expected efficiency of the system is 30%.[8] Further improvement in holmium laser performance was achieved when holmium was doped in a crystal with low nonradiative losses. An example is $YLiF_4$ (YLF), discussed in Chapter 5. Laser experiments in Er:Tm:Ho:$YliF_4$ ($\alpha\beta$Ho:YLF) were performed by Chicklis et al.[9] This system had several fundamental advantages that led to efficient pumping. Holmium was codoped with Tm^{3+} and Er^{3+}, used as efficient energy sensitizers. The crystalline host had lower nonradiative losses compared with oxide crystals; the laser was operated in a pulsed mode. Pulsed-mode operation prevented the accumulation of heat in the laser rod by allowing thermal relaxation (depending on the repetition rate), thereby minimizing the thermal load on the crystal. As a result of these advantages, the 2.1-μm holmium laser emission was observed at room temperature. Chicklis et al.[9] reported a maximum output energy of 400 mJ/pulse with 1.3% slope efficiency in a free-running mode, and 2% slope efficiency in a Q-switched mode. Another important fluoride crystal is Ho^{3+} doped in a $BaYb_2F_8$ crystal.[10, 11] Antipenko et al.[10] calculated the oscillator strengths and radiative transition probabilities of various electronic levels of Ho:$BaYb_2F_8$, including the $^5I_7 \rightarrow {}^5I_8$ transition of Ho^{3+}. Table 9.1 presents some spectroscopic data relevant to the $Ho^{3+}{}^5I_7 \rightarrow {}^5I_8$ lasing transition at $\lambda \cong 2$ μm for $BaYb_2F_8$,[10] $YLiF_4$,[12] $YAlO_3$, and YAG[13] laser crystals.

As noted by Johnson et al.,[11] $BaYb_2F_8$, like other fluorides such as YLF or LaF_3, has low phonon energies, and the orbital coupling of the ion to the lattice is relatively weak. These characteristics permit longer fluorescence lifetimes and higher stimulated transitions among a variety of excited states.

An overall historical summary of the laser system based on Ho^{3+} codoped with $Tm^{3+}$and Er^{3+} ions is presented briefly in Refs. 15, 16, and 17.

Table 9.1 Oscillator strength (f), radiative transition rates (A), and stimulated emission cross section at ≈2 μm (σ_{em}), in holmium-doped fluorides for the $^5I_7 \rightarrow {}^5I_8$ transition (the data relates to electric-dipole transitions only). The data for oxide crystals are presented for comparison.

Host	λ_{em} (nm)	$f \times 10^6$	A (sec^{-1})	σ_{em} (cm^2) (at 295 K)
$BaYb_2F_8$	2.05	1.67 [Ref. 10]	73 [Ref. 10]	0.78×10^{-19} [Ref. 10]
YLF	2.06	1.12 [Ref. 12]	70 [Ref. 13]	$1.4 \times 10 - 19$ [Ref. 14]
		1.28 [Ref. 12]	59 [Ref. 12]	$1.12 \times 10 - 19$ [Ref. 12]
YAG	2.09		145 [Ref. 13]	1.3×10^{-20} [Ref. 13]
				2×10^{-19} [Ref. 14]
$YAlO_3$	2.05	1.28	143 [Ref. 13]	1.1×10^{-20} [Ref. 13]

9.2 Advantages of the Holmium Laser

A significant advantage of the holmium laser is its high-gain cross section and the long lifetime of the $^5I_7$ (7–14 ms) upper laser level, which results in high energy-storage capability and efficient Q-switched operation. The special characteristics of a Ho^{3+}-doped solid matrix, especially when the holmium is codoped with $Er^{3+}$and Tm^{3+} or with Cr^{3+} and Tm^{3+}, have motivated extensive research on CW and pulsed holmium laser operation, as well as spectroscopic studies of several holmium-doped host materials, with an emphasis on YLF and YAG. A few aspects of the subject, mainly those relevant to $\alpha\beta$Ho-doped hosts, were summarized long ago.[18] Both thulium and holmium are quasi-three-level laser systems at room temperature. The lower $^5I_8$ ground state of holmium has Stark components over a 300–500 cm^{-1} energy domain. When cooled, the lower $^5I_8$ Stark levels are populated and the molecular system becomes a quasi-four-level system. Therefore, it is expected to obtain an efficient laser emission of the holmium ion at low temperatures.

Despite the fact that lasers based on both thulium and holmium ions are of a quasi-three-level nature, Ho^{3+} is a better laser candidate than Tm^{3+}, mainly because Tm^{3+} has a lower emission cross section than Ho^{3+}, e.g., $\sigma_{em}(Tm^{3+}) = 0.25 \times 10^{-20}$ cm^2 and $\sigma_{em}(Ho^{3+}) = 1.2 \times 10^{-20}$ cm^2, respectively, in YAG.[13] The measured emission lifetimes of the lasing levels of thulium ($^3F_4$) and holmium ($^5I_7$) are 5 ms and 8.1 ms, respectively, and hence the ratio of the product $\sigma_{em} \cdot \tau$ for holmium and thulium is $\approx$7.7. Additionally, upconversion losses in holmium are much smaller than in thulium, which leads to a much longer effective lifetime of the holmium $^5I_7$ lasing level compared to the thulium $^3H_6$ level. In order to reach threshold, the pump intensity in thulium should be high; this leads to thermally induced aberrations and birefringence.

9.2.1 Utilizing energy transfer

Codoping Ho^{3+} with Tm^{3+} and Er^{3+} in YAG or YLF ($\alpha\beta$Ho:YAG or $\alpha\beta$Ho:YLF, respectively) leads to efficient (6.5% slope efficiency) laser operation.[19] This is explained as a result of energy transfer from high energy levels of Er^{3+} to the $^3H_4$ level of Tm^{3+} and then, by triple cross-relaxation, to the $^5I_7$ electronic level of Ho^{3+}. An alternate way to improve holmium laser efficiency at 2.1 μm was suggested by Antipenko et al.[20, 21] and discussed in Chapter 8. This will be briefly reviewed for clarity. They suggested codoping Ho^{3+} with Tm^{3+} and Cr^{3+}. As a result of this ionic combination, a significant part of the flashlamp pumping light is absorbed efficiently by the broadband, electronically allowed transitions in Cr^{3+}(the $^4T_2$ and $^4T_1$ levels), which is then transferred efficiently to the $^3H_4$ level of Tm^{3+}, and then, by double cross-relaxation, is transferred to the $^5I_7$ electronic level of holmium. The process is described schematically in Fig. 9.1.

When higher repetition rates are required, a cooling system must be used to eliminate thermal effects in the lasing crystal and maintain a good beam quality. In these cases, the use of the YLF crystal as a host is favorable because of

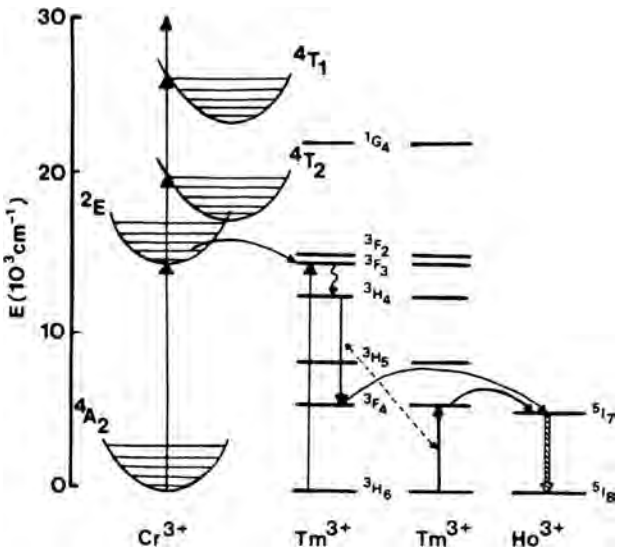

Figure 9.1 Schematic description of the energy sensitization of 2.1-μm Ho^{3+} laser emission with Cr-Tm energy transfer, Tm-Tm cross-relaxation, and Tm-Ho energy transfer. (Reprinted from Ref. 39 with permission from the American Institute of Physics.)

its negative change of refraction index with temperature. The YLF-doped crystals have additional advantages, which make the holmium-doped YLF a favorable laser host. YLF is characterized by low phonon energies that result in low nonradiative rates and low UV absorption, which minimize the formation of color centers. See Tables 4.1 and 4.2 for more details.

Holmium laser emission at ~2.1 μm can be achieved by two methods:

1. Conventional lamp pumping scheme, using a flashlamp or CW source to produce pulsed or CW laser operation.
2. Diode pumping scheme.

9.3 Conventional Pumping

9.3.1 CW laser operation

The nature of the 2-μm Ho^{3+} laser level structure requires cryogenic cooling in order to obtain population inversion and efficient CW laser operation. Beck and Gurs[19] operated a Ho:YAG laser successfully. It was cryogenically cooled with 50-W output power and 6.5% slope efficiency; and 60-W output power with 4.7% slope efficiency was reported later by Lotem et al.,[22] using αβHo:YLF with a nominal concentration of holmium ion of 0.1 at. %.

A systematic comparison between YAG and YLF[14, 18] reveals that for systems designed for a high average output power (≈40 W), the two host crystals may perform similarly. In such systems, if the maximum laser power is not the important

issue, the YAG is a better choice owing to its availability and superior mechanical properties. In cases where linearly polarized laser radiation is required, YLF would be the appropriate choice.

Laser parameters such as the stimulated emission cross section, round-trip loss, and population inversion at threshold were calculated[14] using Findley-Clay analysis for a CW holmium laser. The value of the stimulated emission cross section for Ho:YLF is $\sigma_{em} = 1.4 \times 10^{-19}$ cm^2, while that for YAG is $\sigma_{em} = 2 \times 10^{-19}$ cm^2 (see data in Table 9.1). The population inversion densities at threshold were calculated for both crystals and found to be very similar for $\alpha\beta$Ho:YAG and $\alpha\beta$Ho:YLF, namely, $(N_2 - N_1)_{th} \cong 1.6 \times 10^{17}$ cm^{-3}.

The thermal effect on the laser rod is an important parameter that may cause beam quality degradation and laser rod fracture. It was found that the net heat dissipation while lasing at a pumping level of 1500 W (lamp input power) was 17.4 W/cm and 19.4 W/cm for $\alpha\beta$Ho:YLF and $\alpha\beta$Ho:YAG laser rods, respectively. This thermal load is within the theoretical fracture ranges for YAG and YLF, which are, at room temperature, 60 W/cm and 11 W/cm, respectively.

The laser setup for CW operation of a cryogenically cooled holmium laser has been described by several authors and summarized in Refs. 18, 19, and 22. As stated previously, the $^5I_7 \rightarrow {}^5I_8$ transition of a holmium laser is a three-level system at room temperature. This requires cryogenic cooling in order to obtain efficient CW laser operation. The laser rod is usually cooled by a massive fast flow of liquid nitrogen (7 liter/min) at a pressure range of 2–3 atm. The laser head used in various experiments is a water-cooled, gold-plated elliptical reflector. The elliptical cavity[18, 19] is almost circular to promote low order modes. See Fig. 9.2 for a schematic description of the water-cooled elliptical laser head reflector. The CW pumping is achieved by using a linear, air-cooled tungsten-halogen lamp with a nominal electrical power of 1000 W or 1500 W. In order to achieve thermal insulation, the laser head chamber is evacuated.

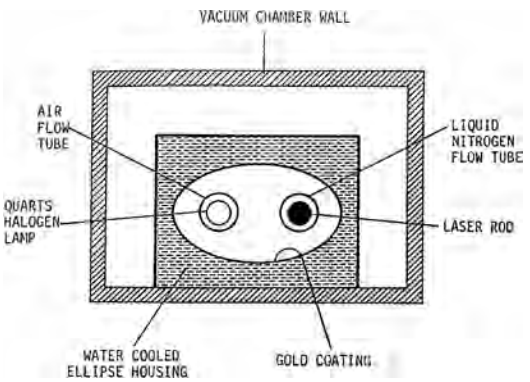

Figure 9.2 Schematic description of the water-cooled, elliptical reflector laser head. (Reprinted from Ref. 18 with permission from the IEEE.)

9.3.2 Pulsed operation of holmium lasers

Pulsed flashlamp operation of the holmium laser is essential for reducing the thermal load on the laser rod. It was found[18] that the optimal performance of αβHo:YLF or αβHo:YAG was around 150–160 K, where the maximum slope efficiency could be obtained. The value of the threshold energy increased steadily with an increase in temperature without any maximum value.

Laser crystals such as αβHo:YAG, αβHo:YLF, Cr:Tm:Ho:YAG (CTH:YAG), CTH:GSGG, CTH:GSAG, or Cr:Tm:Ho:YSGG have high quantum efficiency and low thermal load owing to cross-relaxation processes, and have been operated successfully at ambient temperatures with large values of energy per pulse. For example, the αβHo crystals performed well at $T \approx 290$ K with an output energy of 2.5 J/pulse, an efficiency of 0.8%, and a threshold pump energy of ≈100 J. The CTH crystals of Ho^{3+} codoped with Cr^{3+} produced up to 1.4 J/pulse with 0.75% slope efficiency at room temperature,[20] or even higher slope efficiency (2.9%) in an optimized system.[23] These crystals absorb the visible part of the pumping light and convert it efficiently into a population inversion, as explained earlier, and as can be seen from Fig. 9.1.

9.4 Diode Pumping

9.4.1 End-pumped 2-μm lasers

Diode pumping of 2-μm lasers is achieved in the codoped Tm:Ho:YAG or YLF system with an efficiency as high as 70%, much larger than the 39% maximum value expected from the quantum defect of the atomic system. More information as to the Tm^{3+}, Ho^{3+}-doped laser crystals and their performance can be found in Ref. 17. A holmium 2.1-μm laser emission from diode-pumped Ho:YLF crystals was first reported to operate at 77 K. However, with the advent of stable, high-power diode arrays and optical coupling systems such as fiber coupling, microlenses or lens ducts, it has become possible to pump the Tm^{3+} and the Ho^{3+} ions efficiently even at ambient temperatures. The pumping scheme is much simpler than that of a flashlamp, utilizing direct pumping into the Tm^{3+} ions at 780–800 nm. The excited Tm^{3+} ions sensitize the holmium ions to operate at the $^5I_7 \rightarrow {}^5I_8$ transition. The spectroscopic scheme in Tm:Ho:YAG is illustrated in Fig. 9.3.

It should be noted that the Cr^{3+} ion, codoped with Tm^{3+} and Ho^{3+} ions, does not play an active role in diode pumping. However, its presence allows us to obtain 2-μm lasing with pump sources that have broadbands in the visible or UV spectral range. It also allows the use of a visible laser source such as Kr^+ laser, or a dye laser such as rhodamine 6G, on using the laser dye. The pumping scheme using a Kr^+ laser, which was performed via Cr^{3+} ($^4T_2$ or $^4T_1$ levels), is inefficient and yielded output power of only ≈60 mW, with 13% slope efficiency. The laser performance is presented in Fig. 9.4.[25]

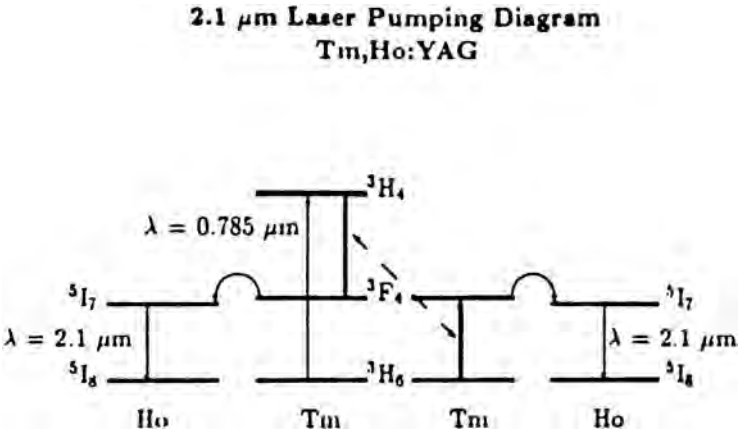

Figure 9.3 Pumping scheme of Tm, Ho:YAG. In some descriptions the $^3H_4$ and $^3F_4$ energy positions are reversed; currently, it is widely accepted that $^3F_4$ is lower than the $^3H_4$ level. (Reprinted from Ref. 24.)

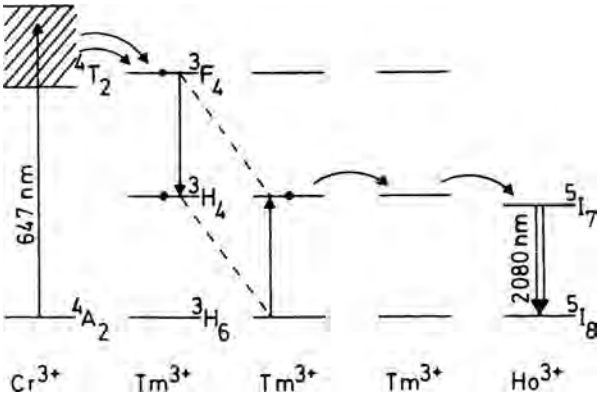

Figure 9.4 A pumping scheme of the 2.1-μm Ho^{3+} laser with Cr-Tm energy-transfer scheme in a YSGG laser crystal. The holmium ion was pumped with a krypton ion laser. (Reprinted from Ref. 25 with permission from the American Institute of Physics.)

At high concentrations, usually above 3 at. % of Tm^{3+}, cross-relaxation between two Tm^{3+} ions is responsible for the depletion of the $^3H_4$ level. The cross-relaxation process provides two excited Tm^{3+} in the $^3F_4$ state for every 785-nm pump photon. Theoretically, the quantum efficiency of such a process is 2. Schematically, the cross-relaxation process can be described as follows:

$$Tm(^3H_4 \rightarrow {}^3F_4) \rightarrow Tm(^3H_6 \rightarrow {}^3F_4)$$

or

$$Tm(^3H_4,{}^3H_6) \rightarrow Tm(^3F_4,{}^3F_4).$$

This efficient double cross-relaxation is associated with a fast spatial energy migration among Tm^{3+} ions, subsequent energy transfer to the $^5I_7$ level of Ho^{3+}, and finally laser emission via the $Ho^{3+}{}^5I_7 \rightarrow {}^5I_8$ transition. The energy transfer from $Tm^{3+}(^3F_4)$ to $Ho^{3+}(^5I_7)$ occurs in both directions, energy transfer and back transfer, which leads to thermal equilibrium between the Tm^{3+} ions in the $^3F_4$ manifold and the Ho^{3+} ions in the $^5I_7$ spectral manifold. This temperature-dependent energy transfer is a phonon-assisted interaction type.[26]

The $^3H_4$ manifold of Tm^{3+} is pumped by the AlGaAs diode laser at 780–790 nm. Direct pumping into the $^3F_4$ level of Tm^{3+} or $^5I_7$ level of Ho^{3+} at 1.9 μm is possible with an output power of 0.7 W and 35% slope efficiency (relative to the absorbed power) at a temperature of $-53°C$, at 2.1 μm, using 4 at. % doping level of Ho^{3+}. Owing to the low Stokes shift for direct pumping of Ho^{3+} at 1.9 to 2 μm, the quantum defect heating is $<10\%$ of the absorbed pumping power. Therefore, a reduction in the thermal load is obtained, allowing operation of the laser at high temperatures up to 60°C. Direct pumping of Ho:YLF by a diode-pumped Tm:YLF laser at 1.9 μm yielded both CW and pulsed output operation of Ho:YLF with 20-W average output power at 2 μm, beam quality of $M^2 \approx 1.45$, and a 10–20 kHz repetition rate.[27] A similar technique was used by Hayward et al.[28] in the case of Ho:YAG pumped by a Tm:YAG laser at 2.013 μm. The Tm:YAG yielded 17.5 W of 2.013-μm emission, which was then utilized to pump the Ho:YAG. The maximum output power of Ho:YAG at 2.097 μm, obtained by the direct-pumping method, was 7.2 W for ≈53-W incident diode-pumping power (17.5% slope efficiency), with beam quality factor of $M^2 \approx 5–6$.

Using Tm:Ho:YLF, it is possible to obtain cascade laser emission at both 2.06 μm and 2.31 μm because of the lower nonradiative losses in rare-earth-doped YLF relative to other oxide hosts. For the 790-nm pumping, the ground state $^3H_6$ absorbs one photon at 790 nm into the $^3H_4$ level (Fig. 9.5). The emission wavelength is controlled by the dopant concentration, laser pumping scheme, or pumping rates. At low Tm^{3+} ion density (<2 at. %), where ion-ion interactions are small, the $^3H_4$ level decays to the $^3F_4$ level radiatively or nonradiatively via a multiphonon process, which then subsequently transfers its energy from the $^3F_4$ state

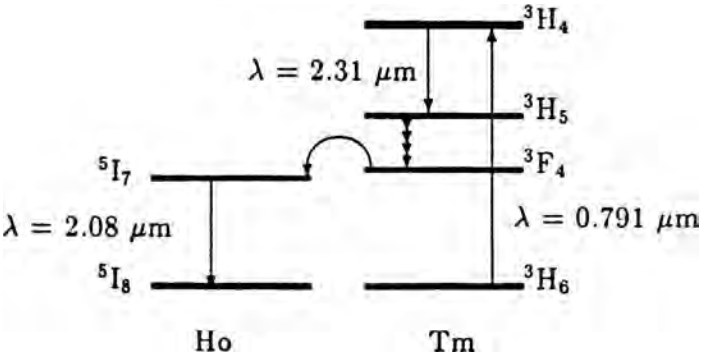

Figure 9.5 Pumping diagram for cascade laser emission in Tm:Ho:YLF. (Reprinted from Ref. 24.)

into the $^5I_7$ level of holmium. At a low pumping rate of the $^3H_4$ level, the dominant process is a nonradiative multiphonon decay into the $^3F_4$ state of Tm^{3+} ion, with subsequent energy transfer to the $Ho^{3+}{}^3H_4 \rightarrow {}^3H_5$ ($\lambda = 2.31$ μm) transition in Tm^{3+}, and cascade emission, which involves two different ions.

This figure shows that the terminal $^3H_5$ transition decays nonradiatively to the $^3F_4$ state, which then transfers its energy to the neighboring $^5I_7$ level of holmium. This cascade operation produces a change in the slope efficiency when a Tm^{3+} laser is operated, resulting from the change of the emission wavelength from 2.31 to 2.08 μm.

From the mechanism presented here, one can observe that two infrared photons are produced as a result of one absorbed photon. The output power of the system is plotted in Fig. 9.6. The initial slope efficiency for the holmium emission $^5I_7 \rightarrow {}^5I_8$ is 26%. The slope efficiency changes at the onset of the 2.31-μm emission; above that threshold, for both laser wavelengths, the slope efficiency is 42%.

The absorption spectra of Tm^{3+} in a Tm:Ho:Cr:YAG sample is presented in Fig. 9.7. The absorption line centered at 780 nm has a linewidth of 4 nm (FWHM) and is attractive for GaAlAs diode pumping. The absorption peak suitable for diode pumping is at 785.5 nm, and the absorption coefficient at this wavelength is $\alpha = 6\ \text{cm}^{-1}$. For a Tm^{3+} concentration of $8 \times 10^{20}\ \text{cm}^{-3}$, the absorption cross-section at 785.5 nm is $\sigma_{ab} \approx 7 \times 10^{-21}\ \text{cm}^2$. We assume that 95% of the incident light is absorbed by the Tm:Ho:YAG crystal. From the knowledge of the absorption coefficient α at 785 nm and the crystal transmission (as a percentage) T, the crystal length is $\ell = \ln(T)/\alpha \approx 0.5$ cm. This optical length is small enough to keep unwanted re-absorption losses at 300 K in the holmium ion owing to the population of the various Stark J-components of its ground state $^5I_8$ level ($\approx$450 cm^{-1}), to a low level ($<$0.07 cm^{-1}). Tm:YLF has two absorption peaks, at 780 nm and at

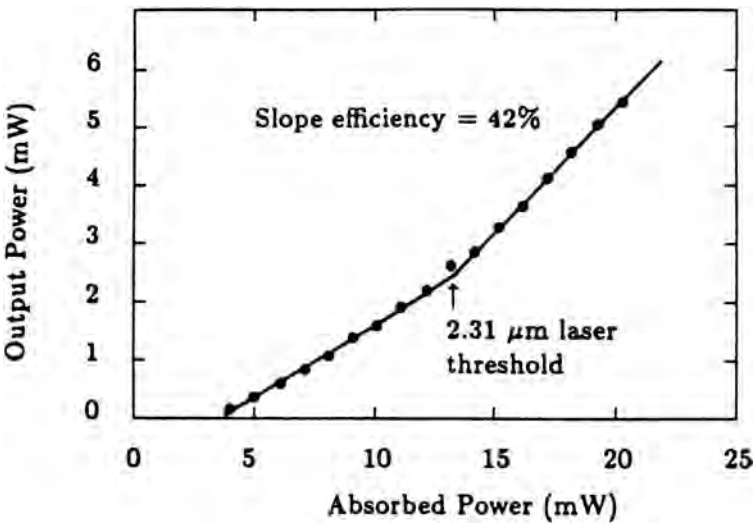

Figure 9.6 Slope efficiency for the Tm,Ho:YLF laser system. (Reprinted from Ref. 24.)

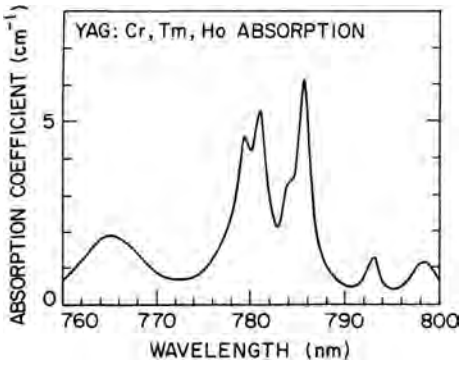

Figure 9.7 Absorption spectrum of Tm:YAG in the near IR. (Reprinted from Ref. 38 with permission from the Optical Society of America.)

792 nm. The absorption coefficients for 6 at. % Tm:YLF at ($E||c$, π polarization) are 5.4 cm^{-1} and $\approx$5 cm^{-1}, for both absorption peaks respectively, so the crystal length for Tm:YLF should be similar to that of Tm:YAG.

The spectral width of ion-doped crystal lasers is determined by the ion-lattice interaction and inhomogeneous broadening. The spectral bandwidth will increase with the crystal field resulting from Stark splitting of both ground and excited state J components of the electronic levels. The lasers described above can be tunable over $\approx$80 nm (continuously) because of the inhomogeneous broadening of the rare-earth ions doped in garnets, especially mixed or scandium-based garnets, as was discussed in Chapter 4. Although the Tm^{3+}−based lasers posses a broader lasing tunable range, the saturation fluence of Tm:YAG is $\approx$50 J/cm^2 compared with $\approx$10 J/cm^2 for Ho:YAG, which implies fewer problems with the damage threshold mainly during the production of short pulses with a Ho:YAG laser system.[29]

The $^3F_4 \rightarrow {}^3H_6$ laser transition of Tm:YAG at 2.01 μm has a relatively high gain (0.04 cm^{-1}) and a relatively low saturation flux (−13 kW/cm^2).[30] Therefore, this laser is attractive for high-power applications. With high-power, high-brightness diode arrays and high-quality crystal now available, high output power laser radiation from a Tm:YAG laser system can be generated. By using a Tm^{3+} doping level of 2 at. % with diffusion-bonded, undoped YAG endcaps, the end-diode-pumped Tm:YAG produced 115-W CW output power at 2.01 μm, a 40% slope efficiency, and a beam quality of M^2 values between 14–23 depending on the input pumping power.[31] Figure 9.8 presents the experimental setup. The pumping light was delivered into the end of the laser rod using a microlensed diode array and a lens duct. The diffusion-bonded, undoped YAG endcaps were designed to minimize the thermal stresses at the rod ends and to reduce end-face distortions and thermal lensing. The nominal Tm^{3+} concentration was only 2 at. % to reduce the absorption length, thermal load, and ground state absorption. The pumping wavelength of the improved Tm:YAG laser rod was at the low absorption part of the spectrum, 805 nm, not at 785 nm ("wing pumping"), which results in stresses that are only 15% of the fracture limit.

The laser output power as a function of the input pumping power for both 2 at. % and 4 at. % is presented in Fig. 9.9. The 4 at. % sample has a higher threshold than the 2 at. % sample, indicating undesired losses resulting from ground state absorption and excess thermal load, which is unfavorable for the efficient operation of a quasi-three-level system. The benefit of diffusion-bonded, undoped elements is obvious. For example, it was found that using diffusion-bonded endcaps improved some temperature-related parameters, such as reducing the peak temperature rise in the active laser rod by 19%, reducing the pump threshold by 10%, and improving the focal power (in cm^{-1}) of the thermal lensing by 15% relative to the noncomposite material.[32]

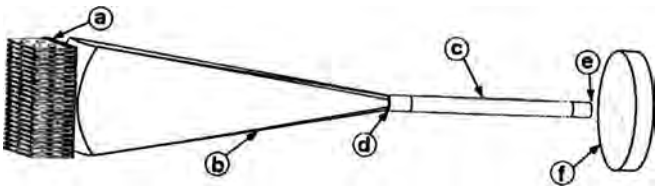

Figure 9.8 Experimental setup of diode-end-pumped Tm:YAG: (a) microlensed diode array; (b) fused silica lens duct; (c) composite Tm:YAG laser rod; (d) dichroic coating on the pump input face of the laser rod; (e) dichroic coating on the output face of the laser rod (high reflectivity for the pumping wavelength, AR for the laser wavelength); (f) flat or concave output couple. (Reprinted from Ref. 31 with permission from IEEE. Credit must be given to the University of California, Lawrence Livermore National Laboratory, and the U.S. Department of Energy, under whose auspices the work was performed, when this information or a reproduction of it is used.)

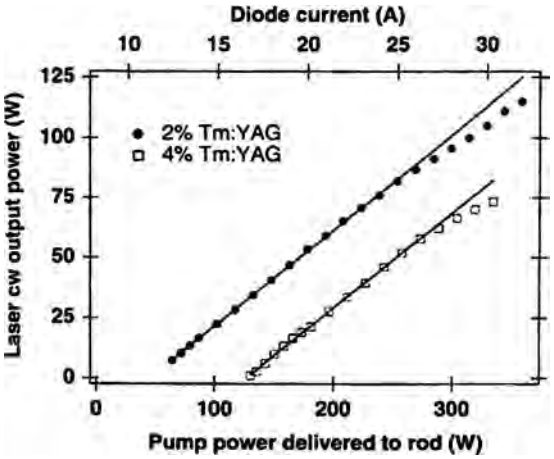

Figure 9.9 Laser output power at 2.01 μm as a function of input pumping power for 2 at. % and 4 at. % of Tm:YAG. (Reprinted from Ref. 31 with permission from IEEE. Credit must be given to the University of California, Lawrence Livermore National Laboratory, and the U.S. Department of Energy, under whose auspices the work was performed, when this information or a reproduction of it is used.)

9.4.2 Side-pumped 2-μm lasers

The quasi-three-level nature of both Tm^{3+} and Ho^{3+} lasers has a crucial impact on the operation of any room-temperature, side-pumped laser system based on holmium and thulium ions, since the laser action terminates on the ground state manifold. One expects an increase in the pumping threshold owing to ground state absorption when the laser mode passes through the unpumped volume in the crystal, as well as a result of the population of the Stark components of the ground $^3H_6$ level, at ambient temperature. To overcome the thermal population of the ground state Stark components (300–500 cm^{-1}) as well as the ground state absorption in the unpumped region, especially in CW operating mode, a high-brightness pumping diode will be required. In a side-pumped configuration, this is achieved by a special resonator design to support a multipass side-pumping configuration. The multipass design minimizes the unpumped regions in the crystal and hence the thermal load, and therefore significantly increases laser efficiency. In the laser configuration presented in Fig. 9.10, a Tm:YLF slab was side-pumped by two diode laser bars from opposite sides. The diode bars were tuned to the Tm:YLF absorption peak at 792 nm, and the resonator was designed to provide three passes of the laser beam through the Tm:YLF slab. This laser produced ≈28-W CW output power at 1940 nm with 25% slope efficiency.[33]

A diode-side-pumping technique was also carried out, placing the pumping diodes symmetrically around the perimeter of the composite, diffusion-bonded Tm:Ho:YLF laser rod. The Tm:Ho:YLF crystal was water cooled to 16°C with 13–14% slope efficiency at a 10-Hz repetition rate.[34] An alternative approach is to close-couple the pump diodes around a conductively cooled Tm:Ho:YLF, producing 10–20% slope efficiency, depending on the heat-sink temperature, laser rod orientation, and pulse repetition rate.[35]

The Tm:Ho:YLF can also be operated efficiently in a quasi-CW (QCW) mode at ambient temperature. This laser produced 1.7 W of peak power when pumped up to 14 W at 792 nm, with 10% duty cycle.[36]

The laser operation of a 2-μm diode-pumped microchip laser operated at room temperature with an external etalon produced 27-mW output power in a single-mode operation.[37] The maximum tunable bandwidth at an oscillation wavelength

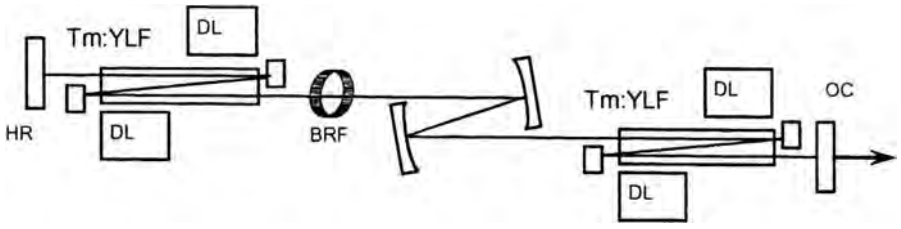

Figure 9.10 Experimental setup of the side-pumped, three-pass Tm:YLF laser, where DL is the diode laser, OC is the output coupler, HR is the high reflector, and BRF is the birefringent filter. (Reprinted from Ref. 33 with permission from the Optical Society of America.)

of 2.06 μm was 3.5 GHz, with temperature stability of 1.9 GHz/°C. The holmium microchip laser was a disk 3 mm in diameter and 0.7 mm thick, with flat/flat and parallel surfaces. One surface was coated for high transmission at 781 nm and high reflectivity at 2.1 μm; the opposite side was coated for AR at 2.06 μm.

References

1. D. Aravot, E. Lachman, S. Giler, et al., "The holmium laser in intravascular coagulation," in *7th Congr. Int. Soc. Laser Surgery Med.* **303** (1987).
2. S. W. Henderson, C. P. Hale, J. R. Magee, M. J. Kavayd, and A. V. Huffaker, "Eye safe coherent laser radar systems at 2.1 μm using Tm,Ho:YAG lasers," *Opt. Letters* **16**, 773–775 (1991).
3. S. E. Moody, "Evaluation of laser technologies for an aircraft wind shear detection," *SPIE Proc.* **783**, 124–131 (1987).
4. N. P. Barnes, "Solid state lasers for monitoring the health of planet earth," in *Laser M2P and the 2nd French-Israeli Meeting*, Lyon, Dec. 8–10, 1993, Paper # VCP1.
5. L. F. Johnson, G. D. Boyd, and K. Nassau, "Optical laser characteristics of Ho^{3+} in $CaWO_4$," *Proc. IRE (Corresp.)* **50**, 87–88 (1962).
6. H. W. Gandy, R. J. Ginther, and J. F. Weller, "Internal Q-switching of Ho^{3+}-stimulated emission in iron containing glasses," *Appl. Phys. Letters* **9**, 277–279 (1966).
7. D. P. Devor, B. H. Soffer, and M. Robinson, "Stimulated emission from Ho^{3+} at 2 μm in HoF_3," *Appl. Phys. Letters* **18**, 122–124 (1971).
8. L. F. Johnson, J. E. Geusic, and L. G. Van Uitert, "Efficient high power coherent emission from Ho^{3+} ions in yttrium aluminum garnet assisted by energy transfer," *Appl. Phys. Letters* **8**, 200–202 (1966).
9. E. P. Chicklis, C. S. Naiman, R. C. Folweiler, et al., "High efficiency room temperature 2.06 μm laser using sensitized Ho^{3+}:YLF," *Appl. Phys. Letters* **19**, 119–121 (1971).
10. B. M. Antipenko, I. V. Vorykhalov, B. V. Sinitsyn, and T. V. Uvarova, "Laser frequency converter based on a $BaYb_2F_8$:Ho^{3+} crystal: Stimulated emission at 2 μm," *Sov. J. Quantum Electron*. **10,** 114–115 (1980).
11. L. F. Johnson and H. J. Guggenheim, "Laser emission at 3 μm from Dy^{3+} in BaY_2F_8," *Appl. Phys. Letters* **23**, 96–98 (1973).
12. A. M. Tkachuk, A. V. Khilko, and M. V. Petrov, "Probabilities of intracenter spontaneous radiative and non-radiative multiplet transitions in the Ho^{3+} ion in a $LiYF_4$ crystal," *Opt. Spectrosc. (USSR)* **58**(1), 55–59 (1985).
13. S. A. Payne, L. L. Chase, L. K. Smith, W. L. Kway, and W. F. Krupke, "Infrared cross-section measurements for crystals doped with Er^{3+}, Tm^{3+} and Ho^{3+}," *IEEE J. Quant. Electron.* **28**(11), 2619–2630 (1992).
14. Y. Kalisky, J. Kagan, H. Lotem, and D. Sagie, "Continuous wave operation of multiply doped Ho:YLF and Ho:YAG laser," *Opt. Commun*. **65**, 359–363 (1988).

15. R. Reisfeld and C. K. Jorgensen, "Lasers and excited states of rare earth," *Inorganic Chemistry Concepts* **1**, Springer-Verlag, Berlin, Heidelberg, and New York (1977).
16. W. Koechner, *Solid State Laser Engineering*, Fifth Edition, Chapter 2, Springer-Verlag, Berlin, Heidelberg, and New York (1999).
17. I. T. Sorokina, "Crystalline mid-IR lasers," in *Solid State Mid-Infrared Laser Sources*, 255–349, Topics in Applied Physics, Springer-Verlag, Berlin and Heidelberg (2003).
18. H. Lotem, Y. Kalisky, J. Kagan, and D. Sagie, "A 2 μm holmium laser," *IEEE J. Quantum Electron.* **24**, 1193–1200 (1988).
19. R. Beck and K. Gurs, "Ho laser with 50-W output and 6.5% slope efficiency," *J. Appl. Phys.* **46**, 5224–5225 (1975).
20. B. M. Antipenko, A. S. Glebov, T. I. Kiseleva, and V. A. Pis'mennyi, "2.12 μm Ho:YAG laser," *Sov. Tech. Phys*. **11**(6), 284–285 (1985).
21. B. M. Antipenko, A. S. Glebov, T. I. Kisileva, and V. A. Pis'mennyi, "A new spectroscopic scheme of an active medium for the 2-μm band," *Opt. Spectrosc. (USSR)*, **60**(1), 95–97 (1986), translated from *Optika I Spektroskopiya* **60**(1), 153–157 (1986).
22. H. Lotem, J. Kagan, D. Sagie, and L. A. Levine, "60 W 2.06 μm Ho^{3+}:YLF laser," *J. Opt. Soc. Amer.* **A2**, 107 (1985).
23. S. R. Bowman, M. J. Winings, S. Searles, and B. J. Feldman, "Short pulsed 2.1 μm laser performance of Cr,Tm,Ho:YAG," *IEEE J. Quantum Electron.* **27**(5), 1129–1131 (1991).
24. L. Esterowitz, "Diode pumped solid state lasers at 2 and 3 micron for biomedical field," *SPIE Proc*. **1182**, 49–58 (1989).
25. E. W. Duczynski, G. Huber, V. G. Ostroumov, and I. A. Shcherbakov, "CW double cross pumping of the $^5I_7$-$^5I_8$ laser transition in Ho^{3+} doped garnets," *Appl. Phys. Letters* **48**, 1562–1563 (1986).
26. G. Ozen and B. DiBartolo, "Energy transfer and thermalization in $LiYF_4$:Tm,Ho," *Appl. Phys. B* **70**, 189–193 (2000).
27. P. A. Bundi, C. A. Miller, M. L. Lemons, et al., "High power/energy thulium pumped holmium lasers," *LEOS 2000, 2000 IEEE Annual Meeting Conference Proceedings*, 609–610 (2000).
28. A. Hayward, W. A. Clarkson, and D. C. Hanna, "High power diode-pumped room-temperature Tm:YAG and intracavity-pumped Ho:YAG lasers," *OSA Trends in Optics and Photonics (TOPS)* **34**, *Advanced Solid State Lasers*, 45–47 (2000).
29. C. D. Nabors, J. Ochoa, T. Y. Fan, et al., "Ho:YAG laser pumped by 1.9 μm diode lasers," *IEEE J. Quantum Electron.* **31**(9), 1603–1605 (1995).
30. F. Mattsuzaka and H. Hara, "Small signal gain and a saturation parameter of a LD-pumped Tm:YAG laser in a single mode operation," *SPIE Proc.* **3265**, 83–90 (1998).
31. E. C. Honea, R. J. Beach, S. B. Sutton, et al., "115-W Tm:YAG diode-pumped solid state laser," *IEEE J. Quantum Electron.* **33**(9), 1592–1600 (1997).

32. M. Tsunekane, N. Taguchi, and H. Inaba, "Improvement of thermal effects in a diode-end-pumped composite Tm:YAG rod with undoped ends," *Appl. Opt*. **38**(9), 1788–1791 (1999).
33. A. Dergachev and P. F. Moulton, "High power, high energy diode-pumped Tm:YLF-Ho:YLF-ZGP laser system," *OSA Trends in Optics and Photonics* **83**, *Advanced Solid State Photonics*, 137–141 (2003).
34. M. G. Jani, "Diode-pumped, long pulse length Ho:Tm:$YLiF_4$ laser at 10 Hz," *OSA Proc. on Advanced Solid State Lasers* **24**, 362–365 (1995).
35. N. Sims, M. Cimolino, N. P. Barnes, and B. G. Asbury, "10 Hz PRF operation and temperature estimation of a conductively cooled room temperature, diode-pumped Ho:Tm:YLF Laser, *OSA Proc. on Advanced Solid State Lasers* **24**, 396–400 (1995).
36. N. U. Wetter, S. F. de Matos, I. M. Ranieri, E. P. Maldonado, and N. D. Vieira, "QCW-Tm,Ho:YLF laser pumped by a 20-W diode bar using a two mirror beam shaper," *Revista de Fisica Aplicada e Instrumentacao* **13**(4), 83–85 (1998).
37. J. Izawa, H. Nakajima, H. Hara, and Y. Arimoto, "A tunable and longitudinal mode oscillation of a Tm,Ho:YLF microchip laser using an external etalon," *Opt. Commun*. **180**(1–3), 137–140 (2000).
38. T. Y. Fan, G. Huber, R. L. Byer, and P. Mitzscherlich, "Continuous-wave operation at 2.1 μm of a diode-laser-pumped Tm-sensitized Ho:$Y_3Al_5O_{12}$ at 300 K," *Opt. Letters* **12**(9), 678–680, Fig. 2 (1987).
39. G. Quarles, A. Rosenbaum, C. L. Marquardt, and L. Esterowitz, "High efficiency 2.09 μm flashlamp-pumped laser," *Appl. Phys. Letters* **55**(11), 1062–1064 (1989).

Chapter 10

Yb:YAG Laser

10.1 Introduction

The ytterbium laser is currently regarded as a suitable candidate for generating pulses with relatively high peak power or as a source for high-power CW output, because of the long lifetime of the excited level $^2F_{5/2}$ of the Yb^{3+} ion. This characteristic, coupled with the ability to obtain high Yb^{3+} doping levels (up to 20 at. % without concentration quenching), makes the ytterbium-doped solid an ideal candidate for high-power industrial laser applications as well as a microlaser in the 1030–1050 nm spectral range. This laser emission is absorbed by saturable absorbers such as Cr^{4+}:YAG and other quadrivalent chromium-doped garnets, yielding repetitive modulation and high peak power.

The energy-level scheme of Yb^{3+} is a simple configuration and is presented in Fig. 10.1.

Solid state lasers based on Yb^{3+}-doped solid hosts emit coherent radiation that peaks at 1030 nm via a $^2F_{5/2}(A_1) \rightarrow {}^2F_{7/2}(Z_3)$ transition, where A_1 and Z_3 are the J-Stark components located at 10,327 cm^{-1} and 612 cm^{-1}, respectively.[1] Yb-based solid state lasers have several advantages over Nd-doped lasers, including:

- They have a low quantum defect, e.g., 91% quantum efficiency.
- As a result of the low quantum defect, they have a relatively low fractional heating ($<$11% as compared with 37–43% in Nd^{3+}:YAG), and therefore a smaller thermal load on the Yb:YAG crystal is expected. When pumped at the zero phonon line of Yb^{3+} (975 nm), the fractional heating is only 5%.
- They have a broad absorption band of about 18 nm at 940 nm, which implies more flexibility on the pumping-wavelength range of the diode wavelength within the absorption band of the gain medium and more flexibility on the diode operating temperature. The absorption bandwidth of Nd:YAG at 808 nm is 10 times smaller.
- They have a broad emission band, which results in tunability (1018–1053 nm) and the ability to generate short pulses.

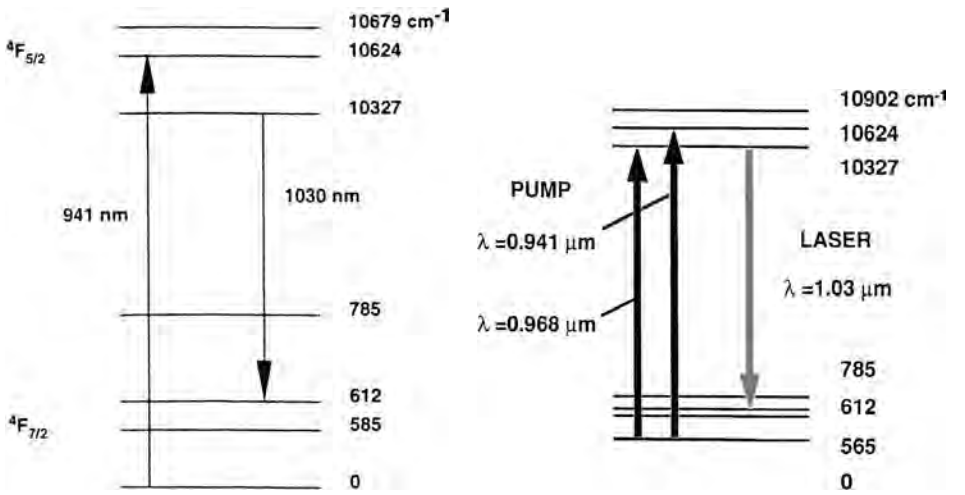

Figure 10.1 The energy-level diagram of a Yb:YAG laser crystal with the Stark level splitting.

- They have high doping levels, up to 20 at. % and higher, without concentration quenching of the excited states.
- As a result of the simple $4f^{13}$ electronic configuration of Yb^{3+} ion, there are no relevant higher-lying excited states, and therefore, no excited state absorption, upconversion phenomena, nonradiative processes among excited states, or quenching of excited state luminescence.
- Pumping wavelengths at 940 or 970 nm allows for the use of the reliable Al-free InGaAs diode lasers.
- Yb is capable of good energy storage due to its long lifetime—in the 0.95–1.2 ms temporal domain—and the low emission cross section.
- Yb-doped YAG possesses the robust thermal and mechanical properties of the hosting YAG material.

The main physical and optical characteristics of Yb^{3+}:YAG are presented in Table 10.1.

Figure 10.2 presents the absorption spectrum of Yb:YAG ($^4F_{5/2} \rightarrow {}^4F_{7/2}$) at room temperature. The maximum absorption peak of the pumping band is at 940 nm, and the absorption bandwidth is approximately five to ten times broader than the 808-nm absorption transition of Nd:YAG. Since the spectral overlap between the absorption band and the emission of conventional flashlamps is poor, it is expected that a lamp-pumped Yb laser will be very inefficient. However, diode pumping is suitable for efficient operation of an Yb laser. The relatively broad absorption bandwidth and long fluorescence lifetime presents significant advantages relative to Nd:YAG in terms of performance and reliability. The broad absorption band allows flexibility in the pumping wavelength and therefore flexibility in the diode temperature control when applied to a Yb:YAG system. The longer fluorescence lifetime (Table 10.1) of Yb:YAG allows the use of CW pumping diodes,

Table 10.1 The main physical characteristics of Yb:YAG crystals.

Characteristics	Nomenclature	Yb:YAG	Nd:YAG	Reference No.
σ_p (cm^2)	Absorption cross section	7.4×10^{-21} 7.7×10^{-21}	6.7×10^{-20}	2 3
σ_{em} (cm^2)	Emission cross section	$2.3\ 10^{-20}$ $3.3\ 10^{-20}$	2.8×10^{-19}	1, 2
κ (W/m K)	Thermal conductivity	13	13	
dn/dT (K^{-1})	Change of refractive index with temperature	8.9×10^{-6} 7.3×10^{-6} 9.86×10^{-6}	7.3×10^{-6}	4 5, 6 7
τ_{fl} (ms) (at 300 K)	Fluorescence lifetime	0.951	0.23–0.24	8
λ_p (nm)	Pumping wavelength	940	808	
λ_{em} (nm)	Emission wavelength	1030	1064	
α (cm^{-1})	Absorption coefficient (8 at. %)	8	7–8 (1.0 at. %)	9
	Absorption coefficient (10 at. %)	10		
η_{th} (%)	Fractional thermal load	11	37–43	10
I_{sat} (kW/cm^2)	Pump saturation flux	22	16	11
C_{Yb} (ions/cm^3)	Ionic concentration	1.38×10^{20} (1.0 at. %)	$\approx 1.2 \times 10^{20}$	

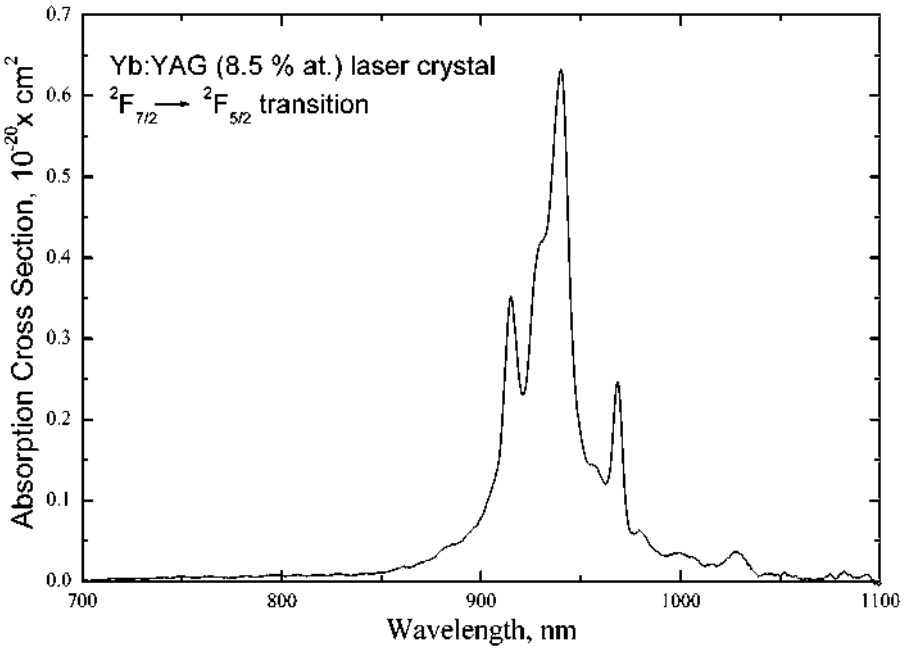

Figure 10.2 Room-temperature Yb:YAG effective absorption cross-section spectrum.

which have much longer operating lifetimes and much less fluorescence loss than the quasi-CW diodes, which are usually preferred for pumping the Nd:YAG lasers to avoid fluorescence loss.

The main disadvantage of a Yb-doped host is its quasi-three-level nature owing to the thermal population of the highest J splitting of the $^4F_{7/2}$ lower terminating lasing level, which is about 612 cm^{-1} above the ground level. (The terminal laser level in Nd:YAG is $\approx$2000 cm^{-1} above the ground state.) This thermal population has deleterious effects of resonant re-absorption of the laser emission from the ground terminal Stark state, which is thermally populated at 300 K by about 5% of the $^4F_{7/2}$ population. As a result, it is difficult to obtain population inversion at room temperature, and therefore, the lasing threshold is high and its efficiency is consequently low. Moreover, Yb:YAG has smaller absorption and emission cross sections as well as a higher saturation intensity than Nd:YAG, which dictates relatively high pumping intensities to reach threshold and obtain gain. Efficient population inversion is achieved by either pumping at high pump power densities at 300 K (1.5 to 10 kW/cm^2),[12] or by depopulation of the highest Stark components. The latter option is achieved by cooling the system to low temperatures (in the range of 60–100 K), where only the lowest Stark levels are thermally populated. Even at higher temperature, for example 200 K, the pumping threshold density is much lower, $\sim$150-W/cm^2. A cryogenically cooled, longitudinally diode-pumped Yb:YAG laser generated 165 W with a near-diffraction-limit beam quality ($M^2 = 1.02$), 76% optical-to-optical efficiency, and 85% slope efficiency.[13] Above 220 K, the laser slope efficiency decreases and the pump threshold increases quadratically with the temperature. Figure 10.3 illustrates the dependence of the Yb:YAG lasing slope efficiency on the crystal and the pumping threshold on the crystal temperature.

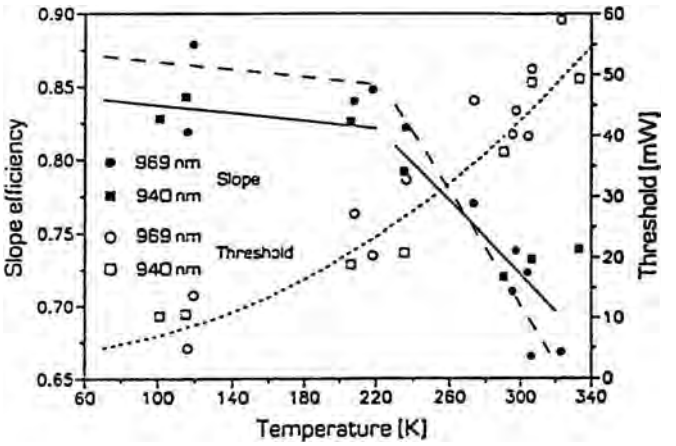

Figure 10.3 Slope efficiency and extrapolated threshold for absorbed pump power as a function of Yb:YAG temperature for two pumping wavelengths. (Reprinted from Ref. 12 with permission from Springer-Verlag.)

The special characteristics of the Yb^{3+} ion determine the various pumping configurations of an Yb:YAG laser. The high saturation intensity necessary to pump the Yb^{3+} laser means a high-power, high-brightness source, e.g., high intensity within a smaller beam diameter, and hence a smaller laser crystal dimension, only a few mm in diameter for a few kW of laser output power. The Yb-doped laser can be pumped by three main geometries: end- or longitudinal pumping, side- or transverse pumping, and thin disk or face-pumping.

10.2 End-pumping

The diode end-pumping configuration of solid state lasers has it own advantages and limitations as will be discussed in the appendix. Thermal effects, which deteriorate laser beam quality, limit the performance of high-power solid state lasers, especially those based on Nd:YAG. Such thermal effects include thermally induced birefringence; optical aberrations of the laser beam resulting from temperature gradients in the laser rod and consequent thermally induced refractive index changes in the crystal; and thermally induced laser rod fracture owing to thermally induced stress and strain. YAG is usually the best candidate for a high-power laser (either lamp-pumped or diode-pumped) because of its thermal, mechanical, and optical properties. Lasers based on the Yb^{3+} ion have additional specific advantages over Nd^{3+} because of the reasons discussed above. Most important is the lower thermal load of Yb^{3+} relative to Nd^{3+}, $<11\%$ and $>35\%$, respectively. The reduced thermal load results from the smaller quantum gap in Yb^{3+} (9%) relative to Nd^{3+} (24%). For high-power applications, it is necessary to use pumping sources with a high power density of several kW/cm^2, which must be delivered into a rod 2 mm in diameter by 50 mm in length. This was accomplished by first collimating the pumping light using a cylindrical, microlensed diode, and then directing the collimated light into a hollow lens duct, which allowed the delivery of high-irradiance microlensed diode pump power at $\approx$80% efficiency.[14] The hollow lens duct has another purpose in allowing access to the laser beam at 1.03 μm to the external cavity high-reflectivity mirror at the pump end of the laser rod. This novel end-pumped configuration is demonstrated in Fig. 10.4.

Composite Yb:YAG laser rods with undoped, diffusion-bonded endcaps and a doped central part were used to avoid fracture at the pumped input face by compressing the tensile strain that would otherwise develop. The use of composite laser rods with undoped endcaps has other significant advantages, including:

- The flanged endcaps on both ends of the laser rod distance the O-ring water seal from the high-intensity laser beam, as compared with a case in which no such flanges were used, reducing O-ring degradation under thermal loading. When endcaps with a rectangular cross section were used, a better impedance match of the diode light from the lens duct to the laser rod was achieved, since the flanged rectangular part of the endcaps served as a continuation of the laser rod through the lens duct to the pump light.

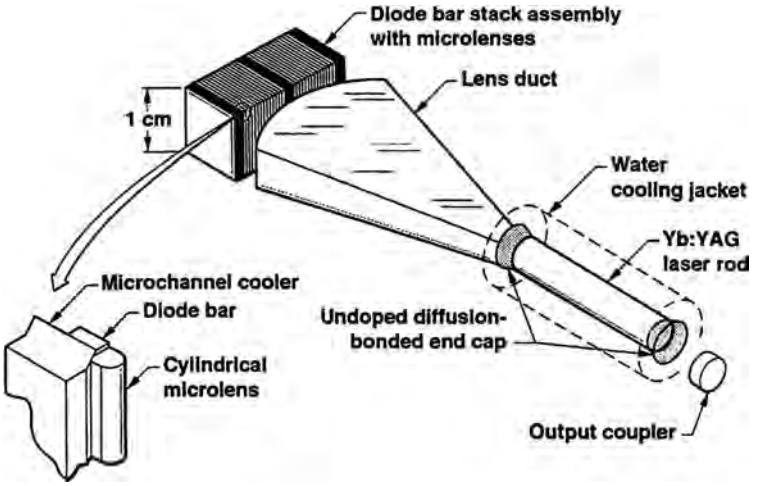

Figure 10.4 Schematics of a diode-pumped Yb:YAG laser. (Reprinted from Ref. 15 with permission from IEEE. Credit must be given to the University of California, Lawrence Livermore National Laboratory, and the U.S. Department of Energy, under whose auspices the work was performed, when this information or a reproduction of it is used.)

- The undoped endcaps also thermally isolate the optical coating on the pumped surface by keeping the temperature gradients along the rod as small as possible.
- The flanged endcaps are effective in suppressing amplified spontaneous emission (ASE) and parasitic oscillations that develop and are confined in the polished barrel rods. The result of the trapped ASE is that the gain in the annular region or the outer portion of the laser rod is depleted. The effective circular area useful for lasing has a radius of $(n_s/n_r)r_{rod}$, where r_{rod} is the radius of the laser rod, n_r is the refraction index of the laser rod ($n_r = 1.82$ for YAG), and n_s is the refraction index of the cooling material surrounding the laser rod ($n_s = 1.33$ for the laser coolant). In the case of Yb:YAG, the effective gain area or a fill factor is only $100 \times (1.33/1.82)^2 = 53\%$ of the rod's cross-sectional area. The flanged endcaps limit the ASE and parasitic oscillations to about one pass along the length of the laser rod. Further reduction of the trapped, unwanted light is achieved by tapering the laser rod diameter over its length, thus significantly reducing the trapped path length. For an average taper value of $\varepsilon \approx 0.2$ mm, the maximum trapped ASE and parasitic oscillation is reduced by 60–70% and the effective fractional rod volume that can be extracted efficiently is $\approx$0.9.

Birefringence and bifocusing compensation was achieved by using a dual-rod configuration with a 90-deg quartz rotator. The maximum output power of 1080-W at 1030 nm was achieved with 27.5% optical-to-optical efficiency, 12.3% electrical-to-optical conversion efficiency, and beam quality of $M^2 = 13.5$ at 1080-W output power. Figure 10.5 presents the measured CW, free-running laser output power

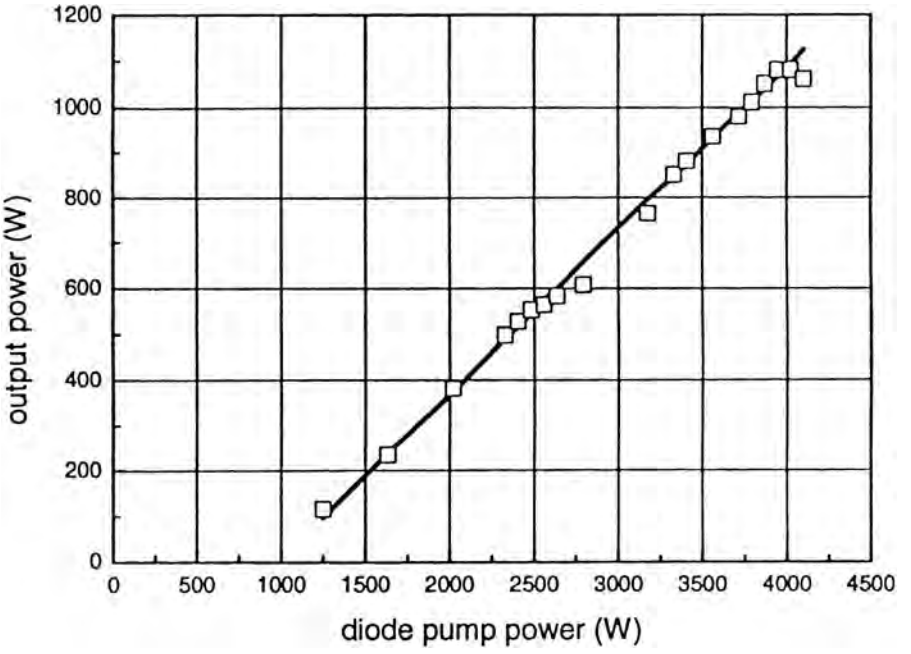

Figure 10.5 Yb:YAG CW output power as a function of the total pumping power in a dual-rod configuration with $M^2 \approx 13.5$. (Reprinted from Ref. 16. Credit must be given to the University of California, Lawrence Livermore National Laboratory, and the U.S. Department of Energy, under whose auspices the work was performed, when this information or a reproduction of it is used.)

as a function of the applied diode pumping power. Above 3-kW diode pumping power, a negative lens was added to the quartz rotator between the two laser rods to maintain resonator stability. By employing a Q-switched operation mode, an average output power of 532 W at a 10-kHz repetition rate and a 77-ns pulse-width were obtained, with 17% optical-to-optical conversion efficiency and with a beam quality of $M^2 < 2.5$.[10, 16] An interesting point is that the ≈1-kW output power was extracted from a small volume of Yb:YAG laser rod doped nominally at 1×10^{-20} cm^{20} cm^{-3} (≈0.7 at. %). This small doping level was sufficient to provide enough gain with significant reduction of self-laser emission re-absorption and heat generation.

10.3 Side-Pumping

End diode-pumping has several limitations, the most significant of which are listed below.

- First, a limitation exists as to the number of diode apertures that can be combined and focused onto a small area, especially in a system where high power densities are required.

- A second limitation results from the low brightness of the two-dimensional emitting apertures of any diode-array bars, which yields a laser output beam with a large divergence angle (40–60 deg) in one direction.

The unique properties of the Yb^{3+} ion add further limitations to the side-pumping of Yb:YAG as a result of the quasi-three-level nature, high saturation fluence, and the smaller (than Nd:YAG) absorption and emission cross sections. This can be observed clearly in Table 10.1. In order to obtain high output power from a Yb:YAG laser by side-pumping, a different pumping architecture from the four-level laser system such as the Nd:YAG system is required. This architecture is valid also for the quasi-CW operation mode. A schematic description of a part of the integrated pump head is presented in Fig. 10.6.[17, 18]

Thermal management of the Yb:YAG laser rod was achieved by impingement cooling of the laser rod barrel surface via jet holes in the inner sleeve. (The rod coolant was at 18°C.) An outer sleeve made of solid glass was used for the pumping light. The outer sleeve had three equally spaced, AR-coated windows at 941 nm on its surface, while the other parts of the outer sleeve were HR coated (at 941 nm) and provided ≈50% reflectivity at 1.03 μm to maintain several passes of the pumping light through the rod diameter to ensure full absorption of the pump light.

The laser rods (∅ 2 × 20 mm or ∅ 3 × 30 mm) were doped by ≈1.5 at. % to reduce re-absorption processes. Further reduction in re-absorption loss of the laser light at 1.03 μm was achieved by employing diffusion-bonded, undoped YAG end-caps on both ends of the Yb:YAG rod. The diffusion-bonded endcaps also had additional advantages in terms of laser pumping head engineering. They facilitated laser rod mounting, cooling, and sealing the coolant as well as optical access. The side-pumping was achieved by using InGaAs 10 mm-wide diode bars, which were pre-collimated in their fast axis by microlens arrays and further imaged onto the rod surface by appropriate focusing optics. A three-fold pumping symmetry ensured uniform gain distribution across the transverse dimension of the Yb:YAG

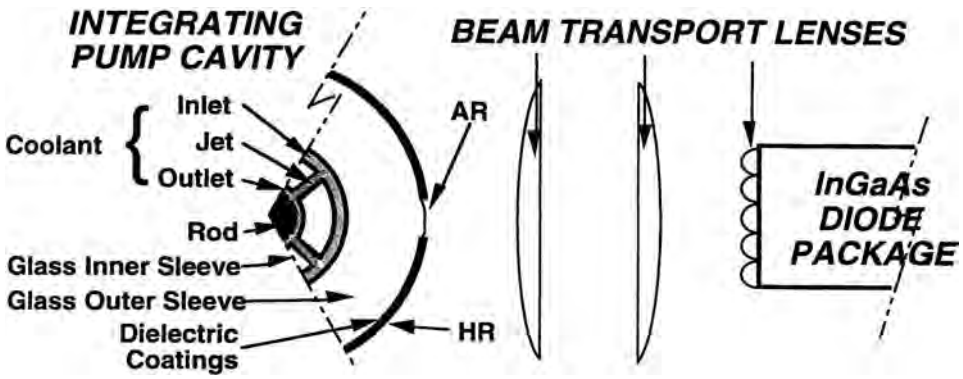

Figure 10.6 Schematic view showing one-third of the cross section of a Yb:YAG laser pumping chamber. The other two-thirds of the pump chamber are identical. (Reprinted from Ref. 18.)

rod. A quasi-CW output energy of 173 mJ at a 400-Hz repetition rate was obtained at room temperature. These values correspond to 69-W average output power at 150-W average pumping power.[17] The maximum CW output power of 0.95 kW from a 3-mm-diameter rod was obtained by pumping at ≈5-kW diode power, with ≈27% slope efficiency and ≈19% total efficiency.[18] The laser performance of CW diode side-pumped Yb:YAG is presented in Fig. 10.7.

10.4 Face-Pumping or Thin Disk Configuration

Face-pumping Yb:YAG using a thin disk crystal is another novel, scalable concept.[12] This method utilizes the benefits of longitudinal pumping, while allowing a scale-up of laser performance to high power levels. A major issue in longitudinal pumping is the temperature gradient between the center of the laser rod and its cooled surface, which can be about 100 K or more, especially under high pump power densities, and which is deleterious to any three-level system operation. One way to overcome this is to reduce the dopant concentration and diameter of the laser rod and increase the gain length, creating a fiber or waveguide laser. These configurations exhibit nonlinear effects as well as optical damage, particularly at high power densities. Also, although in a reduced-diameter geometry the generated heat can be removed efficiently in the radial direction, the heat flux and thermal gradients are also radial, which leads to thermal lensing, thermally induced birefringence, laser beam distortions, and laser efficiency reduction (because of heat accumulation in the crystal and subsequent laser ground state manifold population). Reducing the rod length into a thin disk (100–400 μm width) with two parallel faces and mounting one of them onto a heat sink leads to effective axial

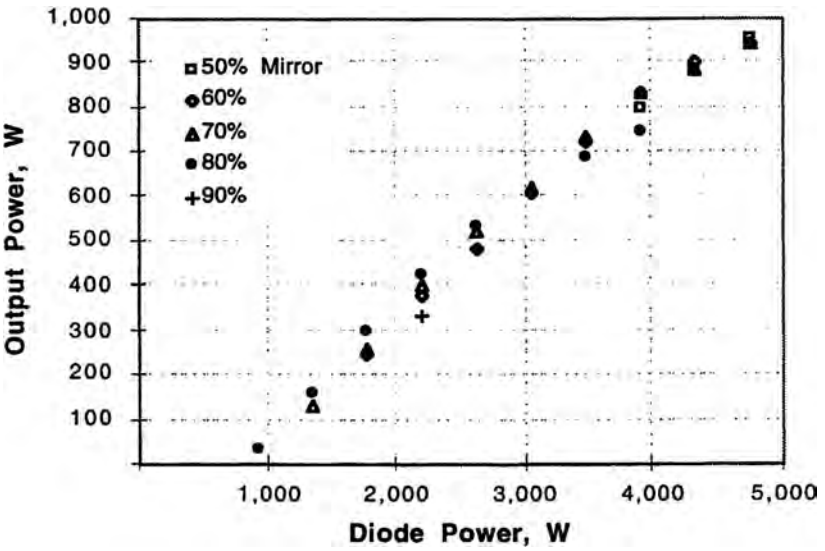

Figure 10.7 Output power of a side-pumped Yb:YAG (1.5 at. % doping level) laser oscillator at various output coupling reflectivities. (Reprinted from Ref. 18.)

disk cooling. The heat-sink-mounted face can be coated for high reflectivity (HR) at the pumping and laser wavelengths to reduce pumping beam optical distortions. The back mirror also serves as a folding mirror, which allows multiple passes of the pump beam through the gain medium. The front face is AR coated for both wavelengths. Effective heat transfer from the thin disk to the water-cooled heat sink was obtained by using indium-tin thin foil and expansion-matched Cu-W material for the heat sink. Since the heat generated in the disk volume is removed through the back surface of the disk, which also has dual HR coating, a temperature gradient is expected to develop across the multiple coating layers. Figure 10.8 represents a general schematic view of the thin disk laser design.

The Yb:YAG laser requires power densities in the range of 10 kW/cm^2 for efficient room-temperature operation, and the multiple passes of the pumping beam can create such effective high pump power densities. The multiple passes also allow the doping level and thickness to be adjusted, while still maintaining high absorption of the pump power within the crystal. In addition, the large surface-to-volume ratio enhances heat dissipation from the thin disk into the heat sink, which allows pumping of the Yb:YAG disk at levels as high as ≈1-MW/cm^3 pump densities. Since the threshold power depends on the population inversion density, reducing the number of the excited ions necessary for laser action significantly reduces the laser threshold. The laser threshold increased with the increase of the pump spot diameter because of the large number of pumped ions, as discussed before. For the same reason, a significant increase of output power was observed compared with a smaller spot diameter of the pumping diode beam. A three-dimensional view of the pumping scheme of an eight-fold pass of the pumping beam through the crystal is presented in Fig. 10.9.

The thin disk configuration yields one-dimensional thermal gradients that are collinear with the laser beam, while keeping the radial thermal gradients, stresses, and refraction index distribution almost homogeneous. In particular, this is true

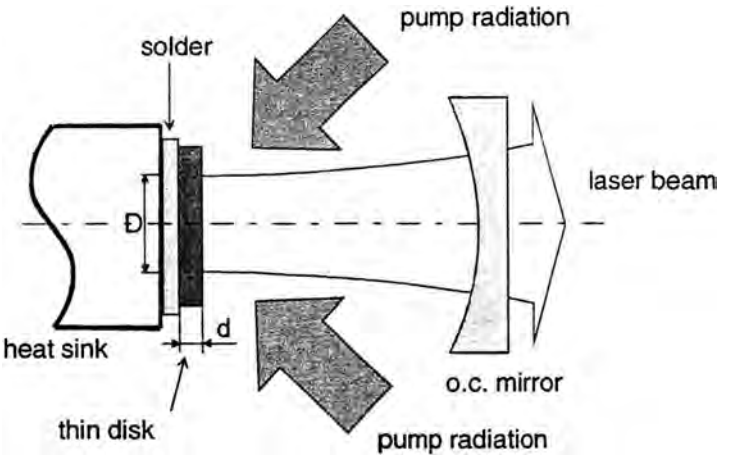

Figure 10.8 Schematic view of the thin disk laser design. (Reprinted from Ref. 19.)

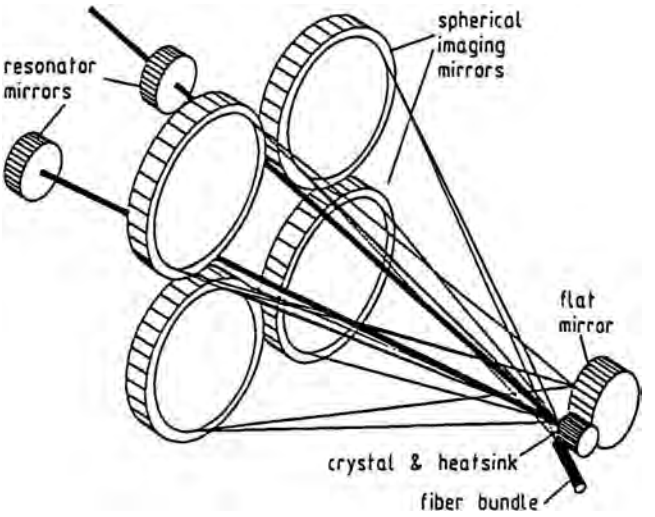

Figure 10.9 Three-dimensional view of a diode-pumped Yb:YAG laser head with an eight-fold pass of the laser beam through the crystal. (Reprinted from Ref. 12 with permission from Springer-Verlag.)

when the thickness of the thin disk is negligible relative to its diameter or to the top-hat pumping beam. This design significantly reduces the effects of thermal lensing, stresses, and thermal distortions within the laser rod, compared to regular surface cooling. It also allows the use of the high pump power densities that are necessary for efficient operation of a quasi-three-level system without degrading laser performance, beam quality, and efficiency.

The face-pumping is actually longitudinal pumping and is expected to obtain efficient, near-diffraction-limited beam quality. The use of a high-brightness, fiber-coupled pumping diode allows high pump power densities to be achieved. The laser performance can be further scaled by increasing the pump beam diameter,[19] reducing the crystal thickness, and increasing the multiple passes via several folding imaging mirrors through the disk or through an array of several thin disks in a zig-zag configuration. The thin disk setup can be operated in both CW and pulsed modes. The subject of both CW and pulsed (Q-switched[20]) thin disk laser operation is summarized in Ref. 19. The CW performance of a one-disk configuration of an Yb:YAG laser is presented in Fig. 10.10. This industrial prototype produced output power greater than 2 kW, with optical-to-optical efficiency of 64% and $M^2 < 20$.[19] Several thin disks coupled in the same resonator yielded up to 4-kW output power with the same efficiency and beam quality.

Single-frequency operation (up to 30 W) and tunability over the spectral range of 1000–1060 nm was obtained in a Yb:YAG disk laser by using appropriate optical elements such as birefringent filters and etalons. Based on these properties, the tunable intracavity frequency of the CW fundamental wavelength of Yb^{3+}:YAG doubled in the 500–530 nm spectral range with 15-W output power at 515 nm and 12 W at 532 nm for Yb:YVO_4. A thin disk configuration of diode-pumped

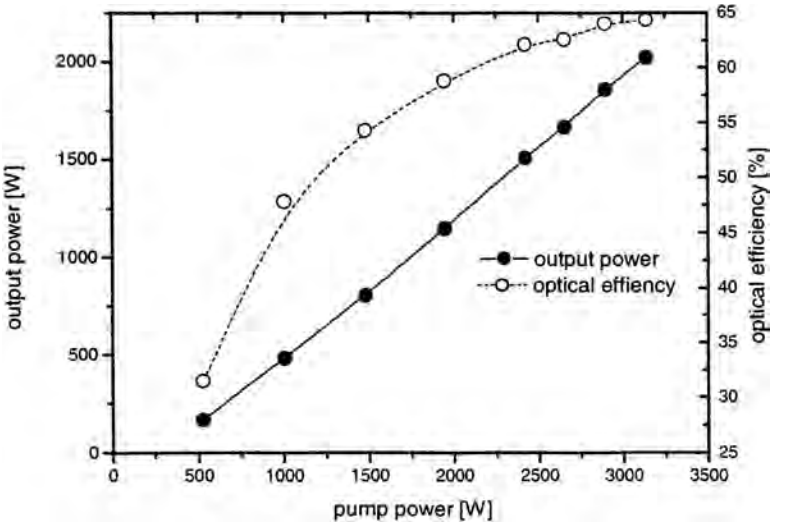

Figure 10.10 Laser performance and optical efficiency of a single disk laser. (Reprinted from Ref. 19.)

Yb:YVO_4 can be utilized to generate laser emission at other wavelengths such as the quasi-three-level transition at 914 nm ($^4F_{3/2} \rightarrow {}^4I_{9/2}$), which produced 5.8 W or >1 W upon doubling this transition at 457 nm.[19]

The thin disk configuration was also operated in pulsed mode with maximum output energy of 18 mJ at 1 kHz, and ≈5 mJ at 13-kHz repetition rates with a pulse duration of ≈200 ns. The average output power of 64 W corresponds to a 34% optical efficiency, and the beam quality was $M^2 < 2$ in all the experiments. The pulse length of the Yb:YAG thin disk oscillator was in the ns time domain at 200–570 ns. By using a regenerative amplification stage and an Yb:YAG thin disk as the amplifying medium, pulses of 5-mJ energy at a 1-kHz repetition rate or 1 mJ at 20 kHz with 4-ps pulsewidth in the amplifier stage were obtained. Using other crystals such as the tungstates (Yb:KYW), it was possible to extract laser energy of 100 μJ at a 45-kHz repetition rate with a 4.5-W average output power and a pulse duration as low as 750 fs without using the chirped pulse amplification (CPA) technique.

Another concept of thin disk lasers was developed at The Boeing Company.[21] This concept utilizes a composite laser disk in which the laser-active region is the central part and the undoped perimetral edge has an octagonal shape. The disk material can be a garnet, a glass such as Q-98 phosphate (glass of Kigre), or any other crystal, and the dopants are either Yb^{3+} or Nd^{3+} ions. The thin disk is edge-pumped by high-power diode arrays and its output can be scaled in the range of 20–60-kW output power.

Rare-earth–doped, diffusion-bonded, planar-channel waveguide geometries are attractive for highly efficient diode-pumped lasers and amplifiers. The demands on the cladding pump are determined by the numerical aperture (NA) of the waveguide geometry. A sufficiently high NA will reduce the requirements on the beam qual-

ity of the pumping beam. The high NA is obtained by employing a large refraction index difference between the doped channel-waveguide core and the undoped cladding. A high doping level, >15 at. %, helps set a large refractive index difference as well. (Usually the change of refraction index with the doping level is $\approx 0.2 \times 10^{-3}$/ at. %.) However, the efficiency of the end-diode-pumped planar-waveguide laser is limited because of the small confocal parameter, which results in poor overlap of the pump and cavity modes over the waveguide length. This issue is crucial in the case of end-pumping. By properly controlling the pumping beam NA, the bulk crystal length, and the waveguiding slow-axis perpendicular to the active laser layer, 4 W of pumping power yielded 0.7 W of diffraction-limited ($M^2 < 1.5$) output power, with 45% slope efficiency at 15°C.[22] The experimental setup of the pumping scheme is presented in Fig. 10.11.

The laser output power at 1032 nm of the end-pumped planar-waveguide laser was measured with different output coupling mirrors. Laser oscillation at 1030 nm was observed at the ≈600-mW threshold with a maximum slope efficiency of 45%. The laser performance results are presented in Fig. 10.12, which also shows the various slope efficiencies.

The channel waveguide in the end-pumped case was rectangular, 100 μm × 80 μm surrounded by a 300-μm cladding of undoped YAG and pumped at 940 nm. The doping level was in the range of 5–20 at. % to ensure a large refractive index difference. It is not possible to increase the doping level to higher concentrations because of pairing effects in a highly doped Yb^{3+} system.

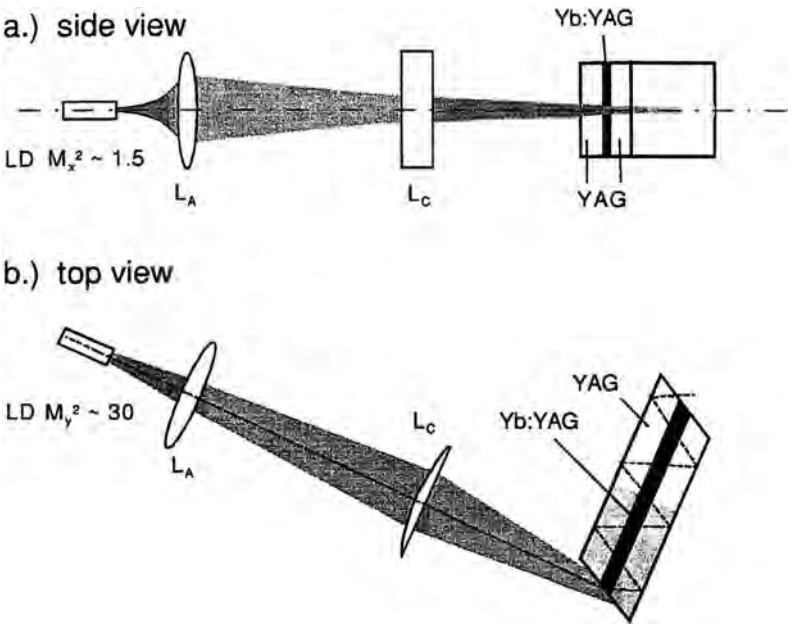

Figure 10.11 Pumping scheme of a double-clad planar-waveguide diode-pumped laser, where L_A and L_C are aspherical and cylindrical lenses, respectively. (Reprinted from Ref. 23 with permission from the Optical Society of America.)

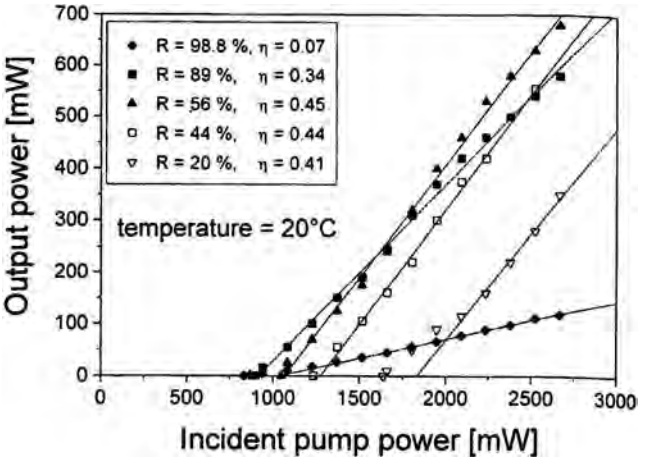

Figure 10.12 Laser output power as a function of diode-pumping power and slope efficiencies of end-pumped Yb (15 at. %):YAG channel waveguide laser. The experiment was performed with several output coupling reflectivities at 20°C. (Reprinted from Ref. 22 with permission from the American Institute of Physics.)

Diode-side-pumping of a diffusion-bonded Yb:YAG/YAG (core/double cladding) channel waveguide laser was reported as well by Griebner et al.[24, 25] The Yb (15 at. %):YAG channel waveguide laser with dimensions similar to those in end-pumping was operated at ambient temperature and produced ≈1-W output power with 43% slope efficiency and near diffraction-limited beam.[24] By improving the resonator optics to compensate for pumping-beam astigmatism, the waveguide channel laser produced 1.2 W at 1032 nm, with 30% slope efficiency.[25]

Recently two groups evaluated Yb-doped crystals as potential laser materials and amplifiers.[26, 27] Their results provide an analysis of the optimal length and concentration of the Yb^{3+} ion in various hosts. It was found that for several applications, particularly those involving small pumping densities and amplifiers, fluoroapatites and tungstate-doped crystals are attractive laser candidates.

References

1. H. W. Bruesselbach, D. S. Sumida, R. A. Reeder, and R. W. Byren, "Low heat high-power scaling using InGaAs-diode-pumping Yb:YAG lasers," *IEEE J. of Selected Topics in Quant. Electron.* **3**(1), 105–116 (1997); see also P. Lacovara, H. K. Choi, C. A. Wang, R. I. Aggarwal, and T. Y. Fan, "Room-temperature diode pumped Yb:YAG laser," *Opt. Letters* **16**(14), 1089–1091 (1991).
2. R. J. Beach, "CW theory of quasi-three level end-pumped laser oscillators," *Opt. Commun*. **123**, 385–393 (1995).
3. L. D. DeLoach, S. A. Payne, L. L. Chase, L. K. Smith, W. L. Kway, and W. F. Krupke, "Evaluation of absorption and emission properties of Yb^{3+} doped crystals for laser applications," *IEEE J. Quant. Electron*. **29**(4), 1179–1191 (1994).

4. S. A. Payne, L. K. Smith, L. D. DeLoach, et al., "Laser, optical, and thermomechanical properties of Yb-doped fluoroapatite," *IEEE J. Quant. Electron*. **30**, 170–179 (1994).
5. M. E. Innocenzi, H. T. Yura, C. L. Fincher, and R. A. Fields, "Thermal modeling of continuous-wave end pumped solid state lasers," *Appl. Phys. Lett*. **56**(19), 1831–1833 (1990).
6. W. Koechner, *Solid State Laser Engineering*, 5th Ed., p. 49, Springer-Verlag, Berlin, Heidelberg, and New York (1999).
7. D. C. Brown, "Ultrahigh-average-power diode-pumped Nd:YAG and Yb:YAG lasers," *IEEE J. Quant. Electron*. **33**, 861–873 (1997).
8. D. S. Sumida and T. Y. Fan, "Effect of radiation trapping on fluorescence lifetime and emission cross section measurements in solid state laser media," *Opt. Letters* **19**(17), 1343–1345 (1994).
9. Y. Kalisky, C. Labbe, K. Waichman, et al., "Passively Q-switched diode pumped Yb:YAG laser using Cr^{4+}-doped garnets," *Opt. Mater*. **19**, 403–413 (2002).
10. T. Y. Fan, "Heat generation in Nd:YAG and Yb:YAG," *IEEE J. Quant. Electron*. **29**(6), 1457–1459 (1993).
11. L. L. Chase, L. E. Davis, W. F. Krupke, and S. A. Payne, "Materials for diode pumped solid state lasers," *J. De Physique, Colloque C7, Supplément au Journal de Physique III* **1** C7-17–C7-22 (1991).
12. A. Giesen, H. Hugel, A. Voss, K. Wittig, U. Brauch, and H. Opower, "Scalable concept for diode-pumped high power solid state lasers," *Appl. Phys. B* **58**, 365–372 (1994).
13. D. J. Ripin, J. R. Ochoa, R. L. Aggarwal, and T. S. Fan, "165-W cryogenically cooled Yb:YAG laser," *Opt. Lett*. **29**(18), 2154–2156 (2004).
14. E. C. Honea, R. J. Beach, S. C. Mitchell, et al., "High power dual-rod Yb:YAG laser," *Opt. Lett*. **25**(11), 805–807 (2000).
15. C. Bibeau, R. J. Beach, S. C. Mitchell, et al., "High-average-power 1-μm performance and frequency conversion of a diode-end-pumped Yb:YAG laser," *IEEE J. Quant. Electron*. **34**(10), 2010–2019 (1998).
16. R. J. Beach, E. C. Honea, S. B. Sutton, et al., "High-average-power diode-pumped Yb:YAG lasers," Report UCRL-JC-133848 (1998); see also R. J. Beach, E. C. Honea, S. B. Sutton, et al., "High-average-power diode-pumped Yb:YAG lasers," *SPIE Proc.* **3889**, 246–260 (2000).
17. H. Bruesselbach and D. S. Sumida, "69-W-average-power Yb:YAG laser," *Opt. Lett.* **21**(7), 480–482 (1996).
18. D. S. Sumida, H. Bruesselbach, R. W. Byren, M. Magnir, and R. Reeder, "High power Yb:YAG rod oscillators and amplifiers," *SPIE Proc.* **3265**, 100–105 (1998).
19. A. Giesen, "Results and scaling laws of thin disk lasers," *SPIE Proc*. **5332**, 212–227 (2004).
20. L. Johannsen, S. Erhard, and A. Giesen, "Q-switched Yb:YAG thin disk laser," *OSA Trends in Optics and Photonics* **50**, 191–196, *Advanced Solid State Lasers* (2001).

21. J. Vetrovec, R. Shah, T. Endo, et al., "Progress in the development of solid state disk laser," *SPIE Proc*. **5332**, 235–243 (2004).
22. U. Griebner, R. Grunwald, H. Schoennagel, J. Huschke, and G. Erbert, "Laser with guided pump and free propagating resonator mode using diffusion bonded rectangular channel waveguides," *Appl. Phys. Lett*. **77**(22), 3505–3507 (2000).
23. U. Griebner, J. Huschke, R. Grunwald, S. Schoennagel, and C. Erbert, "Cladding-pumped Yb:YAG planar waveguide laser," *OSA Trends in Optics and Photonics (TOPS)* **34**, *Advanced Solid State Lasers*, 431–433 (2000).
24. U. Griebner, H. Schonnagel, "Laser operation with nearly diffraction-limited output from a Yb:YAG multimode channel waveguide," *Opt. Lett*. **24(**11), 750–752 (1999).
25. U. Griebner, R. Grunwald, and H. Schonnagel, "Thermally bonded Yb:YAG planar waveguide laser," *Opt. Commun*. **164**(4–6), 185–190 (1999).
26. G. L. Bourdet, "New evaluation of ytterbium-doped materials for CW laser applications," *Opt. Commun.* **198**, 411–417 (2001).
27. A. Brenier and G. Boulon, "New criteria to choose the best Yb^{3+}-doped laser crystals," *Europhys. Lett*. **55**(5), 647–652 (2001).

Chapter 11

More on Other Crystals: Fluorides and Vanadates

11.1 Introduction

The development of laser diode-pumped solid state lasers (LDPSSL) and laser diode technology has accelerated in the last 20 years and revolutionized solid state laser technology. The advent of new diode laser arrays, bars, and stackable diodes, as well as developments in other material science and optics fields, enhanced the development of LDPSSLs. These developments have led to novel laser crystals and unique optical methods to couple the diode light into the crystal.

A solid state laser system is a combination of both the hosting crystal and the doped ion. In the case of rare-earth ions, the emission bandwidth is relatively narrow. The type of the doped ion determines the peak of the laser emission wavelength. Therefore, one can control the emission-wavelength peak by selecting the appropriate ion. Examples were discussed previously and include Nd^{3+}, Yb^{3+}, Tm^{3+}, Ho^{3+}, and Er^{3+} for laser emission in the spectral range of 1–3 μm. Also, a spectral shift of the emission peak of the same ion doped in various hosts is influenced to a small extent by the crystal field of the solid state host. The emission peak of Nd:YAG is centered at 1060 nm, Nd:YVO_4 at 1064 nm, and Nd:YLF at 1047 or 1057 nm, depending on the emission polarization.

The thermal and mechanical properties of the laser crystals are dominated by the nature of the host laser crystal through the mechanical-strength parameters, thermal coefficient, hardness, elastic properties, thermal expansion coefficient, and other properties. The subject was discussed in more detail in Secs. 4.1 and 5.1.

Diode pumping is applied mainly to solid state laser systems that emit laser radiation in the spectral range of 1–3 microns; these ions include the rare-earth ions listed above doped in hosts such as YAG, YLF, YVO_4, SFAP [$Sr_5(PO_4)_3F$], SVAP [$Sr_5(VO_4)_3F$], and others. The main advantages of a LDPSSL, which make it technologically useful, are its efficiency, reliability, and compactness (see the appendix for more detail).

Efficient pumping depends on the pump power per unit area (pump density) of the pumping source. In particular, increasing the efficiency of the diode array

means an increase in the operating lifetime of the diodes, the reliability of the system, and the LDPSSL performance.

A main drawback of diode lasers (bars or stacked diode lasers) is their beam quality. Diodes usually have a highly divergent, astigmatic and noncircular beam profile as a result of the dimensions of the emitting region of the diode. The divergent angles (in degrees) are about 10 deg in the slow axis and 40 deg in the fast axis. This property significantly reduces the pump power density and the efficiency of the system.

11.2 Laser Crystals: YLF ($YLiF_4$) and YVO_4

An YLF-based fluoride laser host was discussed in Chapters 5 and 9. It was noted that an YLF crystal can be an alternative to YAG for specific applications, where the longer emitting level lifetime and the lower (than YAG) phonon energy are both exploited. This chapter explores another alternative host to YAG—crystals that belong to the vanadate family (YVO_4, $GdVO_4$)—and compares the properties of vanadates to both YLF and YAG and discusses their specific characteristics.

Both YLF and YVO_4 have unique properties that make them favorable candidates for laser materials. Both crystals produce polarized light. YLF-doped ions show weak thermal lensing because of the negative dn/dT, and this fact leads to better beam properties. The longer lifetime of Nd in YLF maximizes the energy stored in the Q-switched pulse; the natural birefringence eliminates the effects of stress-induced birefringence. However, one must take into account that the fracture strength of YLF is much greater than that of YAG. In terms of laser properties, the stimulated emission cross section in Nd:YVO_4 is much higher than in YAG and YLF. Also, Nd:YVO_4 can be diode-pumped continuously over the spectral range 801–821 nm. The YAG or YLF absorption band pumped by diodes is spiky, effective over 805–810 nm and 795–805 nm for Nd:YAG and Nd:YLF, respectively. The absorption peaks in the spectral region of 800 nm are 807.5 nm for Nd:YAG, 809 nm for Nd:YVO_4, and for Nd:YLF, 806 nm for σ polarization and 792.5 nm for π polarization. The broader absorption width of Nd:YVO_4 is advantageous in diode pumping where the wavelength stability requirements of the pumping diodes are not as critical as in YAG or YLF crystals.

The optical, mechanical, and thermal properties of YLF and YVO_4 are summarized in Tables 11.1 and 11.2. The data were taken from a data sheet from Northrop Grumman Corp., Poly-Scientific (formerly Litton Airtron, www.polysci.com), Saint Gobain Crystals and Detectors (formerly Union Carbide Corporation, www.crystals.saint-gobain.com), and from the home page of Schwartz Electro-Optics, Inc., Research Division (www.seord.com/research/cleo95pd.htm).

11.3 Pumping Schemes

With such highly divergent pump sources available, the goal in choosing a pumping scheme should be in finding one with a high power density and a good match

Table 11.1 Optical properties of YLF, YVO_4, and YAG.

Crystal	Wavelength (nm) $^4F_{3/2} \rightarrow {}^4I_{11/2}$	Gain cross section (10^{-19} cm^2)	Lifetime (μs)	Peak absorption (cm^{-1})
YLF (π)	1047	1.9–2.3	480–520	11
YLF (σ)	1053	π/1.5		4
YVO_4 (π)	1064	9.8–15.6 20	97	40
YAG	1065	3.3 7.6	240	10

Table 11.2 Thermal and mechanical properties of YLF, YVO_4, and YAG.

Crystal	Thermal conductivity (W/m K)	Expansion coeff. (10^{-6}/°C)	Refractive index at 1064 (nm)	Thermal shock (W/m)	dn/dT (10^{-6})
YLF	5.8 (c-axis) 7.2 (a-axis)	8 (c) 13 (a)	N(e) = 1.47 N(o) = 1.448	240	–4.3(e) –2.0(o)
YVO_4	5.2	11.4 (c) 4.43 (a)	N(e) = 2.168 N(o) = 1.958	—	+2.9(e) +8.5(o)
YAG	13	6.7	N = 1.82	1450	+7.3

(e) = extraordinary axis; (o) = ordinary axis; (a), (b), (c) = crystallographic axes.

between the pump and the laser mode volumes to ensure efficient operation of the whole laser system. Two pumping methods can achieve this goal: first, longitudinal or end-pumping, and second, transverse or side-pumping. The lasing medium can be either rod, disk, or slab geometry. In transverse or side-pumping, the laser material is illuminated perpendicular to the laser axis. The incident light must be absorbed within the laser host to obtain high gain from the lasing host and provide efficient side-pumping. This means that a trade-off occurs between the concentration of the active ions and the thickness of the laser material. The absorption length, which is relatively long in most solid state laser materials, can be controlled by changing either the rod size (diameter, length, or dopant concentration). Control over these two parameters is not always possible because of mechanical and physical constraints.

Side-pumping allows scaling of the output power to relatively high levels, beyond 10 W. Increasing the number of diodes around the laser rod is one technique for achieving this goal. However, the power of the pumping diodes cannot always vary to maximum levels and therefore quasi-CW diode lasers with high peak powers are usually used for transverse pumping. Side diode pumping is achieved by close-coupling (with or without collimating optics) the diode array to the lasing medium. This method requires special geometrical considerations and design to ensure homogeneous pumping; the output beam that results from such a scheme is not necessarily of high quality because of the poorer matching of the pump and the resonator mode volumes. A substantial increase in the output power of a side-

pumped laser can be achieved by using other geometries of the laser material such as "zig-zag" slabs or disks.

Another way to diode-pump solid state crystals, which leads to lower laser thresholds, is longitudinal- or end-pumping of the gain medium. In this method, the pumping beam is focused to a small spot area and is directed along the laser axis. If the beam quality is good enough it can be focused into a small spot area, thus increasing the laser gain and reducing the lasing threshold. The increase in the gain due to the tight focusing compensates for the relatively low output power of the end-pumping diode and enables the construction of efficient lasers. Reduction in the beam spot size, although desirable from mode-matching, gain, and laser threshold considerations, leads to undesirable diffraction effects. These effects can be controlled by manipulating the structure or the geometry of the lasing material. Longitudinal pumping results in an efficient, single-mode laser operation because of the possibility of mode-matching between the pump and the laser mode volumes.

The main drawback of end-pumping is that for high-power operation it is difficult to couple several diodes into small volume. This limitation may be overcome by using one of these methods:

1. Fiber coupling
2. Lens-duct coupling
3. Spatial stacking of diode arrays

Table 11.3 summarizes the main characteristics of side-pumping and end-pumping schemes.

Reports on the use of diode-pumped, Nd-doped crystals are published both in periodicals and numerous conference proceedings. These reports emphasize the performance of a system towards a specific use. Some of the main results of end-pumping and side-pumping of Nd-doped YVO_4 and YLF reported during the last

Table 11.3 Comparative characteristics of diode end- and side-pumping schemes.

Laser parameter	End-pumping	Side-pumping
Threshold	Low threshold power	More power can be concentrated into gain medium.
Gain	High-gain laser	Requires special engineering design to obtain high gain.
Efficiency	Efficient system	Gain depends on absorption length. Absorption length is limited by dopant density or rod diameter.
Mode matching	Possibility of mode-matching	There is no mode-matching; less efficient laser system.
Available output power	Limited to relatively low power diodes	High power can be achieved by surrounding diodes around the laser rod.

decade on both free-running and Q-switched devices will be presented and analyzed here. The diode-pumped rare-earth ions in YLF, including Nd:YLF, were discussed in Chapters 5 and 9. Further information on diode-pumped Nd:YLF will be presented, illustrating the specific advantages of Nd:YLF and Nd:YVO_4 over Nd:YAG.

11.3.1 Diode end-pumping of Nd:YLF

Nd:YLF is currently used for the generation of mode-locked short pulses with high peak power or frequency conversion techniques. (See, for example, general reviews on the subject in Refs. 1 and 2.)

The basic configuration of a diode end-pumped Nd laser (YLF or YVO_4) consists schematically of a diode-array pumping source, coupling optics that direct the diode light into the laser rod, and a resonator as first described by Sipes,[3] for a diode-pumped Nd:YAG system. The diode laser emits at about 806 to 809 nm at 25°C. Usually the diode emission is centered at 808 nm. The resonator has a two-mirror configuration (an output coupler and a high-reflectivity back mirror), and the laser rod is placed between them. Figure 11.1 shows schematically the simple linear configuration of an end-pumped Nd:YAG laser as operated by Sipes.[3]

Alternatively, the resonator can have a V-shaped geometry requiring three mirrors, as described below. The back mirror is also coated for high transmission (HT) at the pump wavelength, 808 nm. The back mirror can be the back surface of the crystal (e.g., YAG, YLF, or YVO_4), coated for HR at 1.06 μm and HT at 808 nm (see Ref. 3, Sipes). One important point to note from that work is the effect of pump beam spot size on photon conversion efficiency. For a spot size of 50 μm on the laser crystal, the photon conversion efficiency reaches the theoretical limit, which is about 65–70%. This general statement is true for most hosts doped with either rare-earth or transition-metal ions.

An interesting pumping geometry that ensures efficient end-pumping with good beam quality was presented by Turi and Juhasz.[4, 5] Their laser was intended to generate high peak power pulses in the picosecond time domain. This V-shape

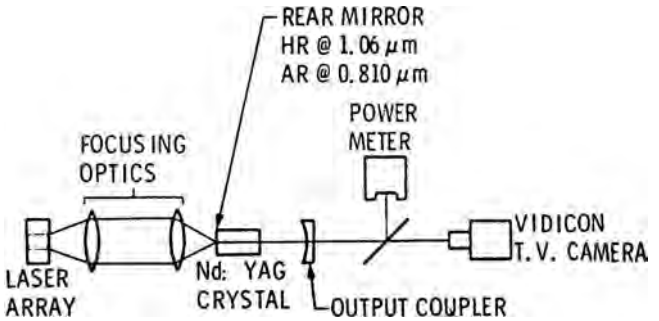

Figure 11.1 Schematic presentation of the experimental setup of a diode-pumped Nd:YAG in a linear, tightly focused resonator. (Reprinted from Ref. 3 with permission from the American Institute of Physics.)

or folded-cavity geometry is based on a Nd:YLF crystal, flat on one side and cut at Brewster angle for laser operation at 1047 nm (π polarization, $E \parallel c$) on the other side. This configuration compensates for astigmatism and ensures good beam quality without the need to use a mode-limiting aperture. A schematic diagram of this laser is presented in Fig. 11.2.

Note that the flat side of the crystal as well as the mirrors M1 and M2 are coated for HR at 1047 nm. The flat side of the crystal is also coated for HT at 798 nm for the pump source. The second mirror, M2, is of high reflectivity only for the application reported here, but can serve as an output coupler. The radius of curvature (ROC) of the two mirrors M1 and M2 are 75 cm and 200 cm, respectively. The 3-W diode laser was focused onto a 10-mm Nd:YLF (1.1 at. %) to a spot size of 150 μm × 220 μm. The laser also operated as a picosecond (ps) oscillator-amplifier and produced 500 μJ at 1-kHz repetition rate, with 7-W incident pump power (~7% total efficiency). Mercer et al.[6] used the same laser setup and pumping scheme, but introduced a half-wave plate to rotate the pump polarization vector to parallel the π axis to maximize the absorption of 798 nm in the Nd:YLF crystal. They obtained laser emission at 1053 nm with slope efficiency of 33%. The 1053-nm emission is σ polarized and is weaker by a factor of 1.5 than the π-polarized emission at 1047 nm. The experimental setup used by Mercer et al. to end pump Nd:YLF is presented in Fig. 11.3.

The importance of the pump diode spot size on laser performance can be seen in an earlier work of Turi et al.[7], using a V-shaped resonator. The spot size of their 15-W diode laser was higher than that usually employed for pumping a laser. They focused the pumping beam to a size of ~350 μm × ~750 μm. The slope efficiencies obtained were lower, with values of 18% TEM_{00} or 27% for multimode operation. Some of the significant results of diode-pumped laser performance characteristics of Nd:YLF are presented in Table 11.4. These results prove that using a tightly focused pump beam improves laser performance in terms of output power and efficiencies, which allows the use of less pump power.

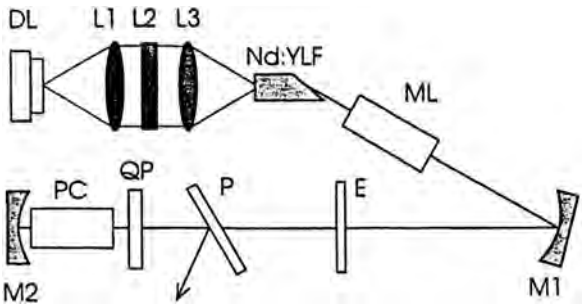

Figure 11.2 Schematic diagram of an end-pumped Nd:YLF laser, where DL is an SDL 2882 CW diode laser; L1, L2, and L3 are collimating lenses; ML is a mode locker; M1 and M2 are high reflectivity mirrors; E is an etalon; P is a polarizer; QP is a quarter plate; and PC is a Pockels cell. (Reprinted from Ref. 4 with permission from the Optical Society of America.)

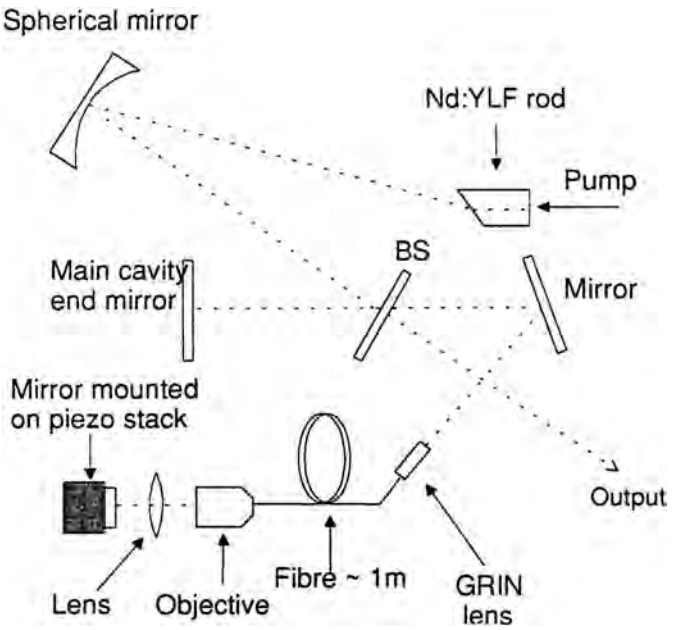

Figure 11.3 Experimental setup as described by Mercer et al.[6] and used for end-pumping of an Nd:YLF laser. (Reprinted from Ref. 6 with permission from Elsevier.)

Table 11.4 Typical performance characteristics of an end diode-pumped Nd:YLF laser. The last row in the table presents transverse pumping data for Nd:YLF.

Author/Year	Configuration	Maximum output power (W)	Efficiency	Remarks
Mercer et al.[6] (1994)	V-shaped	1.0	33% TEM_{00}	$R_{out} = 90\%$
Turi et al.[4, 5] (1995)	V-shaped	1.26 1.9	18% TEM_{00} 27% multimode	$P_{th} = 0.6$ Watt
Turi et al.[4, 5] (1995)	V-shaped	1.2 TEM_{00}	40%	$R_{out} = 90\%$
Zehetner[8] (1995)	V-shaped	1.150 multimode 1.05 TEM_{00}	68% (slope) 71% (slope)	$R_{out} = 93\%$
Lee et al.[10] (1997)	Plano-concave	2.6	38%	$R_{out} = 93\%$
Model MPS-1047-CW (Schwartz Electro-Optics, Inc., data sheet)	Segmented configuration	13, $M^2 < 1.2$ 16, multimode	70% (total efficiency)	Side-pumping

Zehetner[8] reported a similar setup with slightly different collimating optics. The pump source, a 3-W SDL CW operated at 798 nm, was focused into a 380-μm spot size inside the 10-mm YLF crystal. The crystal was mounted on a heat sink with Peltier cooler. The laser performance characteristics at room temperature are

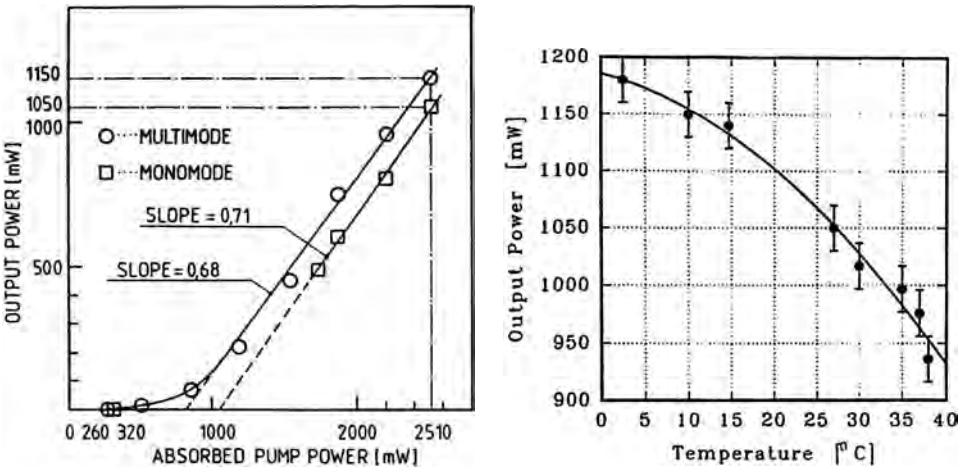

(a) (b)

Figure 11.4 (a) CW diode-pumped Nd:YLF laser performance operated both in single mode and multimode at room temperature; (b) laser performance of multimode Nd:YLF laser crystal at 2510-mW absorbed power as a function of surface temperature of the crystal. (Reprinted from Ref. 8 with permission from Elsevier.)

presented in Fig. 11.4(a) and are also summarized in Table 11.4. An improvement in laser performance was obtained by cooling the crystal, as is clearly shown in Fig. 11.4(b).

Another end-pumping option is to use a fiber-coupled diode array to pump the Nd:YLF, as reported by Lincoln and Ferguson.[9] The experimental setup is similar to those reported earlier, but the Nd:YLF was end-pumped by a 5-W, fiber-coupled diode array (SDL 3490) with wavelength peak at 797 nm. The pump light coming from the fiber (with a core diameter of 400 μm) was focused into the laser rod by a pair of 8-mm focal length collimating lenses. That focusing technique produced a beam waist that matches the fundamental mode size of the resonator and yields efficient laser output.

Free-running operation of diode-pumped 1 at. % Nd:YLF produced 2.6-W CW output power with 7-W input power at the crystal surface.[10] The Nd:YLF itself was of dimensions $\varnothing 2 \times 20$ mm, flat/flat, with one side coated for HR at 1047 nm. The rod was end-pumped through the HR coating at a 793-nm pumping wavelength. This laser was passively Q-switched by inserting Cr^{4+}:YAG at Brewster angle inside the cavity. It produced 18-ns pulses at a 7-kHz repetition rate, with energy of 93 μJ per pulse. Although the current results are quite impressive, one should keep in mind that in the early 1990s, several reports showed good performance parameters for diode end-pumped Nd:YLF lasers, such as low thresholds (<1 mW) or high efficiencies.[1] The efficiencies reported were up to 40% with 10-W TEM_{00} in the CW operating mode. In a Q-switched mode, diode-pumped Nd:YLF yielded up to 70-kW peak power at a pulse duration of less than 10 ns.

11.3.2 Side-pumping of Nd:YLF

Commercially available diode-pumped Nd:YLF lasers were developed by Schwartz Electro-Optics, Inc. (model MPS-1047-CW), and the details are available from the Internet. Side-pumped Nd:YLF by 20-W diode laser bars in a segmented configuration produced linearly polarized 13 W at 1047 nm, with a total efficiency of 33%, slope efficiency of ~70%, and a beam quality of $M^2 < 1.2$. Multimode output power was near diffraction limited, with output power of >16 W. The experimental setup of this commercial laser design is presented in Fig. 11.5. The diode bars were coupled through a fiber lens into the rod to establish a planar gain region. The Nd:YLF rod (3 cm long) had a segmented dielectric coating to allow for double-pass absorption.

The commercial Nd:YLF laser was also Q-switched (MPS-1047-QS), and it produced pulses of <40-ns pulsewidth at repetition rates of 5–120 kHz. Figure 11.6 presents the results in more detail. The performance of the Q-switched laser is

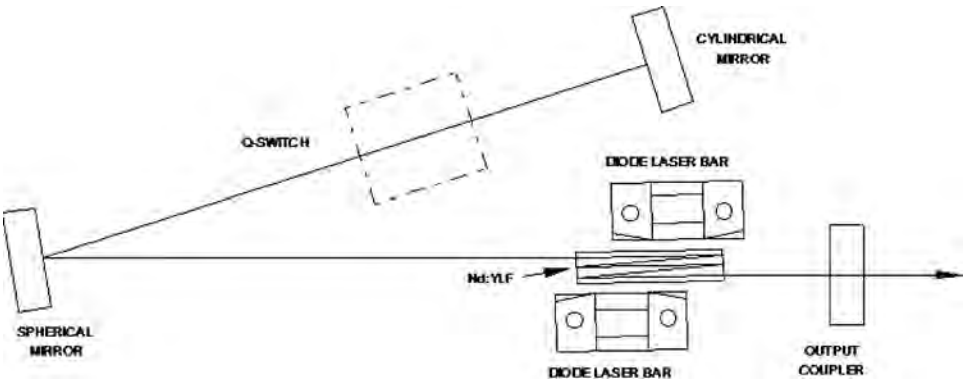

Figure 11.5 Schematic layout of a diode side-pumped Nd:YLF laser. (Courtesy of OSI Systems Inc.)

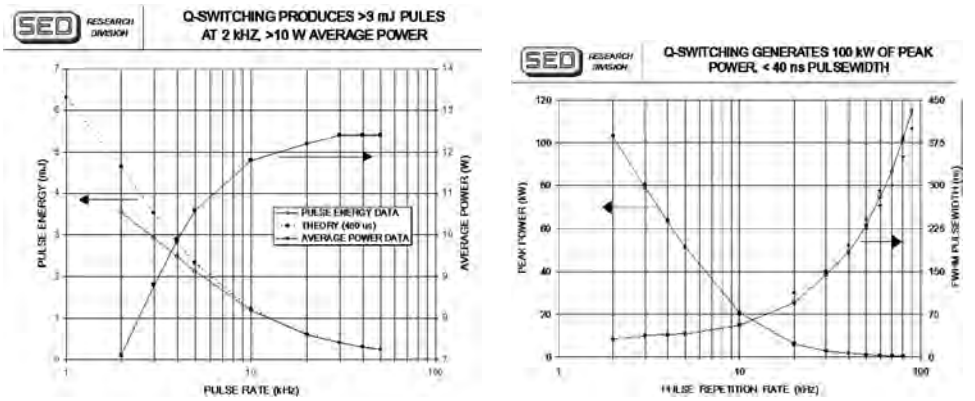

Figure 11.6 Performance of Q-switched option of Nd:YLF laser, model MPS-1047-QS. (Courtesy of OSI Systems Inc.)

quite remarkable. It produced >3 mJ (>100 kW peak power) at a 2-kHz repetition rate. The Q-switching was obtained by incorporating an intracavity, acousto-optic Q-switch element into the laser resonator.

11.4 Diode End-Pumping of Nd:YVO_4 and Nd:$GdVO_4$

Diode-pumped solid state lasers based on vanadate crystals, namely Nd:YVO_4 and Nd:$GdVO_4$, are considered the most efficient diode-pumped lasers for both side and longitudinal pumping modes. In several cases, the vanadate crystals have replaced the commonly used Nd:YAG active medium. The vanadate crystal belongs to the tetrahedral crystallographic system. In doping, the Y^{3+} ions are replaced by the rare-earth ions and surrounded by four O^{-2} ions at the corners of a tetrahedron with a local symmetry that applies to low rare–earth-ion concentration. At high doping levels, the dopant ions may cluster, which affects the crystal field and observed spectra.

A detailed spectroscopic study of Nd:YVO_4 and Nd:$GdVO_4$ described the f-states in terms of the irreducible representations of the T_d group. It was found that the position of the transition lines of Nd^{3+} in the two vanadate crystals was identical, resulting from the shielding of the f-electrons by the closed 5-s and 5-p shells.[11]

The study of the operating parameters of diode-pumped solid state lasers based on vanadate laser crystals has resulted in numerous publications and unique products used as laser sources. The following section outlines some of the special characteristics of vanadate hosts as well as their drawbacks.

11.4.1 Advantages and disadvantages of vanadate crystals

YVO_4 and $GdVO_4$ are uniaxial crystals in which the yttrium (Y) or the gadolinium (Gd) possess eight-fold coordination. The Nd^{3+} ion substitutes the Y^{3+} or Gd^{3+}. However, since the ionic radius of Nd^{3+} is similar to that of Gd^{3+}, the distribution coefficient of Nd^{3+} in the $GdVO_4$ crystal is higher than that in YVO_4 and it is assumed that the former crystal will be of higher quality, with higher and more homogeneous doping levels.

One major drawback of the vanadates is the difficulty of crystal growth, which stems from the fact that under low oxygen pressure during crystal growth, V^{5+} transforms into V^{3+}. On the other hand, higher oxygen pressure, which will drive more V^{5+}, will also enhance the unwanted chemical reaction between the oxygen and the crucible at the temperature of the crystal growth, namely at 1810°C. Other drawbacks are the possibility of upconversion processes, concentration quenching, and excited state absorption (ESA). The ESA was found to be a small loss for the 1064-nm laser emission for both π- and σ-polarizations in vanadates, with a typical ESA cross section of $\sigma_{ESA} \approx 5 \times 10^{-20}$ cm^2, but deleterious to the 1340-nm laser emission.[12] Since an overlap occurs between the ESA and the 1.34-μm

gain curve, the stimulated emission cross section for 1.34 μm will be lower than that of 1.06-μm for both Nd:YVO_4 and $GdVO_4$.

The vanadates have some significant advantages:

- Low lasing threshold and high slope efficiency.
- Higher stimulated emission cross section (five times higher) than Nd:YAG at 1064 nm.
- Higher absorption cross section around 808 nm, up to four times higher relative to Nd:YAG for π polarization. Also, the absorption bandwidth, around 808 nm, is much broader than for Nd:YAG, so more flexibility exists in the available pumping wavelength and diode temperature control. This affects the effective operating lifetime of the diode, especially in cases where aging shifts the diode wavelength.
- The absorption spectrum of Nd:YVO_4 is flat and continuous over 21 nm of the absorption band, compared with $\approx$5 nm for Nd:YAG. The absorption of Nd:YAG is spiky and narrower and therefore the pump light cannot be utilized efficiently. (The diode bandwidth is 2–3 nm in the relevant pumping wavelength range). The wavelength range at which 75% of the pumping power will be absorbed in a 5-mm sample is 15.7 nm and 2.5 nm for Nd:YVO_4 and Nd:YAG, respectively.
- The laser emission is polarized—there is no need for any external device to generate polarized light.
- The $GdVO_4$ crystal has optical and mechanical properties similar to YVO_4. Its absorption coefficient at the pumping wavelength is superior to that of Nd:YVO_4 or Nd:YAG under the same experimental conditions. However, it is important to note that the thermal conductivity along one of its crystallographic axes is much higher than the values for an YVO_4 crystal and is similar to that of YAG. For example, the thermal conductivity of Nd:$GdVO_4$ at 300 K is 12.3 $\mathrm{W\,m^{-1}\,K^{-1}}$.[13] Recent results indicate that the thermal conductivities along the [100] direction for 0.5 at. %. Nd:YVO_4 and 0.5 at. % Nd:$GdVO_4$ are 11 ± 0.8 $\mathrm{W\,m^{-1}\,K^{-1}}$ and 8.3 ± 0.6 $\mathrm{W\,m^{-1}K^{-1}}$, respectively.[14]
- The saturation fluence and the laser threshold of Nd-doped vanadates is higher than the corresponding value of Nd:YAG because of the higher values of $\sigma_{em} \cdot \tau_{em}$ in vanadates ($7.6 \times 10^{-17}\,\mu\mathrm{s\,cm^2}$), compared to the same values in Nd:YAG ($6.7 \times 10^{-17}\,\mu\mathrm{s\,cm^2}$). This point will be discussed further in this chapter.

The comparison between the absorption spectra of Nd:YAG and Nd:YVO_4 is demonstrated in Fig. 11.7.

The difficulties associated with the growth of high-optical-quality vanadate crystals (see, for example, Ref. 16), resulting in the growth of small crystals, makes the vanadates suitable mainly for end-pumping. Most of the results available in the literature are of end-pumping configurations. Table 11.5 summarizes the optical

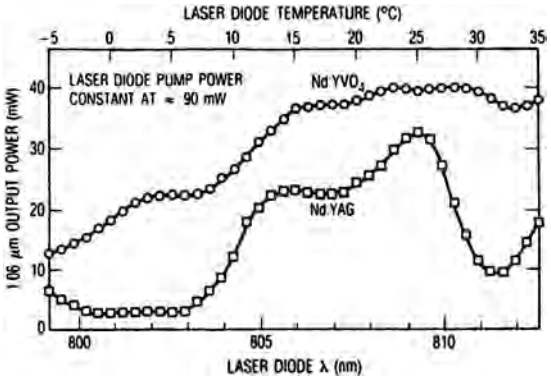

Figure 11.7 Absorption spectra of Nd:YAG and Nd:YVO_4 as a function of the diode-pumping wavelength and its operation temperature. (Reprinted from Ref. 15 with permission from the American Institute of Physics.)

Table 11.5 Different physical and optical properties of Nd:YAG, Nd:YVO_4, and Nd:$GdVO_4$ laser crystals. (Except where noted, data were taken from Ref. 66.)

Characteristics	**Nd^{3+}:YAG**	**Nd^{3+}:YVO_4**	**Nd^{3+}:$GdVO_4$**
Nd^{3+} concentration (10^{20} cm^{-3})	1.38 [1 at. %]	1.37 [1.1 at. %]	1.5 [1.2 at. %]
λ_{em} (nm)	1064.15	1064.30	1063.6
σ_{em} (10^{-19} cm^2) at 1.06 μm	2.8	15.6 25	7.6 [$E \parallel c$]
σ_{abs} (10^{-19} cm^2)	0.7 at 808 nm	2.3 at 810 nm	3.1–5.2 [$E \parallel c$] at 808.5 nm
Fluorescence lifetime (μs)	240 [0.7 at. %]	[1.1 at. %] ≈ 99–90 [2.8 at. %] ≈ 50	[1.2 at. %] ≈ 90–100 [3 at. %] ≈ 50
Refractive index (at 1.06 μm)	1.82	$n_o = 1.9573$ $n_e = 2.1652$	$n_o = 1.97161$ [$E \perp c$] $n_e = 2.19196$ [$E \parallel c$]
Density	4.54	4.22	5.48
Thermal conductivity ($W \cdot m^{-1} \cdot K^{-1}$)	13 9.76	$C_{//} = 5.23$ $C_{\perp} = 5.10$	[110]: 11.7 [001]: 12.3 (Ref. 13)
Thermal expansion coefficient (10^{-6} K^{-1})	[100]: 8.2 [010]: 7.7 [001]: 7.8	[100] and [010]: 4.43 [001]: 11.37	1.5 (along a) 7.3 (along c)
$\frac{dn}{dT}$ (10^{-6} K^{-1})	7.3	[100] and [010]: 8.5 [001]: 3	5.4 (Ref. 17) —
Δλp (nm, FWHM)	0.9	1.7	1.6
Hardness (moh)	8.5	≈5	—

and physical properties of Nd:YVO_4 and Nd:$GdVO_4$ in comparison with the relevant values of Nd:YAG.

As can be observed from Table 11.5, the vanadates have higher thermal lensing and astigmatism than the YAG because of the higher, asymmetric value of the dn/dT value for YVO_4. Nd-doped vanadates have shorter lifetimes than Nd:YAG, requiring more peak power from the pumping diodes. Also, the crystal quality of

YVO_4 is much lower than that of YAG. Passive losses at 1064 nm are 0.003 cm^{-1} for YAG and 0.02 cm^{-1} for YVO_4.

The laser threshold can be calculated using the formula presented in Ref. 18. The estimated laser threshold in Nd:YAG and Nd:YVO_4 is based on the data from Table 11.5 and on a formula that relates the laser threshold to physical parameters,

$$P_{\text{th}} = \frac{L \cdot h \cdot \nu_{\text{p}} \cdot V_{\text{eff}}}{2 \cdot l \cdot \sigma_{\text{em}} \cdot \tau \cdot \eta_{\text{p}} f_{\text{B}}}, \tag{11.1}$$

where P_{th} is the threshold power, L is the round-trip cavity loss, l is the cavity length, V_{eff} is the effective mode volume (which takes into account the overlap of the cavity and pumping modes), σ_{em} is the laser emission cross section, τ is the fluorescence lifetime of the lasing level, η_{p} is the absorption efficiency, f_{B} is the fractional Boltzmann distribution in the emitting state, and $h\nu_{\text{p}}$ is the energy of the pump photon. The value of f_{B} for Nd:YVO_4 is 20% greater than for Nd:YAG. From this formula, the threshold-pumping ratio for vanadates and YAG can be obtained:

$$\frac{P_{\text{th}}(\text{YVO}_4)}{P_{\text{th}}(\text{YAG})} \cong 0.35. \tag{11.2}$$

The first efficient diode end-pumped Nd:YVO_4 was reported by Fields, Birnbaum, and Fincher,[15] who obtained about 50% efficiency by pumping 1 at. % of Nd^{3+} doped in an YVO_4 crystal. The Nd:YVO_4 laser rod was coated on one side for HR at 1064 nm and HT >96% at 809 nm, and pumped at the maximum pump power of 270 mW. The TEM_{00} pump power was focused into a spot with a 180-μm waist diameter. The first performance of the diode end-pumped laser, e.g., output power as a function of the optical diode power for both Nd:YVO_4 and Nd:YAG, is shown in Fig. 11.8 and summarized in Table 11.6, which exhibits comparative results of the Nd:YVO_4 laser performance under different pumping configurations.

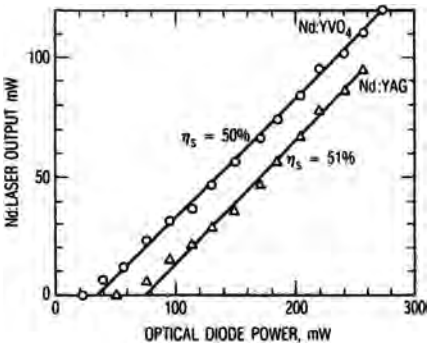

Figure 11.8 The measured output power of diode-pumped Nd:YVO_4 and Nd:YAG lasers as a function of the optical power of diode laser. (Reprinted from Ref. 15 with permission from the American Institute of Physics.)

Table 11.6 Typical performance characteristics of diode end-pumped Nd:YVO_4 and Nd:$GdVO_4$ lasers.

Author/year	Configuration	Maximum output power (W)	Efficiency	Remarks
Fields et al.[15] (1987)	F/F cavity, one face-coated HR	120 mW	50%	10 mW threshold (YVO_4)
Feugnet et al.[18] (1994)	Plano-concave	0.74 mJ	35%	Monolithic surface emitting laser diode (M-SLED) $R_{out} = 96\%$ (YVO_4)
Feugnet et al.[19] (1995)	F/F cavity, one face-coated HR	7 mJ at 100 Hz	50–53% (optical/optical and slope) TEM_{00}, $M^2 \leq 1.1$	$R_{out} = 96\%$ QCW mode at 100 μs (YVO_4)
Koch et al.[21] (1997)	Disk laser, both faces coated, plano concave ROC = 1 M	2.9 W at 10-W input 4.4 W	30% (optical/optical) 35% (slope) $M^2 = 1.05$ 44% $M^2 \approx 1.5$	$R_{out} = 95\%$ (YVO_4)
Brown et al.[47] (1997)	Plano-concave, end-pumping, end-cooled, active mirror config., ROC = 5 cm, resonator length: 4.9 cm	2-W output at 4-W pumping power	49% (optical/optical) $M^2 = 1.08$	$R_{out} = 90\%$, 1-mm crystal thickness, 2 at.% Nd^{3+} doping, HR coating on one face, AR on the other face
Krainer et al.[48] (1999)	Plano concave resonator ROC = 10 mm	198 mW (ave.), 12.6-GHz rep. rate, 8.3-ps pulsewidth	22% (slope)	$R_{out} = 99.6\%$, linear cavity, passive-mode locking by SESAM* (YVO_4), flat Brewster, 3 at. %
Liu et al.[49] (1999)	F/F resonator, end-pumped	8.6-W TEM_{00} $M^2 = 1.22$ Multimode: 11.2 W, $M^2 < 2$	43% (conversion) 48% (slope) 51% (conversion) 55% (slope)	$GdVO_4$
Liu et al.[29] (1999)	Plano-concave, ROC = 200 mm	14.3 W at 26-W pump power	55% (conversion) 62% (slope), $M^2 < 1.8$	Max. results at $R_{out} = 95\%$, Nd^{3+}: 0.5 at. % Laser rod: AR/AR
Wyss et al.[50] (1999)	Monolithic microchip laser at 1.06 μm	5-W at 25-W pumping power	22% (slope) M^2: 3–36	QCW operation $R_{out} \approx 99.5\%$ Cavity length 2.5 mm

Feugnet et al. (Ref. 18) from Thomson CSF Laboratories (now Thales) obtained efficient lasing (32%, diffraction limited) by end-pumping Nd:YVO_4 with monolithic surface-emitting laser diodes (M-SLED), a subject discussed in several

Table 11.6 (Continued).

Author/year	Configuration	Maximum output power (W)	Efficiency	Remarks
Liu et al.[51] (2000)	Concave/concave (532 nm), KTP	3.6 W, 532 nm	22.5% (slope), $M^2 = 1.55$	$R_{out} = 75$–95% (for 1.06 μm), CW operation
	Concave/flat (1.06 μm)	10.1 W, 1.06 μm	55% (slope), 46% (conversion), $M^2 = 1.69$	($GdVO_4$)
Li et al.[52] (2000)	Plano-concave folded V-cavity, ROC = 100 mm, one side HR at 1.06 μm	2.1 W (ave.) 625-W peak, pulsewidth: 45 ns, rep. rate: 125 kHz	31.6%	$R_{out} = 95\%$ Passively Q-switched with Cr^{4+}:YAG
Lupei et al.[23] (2003)	End-pumping, plano-concave, resonator length: 30 mm, ROC = 50 mm	1.34-W output at 1.71-W pumping power	80% (slope)	0.5 at. % and 1/0 at. %, 879 nm Ti:Sapphire pumping at 879 nm, R_{out}: 80–97%
Ostroumov et al.[46] (1996)	End-pumping, plano-concave resonator, 22 mm resonator length, ROC = 50 mm	550 mW at 1.8-W absorbed power	41% (slope)	Nd (1 at. %): $Gd_{0.5}La_{0.5}VO_4$, $R_{out} = 95\%$ (mixed vanadates)
He et al.[17] (2004)	Plano-concave resonator, ROC = 100 cm	15.6 W, 1063 nm 7.5 W, 1342 nm	65.1% (slope), $M^2 = 1.54$ 32.2 % (slope), $M^2 = 1.4$	Nd^{3+}: 0.5 at.%, one side of the rod: HR Dual wavelength: 1.8 W at 1063 nm, 2 W at 1342 nm

* SESAM is the semiconductor saturable absorber mirror.

publications. The method presented in Ref. 18 uses the broad area of a special structure of the emitting diode, which consists of a grooved surface and integrated mirrors. This structure, operated in a QCW mode (200-μs long pulse at 50 Hz), can deliver up to 1-kW peak power from an emitting area of 1.3 cm^2. The 808-nm light was coupled with two AR-coated aspheric lenses into an a-cut Nd:YVO_4, 3 mm long, AR-coated on both sides, uncooled and oriented for maximum absorption. The beam quality was nearly diffraction-limited, with a value of $M^2 \leq 1.1$. A comparative experiment with Nd:YAG at the same experimental conditions yielded 15% optical-optical efficiency.

A novel way to scale up the output energy and still keep good beam quality and efficiency was further proposed by Feugnet et al.[19] In this scheme, the authors used a lens duct to collect the high-power, highly divergent light to pump laser crystals longitudinally. The pumping laser used was a diode-array model SDL-3251 A1, which could deliver 9 mJ in a 100-μs pulse duration. The laser crystal was Nd:YVO_4 (Nd^{3+} density of 1 at. %), whose dimensions were 5×5 mm in cross section and 3.6 mm long. One face of the crystal was HR coated for 1064 nm, while

the other side was AR coated for 1064 nm. The output coupler was a flat (F/F) mirror of $R = 96\%$. The YVO_4 crystal was placed on a copper holder with an indium foil for better thermal contact, and was oriented to maximize the absorption of the polarized pump light. For pump energies up to 7 mJ incident upon the vanadate rod after the lens duct, the laser delivered 3.5 mJ of output energy. The pulsewidth was 100 μs, and the repetition rate was 100 Hz. For the 200-μs pulsewidth, a 7-mJ output for a 14-mJ input was observed. The performance results are presented in Fig. 11.9 and summarized in Table 11.6.

Since the absorption and emission cross section of Nd:YVO_4 parallel to the π polarization vector is high—about 25–30 cm^{-1} at 809 nm—it is possible to use vanadate crystals with a small absorption path length. A result of such argument is an intracavity-doubled Nd:YVO_4 laser highly doped (2 at. % of Nd^{3+}), with small crystal dimensions, 1 mm thick.[20] This setup is similar in principle to a Nd:YVO_4 microlaser. The subject of microlasers based on Nd:YLF and Nd:YVO_4 has been studied extensively worldwide. However, it is beyond the scope of this book. More information about microlasers can be found in Ref. 67. The configuration discussed above[20] combined with a novel beam-shaping technique of the diode bar yielded efficient intracavity-doubled Nd:YVO_4 with an excellent beam quality of $M^2 \leq 1.1$, and an output power of 3.5 W at 532 nm with 14.7-W pump power at the crystal.

Further improvement in CW diode-pumped laser performance of Nd:YVO_4, which utilizes the advantages of the vanadate host, was presented by Koch et al.[21] Detailed experimental results are presented in Table 11.6. They used a thin disk of 0.2-mm thick by 4-mm diameter, doped by 1.1 at. % of Nd^{3+}. The vanadate crystal was AR coated on the front side for the pump and emission wavelengths (808 nm and 1064 nm, respectively) and its back surface was HR coated for both wavelengths. A fiber-coupled diode laser (JENOPTIK JO LD 10FH) pumped the

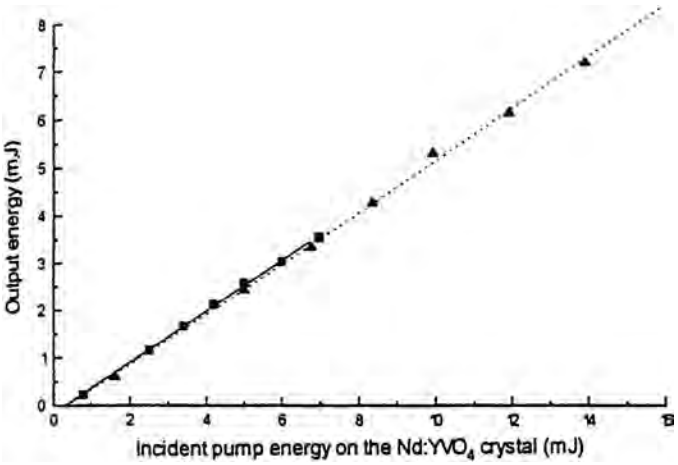

Figure 11.9 Output energy as a function of pump energy for a 100-μs pulsewidth (solid curve) and 200-μs pulsewidth (dotted curve). (Reprinted from Ref. 19 with permission from the Optical Society of America.)

crystal, with power of 10 W at the end of the optical fiber. The pump beam was imaged onto the crystal center by means of several mirrors, therefore obtaining four double passes of the pump light through the crystal. More improvements in thermal management and doping optimization yielded more than 10-W CW output power with 54% slope efficiency in TEM_{00} mode from an end-pumped Nd:YVO_4.[22]

Recently, Lupei et al.[23] reported highly efficient 1063-nm CW laser operation in Nd:$GdVO_4$ by pumping into the $^4F_{3/2}$ state ($^4I_{9/2} \rightarrow {}^4F_{3/2}$) at 879.1 nm ($\pi$ polarization, $E \parallel c$), using a Ti:Sapphire laser. They reported a maximum slope efficiency of ≈80% with 1.34-W output power at 1.71-W pumping power. The slope efficiency reached up to 70% when they changed the pumping wavelength to 808 nm under the same experimental conditions. The laser performance was identical to low and high Nd^{3+} doping levels, e.g., 0.5 at. % and 1.0 at. %, respectively.

Figure 11.10 presents the output power of a Nd:YVO_4 disk laser as a function of the pump power coming from the end of the fiber, with an output coupler of $R_{out} = 95\%$. The experimental results are also summarized in Table 11.6.

Other rare-earth-doped YVO_4 such as Ho:YVO_4, Tm:YVO_4, or Er:YVO_4 have already been investigated in terms of fluorescence dynamics[24] and laser performance, both in doped or codoped configurations. In particular, such a study was focused towards compact laser systems and microchip lasers emitting at 2 μm.[25] The Ho^{3+} emission at ≈2 μm can be sensitized by a Tm^{3+} ion pumped by a diode array at 805 nm. The absorption cross section at 805 nm is 1.4×10^{-20} cm^2, and the uniform absorption bandwidth is 26 nm, which is larger than the absorption features of Tm:YAG or Tm:YLF.[26] The peak emission cross sections of Tm:YVO_4 and Ho:YVO_4 laser crystals are similar: 1.6×10^{-20} cm^2 (at 1800 nm) and 1.6–1.7×10^{-20} cm^2, respectively.[27, 28]

The $GdVO_4$ crystal is also an attractive candidate as a host for ion-doped, diode-pumped solid state lasers, with such ions as Nd^{3+}, Tm^{3+}, Ho^{3+}, or Er^{3+}, as

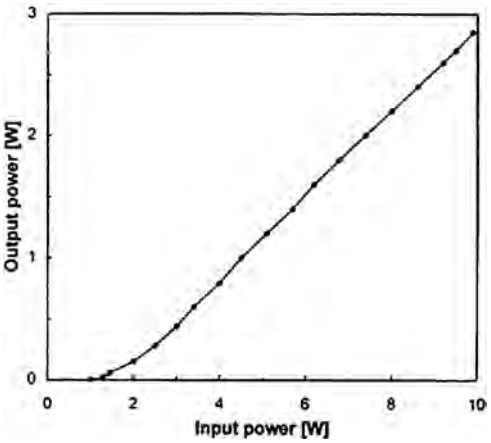

Figure 11.10 Output power of a Nd:YVO_4 disk laser as a function of diode optical input power. (Reprinted from Ref. 21 with permission from the Optical Society of America.)

can be observed from Table 11.5. The $GdVO_4$ crystal has several advantages over an YVO_4 host:

- Generally, the absorption coefficient of Nd:$GdVO_4$ is higher than Nd:YVO_4 or Nd:YAG.
- More specifically, the absorption coefficient (and cross section) around the 808-nm band and in the π polarization is two times higher than Nd:YVO_4 and seven times greater than the value for Nd:YAG. See also Fig. 11.11.
- The thermal conductivity of $GdVO_4$ along the <110> direction is, unexpectedly, as high as the value for YAG.
- The absorption bandwidth is higher than Nd:YAG.

Presently, numerous publications contain information on efficient, free-running, diode-pumped Nd:$GdVO_4$ performance as well as actively or passively Q-switched lasers, at 1062 nm and 1342 nm. The Nd:$GdVO_4$ can be operated on single and dual wavelengths in both CW and quasi-CW modes. A fiber-coupled, diode end-pumped Nd (0.5 at. %):$GdVO_4$ laser emission at 1.06 μm has produced 14.3 W with 62% slope efficiency and 55% optical conversion efficiency.[29] The Nd (2.0 at. %):$GdVO_4$ began to saturate at a high pumping level because of thermal lensing resulting from the high absorption of the pumping light. The beam quality at the maximum pumping power (26 W) was $M^2 < 1.8$. Figure 11.12 demonstrates the laser performance of a diode-pumped Nd (0.5 at. %):$GdVO_4$ as a function of the incident pumping power at three different output couplers.

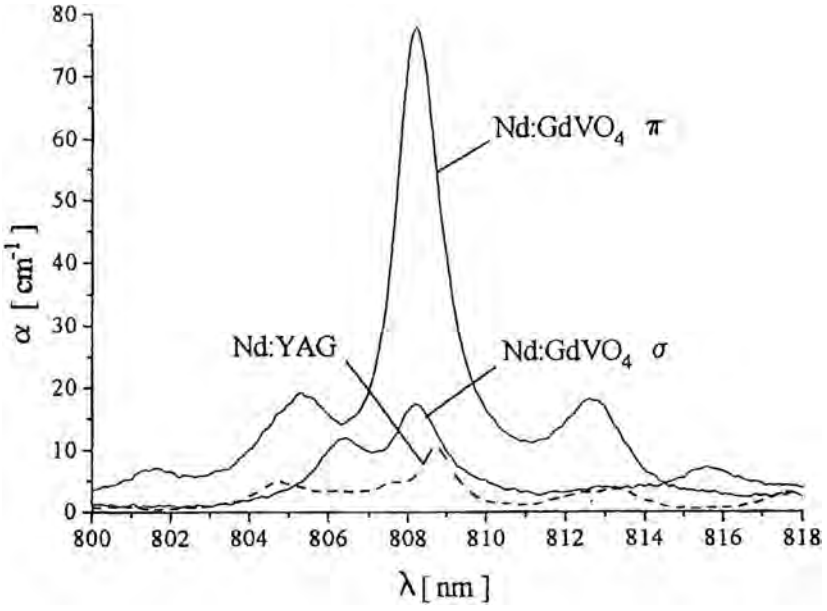

Figure 11.11 Absorption spectra ($^4I_{9/2} \rightarrow {}^4F_{5/2}$ transition) of a Nd (1.2 at. %):$GdVO_4$ in π- and σ-polarizations, and of Nd (1.1 at. %):YAG (unpolarized) at a temperature of 300 K. (Reprinted from Ref. 65 with permission from Springer-Verlag.)

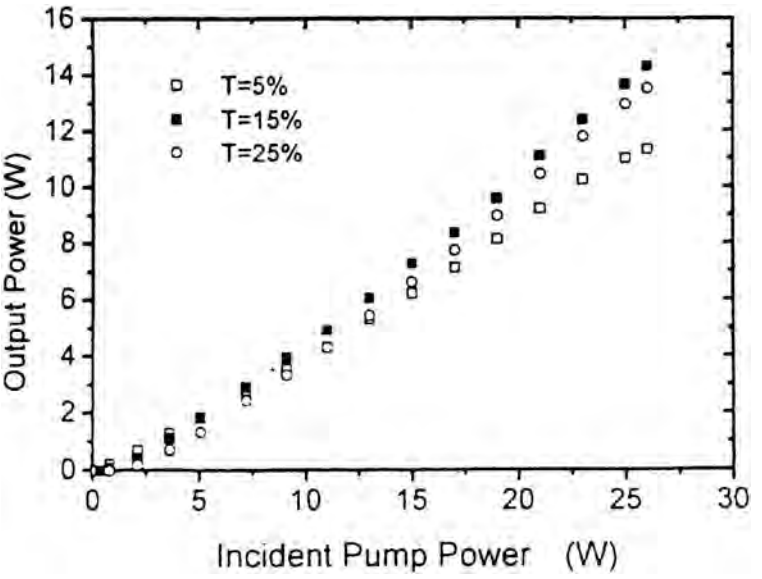

Figure 11.12 Output power as a function of incident pumping power of a fiber-coupled, diode-pumped Nd:$GdVO_4$ laser. (Reprinted from Ref. 29 with permission from Springer-Verlag.)

The simultaneous generation of efficient red, green, and blue (RGB) light has important technological implications and can be obtained by doubling and tripling a diode-pumped, Q-switched 1342-nm and 1063-nm Nd:$GdVO_4$ laser emission.[30] CW dual-mode operation of Nd:$GdVO_4$ produced 1 W at 1.063μm and 1.4 W at 1.34 μm.[13] Low concentrations (0.3 at. %) of Nd:$GdVO_4$ performed better than the high doping level (1.14 at. %) and produced 8.2 W at 1.34 μm under laser diode-array pumping, with ≈30% slope efficiency. By using intracavity doubling of the 1.34-μm emission of Nd:$GdVO_4$, 2.4 W of red emission at 670 nm with a 26% optical efficiency and a near-diffraction-limited beam were obtained.[31] Previous results indicated that 670-nm red emission could be modulated up to 15 kHz and a laser peak power of ∼11 kW.[32] Using intracavity, frequency-doubled, end-pumped Nd:$GdVO_4$/KTP that was also acousto-optically Q-switched, an output power of 3.75 W at 532 nm, with repetition rates in the 10- to 50-kHz range and pulsewidths as short as 35 ns, was achieved.[33] The optical and intracavity frequency-doubling efficiencies in this experiment were 25% and 72%, respectively. The Nd:$GdVO_4$ has a large absorption coefficient at 808 nm: $\alpha = 78\ \text{cm}^{-1}$ for $E \parallel c$, and $\alpha = 10\ \text{cm}^{-1}$ for $E \perp c$ in Nd^{3+}-doping of 1.2 at. %. For comparison, the absorption coefficient of Nd:YVO_4 at 808 nm at the same doping level is $\alpha = 40\ \text{cm}^{-1}$ and that of Nd:S-FAP ($Sr_5(PO_4)_3F$) is $\alpha = 23\ \text{cm}^{-1}$.

Furthermore, the vanadates can be doped with Nd^{3+} to higher doping levels because the ionic radius of Gd^{3+} (1.053 Å) is larger that that of Y^{3+} (1.019 Å) and is closer to the ionic radius of Nd^{3+} (1.109 Å). Therefore, the Gd-based laser crystals maintain the excellent spectral properties of Y-based crystals while allow-

ing for larger doping levels of the Nd^{3+} ion. Consequently, it is possible to construct ultracompact, monolithic microchip Nd-lasers. A quasi-CW microchip laser of Nd^{3+} (1.3 at. %):$GdVO_4$ gave a maximum output power of 5 W, with 22% slope efficiency and beam quality of $M^2 \approx 3$, without special optimization.

11.4.2 Q-switching and mode-locking operation

Nd:YVO_4 can be Q-switched using either active or passive techniques. Commercial lasers like the Millenia Pro are based on a Nd:YVO_4 crystal as the gain medium to produce output power in the range of 2 to 10 W at 532 nm, power stability of $\pm 1\%$, and with TEM_{00} laser mode and beam quality of $M^2 < 1$. See, for example, www.spectra-physics.com or www.newport.com/lasers.

The crystal is pumped by a fiber-coupled diode laser bar of at least 20 W. In several cases in which compactness is desirable, such as in microlasers, the passive Q-switches currently used are based on Cr^{4+}:YAG or on semiconductor thin plates such as GaAs. By using a multi-quantum well (InGaAs/GaAs) as a saturable absorber, passive Q-switch pulses as narrow as 56 ps can be obtained.[34] Figure 11.13 presents a layout of such a system and a temporal profile of the Q-switched pulse.

The Nd:$GdVO_4$ laser also has been operated at high repetition rates and with short pulses. This can be obtained by passively Q-switching or mode locking, using saturable absorbers such as a GaAs semiconductor saturable absorber mirror or a Cr^{4+}:YAG. Efficient Q-switching (35.5% conversion efficiency, 46.8% slope efficiency) with 4.05-W average output power, 13-ns pulse duration, and a 45-kHz repetition rate was obtained from a passively Q-switched, diode-pumped Nd:$GdVO_4$ with Cr^{4+}:YAG saturable absorber.[35] Better performance in terms of peak power and pulsewidth, with maximum peak power of 26.4 kW, pulse duration of 6 ns, and

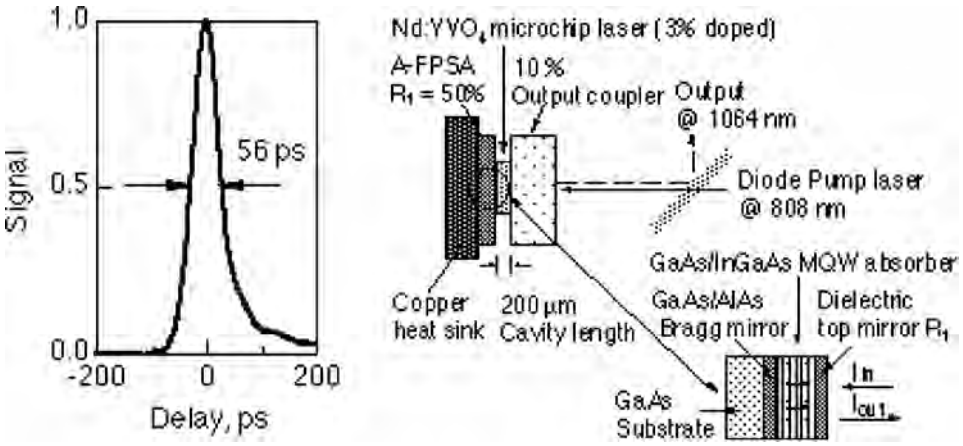

Figure 11.13 The configuration of a Q-switched Nd:YVO_4 microchip laser and the temporal profile of a 56-ps output pulse produced by this laser. (Reprinted from Ref. 34 with permission from the Optical Society of America.)

average output power of 2.1 W at a 37-kHz repetition rate were obtained with a diode-pumped Nd:$GdVO_4$/Cr^{4+}:YAG system.[36, 37] The diode-pumped, passively Q-switched Nd:$GdVO_4$/GaAs produced 1.64 W at an incident pump power of 12 W (13.7% conversion efficiency), with peak power and peak energy of ≈117 W and 19 μJ, respectively, and a repetition rate in the kHz frequency regime.[38] Using intracavity frequency-doubling techniques in a diode-pumped and passively Q-switched laser composed of Nd:$GdVO_4$/Cr^{4+}:YAG/KTP produced output power in the range of ≈400-mW to 440-mW with a pulsewidth of 30–40 ns and repetition rates of 40 kHz.[39] Passive mode locking was obtained using GaAs or Cr^{4+} saturable absorbers, with average output power in the mW range (depending on the coupling optics). The mode-locked pulses within the Q-switched envelope had repetition rates and pulsewidths in the MHz frequency and picosecond (ps) temporal regimes, respectively. For example, passive mode locking was obtained using GaAs or Cr^{4+}:YAG as a saturable absorber with a pulse repetition rate of 140 MHz and duration of 11.5 ps.[37, 40] The pulse repetition rate of a mode-locked Nd:$GdVO_4$ showed a wide dynamic range, from 370 MHz to 3.348 GHz depending on the cavity length, with pulsewidth in the ps time domain and average output of 3.46 W at 3.348 GHz.[41] Passive Q-switched laser transitions at 1063 nm and 1342 nm can be used for simultaneous generation of RGB light for display applications.

Laser diode pumping of a free-running, passively Q-switched Nd:$Y_xGd_{x-1}VO_4$ with GaAs or Cr^{4+}:YAG saturable absorber has been reported recently. The lattice constants of the mixed crystal are between those of YVO_4 and $GdVO_4$ crystals. The free-running operation of such polycrystalline mixed crystal yielded a 7-W output power at 1.064 μm, and >3 W at 1.34 μm.[42] The use of a semiconductor GaAs saturable absorber mirror yielded 2.2-W average output power with 63% slope efficiency, 12-ns pulsewidth, and 199-kHz repetition rate.[43] With Cr^{4+}:YAG saturable absorber, 1.3-W average output power at 9.6-W incident pumping power was obtained. Both output and peak power were enhanced compared to Nd:YVO_4 and Nd:$GdVO_4$. The repetition rate and peak power were 7.7 kHz and 24.5 kW, respectively. Other crystals, such as Nd:$Gd_xLa_{1-x}VO_4$ ($x = 0.8, 0.6, 0.5, 0.45$, also denoted as Nd:LGVO), were studied for spectroscopic properties and laser performance under 808-nm diode pumping, with laser emission at the fundamental (1.06 μm, 1.34 μm) and frequency-doubled (532 nm, 670 nm) wavelengths. The optical properties of the Nd-doped mixed vanadate crystal (Nd:LGVO) were similar to the ytterbium- or gadolinium-based vanadates. The experimental and calculated spectral properties of Nd (1.5 at. %):LGVO ($x = 0.8$) are summarized in Table 11.7.[44]

The laser was operated with slope efficiency of 41% at 1.06 μm and produced 550 mW with emission bandwidth of 4.8 to 5 nm (FWHM) resulting from inhomogeneous broadening. The absorption bandwidth was 2 nm, which is broader than the other vanadates; however, the π polarization emission cross section (3.3×10^{-19} cm^2 at 1.06 μm) is lower than that of Nd:$GdVO_4$ and similar to that of Nd:YAG, as can be seen by comparing with the data in Table 11.6.[45, 56] The reasons for the lower emission cross section values for Nd:LGVO include its larger

inhomogeneous broadening and the Stark splitting of the $^4F_{3/2}$ level in Nd:LGVO ($\approx$26 cm^{-1}), while in Nd:$GdVO_4$ the $^4F_{3/2}$ level is degenerate.

The Tm^{3+}-doped vanadates such as Tm:YVO_4 and Tm:$GdVO_4$ are attractive laser gain media as well. The laser emission of Tm-doped vanadates, centered at 1940 nm, can be used for several applications such as medical, remote sensing, or water detection by tuning into the 1940-nm absorption peak of water. Table 11.8 summarizes the important physical and material parameters of the Tm:$GdVO_4$ that are relevant to laser action.

The data presented in Table 11.8 demonstrate the obvious advantages of Tm:$GdVO_4$ as laser crystals. Solid state lasers based on other Tm-doped hosts, such as YAG or YLF, have narrow absorption and emission bands and low absorption and emission cross sections. The narrow bandwidth transitions ($\approx$4 nm,

Table 11.7 Spectral properties of Nd:LGVO crystals (π polarization).

Properties	Values
Absorption coefficient at 808 nm ($^4I_{9/2} \rightarrow {}^2H_{9/2}$, $^4F_{5/2}$), cm^{-1}	26.8 (1.5 at. % Nd^{3+})
Absorption cross-section, cm^2 at 808 nm	1.47×10^{-19}
Absorption bandwidth (FWHM), nm	6.2
Emission bandwidth (FWHM), nm	4.2
Emission cross-section, cm^2 at 1.06 μm	3.3×10^{-19}
Radiative lifetime, μs	209

Table 11.8 Physical and material characteristics of Tm:$GdVO_4$ (some data taken from Refs. 53 and 54).

Physical parameters, units	Values
Doping level, at. %	5
Ionic density, cm^{-3}	6×10^{-20}
Peak pump wavelength, nm	797.5
Peak absorption coefficient at 797.5 nm, cm^{-1} (π polarization)	15
Peak absorption cross section at 797.5 nm, cm^2 (π polarization)	2.5×10^{-20}
Absorption bandwidth, FWHM, nm	5 (π polarization)
Peak absorption coefficient at 797.5 nm, cm^{-1} (σ polarization)	7.5
Peak absorption cross-section at 797.5 nm, cm^2 (σ polarization)	1.25×10^{-20}
Absorption bandwidth, FWHM, nm	22.5
Fluorescence lifetime, μsec ($^3F_4 \rightarrow {}^3H_6$, 1.9 μm)	800
Fluorescence lifetime, μs ($^3H_4 \rightarrow {}^3H_6$, $\approx$800 nm)	48
Laser emission cross-section at 1800 nm, cm^2 (π polarization)	1.6×10^{-20}
Laser emission cross-section at 1800 nm, cm^2 (σ polarization)	2.9×10^{-20}
Saturation intensity at pumping, kW/cm^2	$\approx$4.5 (σ polarization) $\approx$8.2 (π polarization)
Emission bandwidth, FWHM, nm	$\approx$20

FWHM) imply the need to control the diode-array pumping wavelength by controlling the diode temperature. On the other hand, the broad bandwidth of the electronic transitions in vanadates is advantageous for diode-pumped systems because of the difficulties in fabricating diode lasers with precisely predetermined wavelengths.

In the case of diode end-pumping of Tm:YAG or Tm:YLF, a low-numerical-aperture pumping diode is required for efficient overlap of the pump and resonator modes over the relatively long crystal lengths. This is not relevant to vanadates, which are operated with short crystal length owing to their high absorption coefficient.

The absorption peaks of Tm:YAG or Tm:YLF are blue-shifted relative to the wavelength of the pumping diode of a Nd:YAG, in the spectral range of 780–795 nm. The AlGaAs pumping laser diodes emitting in this range are not as commonly used as in the case of the 808-nm diodes available for pumping the Nd:YAG lasers. The diode lasers operating in the 780–795 nm range have lower brightness, and therefore are more expensive and less efficient. However, as a result of the high absorption coefficient of Tm:YVO_4 or Tm:$GdVO_4$, it is possible to pump the crystals even at 808 nm, which is the "wing" of the absorption profile of Tm-doped vanadates, by these commonly used, inexpensive laser diodes. Figure 11.14 presents a schematic energy-level diagram of Tm:YVO_4 with the laser-pumping diode and the cross-relaxation schemes. Figures 11.15 and 11.16 present the absorption spectra of the $^3H_6 \rightarrow {}^3H_4$ transition ($\approx$800 nm) of the Tm:YVO_4 as well as the fluorescence spectra of the $^3F_4 \rightarrow {}^3H_6$ transition ($\approx$1.9 μm) in both π ($E \parallel c$) and σ ($E \perp c$) polarizations.

Tm:YVO_4 and Tm:$GdVO_4$ have higher absorption and emission cross sections than a Tm:YAG crystal, as Table 11.8 shows. The emission cross section of Tm:YAG is $\sigma_{em} \approx 3 \times 10^{-21}$ cm^2 in the spectral range of 1950 to 2025 nm, and $\sigma_{em} \approx 2 \times 10^{-21}$ cm^2 at 2011 nm. This is an order of magnitude lower than the values of Tm:$GdVO_4$ presented in Table 11.8. The peak absorption cross section in Tm-doped vanadates at 797–800 nm is higher than for Tm:YAG. Recalling the data, for Tm:$GdVO_4$, π polarization, the absorption cross section is $\sigma_{ab} = 2.5 \times 10^{-20}$ cm^2, whereas for Tm:YAG, it has the value of $\sigma_{ab} = 6 \times 10^{-21}$ cm^2

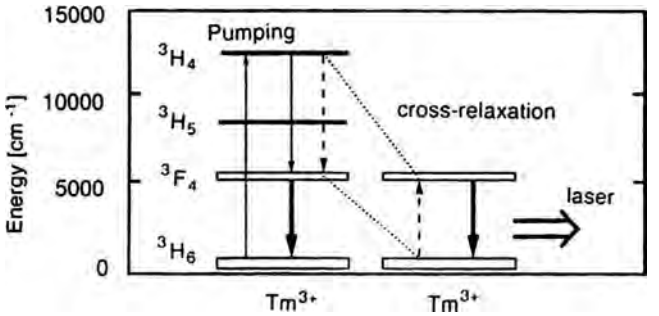

Figure 11.14 Schematic energy-level diagram with diode-pumping and cross-relaxation pathways. (Reprinted from Ref. 27 with permission from the American Institute of Physics.)

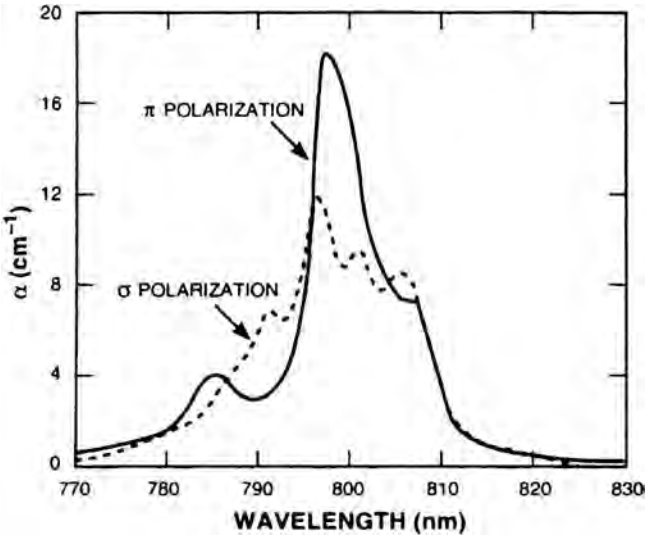

Figure 11.15 Absorption spectrum of the $^3H_6 \rightarrow {}^3H_4$ transition of Tm^{3+} (5 at. %):YVO_4 for both π- and σ-polarizations. (Reprinted from Ref. 56 with permission from the Optical Society of America and MIT Lincoln Laboratory, Lexington, Massachusetts.)

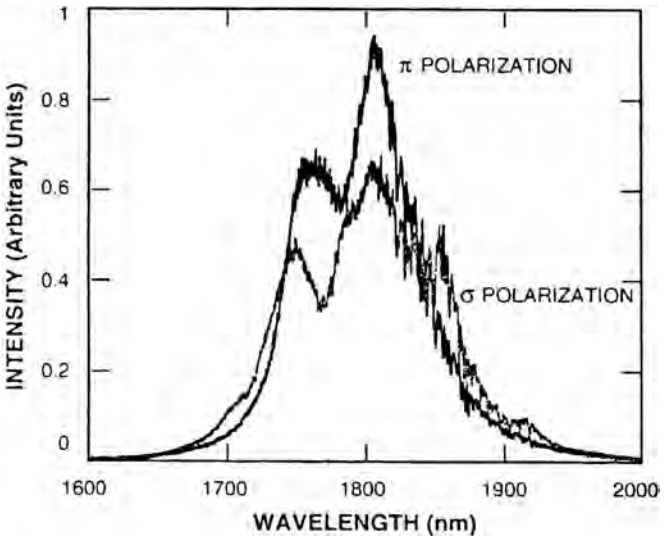

Figure 11.16 Polarized fluorescence spectra of Tm (5 at. %):YVO_4 laser crystal for both π- and σ-polarizations. (Reprinted from Ref. 56 with permission from the Optical Society of America and MIT Lincoln Laboratory, Lexington, Massachusetts.)

at the same wavelength. Therefore, vanadates are more suitable for a diode side-pumping configuration[57] or for microchip lasers.[58]

The natural birefringence of vanadates dominates the thermally induced birefringence effects typical to cubic crystals like YAG, with reduced thermal effects on laser performance and beam quality.

The saturation flux in a quasi-four-level system is given by

$$I_{\text{sat}} = \frac{h\nu}{\sigma_{\text{em}}\tau_{\text{em}}},$$

where h is Planck's constant, ν is the laser transition frequency, σ_{em} is the stimulated emission cross-section, and τ_{em} is the spontaneous fluorescence lifetime of the lasing level. One assumes that the $^3F_4 \rightarrow {}^3H_6$ laser transition in Tm-vanadates and Tm:YAG, peaking at $\approx$1.9 μm, is a quasi-four-level. The saturation flux of Tm:$GdVO_4$ can be calculated from the data presented in Table 11.8, and has the value of $I_{\text{sat}}(GdVO_4) \approx$ 4.5-kW/cm^2 for σ polarization and $\approx$8.2-kW/cm^2 for π polarization. Knowing the values of the stimulated emission cross section ($\sigma_{\text{em}} \approx 3 \times 10^{-21}$ cm^2) in the range 1950 to 2025 nm and the fluorescence lifetime ($\tau_{\text{em}} = 8.5$ ms for Tm^{3+} 1.0 at. %) of the $^3F_4$ level in Tm:YAG yields the value of $I_{\text{sat}} \approx$ 4.1 kW/cm^2 to 3.3 kW/cm^2 (depending on the Tm^{3+} concentration) for Tm:YAG. It is clear that the saturation values of both Tm:$GdVO_4$ (σ polarization) and Tm:YAG are similar, while the saturation flux for π polarization is higher as a result of the smaller absorption peak cross section in this polarization direction. The large absorption cross-section of Tm-vanadates in the 797–808 nm spectral range is useful for sensitized Ho^{3+} $^5I_7 \rightarrow {}^5I_8$ ($\approx$2 μm) lasing action in a Tm^{3+}, Ho^{3+} codoped system. This results from the fact that the large absorption cross-section allows for lowering the Tm^{3+} doping level in a Tm:Ho:YVO_4 system and consequently inhibits the $Ho^{3+} \rightarrow Tm^{3+}$ back transfer. Therefore, it is possible to obtain efficient Tm → Ho energy transfer (up to 87%) and a low pumping threshold.[26]

Tm-doped vanadates have been operated mostly in compact or monolithic microchip diode-pumped configurations. By employing an AlGaAs diode laser at 806 nm to pump a Tm^{3+} (6.9 at. %):$GdVO_4$ microchip laser, a maximum output power of 1.4 W at 1.9 μm with very low slope efficiency (5.5%) was obtained. Under Ti:Sapphire pumping at 797 nm or 806 nm, slope efficiency of 58% was obtained.[59] However, one should notice that the extrapolated pumping threshold was very high, $\approx$680 mW of absorbed power, and the total efficiency was only $\approx$10%.

Other various microchip $GdVO_4$ and YVO_4 lasers doped with Nd^{3+}, Tm^{3+}, or Er^{3+} were investigated and reported by Bourdet et al.[60] and Zagumennyi et al.[13] (for example, 48% slope efficiency for Tm:YVO_4 pumped at 800 nm) and Zayhowski et al.[56] Zayhowski et al. used a monolithic Fabry-Perot linear resonator with Tm (5 at. %):YVO_4 (440-μm thickness), pumped by a Ti:Sapphire laser at $\approx$800 nm with π ($E \parallel c$) polarization. They obtained a near-diffraction-limited, 1.92-μm laser beam at ambient temperature, with output power of 150 mW and slope efficiencies of 41% to 48% in the temperature range of 10 to 30°C, respectively. Impressive results in terms of slope efficiency, beam quality, tunability, and pumping threshold were obtained by Sorokin et al.[61] The Tm:$GdVO_4$ was end-pumped at 797 nm in the π polarization ($E \parallel c$) direction by a Ti:Sapphire laser and produced $\approx$230-mW output power (TEM_{00}) at $\approx$640-mW of absorbed pumping

power, with output coupling mirror of $R_{out} = 96.5\%$. The slope efficiency under these conditions was 55%, the total efficiency ≈36%, and the pumping threshold as low as 75 mW of absorbed power. The Tm:$GdVO_4$ laser also exhibited tunability over 140 nm around the peak of emission (≈1.9 μm), spanning a spectral range of 1860–2000 nm.

It is worthwhile to mention another laser host, $YAlO_3$, a biaxial crystal also called yttrium aluminum perovskite (YAP). This crystal formula is derived from the Y_2O_3-Al_2O_3 system and is similar to that of YAG. When doped with Tm^{3+}, the Tm:YAP crystal exhibits excellent optical properties relative to Tm:YAG. For example, the emission cross section is almost two times higher than for Tm:YAG. This fact, combined with the excellent mechanical properties of YAP (similar to those of YAG) and its natural birefringence, makes it potentially an excellent laser-host material. Initial results of room-temperature operation of diode-pumped Tm:YAP indicated its potential performance: the Tm:YAP diode-pumped system produced 730-mW output power at 3-W input power with a 40.3% slope efficiency and 24% optical-to-optical efficiency. The Tm:YAP laser is less sensitive to temperature changes than a codoped Tm:Ho:YAP, namely, 4.5 mW/°C and 7.5 mW/°C, respectively. Codoping the Tm:YAP with Ho^{3+} ions generated 270-mW output power (9% optical-to-optical conversion efficiency) under the same experimental conditions. Deleterious upconversion processes in the doubly doped system, which reduced the excited state population, explain this performance reduction.[62]

The main physical and material characteristics of Tm:YAP laser crystal are summarized in Table 11.9.

Vanadate crystals can be doped with other rare-earth ions to produce crystals such as Yb^{3+}:YVO_4, which is another potential candidate for efficient diode-pumped solid state lasers emitting at around 1.0 μm. It has very close absorp-

Table 11.9 Physical and material characteristics of Tm:YAP (some data taken from Refs. 63 and 64).

Physical parameters, units	Values
Tm^{3+} concentration, at. %	4.2
Refraction index at 1060 nm	$a = 1.914$, $b = 1.925$, $c = 1.940$
dn/dT, K^{-1}	$a = 9.7 \times 10^{-6}$, $b = 14.5 \times 10^{-6}$
Thermal conductivity, W/m · K	11
Hardness, moh	8.5
Thermal expansion coefficient, $°C^{-1}$	$a = 9.5 \times 10^{-6}$, $b = 4.2 \times 10^{-6}$, $c = 10.8 \times 10^{-6}$
Peak absorption wavelength, nm (π- and σ-polarizations)	≈7.75 (π) ≈793 (σ), ≈800 (σ)
Peak absorption coefficient, cm^{-1} (π- and σ-polarizations)	≈6
Emission wavelength, μm	1.96–2.02
Peak emission cross-section at 1.95 μm, cm^2	6.0×10^{-21}
Fluorescence lifetime, ms ($^3F_4 \rightarrow {}^3H_6$, 1.9 μm)	4.4 ± 0.3
Saturation intensity at pumping, kW/cm^2	≈3.9

Table 11.10 Physical and material characteristics of Yb:YVO_4 (some data taken from Ref. 14).

Physical parameters, units	Values
Peak absorption cross-section at 984.5 nm, cm^2 (π polarization)	6.74×10^{-20}
Peak absorption cross-section at 970.0 nm, cm^2 (σ polarization)	1.8×10^{-20}
Peak emission cross-section at 975 nm, cm^2 (σ polarization)	0.98×10^{-20}
Peak emission cross-section at 986 nm, cm^2 (σ polarization)	1.73×10^{-20}
Peak emission cross-section at 1010 nm, cm^2 (σ polarization)	0.84×10^{-20}
Peak emission cross-section at 985.5 nm, cm^2 (π polarization)	4.28×10^{-20}
Fluorescence lifetime, μs ($^3F_4 \rightarrow {}^3H_6$, 1.9 μm)	318 ± 25

tion and emission peaks. Table 11.10 presents some of the laser characteristics of Yb:YVO_4 crystal. The absorption cross section of Yb:YVO_4 is higher by an order of magnitude than that of Yb:YAG, and its emission cross section is of the same order of magnitude.

References

1. D. W. Hughes and J. R. M. Barr, "Laser diode pumped solid state lasers," *J. Phys. D: Appl. Phys.* **25**, 563–586 (1992).
2. G. P. A. Malcolm and A. I. Ferguson, "Diode pumped solid state lasers," *Contemporary Physics* **32**(5), 305–319 (1991).
3. D. L. Sipes, "Highly efficient neodymium yttrium aluminum garnet laser end pumped by a semiconductor laser array," *Appl. Phys. Lett.* **47**(2), 74–76 (1985).
4. L. Turi and T. Juhasz, "Diode-pumped Nd:YLF all-in-one laser," *Opt. Letters* **20**(14), 1541–1543 (1995).
5. L. Turi and T. Juhasz, "High power diode-pumped Nd:YLF all-in-one laser," *Conference on Lasers and Electro-Optics* **15**, 122–123, *OSA Technical Digest Series* (1995).
6. I. P. Mercer, Z. Chang, C. N. Dansan, et al., "Diode-pumped picosecond Nd:YLF laser oscillation at 1053 nm," *Opt. Commun.* **107**, 77–82 (1994).
7. L. Turi and T. J Juhasz, "High power longitudinally end-diode-pumped Nd:YLF regenerative amplifier," *Opt. Letters* **20**(2), 154–156 (1995).
8. J. Zehetner, "Highly efficient diode-pumped elliptical mode Nd:YLF laser," *Opt. Commun.* **117**, 273–276 (1995).
9. J. K. Lincoln and A. I. Ferguson, "All solid state intracavity doubled Nd:YLF laser producing 300 mW of 659 nm light," *Opt. Letters* **19**(16), 1213–1215 (1994).
10. I. Lee, L. P. Ketteridge, and P. A. Bundi, "Passive Q-switched CW pumped Nd:YLF oscillator," *Conference on Lasers and Electro-Optics* **11**, Paper CFJ4, 500–501, *OSA Technical Digest Series* (1997).

11. F. G. Anderson, P. L. Summers, H. Weidner, P. Hong, and R. E. Peale, "Interpretive crystal-field parameters: Application to Nd^{3+} in $GdVO_4$ and YVO_4," *Phys. Rev. B* **50**(20), 14802–14808 (1994).
12. L. Fornasiero, S. Kuck, T. Jensen, G. Huber, and B. H. T. Chai, "Excited state absorption and stimulated emission of Nd^{3+} in crystals. Part 2: YVO_4, $GdVO_4$, and $Sr_5(PO_4)_3F$," *Appl. Phys. B* **67**(5), 549–553 (1998).
13. A. I. Zagumennyi, T. D. Zavartsev, P. A. Studenikin, et al., "$GdVO_4$ crystals with Nd^{3+}, Tm^{3+}, Ho^{3+}, Er^{3+} ions for diode pumped microchip laser," *Proc. SPIE* **2698**, 182–192 (1996).
14. C. Frankel, D. Fagundes-Peters, S. T. Fredrich, et al., "Continuous wave laser operation of Yb^{3+}:YVO_4," *Appl. Phys. B* **79**, 543–546 (2004).
15. R. A. Fields, M. Birnbaum, and C. L. Fincher, "Highly efficient Nd:YVO_4 diode-laser end-pumped laser," *Appl. Phys. Lett.* **51**, 1885–1886 (1987).
16. Y. Nobe, H. Takashima, and T. Katsumata, "Decoloration of yttrium orthovanadate laser host crystals by annealing," *Opt. Letters* **19**, 1216–1218 (1994).
17. J. L. He, J. Du, J. Sun, et al., "High efficiency single- and dual-wavelength Nd:$GdVO_4$ lasers pumped by a fiber-coupled diode," *Appl. Phys. B* **79**, 301–304 (2004).
18. G. Feugnet, M. Schwartz, C. Larat, J. P. Pocholle, and M. Papuchon, "TEM_{00} high efficiency surface emitting laser diode longitudinally pumped Nd:YVO_4 laser," *Proc. on Advanced Solid State Lasers* **20**, 15–19 (1994).
19. G. Feugnet, C. Bussac, C. Larat, M. Schwartz, and J. P. Pocholle, "High efficiency TEM_{00} Nd:YVO_4 laser longitudinally pumped by a high power array," *Opt. Lett.* **20**, 157–159 (1995).
20. H. Nagai, M. Kume, A. Yoshikawa, K. Itoh, and C. Hamaguchi, "Periodic pulse oscillation in an intracavity-doubled Nd:YVO_4 laser," *Appl. Optics* **35**(27), 5392–5394 (1996).
21. R. Koch, G. Hollemann, R. Clemens, et al., "Effective near diffraction-limited diode-pumped thin disk Nd: YVO_4 laser," *Conference on Lasers and Electro-Optics* **11**, *OSA Technical Digest Series*, 480 (1997).
22. J. Zhang, M. Quade, K. M. Du, et al., "Efficient TEM_{00} operation of Nd:YVO_4 laser end pumped by fibre-coupled diode laser," *Electron. Lett.* **33**(9), 775–777 (1997).
23. V. Lupei, N. Pavel, Y. Sato, and T. Taira, "Highly efficient 1063 nm continuous-wave laser emission in Nd:$GdVO_4$," *Opt. Letters* **28**(23), 2366–2368 (2003).
24. M. Bettinelli, F. S. Ermeneux, R. Moncorge, and E. Cavalli, "Fluorescence dynamics of YVO_4:Tm^{3+}, YVO_4:Tm^{3+}, Tb^{3+} and YVO_4:Tm^{3+}, Ho^{3+} crystals," *J. Phys: Cond. Matt.* **10**(37), 8207–8215 (1998).
25. G. L. Bourdet, G. Lescroart, and R. Muller, "Performance and efficiency of 2 microns Tm:YVO_4 and Tm,Ho:YLF microchip lasers," *Proc. SPIE* **3549**, 48–56 (1998).
26. W.-q. Yang, "Sensitized luminescence of Ho^{3+} by Tm^{3+} in Tm,Ho co-doped YVO_4 crystal," *Chinese J. Lumen.* **22**(2), 175–181 (2001).

27. K. Ohta, H. Saito, and M. Obara, "Spectroscopic characterization of Tm^{3+}:YVO_4 crystal as an efficient diode pumped laser source near 2000 nm," *J. Appl. Phys.* **73**(7), 3149–3152 (1993).
28. S. Golab, P. Solarz, G. Dominiak-Dzik, T. Lukasiewicz, and W. Ryba-Romanowski, "Spectroscopy of YVO_4:Ho^{3+} crystals," *Appl. Phys. B* **74**, 237–241 (2002).
29. J. Liu, Z. Shao, H. Zhang, et al., "Diode laser array end-pumped 14.3-W CW Nd:$GdVO_4$ solid state laser at 1.06 μm," *Appl. Phys. B* **69**(3), 241–243 (1999).
30. T. W. Ren, J. L. He, C. Zhang , et al., "Simultaneous generation of three primary colours using aperiodically poled $LiTaO_3$," *J. of Physics: Cond. Matt.* **16**(18), 3289–3294 (2004).
31. A. Agnesi, A. Guandalini, G. Reali, S. Dell'Acqua, and G. Piccinno, "High brightness 2.4-W continuous-wave Nd:$GdVO_4$ laser at 670 nm," *Opt. Lett.* **29**(1), 56–58 (2004).
32. J. Liu, B. Ozygus, J. Ehard, et al., "Diode-pumped CW and Q-switched Nd:$GdVO_4$ laser operating at 1.34 μm," *Opt. and Quantum Electron.* **35**(8), 811–824 (2003).
33. J. Liu, C. Wang, C. Q. Wang, et al., "Diode end-pumped Q-switched high-power intracavity frequency-doubled Nd:$GdVO_4$/KTP green laser," *Appl. Phys. B* **72**(2), 171–174 (2001).
34. B. Braun, F. X. Kartner, G. Zhang, M. Moser, and U. Keller, "Passively Q-switched diode-pumped 56-ps microchip laser," *Conference on Lasers and Electro-Optics* **11**, *OSA Technical Digest Series*, 499 (1997).
35. J. Liu, B. Ozygus, Y. Suhui, et al., "Efficient passive Q-switching operation of a diode-pumped Nd:$GdVO_4$ laser with a Gr^{4+}:YAG saturable absorber," *J. Opt. Soc. Amer. B* **20**(4), 652–661 (2003).
36. S. P. Ng, D. Y. Tang, L. J. Qin, and X. L. Meng, "High power passively Q-switched Nd:$GdVO_4$ lasers," *Opt. Commun*. **229**(1–6), 331–336 (2004).
37. S. Zhang, E. Wu, and H. Zeng, "Q-switched mode-locking by Cr^{4+}:YAG in a laser-diode-pumped c-cut Nd:$GdVO_4$ laser," *Opt. Commun.* **231**(1–6), 365–369 (2004).
38. L. J. Quin, X. L. Meng, Ch.L. Du, et al., "A diode-pumped passively Q-switched Nd:$GdVO_4$ laser with GaAs saturable absorption," *Opt. and Laser Technology* **36**(1), 47–50 (2004).
39. J. Liu, J. Yang, and J. He, "Diode-pumped passively Q-switched intracavity frequency doubled Nd:$GdVO_4$/KTP green laser," *Opt. and Laser Technology* **36**(1), 31–33 (2004).
40. S. Zhang, E. Wu, H. Pan, and H. Zeng, "Passive mode locking in a diode-pumped Nd:$GdVO_4$ laser with a semiconductor saturable absorber mirror," *IEEE J. Quant. Electron.* **40**(5), 505–508 (2004).
41. J. Kong, D. Y. Tang, S. P. Ng, et al., "Diode-pumped passively mode-locked Nd:$GdVO_4$ laser with GaAs saturable absorber," *Appl. Phys. B* **79**(2), 203–206 (2004).

42. L. Zhu, L. Quin, X. Meng, et al., "New high-efficiency laser crystal Nd:$YGdVO_4$," *J. Synthetic Crystals* **32**(2), 148–151 (2003).
43. Y. He, X. Hou, L. Qin, et al., "Laser diode pumped passively Q-switched Nd:$Y_xGd_{1-x}VO_4$ laser with GaAs saturable absorber," *Opt. Commun.* **234**(1–6), 305–308 (2004).
44. H. D. Jiang, J. Y. Wang, H. J. Zhang, X. B. Hu, and H. Liu, "Optical-transition properties of the Nd^{3+} ion in $Gd_{0.8}La_{0.2}VO_4$ crystal," *J. Appl. Phys.* **92**(7), 3647–3650 (2002).
45. H. Zhang, C. Wang, L. Zhu, et al., "Growth and characterization of series Nd:$Gd_xLa_{1-x}VO_4$ ($x = 0.8, 0.6, 0.45$) crystals," *J. Materials Res.* **17**(3), 556–562 (2002).
46. V. G. Ostroumov, G. Huber, A. I. Zagumennyi, et al., "Spectroscopic properties and lasing of Nd:$Gd_{0.5}La_{0.5}VO_4$ crystals," *Opt. Commun.* **124**(1–2), 63–68 (1996).
47. D. C. Brown, R. Nelson, and L. Billings, "Efficient CW end-pumped, end-cooled Nd:YVO_4 diode-pumped laser," *Appl. Optics* **36**(33), 8611–8613 (1997).
48. L. Krainer, R. Paschotta, J. Aus de Au, et al., "Passively mode-locked Nd:YVO_4 laser with up to 13 GHz repetition rate," *Appl. Phys. B* **69**, 245–247 (1999).
49. J. Liu, Z. Shao, H. Zhang, et al., "High power end-pumped CW Nd:$GdVO_4$ laser formed with flat-flat cavity," *Optics and Laser Technology* **31**(6), 459–462 (1999).
50. C. P. Wyss, W. Luthy, H. P. Weber, et al., "Performance of a diode-pumped 5 W Nd^{3+}:$GdVO_4$ microchip laser at 1.06 μm," *Appl. Phys. B* **68**, 859–661 (1999).
51. J. Liu, Z. Shao, H. Zhang, et al., "Diode-laser-array end-pumped intracavity frequency-doubled 3.6 W CW Nd:$GdVO_4$/KTP green laser," *Opt. Commun.* **173**(1–6), 311–314 (2000).
52. C. Li, J. Song, D. Shen, et al., "Diode pumped passively Q-switched Nd:$GdVO_4$ lasers operating at 1.06 mm wavelength," *Appl. Phys. B* **70**, 471–474 (2000).
53. K. Ohta, H. Saito, M. Obara, and N. Djeu, "Characterization of a longitudinally pumped CW, room temperature operation of Tm^{3+}:YVO_4 laser," *Jpn. J. Appl. Phys.* **32**(4), Part 1, 1651–1657 (1993).
54. H. Saito, S. Chaddha, R. S. F. Chang, and N. Djeu, "Efficient 1.94-μm Tm^{3+} laser in YVO_4 host," *Optics. Lett.* **17**(3), 189–191 (1992).
55. K. Ohta, H. Saito, and M. Obara, "Spectroscopic characterization of Tm^{3+}:YVO_4 crystal as an efficient diode pumped laser source near 2000 nm," *J. Appl. Phys.* **73**(7), 3149–3152 (1993).
56. J. J. Zayhowski, J. Harrison, C. Dill III, and J. Ochoa, "Tm:YVO_4 microchip laser," *Appl. Opt.* **34**(3), 435–437 (1995).
57. K. Waichman, L. Kravchik, J. Kagan, C. Labbe, and Y. Kalisky, "Gain mode and laser mode matching in side-pumped Nd:YVO_4 and Nd:YAG lasers," *Opt. Mater.* **16**, 163–172 (2001).

58. C. P. Wyss, W. Luthy, H. P. Weber, et al., "Emission properties of a Tm^{3+}:$GdVO_4$ microchip laser at 1.9 μm," *Appl. Phys. B* **67**(5), 545–548 (1998).
59. C. P. Wyss, W. Luthy, H. P. Weber, et al., "A diode-pumped 1.4-W Tm^{3+}:$GdVO_4$ microchip laser at 1.9 μm," *IEEE J. Quant. Electron.* **34**(12), 2380–2382 (1988).
60. G. L. Bourdet, G. Lescroart, and R. Muller, "Spectral characteristics of 2 μm microchip Tm:YVO_4 and Tm,Ho:YLF lasers," *Opt. Commun.* **150**(1-6), 141–146 (1998).
61. E. Sorokin, A. N. Alpatiev, I. T. Sorokina, A. I. Zagumennyi, and I. A. Shcherbakov, "Tunable efficient continuous-wave room temperature Tm^{3+}:$GdVO_4$ laser," *OSA Trends in Optics and Photonics (TOPS)* **68**, *Advanced Solid State Lasers*, WA2-1–WA2-3, *OSA Technical Digest, Postconference Edition* (2002).
62. I. F. Elder and J. P. Payne, "Lasing in diode pumped thulium and holmium YAP," *OSA Trends in Optics and Photonics on Advanced Solid State Lasers* **1**, 319–325 (1996).
63. I. F. Elder and J. Payne, "Diode-pumped, room temperature Tm:YAP laser," *Appl. Optics* **36**(33), 8606–8610 (1997).
64. S. A. Payne, L. L. Chase, L. K. Smith, W. L. Kway, and W. F. Krupke, "Infrared cross-section measurements for crystals doped with Er^{3+}, Tm^{3+}, and Ho^{3+}," *IEEE J. Quantum Electron.* **28**, 2619–2630 (1992).
65. T. Jensen, V. G. Ostroumov, J. P. Meyn, et al., "Spectroscopic characterization and laser performance of diode-laser-pumped Nd:$GdVO_4$," *Appl. Phys. B* **58**, 373–379 (1994).
66. H. Zhang, X. Meng, L. Zhu, and Z. Yang, "Growth and thermal properties of Nd:$GdVO_4$ single crystal," *Mat. Res. Bull.* **34**(10-11), 1589–1593 (1999). Also, some date taken from various catalogs and references (for example, Ref. 13).
67. W. Koechner, *Solid State Laser Engineering*, 5th Revised and Updated Edition, Springer-Verlag, Berlin, Heidelberg, and New York, Chapter 5 (1999).

Index

A

absorption coefficient, 8, 68
absorption cross section, 8
activator, 94
antibonding orbitals, 23

B

β-BaB_2O_4, 3
BaY_2F_8, 55
BBO, 3
beam quality, 51, 146, 165
birefringence, 43
bonding orbitals, 23
branching ratio, 77

C

cascade emission, 57
characteristics of lasers, generally, 7
composite Yb:YAG laser rods, 145
concentration quenching, 141
confocal resonator, 50
covalent bonding, 22
critical separation, 96
cross-relaxation, 113
Cr-Tm interaction, 113
crystals
  binding, 18
  structure of, 17
  types, 18
CTH system, 106–107
  efficiencies, 112
Czochralski method, 27

D

design of laser
  material, 8–9
  mechanical, 9
diffusion of energy, 99
diffusion-bonded endcaps, 134, 148
diode array, 197
diode bars, 197
diode-pumping
  advantages and characteristics, 189–191
  longitudinal pumping, 191–193
  schemes, 158–160, 191
  temperature control, 198–200
  transverse pumping, 194–196
diode types, 196–198
dipole-dipole interaction, 95
disk configuration, *see* thin disk pumping
disordered (mixed) garnets, 33
distribution coefficient, 27

E

electric dipole, 1
electric-quadrupole transitions, 79
emission cross section, 8
endcaps, 145
end-pumping, 145
energy acceptor, 77
energy donor, 77
energy-gap dependence, 82, 97
energy-gap law, 83, 98
energy migration, 95
energy sensitization, 105
energy transfer, 2, 93
  models generally, 2
  selective, 121
  standard theory, 101
  statistical model, 100–101
Er:YVO_4, 173
exchange interaction, 96, 101
excited state relaxation, 98
extraordinary polarization, 48

F

face pumping, 145
fiber-coupled pumping, 151
fiber coupling, 160
fluorescence lifetime, 51
folded-cavity geometry, 162
forced electric dipole transition, 79

G

garnet crystal
  chromium and neodymium-doped, 28–33
  disordered (mixed), 33
  properties generally, 26
  structure and composition, 25
Gaussian lineshape, 73
$Gd_3Ga_5O_{12}$, 25
GGG, 25
glass ceramics, 35

H

hollow lens duct, 145
holmium laser, 113, 125
  advantages, 127
  CW operation, 128–129
  end-pumped, 130–135
  pulsed operation, 130
  side-pumped, 136
homogeneous broadening, 73
hopping model, 99
host materials, 13
host properties, 13–15
Ho-Tm back interaction, 117
Ho:YAG, 2
Ho:YVO_4, 173

I

inhomogeneous broadening, 73
ionic bonding, 20

K

$KTiOPO_4$, 3
KTP, 3

L

laser diode-pumped solid state laser (LDSSL), 157
LBO-LiB_3O_5, 5
Lennard-Jones potential, 19
lens duct, 134
lens-duct coupling, 160
$LiNbO_3$, 3
longitudinal pumping, 145, 191–193
loop mechanism, 62
Lorentzian lineshape, 71

M

Madelung constant, 22
magnetic dipole, 1, 79
market for solid state lasers, 10
microlaser, 3, 141, 172
microparameter constant, 96
multiphonon decay rate, 80–87
  temperature dependence of, 88–90
multiphoton excitations, 8
multiphonon relaxation (MPR), 79–88
multistripe array, 197

N

Nd:$GdVO_4$, 174
Nd:YAG, 2
Nd:YAG ceramic laser, 38
Nd:$YAlO_3$ (YALO), 2
Nd:YLF, 2, 161–165
Nd:YVO_4, *see* vanadate crystals
nonradiative decay rates, 8, 50, 77

O

optical parametric oscillation (OPO), 5
optical properties of laser materials, 7–8
ordinary polarization, 48
oscillator strength, 75

P

parity-allowed transitions, 79
phonon-assisted energy transfer, 77, 97
polarization
  extraordinary, 48
  ordinary, 48
properties of laser materials, 7
pumping schemes compared, 158–160

Q

Q-switching, 176
quantum defect, 141
quantum gap, 44
quantum jump, 67
quasi-three-level host, 144

R

radiative decay, 79
radiative energy transfer, 93
radiative quantum efficiency, 77
radiative rates, 8, 77
resonant energy transfer, 94
Russell-Saunders coupling, 11

S

second harmonic generation (SHG), 6
selective energy transfer, 121
sensitizer, 94
SFAP, 157
side-pumping, 145
single-stripe devices, 197
spontaneous emission, 73
standard theory of energy transfer, 101
statistical model of energy transfer, 100–101
stimulated absorption, 72
stimulated emission, 72
SVAP, 157

T

Tanabe-Sugano diagram, 36
temperature dependence, 88–90, 108, 111
thermal conductivity, 45
thermal lensing, 43
thermal load, 44
thermal-shock parameter, 37
thermoelectric cooler, 199
thin disk lasers, 3
thin disk pumping, 145
threshold power, 191
Ti:sapphire laser, 3
Tm^{3+} concentration, effect of, 110
Tm-Ho interaction, 116
Tm:Ho:YAP, 182
Tm-Tm interaction, 114
Tm:YAP, 182
Tm:YVO_4, 173
transverse pumping, 14, 194–196

U

upconversion, 58
  applications, 60
  loop mechanism, 62

V

vanadate crystals
  advantages and disadvantages, 166–167
  as alternative host, 158, 166
  mode-locking, 176
  properties, 168
  performance charactersitics, 170–171
  Q-switching, 176
Van der Waals interaction, 19

W

waveguide lasers, 3

Y

YALO, 2
Yb:YAG laser
  advantages, 141–142
  characteristics, 143
  disadvantages, 144
  end-pumping, 145–146
  face-pumping, 149
  side-pumping, 147–148
  thin disk configuration, 149–153
YLF
  holmium-doped, 53–54
  neodymium-doped, 51–53
  nonradiative decay rates, 50
  properties generally, 43–44
  refractive index, 46–49
  thulium-doped, 54–55
ytterbium laser, *see* Yb-YAG laser

Dr. Yehoshua Kalisky graduated from the Hebrew University of Jerusalem. Since that time he has initiated and conducted research with significant scientific and technical contributions to the field of solid state spectroscopy, photophysical processes in laser materials, photonics, electro-optics, and laser physics. As a researcher, group leader, and manager, he was responsible for research and development of various types of solid state, dye, and gas lasers and implementing them into various applications. In recent years he was instrumental in the design of solid state laser systems, and the development of novel types of passively Q-switched, diode-pumped solid state lasers and relevant technologies for industrial applications. Dr. Kalisky has spent several years in leading laser industries and universities in the U.S., France, and Israel. Currently he is at the Nuclear Research Center Negev (NRCN), Israel, in the Chemistry Division. Dr. Kalisky is the author or coauthor of more than 140 scientific publications, five international patents, and numerous conference presentations.